UNIVERSITÀ
DEGLI STUDI
DI PADOVA

Sede Amministrativa: Università degli Studi di Padova

Dipartimento di Ingegneria Industriale

CORSO DI DOTTORATO DI RICERCA IN: INGEGNERIA INDUSTRIALE
INDIRIZZO: INGEGNERIA DELL'ENERGIA
CICLO XXIX

TWO-PHASE HEAT TRANSFER IN MINICHANNELS: MODELING AND HEAT PUMP APPLICATIONS

Tesi redatta con il contributo finanziario di Riello S.p.A.

Coordinatore: Prof. Paolo Colombo
Supervisore: Prof. Davide Del Col

Dottorando: Paolo Toninelli

ABSTRACT

Nowadays there is an increasing demand for compact devices with high performance in heating and cooling applications; a compact geometry permits to have a lower charge of refrigerant as compared to conventional HX.
The present research activity is focused on the analysis of condensation phenomena inside a single minichannel and on the application of minichannels technology for condensers and evaporators in heating and cooling systems.
When the inner diameter decreases, new parameters can influence in a significant way the two-phase heat transfer. Nowadays powerful numerical tools permit to obtain a detailed analysis of two-phase heat transfer mechanisms inside channels and to model the interaction between the phases without using any empirical closure law.
In this way it is possible to have a numerical approach that can be applied for different fluids and operating conditions being independent from the empirical correlations found in the literature.
In particular the Volume Of Fluid (VOF) method is used to have investigate the main features of condensation phenomena inside a single minichannel and the numerical results have been validated against experimental data.
Since the low mass flux conditions are the least investigated due to the high experimental uncertainly when the heat flow rate is in the order of few watts, numerical simulations have been performed to get an insight into the condensation process at these operating conditions, focusing the investigation on the effect of fluid properties, channel shape, channel size and channel orientation.
The VOF simulations were then extended to the study of interfacial instabilities during the R134a annular-wavy downflow condensation inside a vertical 3.4 mm i.d. minichannel. Computational results about the evolution in time of the vapour-liquid interface along the channel have been validated against experimental visualizations and the influence of the waves on heat transfer has been analyzed.
Besides the numerical analysis of the heat transfer, the application of minichannel technology in heating and cooling systems has also been investigated.
The use of minichannels in heat exchangers allows to significantly decrease the refrigerant charge as compared to conventional finned coil heat exchangers. This is particularly useful in a reversible heat pump when the same heat exchanger can work as a condenser or as an evaporator and it is particularly useful when the refrigerant is flammable or middly flammable.
The development of physical models are necessary to the prediction of the performance and the design of completely innovative systems.
Computational procedures have been thus developed to evaluate the performance of a reversible water-to-water and air-to-water heat pump using minichannels in the heat transfer with air, considering both the air and the ground as possible heat sources.
This work has been possible thanks to the financial support of Riello SpA.

RIASSUNTO

Attualmente vi è una crescente domanda di dispositivi compatti con prestazioni elevate in applicazioni di riscaldamento e raffreddamento; una geometria compatta consente di avere una carica ridotta di refrigerante rispetto agli scambiatori convenzionali.
L'attività di ricerca è focalizzata sull'analisi del fenomeni di condensazione all'interno di un singolo minicanale e sull'applicazione della tecnologia a minicanali per condensatori ed evaporatori in sistemi di riscaldamento e raffreddamento.
Quando il diametro interno diminuisce, nuovi parametri possono influenzare in modo significativo il trasferimento di calore in deflusso bifase. Oggigiorno potenti strumenti numerici permettono di ottenere un'analisi dettagliata dei meccanismi di trasferimento di calore in deflusso bifase all'interno di canali e di modellare l'interazione tra le fasi senza utilizzare alcuna legge empirica di chiusura. In questo modo è possibile avere un approccio puramente numerico che può essere applicato per diversi fluidi e diverse condizioni operative, risultando indipendente dalle correlazioni empiriche in letteratura.
In particolare, il metodo VOF è stato utilizzato per studiare le caratteristiche principali dei fenomeni di condensazione all'interno di un singolo minicanale ed i risultati numerici sono stati poi convalidati con i dati sperimentali.
Poiché le condizioni a bassa portata specifica sono le meno indagate a causa della elevata incertezza sperimentale quando il flusso termico è dell'ordine di pochi watt, simulazioni numeriche sono state effettuate allo scopo di ottenere una panoramica del processo di condensazione in tali condizioni operative, concentrando l'indagine sugli effetti della proprietà del fluido, la forma, le dimensioni e l''inclinazione del canale.
Le simulazioni VOF sono state poi estese allo studio delle instabilità all'interfaccia durante il processo di condensazione di R134a per un deflusso anulare-ondoso all'interno di un minicanale verticale con un diametro interno di 3.4 mm. I risultati numerici sull'evoluzione dell'interfaccia liquido-vapore nel tempo sono stati convalidati con visualizzazioni sperimentali e l'influenza delle onde sullo scambio termico è stata analizzata.
Oltre all'analisi numerica del trasferimento di calore, l'applicazione della tecnologia a minicanali è stata anche investigata in sistemi di riscaldamento e raffreddamento.
L'uso di minicanali negli scambiatori di calore permette di ridurre in modo significativo la carica di refrigerante rispetto ai tradizionali scambiatori di calore a batteria alettata. Questo è particolarmente utile in una pompa di calore reversibile quando lo stesso scambiatore di calore può funzionare come un condensatore o come evaporatore ed è particolarmente utile quando il refrigerante è infiammabile o mediamente infiammabile.
Lo sviluppo di modelli fisici è necessario per la previsione delle prestazioni e per la progettazione di sistemi completamente innovativi.
Procedure di calcolo sono state così implementate per valutare le prestazioni di una pompa di calore reversibile acqua-acqua e aria-acqua utilizzando i minicanali nel trasferimento di calore con l'aria, considerando sia l'aria che il terreno come possibili fonti di calore.
Questo lavoro è stato possibile grazie al sostegno finanziario di Riello SpA .

Contents

LIST OF FIGURES

LIST OF TABLES

1 INTRODUCTION

The present research activity is focused on the analysis of condensation phenomena inside a single minichannel and on the application of minichannels technology for condensers and evaporators in heating and cooling systems.
Nowadays there is an increasing demand for compact devices with high performance in heating and cooling applications and this new geometric configurations permit to have a lower charge of refrigerant as compared to conventional HX. This is useful for safety reasons when using "natural fluids" such as ammonia or hydrocarbons and for reducing greenhouse gas emission when using conventional halogenated fluids. At small diameter, when the mass flux is high (e.g. $G \geq 200$ kg m^{-2} s^{-1} for R134a in 1 mm channel) the empirical correlations available in the literature, developed using data from round conventional-size pipes (Cavallini et al. [1], Moser et al. [2]…), predict the condensation heat transfer coefficient with a degree of accuracy suitable for the design of heat exchangers. This occurs because at high mass velocity, the flow is mostly annular and the condensation heat transfer is dominated by vapour shear stress on the liquid film, hence available correlations can be successfully applied.
When the mass flux is low ($G \leq 200$ kg m^{-2} s^{-1}) new parameters can influence in a significant way the condensation mechanisms.
In the literature, the low mass flux conditions are also the least investigated, mainly because it is a real challenge to perform measurements of heat transfer coefficients with low experimental uncertainly when the heat flow rate is in the order of few watts.
At the moment, no numerical model available in the literature has been fully validated against an experimental data set covering a complete range of operating conditions (primarily at low mass velocity), channel dimensions and geometries.
In fact, it is possible that the empirical correlations available in the literature work well for a limited range of operating conditions or fail when they are applied to predict experimental data obtained by other laboratories.
For this reason, the goal of this work is:

- to obtain numerical results on the complex physics of condensation at small scale, having a numerical approach that can be used for different fluids, channel shape and dimensions;
- to study the main parameters (i.e. fluid properties, cross section shape of channel, gravity, surface tension…) that can influence the heat transfer during condensation inside a single minichannel ($D_h \leq 3$).

Another goal of the present work is to validate the numerical approach comparing the numerical results against experimental data. For this reason new experimental tests have been performed at the Two Phase Heat Transfer Lab at the University of Padova, to widen the operating conditions of a previous experimental database measured by other authors.
In the literature, most of numerical studies on condensation are referred to steady-state configuration and, thus, the intermittent flow (i.e. slug/plug flow) and the interfacial

instabilities, such as the presence of waves at interface and the liquid entrainment, cannot be predicted.
The steady-state numerical simulations can predict with acceptable accuracy the condensation heat transfer coefficients in very small diameter channels where the annular flow is mostly present and the wavy-stratified flow does not occur. But when the channel size is larger (i.e. 3.4 mm) the occurring of wavy-stratified flow has been observed by some studies found in the literature, e.g. Coleman and Garimella ([3],[4]), Nema et al. [5] and El Hajal and Thome [6], and the steady-state assumption has to be relaxed.
For this reason another aim of this work is to develop a new numerical approach able to capture the unsteady-state phenomena that can occur during condensation.
As mentioned above, the technology of minichannel can be applied in heating and cooling system to obtain a significant reduction of refrigerant charge. Furthermore, the performance of the system can be improved by the proper choice of the refrigerant, the components (e.g. compressors, heat exchangers) and by the source (e.g. air/water) used at evaporator during heating mode or at condenser during the cooling mode. In the present study, in parallel with the investigation of the heat transfer phenomena, a physical model of a reversible heat pump using minichannels has been developed.
The aim is to evaluate the heat pump performance, considering the effect of refrigerant properties (e.g. R134a, R290, R32), different configuration (air/water) and sizing of components related to the heating demanded by the user.
In the developed model, there is the possibility to exchange heat transfer with air or water, defining a water-to-water or air-to-water reversible heat pump.
On the air side, a finned coil using minichannels has been considered; on the water side, instead, brazed plate heat exchangers ($D_h \leq 3$ mm) are used as condenser/evaporator.
The application of a compressor coupled to a variable speed electrical motor has been taken into account.
On the water side, there is the possibility to use the ground as source, thus the physical model of a vertical ground heat exchanger has been developed.
These models have been developed and applied in the framework of the GEOTeCH Horizon 2020 Project to analyze the operating behavior of a reversible dual-source heat pump.
The dual-source heat pump is an innovative heating and cooling system. During the heating mode it is possible to use air or ground as source at the evaporator; similarly during the cooling mode at the condenser. The physical model is needed to properly design such a new system.

This manuscript is organized as follows:

- Section 2: experimental data of R134a and R1234ze(E) condensation inside a single 0.96 mm i.d. circular and 1.24 mm i.d. square minichannel are presented to evaluate the heat transfer coefficient at low mass flux.
  In this section the experimental data obtained by other authors are reported to analyze the main parameters that influence the condensation process in the low mass flux region.

Furthermore, experimental data taken inside a 3.4 mm i.d. circular channel in vertical-downflow configuration are also reported.
These data are compared against the experimental tests performed by Azzolin [7,8] in horizontal configuration and against the steady-state numerical simulations at the same operating conditions to analyze the two-phase flow and the condensation heat transfer mechanisms.

- Section 3: steady-state simulations of condensation inside a single minichannel are presented and compared against the experimental data reported in the previous section. Here the influence of various parameter, such as diameter size, diameter shape, gravity and capillary force, fluid transport and thermodynamic properties and orientation, have been analyzed in detail. To improve the investigation on condensation the liquid film thickness, the local heat transfer coefficients and other information have been obtained by numerical simulations and have been discussed to understand the relative importance of parameters on condensation.
- Section 4: unsteady-state simulations of annular-wavy downflow condensation inside a 3.4 mm i.d. circular minichannel are presented. The aim of this section is to set a new numerical approach to predict the two-phase flow and to understand the influence of interfacial instabilities from a heat transfer and momentum point of view. In addition, the comparison between the predicted two-phase flow and the flow visualizations has been reported to discuss the features of annular-wavy downflow condensation.
- Section 5: this part of work is focused on the application of minichannel technology on heating and cooling system. The physical models of a reversible water-to-water and air-to-water heat pump have been built. The aim is to evaluate the heat pump performance, considering the effect of refrigerant properties (e.g. R134a, R290, R32), different configuration (single source or dual source) and sizing of components related to the heating demanded by the user. At first, the physical models have been validated against experimental data obtained in the literature and then they have been applied to analyze the influence of different parameters on the device performance.
- Section 6: here the possibility to use the ground as source has been studied. For this purpose the physical model of a single U-tube as borehole heat exchanger has been built. In this part the coupling between the borehole heat exchanger and the water-to-water heat pump (i.e. ground coupled heat pump)has been analyzed varying the operation conditions of whole system. Finally, the comparison between the reversible air-to-water and the ground-coupled heat pump has been reported to draw the operating maps of a dual-source heat pump to decide the best source (air or ground) to achieve the best performance of the whole system at varying outdoor conditions and the number of borehole heat exchangers.

PART I: ANALYSIS OF CONDENSATION HEAT TRANSFER IN MINICHANNELS

2 EXPERIMENTAL ANALYSIS OF CONDENSATION INSIDE A SINGLE MINICHANNEL

2.1 The importance of investigation at low mass flux

In the literature several predicting models can be found to evaluate the condensation heat transfer coefficients inside macrochannel (i.d. $D > 3$ mm) with a good accuracy ([1], [2], [9], [10]). But at decreasing of inner diameter, other physical parameters can influence the condensation mechanisms to the point that the models developed for macrochannel fail to predict the heat transfer coefficient. At first, to understand the range of applicability of these models it is fundamental to highlight a possible criterion to define the transition from macro-to-microscale condensation and, hereinafter, to found at which operating conditions the model for conventional channel can again work well to evaluate the heat transfer coefficient during condensation process inside mini/microchannel. Obviously, for those operating conditions, it will be necessary to develop a new predicting model to include those effects and forces that in the previous models have not been taken into account.
In a recent paper, starting from a previous visualization study by Coleman and Garimella [4] (R134a, round and square tubes with diameters ranging from 1 to 4.91 mm, G = 150-750 kg $m^{-2}s^{-1}$), Nema et al. [5] developed dimensionless transition criteria to distinguish between the flow regimes. The transition between macro and microscale (i.e the relative importance of surface tension and gravity) has been accounted for by introducing a critical Bond number. For example, in case of R134a condensing at 40°C saturation temperature inside a 1 mm diameter tube, the Bond number is Bo = 1.8 and the critical Bond number is Bo_{cr} = 3.8; therefore surface tension is expected to play a non-negligible role. For Bond number below the critical value, four different types of flow have been observed by the authors: dispersed, annular film, intermittent/annular film and intermittent; the wavy flow regime was not observed. Many more studies on flow patterns have been published afterwards; although no general flow regime map is available for condensation in minichannels, one important result has been repeatedly reported which is the increased importance of the annular flow regime at the expense of stratified and wavy stratified flow.
It should be noticed that there are some working conditions ($Bo < Bo_{cr}$ and high mass velocities) at which empirical correlations available in the literature, developed using data from round conventional-size pipes [1], predict the condensation heat transfer coefficient with a degree of accuracy suitable for the design of heat exchangers ([11], [12], [13]). This fact can be explained considering that at high mass velocity the flow is mostly annular and the condensation heat transfer is dominated by vapour shear stress on the liquid film: hence correlations that do not consider surface tension can be successfully applied. Starting from these considerations, two different regions (respectively high and low mass flux) can

be individuated, each of them showing peculiar characteristics of the condensation heat transfer coefficient. Hereinafter, some experimental works found in literature are reported to highlight the main parameters that influence the condensation in minichannel at high mass flux and then special considerations and new experimental data are introduced in Section 2 to underline the major differences between the two operating regions (high and low mass flux).

At high mass flux, (e.g. $G \geq 400$ kg m^{-2} s^{-1} for of R134a in a 1 mm channel), the main features are:

- Strong influence of the mass flux on the heat transfer coefficient ([14], [15], [12], [16],[17]).
- Negligible difference of the cross-sectional average heat transfer coefficient between round and square cross section channels ([12],[16]). As reported in [18] the shape of the liquid-vapour interface is affected by surface tension, but the average heat transfer coefficient is governed by vapour shear stress.
- No major effect of gravity and channel inclination [19].
- No major difference between macro-scale and micro-scale modeling (models for macro-scale condensation still apply).
- No influence of saturation-to-wall temperature difference [15].

At low mass flux, (e.g. $G \leq 200$ kg m^{-2} s^{-1} for R134a in a 1 mm diameter channel) the main features are:

- Low effect of the mass flux on the heat transfer coefficient (experimental data with R1234ze(E) at G = 100-200 kg m^{-2} s^{-1}, [13]).
- Stratified flow in round minichannels, with some influence of gravity and inclination ([20], [21], [19]).
- Flatter heat transfer coefficient vs vapor quality profile as compared to high mass flux conditions.
- Enhancement of heat transfer coefficients in square channels as compared to the round ones ([12] and [16]).
- Models developed for macroscale display in general a lower accuracy at low mass fluxes, especially in square minichannels.

From the brief review reported above, it is clear as, at low mass velocity, other forces, such as surface tension, may play a relevant role, and a difference between micro-scale and macro-scale heat transfer.

The low mass flux conditions are unfortunately also the least investigated, mainly because it is a real challenge to perform measurements of heat transfer coefficients with low experimental uncertainly when the heat flow rate is in the order of few watts.

For this reason, in the present status of art, no numerical model available in the literature has been fully validated against an experimental data set covering a complete range of fluids operating conditions (primarily at low mass velocity), channel dimensions and geometries.

At first, new experimental tests, performed at the Two Phase Heat Transfer Lab at the University of Padova, are presented to enhance the previous experimental database obtained by other authors ([19], [13], [11], [15]) in the same lab. Furthermore, to have a better general understanding of the condensation phenomena at such conditions, numerical simulations with VOF method have been run and validated against experimental data in Section 3 to allow an "insight view" for a qualitative analysis (e.g. three-dimensional distribution of local heat transfer coefficient and condensate film thickness), which is almost impossible to achieve experimentally without affecting the phenomenon itself.

2.2 Condensation inside a single horizontal minichannel at low mass flux

2.2.1 Test apparatus

In this section, experimental data have been reported to hightlight the miniscale effects that occur at low mass flux during the condensation process.
The new experimental data have been measured at the Two Phase Heat Transfer Lab at the University of Padova during condensation using two different test sections consisting respectively of a 0.96 mm diameter single circular channel and a 1.23 mm hydraulic diameter square cross section channel. Each test section is made of two counter flow heat exchangers: a pre-section and a measuring section. In the pre-section, the refrigerant coming from the evaporator is desuperheated and partially condensed to achieve the desired vapor quality, while in the second one local heat transfer coefficient measurements are collected during the condensation process. Two stainless steel adiabatic sectors are located at the ends of the measuring section providing a place for the measurement of refrigerant temperature and pressure. The presence of both temperature and pressure transducers at the inlet of the measuring section allows a check of the saturation temperature during condensation tests. A refrigerated thermal bath is used to provide the water entering the measuring section and the pre-section at desired temperature.
Two different distilled water loops serve independently the pre-section and the measuring sector and each of them is provided with a flow regulating valve, which allows to set the mass flow rate measured by a dedicated Coriolis effect mass flow meter. The wall and water temperatures are gauged by thermocouples and the water temperature gains are measured by multi-junction copper-constantan thermopiles. A detailed description of the present test rig and test section is reported in [15] for the 0.96 mm circular minichannel and in [12] for the 1.23 mm square minichannel. Data reduction is also described in detail in [13]. However, for sake of clearness, a scheme of experimental test rig is reported in Figure 2.1.

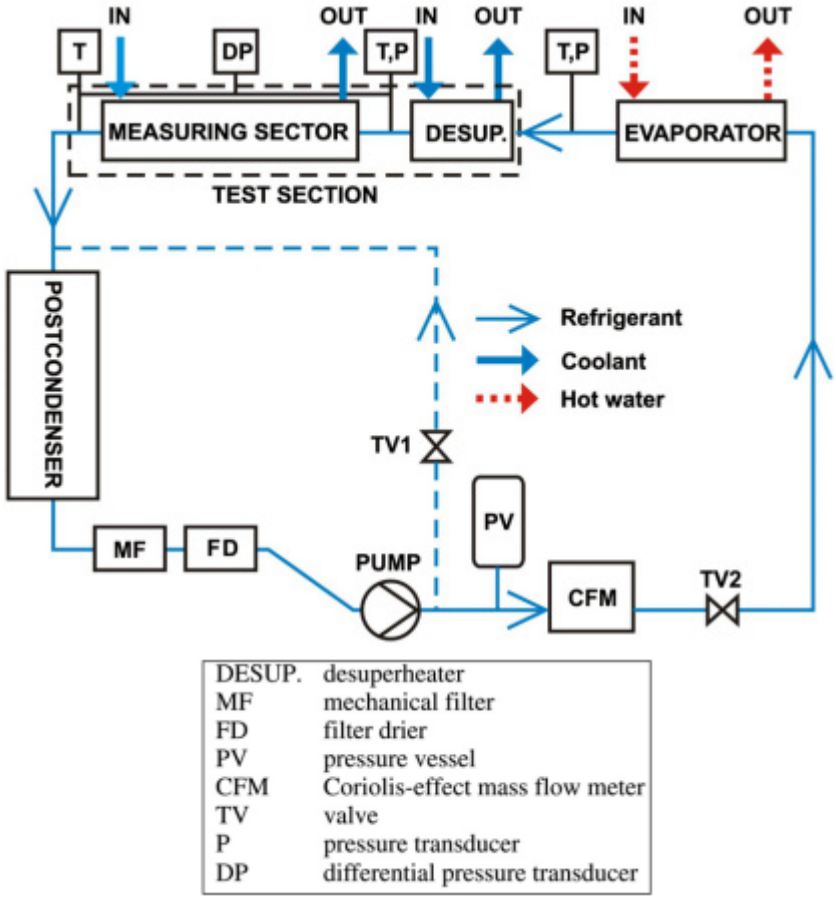

Figure 2.1: Experimental test rig.

2.2.2 Experimental results and discussion

Heat transfer coefficients measured during R134a condensation inside the 0.96 mm circular channel (mass velocity ranging from 65 kg $m^{-2}s^{-1}$ to 150 kg $m^{-2}s^{-1}$) and inside the 1.23 mm square channel (G = 65 kg $m^{-2}s^{-1}$) are reported in Figure 2.2, enlarging the mass flux range of the data set presented in [12] and [15]. The saturation temperature is equal to 40°C for all the data.

Condensation has been also investigated with the halogenated olefin R1234ze(E) inside the square minichannel with mass velocity between 100 kg m^{-2} s^{-1} and 400 kg m^{-2} s^{-1} and 40°C saturation temperature (Figure 2.3). For the sake of comparison, the experimental data by [13] taken inside the circular minichannel are reported.

As depicted by Figure 2.2 -Figure 2.3, the saturation-to-wall temperature difference is also specified since this parameter can influence the local condensation heat transfer coefficients at these values of mass flux. The error bars are also plotted in the graphs.

In Figure 2.2 -Figure 2.3, at constant mass velocity, the heat transfer coefficient is found to increase with vapour quality, but the slope of the HTC-x curve is lower at low mass velocity values. In addition, Figure 2.2 shows that for G < 200 kg $m^{-2}s^{-1}$ the influence of mass velocity on the heat transfer is reduced. In Figure 2.2 -Figure 2.3 it is worth noting that the slope of HTC trends during the condensation inside the circular minichannel changes from 200 to 100 kg m^{-2} s^{-1} as compared against those obtained inside the square minichannel.

This phenomenon could be due to turbulence inside the liquid film, so the transition from high to low mass flux region. These considerations are in agreement with Nebuloni et al. [22] that suspected an earlier laminar to turbulent transition much more evident for the circular channel as compared to the square one.

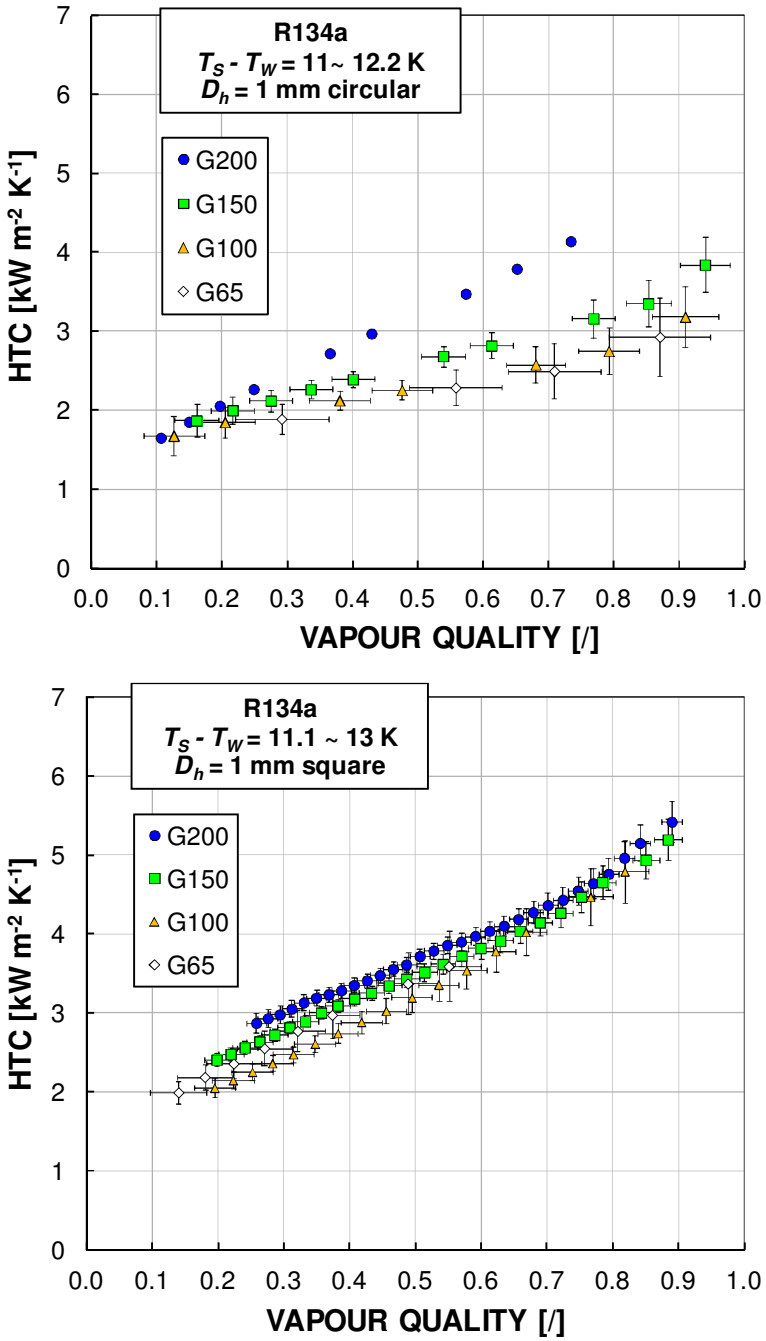

Figure 2.2: New experimental data and values reported by Del Col et al. [19] **and Matkovic et al.** [15] **of R134a condensation at varying mass flux *G* [kg m^{-2} s^{-1}]. Top: circular; bottom: square.**

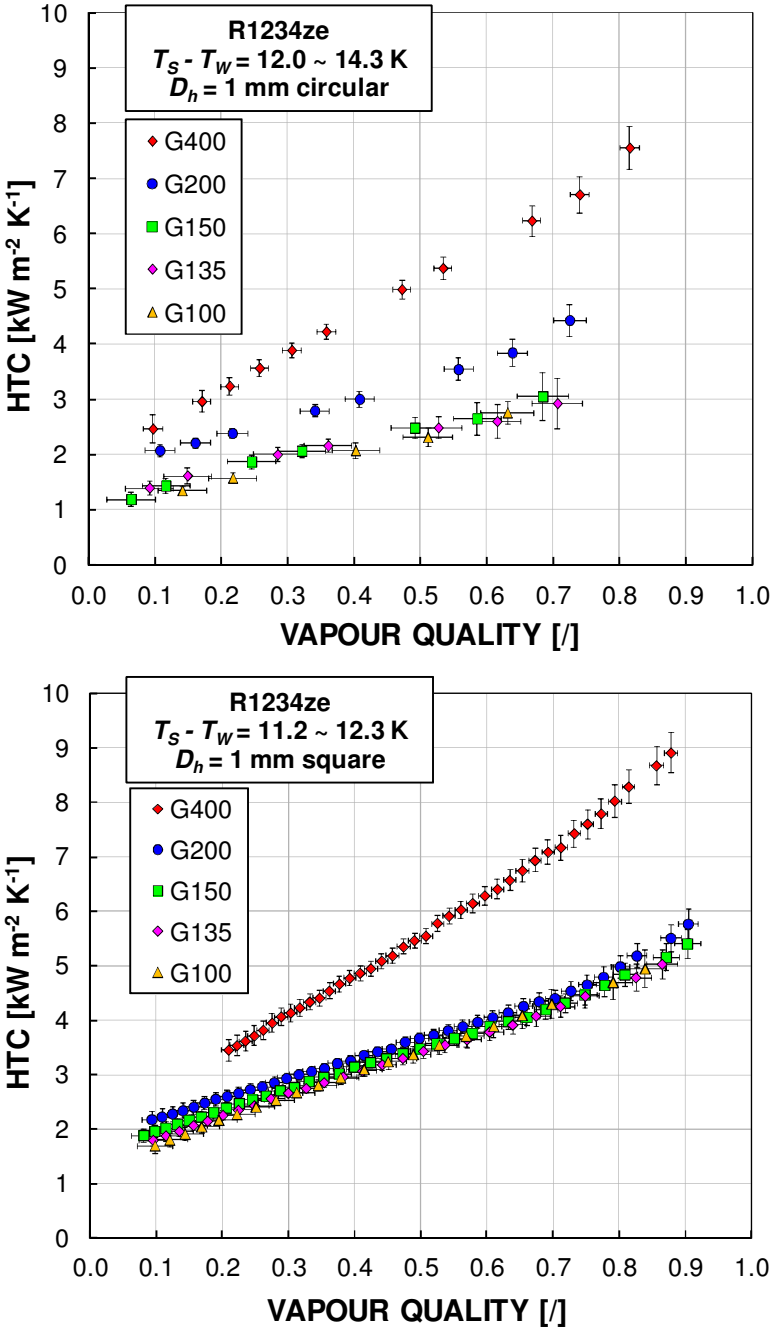

Figure 2.3: New experimental data and values reported by Del Col et al. [13] **of R1234ze(E) condensation at varying mass flux *G* [kg m^{-2} s^{-1}]. Top: circular; bottom: square.**

This effect is reduced for R32 (Figure 2.4) because the vapour density is higher than R1234ze and R134a, having low vapour velocity and low mass velocity influence on the condensation heat transfer coefficients at 200 kg m^{-2} s^{-1}. This topic will be further discussed in Section 3.4.

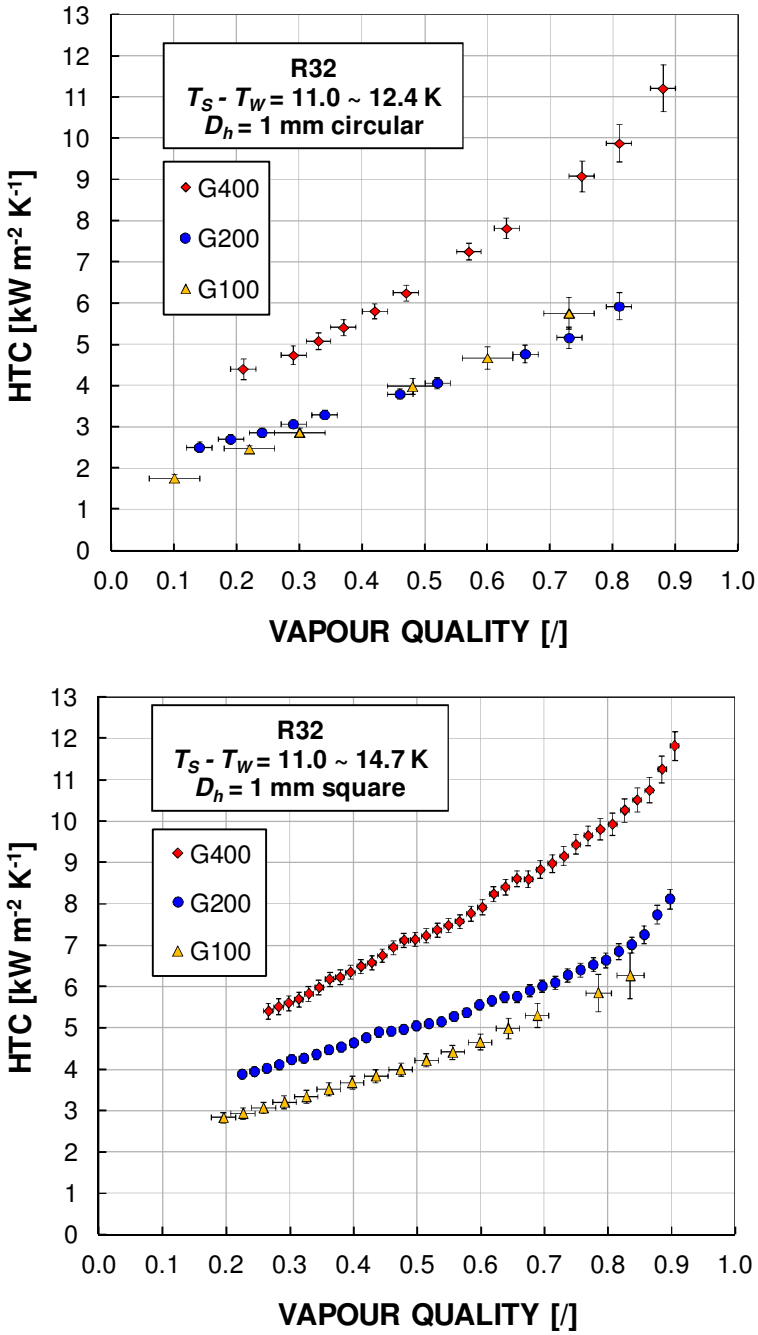

Figure 2.4: Effects of channel geometry on the heat transfer coefficients during R32 condensation at low mass velocity. Top: circular [11]**; bottom: square** [19]**.**

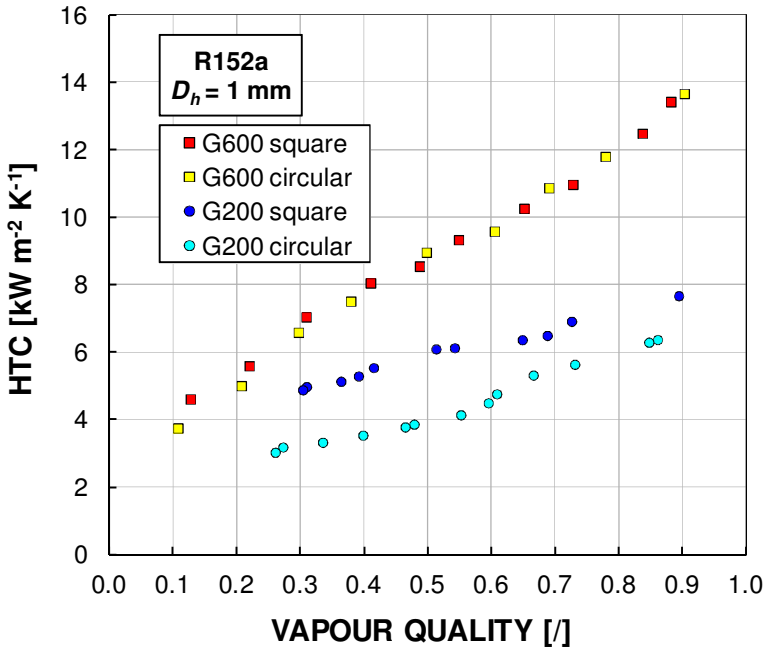

Figure 2.5: Effects of channel geometry on the heat transfer coefficients during R152a condensation at G = 600 kg m^{-2} s^{-1} and at G = 200 kg m^{-2} s^{-1} (Liu et al. [16]**).**

2.2.3 Effect of channel shape

As reported in previous works ([12], [16]) at high mass flow rate, (e.g. $G \geq 400$ kg m^{-2} s^{-1}) the heat transfer coefficient is not significantly affected by the channel shape while it only depends on the channel hydraulic diameter. In Figure 2.5 experimental data during R152a condensation taken inside a 1.152 mm circular channel and in a 0.952 mm square channel by Liu et al. [16] are reported. At G = 600 kg m^{-2} s^{-1} the square and circular channel display roughly the same heat transfer coefficient. This behaviour is confirmed also in the present data with R1234ze(E) at G = 400 kg m^{-2} s^{-1} (Figure 2.3). When moving to lower values of mass velocity (Figure 2.2 toFigure 2.5) there is a clear increase of the heat transfer coefficient in the square channel as compared to the circular one for all the four fluids here presented (R134a, R1234ze, R32, R152a). This heat transfer enhancement is due to the presence of the corners, because the surface tension pulls the liquid toward the corners, leading to a thinner liquid film at flat sides and to a lower average thermal resistance. With the aim of better evaluating the heat transfer coefficient enhancement, in Figure 2.6 - Figure 2.7 the ratio of heat transfer coefficient in the square channel to the one in the circular minichannel is reported versus vapour quality at different mass velocities. It can be observed that there is a value of mass velocity at around 200 kg m^{-2} s^{-1} from which the channel shape effect, due to surface tension, starts to be relevant.

For example, as depicted in Figure 2.6, at the same mass flux of 150 kg m^{-2} s^{-1} and at vapour quality of 0.7, the enhancement of local heat transfer coefficient of square channel against circular one is about 40%, 38% for R134a and R1234ze(E), respectively.

At the mass flux of 200 kg m^{-2} s^{-1} and at vapour quality of 0.7, the enhancement is about 20% for both R152a and R32.

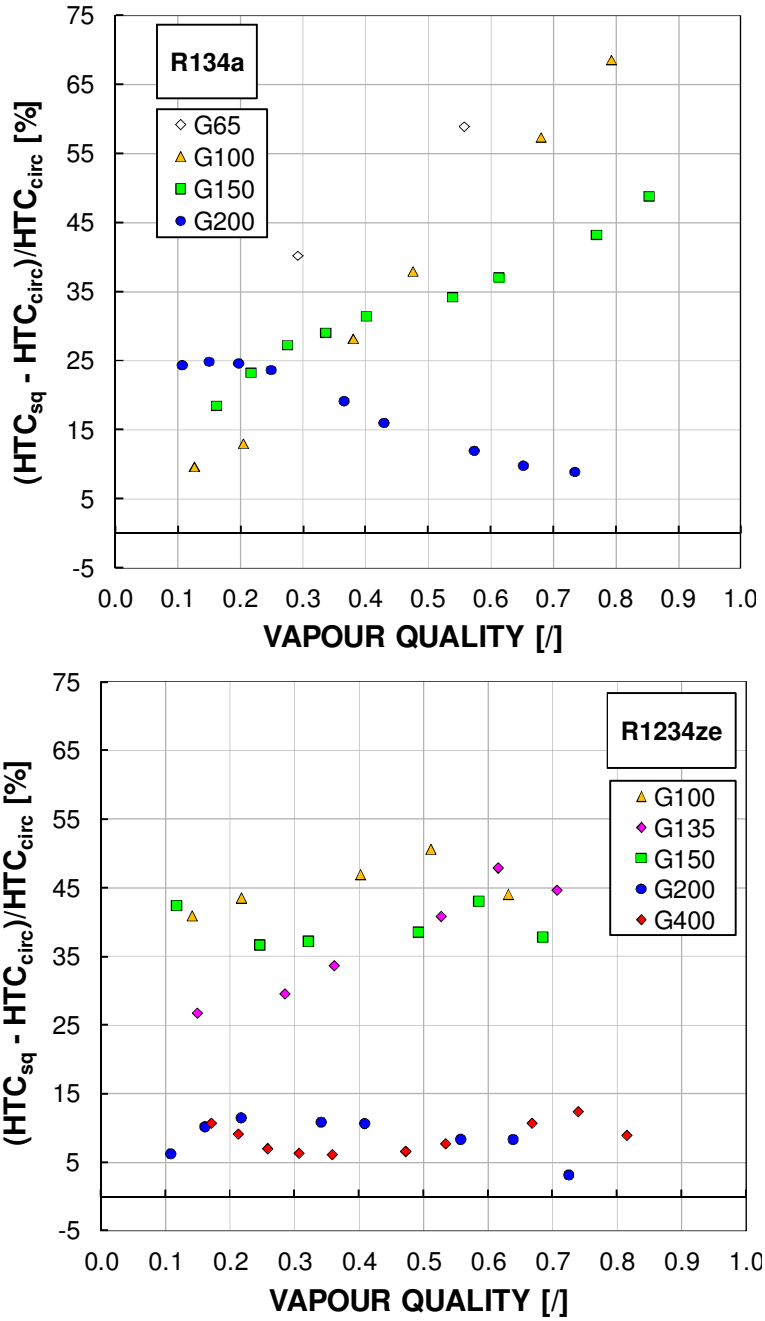

Figure 2.6: Percentage increase of local heat transfer coefficient in the square channel compared to the one in the circular at mass flux between 100 and 400 kg m^{-2}s^{-1} and 40°C saturation temperature. Top: R134a; bottom: R1234ze(E).

At G = 200 kg m^{-2} s^{-1}, the ratio of heat transfer coefficient of square channel as compared to circular one is, instead, only about 10% and 5% for R134a and R1234ze(E), respectively.
Since the saturation-to-wall temperature difference ΔT_{SW} can influence the local heat transfer coefficients during condensation process at these operating conditions, the comparison of circular data against square ones has been done considering a ΔT_{SW} range of 10-13 K.

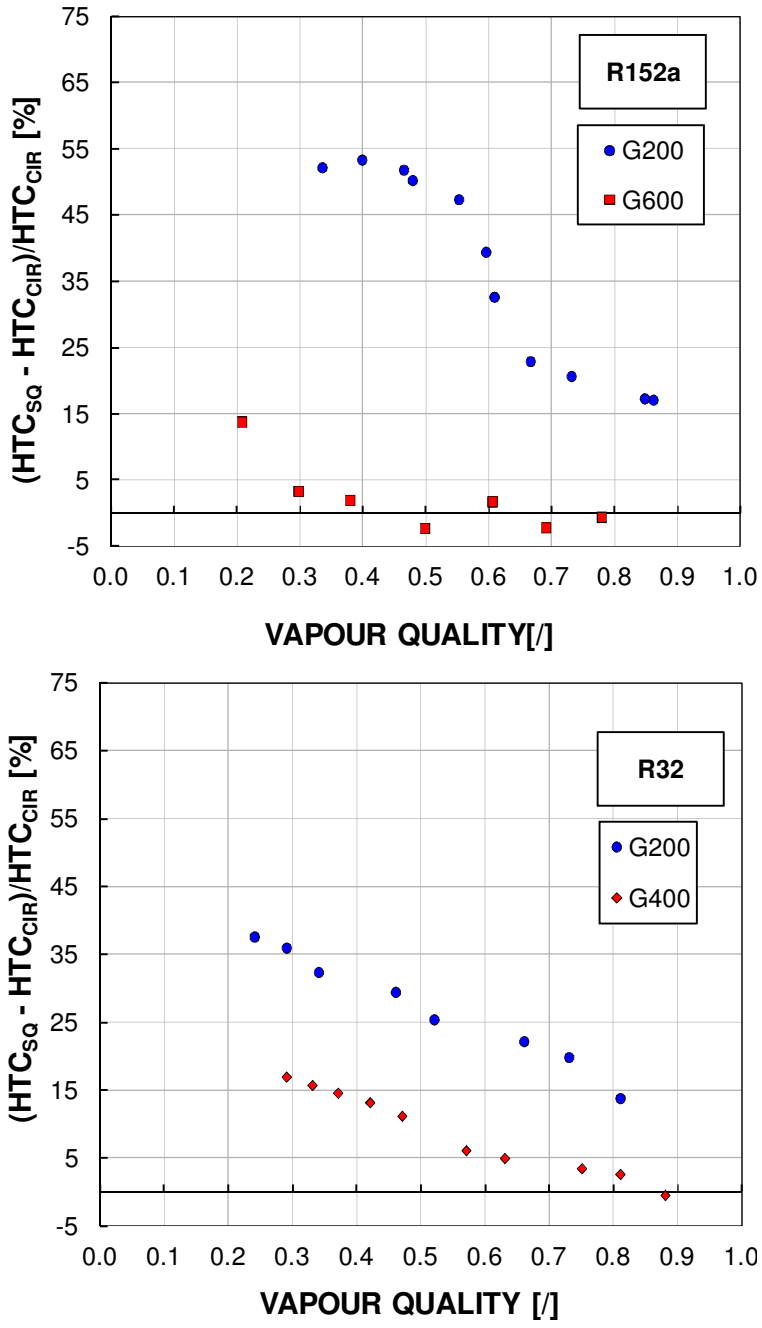

Figure 2.7: Percentage increase of local heat transfer coefficient in the square channel compared to the one in the circular at mass flux between 200 and 600 kg m^{-2}s^{-1} and 40°C saturation temperature. Top: R152a; bottom: R32.

2.2.4 Effect of saturation-to-wall temperature difference

At low mass flux gravity forces and surface tension forces play some role and in such a case the heat transfer coefficient can be affected by the heat flux or – which is the same – the temperature difference between saturation and wall. In this section the effect of saturation-to-wall temperature difference ΔT_{SW} on the R134a condensation at low mass velocity inside circular and square minichannel has been investigated. The experimental data has been measured by varying the water inlet temperature to the measuring section ranging mass flux from 65 to 150 kg m^{-2} s^{-1}.

In Figure 2.8 -Figure 2.9, the HTC values measured at 65 to 150 kg $m^{-2}s^{-1}$, at varying ΔT_{SW} from 5 to 13 K, inside a circular minichannel, have been depicted. For all the operating conditions lower ΔT_{SW} carries out higher HTC. The effect of ΔT_{SW} results more significant when the mass velocity decreases confirming a major role of gravity at these operating conditions against the vapour shear stress. The HTC trends for square minichannel (Figure 2.9) at mass flux of 65 kg m^{-2} s^{-1} and two different ΔT_{SW} (5 and 10 K) tend to overlap as compared to those obtained in the circular minichannel. This aspect confirms that in the square channel the effect of ΔT_{SW} on the local HTC is lower than that inside the circular minichannel.

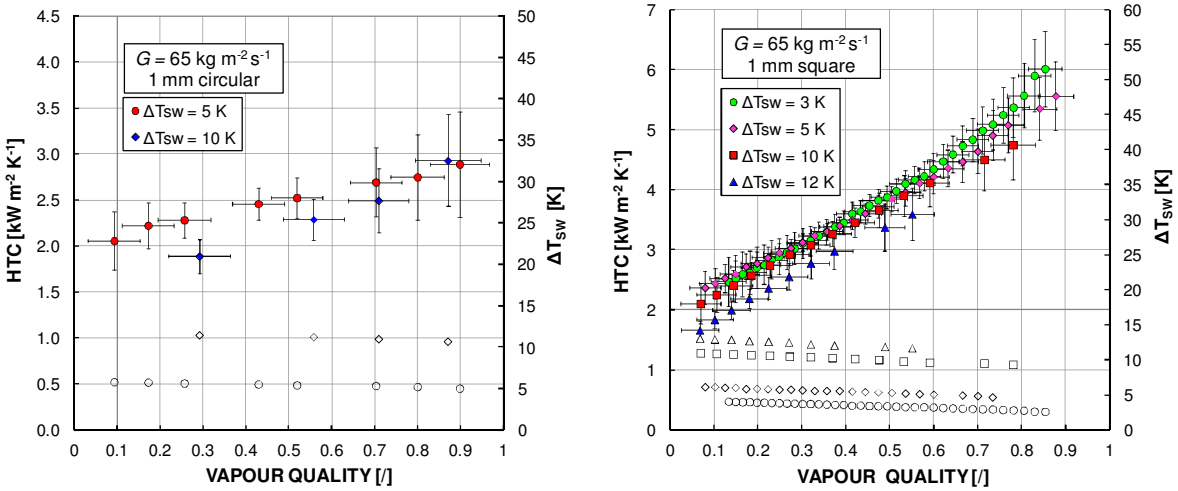

Figure 2.8: Local heat transfer coefficient during R134a condensation inside the circular and square minichannel at G = 65 kg m^{-2} s^{-1} and at varying saturation-to-wall temperature difference ΔT_{SW}.

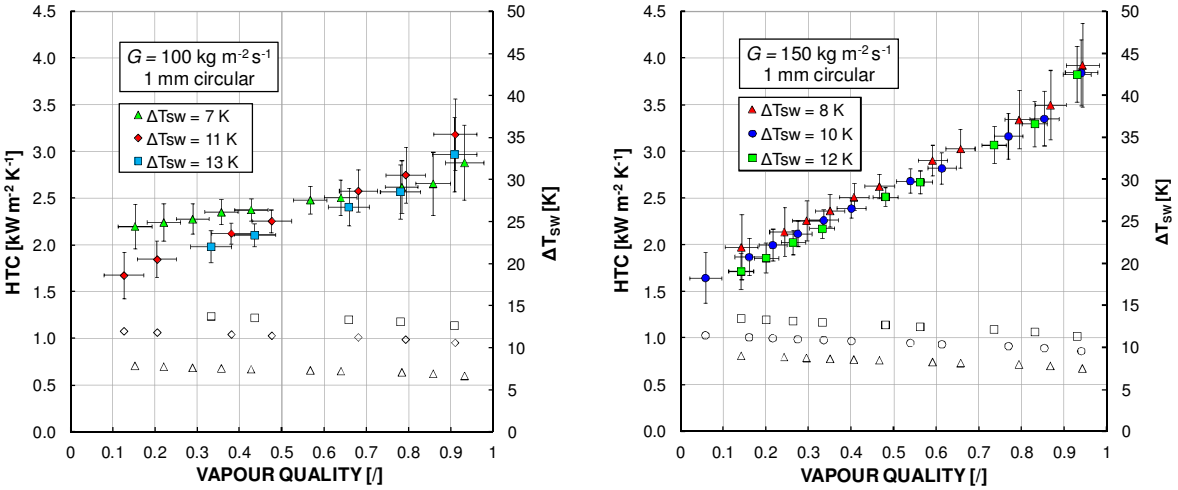

Figure 2.9: Local heat transfer coefficient during R134a condensation inside the circular and square minichannel at G equal to 100 and 150 kg m^{-2} s^{-1} and at varying saturation-to-wall temperature difference ΔT_{SW}.

2.2.5 Effect of fluid properties

In order to highlight the influence of fluid properties on the condensation process at low mass velocity, R717 data by Fronk and Garimella [23] and R290 data by Del Col et al. [24], obtained, respectively, inside a 1.435 mm and 0.96 mm i.d circular minichannel, are also plotted in Figure 2.10. The fluid thermodynamic and transport properties, that can influence the local heat transfer coefficients during condensation process, are listed in Table 2.1.

Table 2.1: Properties of saturated R32, R134a, R1234ze(E), R717 and R290 at 40°C from NIST Refprop Version 9.0 [114].

		R32	R134a	R1234ze(E)	R717	R290
p_S	[bar]	24.783	10.166	7.666	1.555	13.694
ρ_L	[kg m^{-3}]	893.0	1146.7	1111.3	579.4	467.5
ρ_V	[kg m^{-3}]	73.3	50.1	40.7	12.0	30.2
μ_L	[μPa s]	94.99	161.45	167.00	114.04	82.84
μ_V	[μPa s]	13.83	12.37	12.93	10.33	8.89
λ_L	[W m^{-1} K^{-1}]	0.115	0.075	0.069	0.443	0.087
σ	[mN m^{-1}]	4.47	6.13	6.96	20.29	5.21

At mass flux lower than 200 kg m^{-2} s^{-1}, considering the experimental data of R134a, R1234ze(E), R32, R290 and R717 reported in Figure 2.2-Figure 2.3-Figure 2.4 -Figure 2.10 inside the circular minichannel, the following aspects can be drawn:

- the liquid thermal conductivity plays a fundamental role. Inside the circular channel, the highest heat transfer coefficients are, in fact, achieved with R32 and R717 (i.e. at G = 200 kg m^{-2} s^{-1} and x = 0.7 the local HTC is about 5 kW m^{-2} K^{-1} for R32 and at G = 75 kg m^{-2} s^{-1} and x = 0.7 the local HTC is about 22 kW m^{-2} K^{-1} for R717) which have the highest liquid thermal conductivity.
- At G < 200 kg m^{-2} s^{-1} the effect of mass velocity becomes less relevant. In particular this clearly occurs when the vapour density is high. In fact, at the same mass flux, if the vapour density is high, the vapour phase velocity (i.e. interfacial shear stress) becomes low and the turbulence inside the liquid film can be reduced. For example, at two different values of mass flux, in case of R32 (ρ_V = 73.3 kg m^{-3}), the HTC-x curves overlap. R290 (ρ_V = 30.2 kg m^{-3}) and R717 (ρ_V = 12.0 kg m^{-3}), instead, display the largest effect of mass velocity also at the same operating conditions.
  It could be interesting to analyze the ratio of heat transfer coefficient at G = 200 kg m^{-2}s^{-1} to that at G = 100 kg m^{-2}s^{-1} for the different fluids at a fixed value of vapour quality. For example, at x = 0.5 such heat transfer coefficient ratio inside the circular minichannel is about 1.00, 1.24, 1.39, 1.6 and 1.7, respectively for R32, R134a, R1234ze(E), R290 and R717.

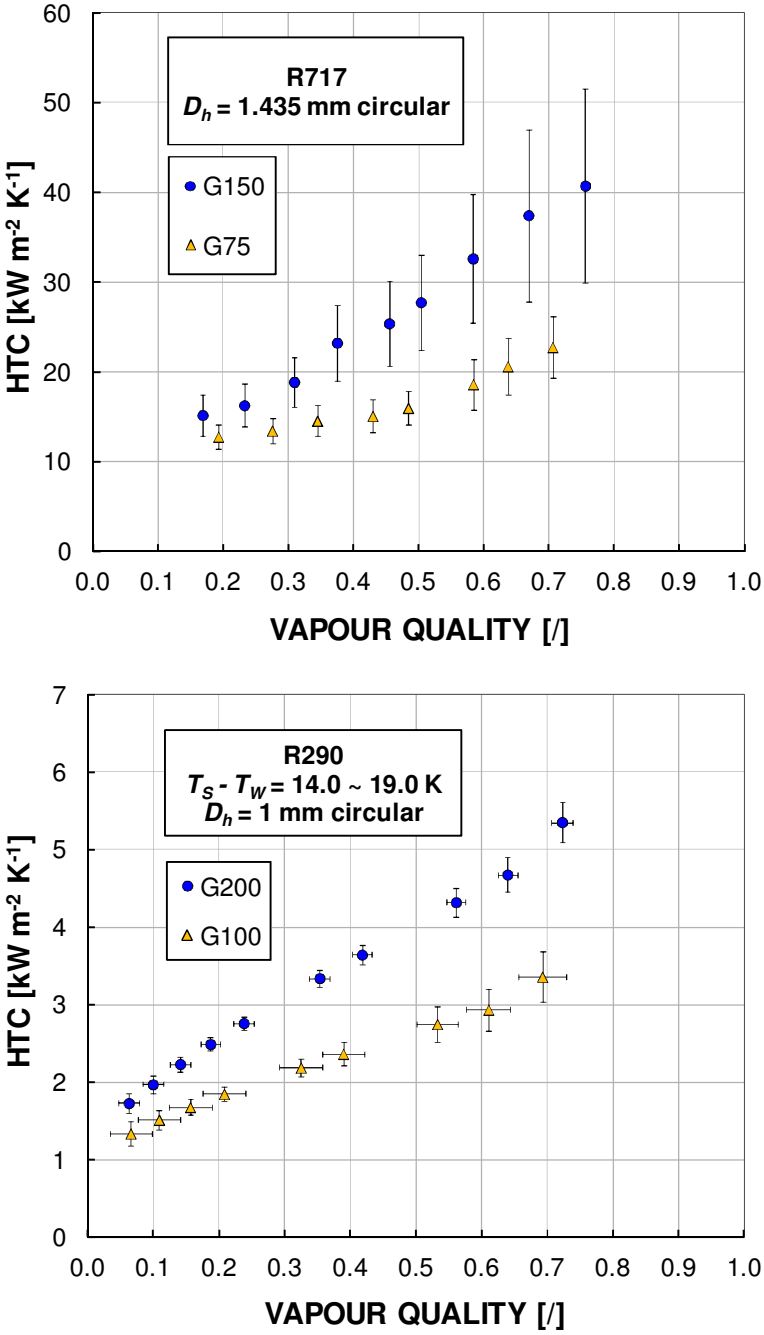

Figure 2.10: Local heat transfer coefficient during condensation inside the two circular minichannels at varying mass flux *G* [kg m^{-2} s^{-1}]. Top: data of R717 [23]**; bottom: data of R290** [24]**.**

2.3 The use of macroscale predicting procedure

From the experimental data reported above, it is demonstrated that at low mass velocity (≤ 200 kg m^{-2}s^{-1}) the microscale effects influence the condensation process. For this reason, the predicting models developed for macroscale condensation, such as [1] and [2], cannot be extended to low diameter channels at these conditions.

For example, in Figure 2.11 experimental data taken with R134a and R32 at mass flux lower than 200 kg m^{-2} s^{-1} in the round minichannel are compared against predictions by Cavallini

et al. [1] model. It can be seen that when reducing the mass flux the experimental heat transfer coefficients may be underpredicted by this model, to a different extent for different fluids. In other words, models developed for macroscale condensation can still be applied to minichannels but with a lower operating conditions range, avoiding the regions where the role of capillary and gravity forces may introduce differences with microscale data.
Here, an attempt has been done considering the dimensionless gas velocity J_V and the two-phase Weber number We as parameters to consider, respectively, the gravity and surface tension effects.

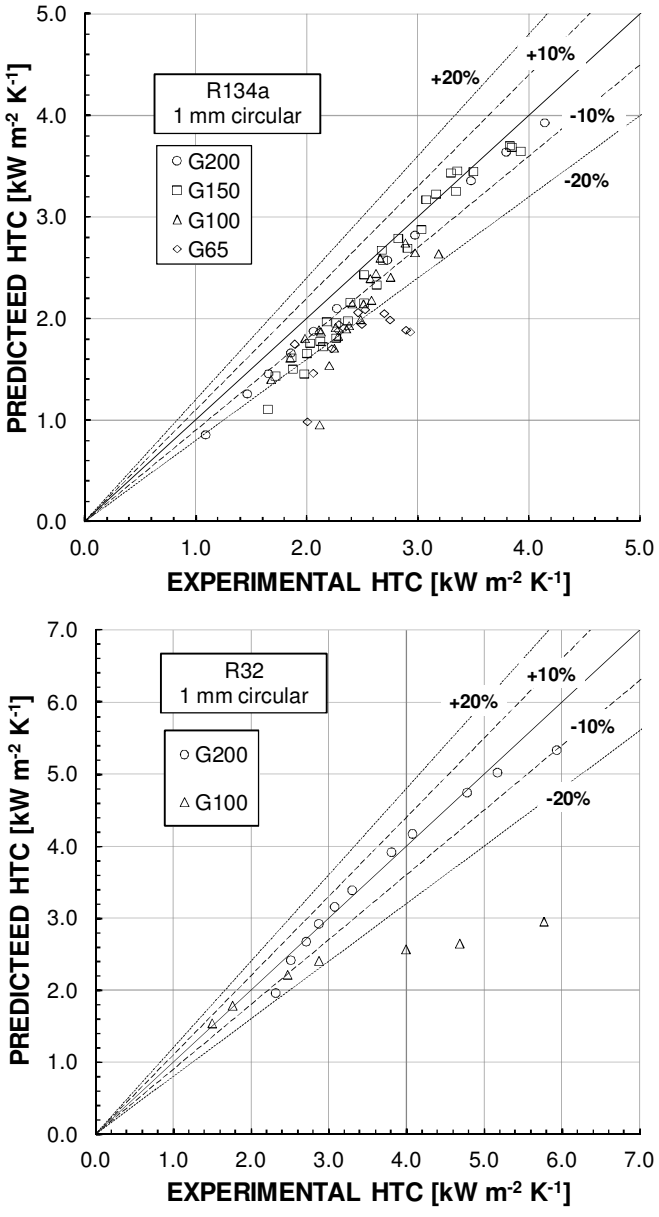

Figure 2.11: Comparison between measurements and calculated heat transfer coefficients using the model by Cavallini et al. [1]**. Top: R134a; bottom: R32.**

In Figure 2.12 the predictions by Cavallini et al. [1] model have been reported for all the experimental data in round minichannel (R134a, R32, R1234ze(E), R290) that satisfy the

following conditions: $J_V \geq J_{VT}$ and $We \geq We_T$, where the transition numbers J_{VT} and We_T are given as a function of the Martinelli parameter in Eqs.2.1-2.2. With such limitations, the model by [1] can be applied also at low mass velocities.

$$J_V^T = \left\{ \left[7.5 / (4.3 X_{tt}^{1.111} + 1) \right]^{-3} + C_T^{-3} \right\}^{-1/3} \qquad \textbf{2.1}$$
$$C_T = 6$$

$$We^T = \left\{ \left[6 / (12 X_{tt}^{3} + 0.1) \right]^{-3} + D_T^{-3} \right\}^{-1/3} \qquad \textbf{2.2}$$
$$D_T = 30$$

This criterion has not applied for R717 data because the predictions by Cavallini et al. [1] model were not good; in fact, applying the model for convectional channels the authors declared an average deviation e_R above of 20% for R717, R744 and R718.
It is worth highlighting that these transition numbers J_{VT} and We_T have been performed analyzing only the experimental data inside the round minichannel.
For this reason, the transition number We_T could not be enough high to consider the surface tension effect inside the square minichannel where the capillary force has the major role on heat transfer, primarily at high vapour quality.
From these considerations, these transition numbers could be defined as function of the different cross section shape that influences the role of gravity and surface tension effect on liquid film distribution and heat transfer coefficients at low mass velocity.

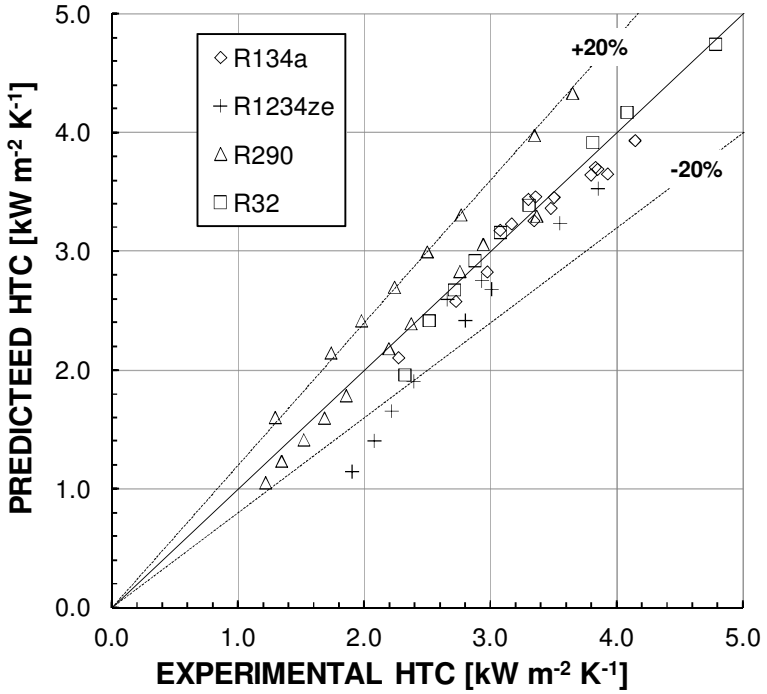

Figure 2.12: Comparison between measurements and calculated heat transfer coefficients using the Cavallini et al. model [1] when $J_V \geq J_{VT}$ and $We \geq We_T$.

2.4 Condensation inside a single vertical minichannel at low mass flux

In this section, the heat transfer coefficients of R134a condensation at 40°C saturation temperature measured inside vertical channel with an inner diameter of 3.38 mm are here reported. These experimental data have been obtained ranging the mass velocity from 50 to 200 kg m^{-2} s^{-1} and the water temperature at inlet of measuring section to, respectively, analyze the effect of mass flux and saturation-to-wall temperature difference on heat transfer during the vertical downflow condensation.

2.4.1 Test section

Before showing the experimental data of R134a condensation in vertical channel, a brief description of test section is here presented. Whereas the test apparatus has been reported in Section 2.2.1.
The experimental test section is composed of two tube-in tube counter-current heat exchangers for the measurements of the quasi-local heat transfer coefficient and of an adiabatic glass tube for the visualization of the flow pattern, as reported in Figure 2.13.

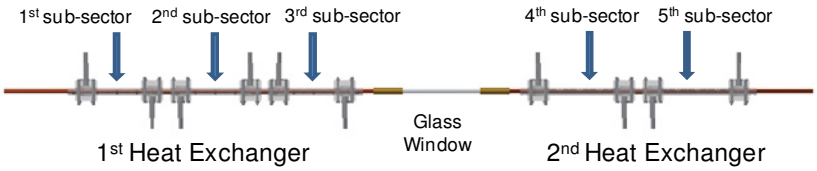

Figure 2.13: Layout of test section.

The refrigerant flows inside the tube, whereas the condensation heat is removed using water flowing on the external side. As in previous test sections presented in 2.2.1, the external surface of the copper tube has been machined with the aim to obtain an enhanced surface on the water cooling side. Each copper heat exchanger consists of several sub-sectors for the measurements of the quasi-local heat transfer coefficient. The first heat exchanger is composed of 3 sub-sectors while the second heat exchanger is composed of 2 sub-sectors. Each sub-sector presents fins on the external surface of the copper tube. On each fin, two grooves have been milled, in order to create the water flow passage: the groves located on two consecutive fins are rotated with an angle of 90° forcing the water flow to change its direction. The water channel is then closed by a Lexan transparent tube having an internal diameter that exactly matches the diameter of the copper fins. Six thermocouples have been embedded in each sub-sector for the measurements of the internal wall temperatures. The present test section allows the accommodation of the wall thermocouples without passing through the water coolant path and therefore limiting the effect of the axial conduction along the thermocouple wires.
On the water side, two thermocouples and a triple junction thermopile are used to double check the temperature difference of the flowing water at the inlet and outlet of each sub-sector. The measurement of the adiabatic mixing cup temperature of the water is

fundamental for a precise evaluation of the heat flow rate and then for the determination of the heat transfer coefficient. For this reason, two mixers have been placed along the water path before the location of the thermopile junctions. Two pressure ports have been soldered at the inlet and outlet of the test section; one at the inlet of the first heat exchanger and one at the outlet of the second heat exchanger. A detailed description of the present test section and data reduction is reported by Azzolin ([7,8]).

2.4.2 Experimental results

Here, the experimental heat transfer coefficient obtained by the present test section are reported for R134a vertical downflow condensation in 3.4 mm circular channel. These experimental data are reported in Figure 2.14 at varying mass flux from 50 to 200 kg m^{-2} s^{-1} and at ranging saturation-to-wall temperature difference from 4 K to 22 K.
These experimental data will be discussed in detail and compared against the steady-state numerical results in Section 3.6 to analyze the condensation features at these operating conditions.

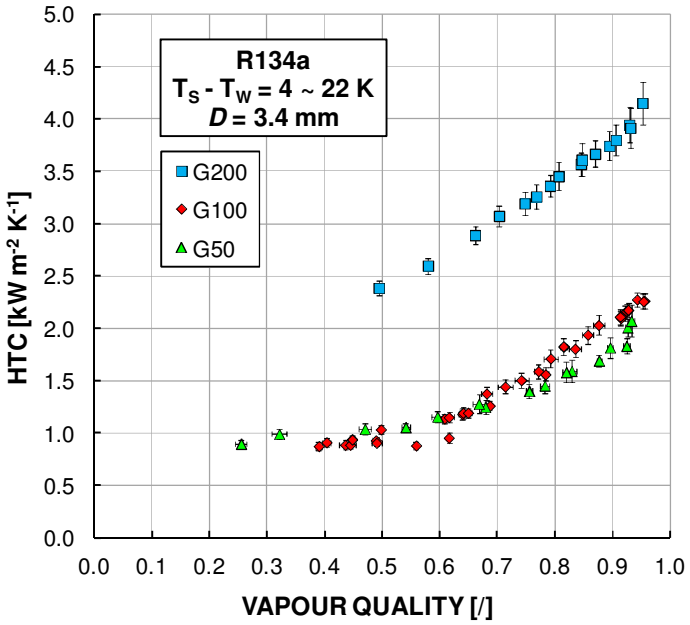

Figure 2.14: Local heat transfer coefficient during downflow condensation inside the vertical circular 3.4 mm channel at varying mass flux *G* [kg m^{-2} s^{-1}].

In addition, since the test section is composed by an adiabatic glass tube between the two heat exchangers, it has been possible to visualize the flow pattern and capture the two-phase flow features using a Photron FASTCAM Mini UX100 high speed camera (CMOS sensor with Bayer colour filter array). The high speed camera has been coupled with a 100 mm Tokina macro lens and a LED illumination system as light source. During condensation tests, the mass velocity has been maintained at a fixed value and different images have been recorded changing the vapor quality in the glass tube. The vapor quality at the inlet of the glass tube is settled changing the water conditions in the 1st heat exchanger. These experimental visualizations has been compared against the two-phase flow predicted by unsteady state numerical simulations reported in Section 4.

3 STEADY-STATE VOF SIMULATIONS OF CONDENSATION INSIDE A SINGLE MINICHANNEL

3.1 The VOF method

In this chapter, the VOF method has been applied to evaluate the heat transfer during the condensation inside a single minichannel (i.d. < 3mm). This method is capable of computing the multiphase flows of immiscible fluids while tracking the motion of the interface without the use of empirical closure laws to model the interaction between the phases.

When the condensation inside channel is dominated by annular and plug/slug flow regimes, the vapour-liquid interface is well defined and this numerical method is suitable to directly track the interface motion and to model the heat transfer. In the case of dispersed flows (e.g. bubbly or mist flows), instead, since the scale of the individual bubbles/drops is smaller than the grid cells size, the adoption of empirical closure laws is necessary.

When the VOF is applied to predict the two-phase flows, a scalar field called "volume fraction" α, which represents the portion of the volume of the computational cell filled with each additional phase beyond the primary, is computed.

In each cell the volume fractions of all phases sum to unity and since an incompressed flow is considered the conservation of volume fraction is equivalent to that of mass.

For example, in case of a vapour-liquid flow, if in a cell the amount of liquid volume fraction α_L is 1, then the cell is filled only by liquid phase; if in the same cell the α_L is 0, the the cell is filled only by vapour phase; but when $0< \alpha_L <1$ then in the cell is located the vapour-liquid interface.

The VOF method solves the updating of the volume fraction field given the fixed mesh, the velocity and volume fraction field at previous step. This procedure occurs into two parts: a reconstruction and a propagation step. The problem of interface reconstruction is that of finding an approximation to the section of the interface in each cut cell, by knowing the volume fraction in that cell and in the neighbouring ones.

Once the interface has been reconstructed, its motion by the underlying flow field is modeled by an advection algorithm. The most accurate VOF techniques are known as Piecewise Linear Interface Construction (PLIC) methods ("geometric reconstruction scheme"), where the interface is fitted through piecewise linear segments.

The VOF method adopted in this thesis has been implemented in the commercial package ANSYS/FLUENT and when the explicit scheme is used for time discretization the geometric reconstruction scheme is available, but it is not present for implicit one.

The numerical simulations presented in this section are steady state and, since the implicit scheme for time discretization has been applied, the modified High Resolution Interface Capturing (HRIC) has been adopted. However, this method is more accurate than a second order scheme and is less computationally expensive than the "geometrical construction scheme".

In the VOF method, the two-phase mixture is considered as a single fluid which thermal and transport properties are computed within each control volume based on the volume fraction of each phase by means of an arithmetic mean:

$$\varphi=\varphi_L\alpha_L+\varphi_V\alpha_V \qquad \textbf{3.1}$$

with φ is the density ρ, the molecular thermal conductivity λ and molecular viscosity μ.
Some implementations of the VOF method adopt a harmonic mean for the computation of viscosity. According to Boeck et al. [25], the arithmetic mean is optimal when the interface is perpendicular to the flow, whereas the harmonic mean is recommended when the interface is parallel.
The governing continuity, momentum, turbulence and energy equations are then resolved for a single set of shared flow variables (velocity, pressure...) adding source terms to take into account the presence of vapour-liquid interface and the phase change process.
The following continuity equations are solved:

$$\nabla\cdot(\vec{u}\alpha_L)=\frac{S}{\rho_L} \qquad \textbf{3.2}$$

$$\nabla\cdot(\vec{u}\alpha_V)=-\frac{S}{\rho_V} \qquad \textbf{3.3}$$

where S is the mass source term due to phase change and u is the velocity vector.
The usual Navier-Stokes equations are solved for momentum in the cell where only one of the two phases is present. At the interface (i.e. $0<\alpha_L<1$), instead, the force due to surface tension F_σ must be taken into account as:

$$\nabla\cdot(\rho\vec{u}\vec{u})=-\nabla p+\nabla\cdot\left[(\mu+\mu_t)\left(\nabla\vec{u}+\nabla\vec{u}^T\right)\right]+\rho\vec{g}+\vec{F}_\sigma \qquad \textbf{3.4}$$

where p is the pressure, g the gravity acceleration vector, μ the molecular viscosity and μ_t the turbulent viscosity.
The effect of surface tension is computed by means of the CSF (Continuum Surface Force) model proposed by Brackbill et al. [26].
The vapour-liquid interface is treated as a transition region of finite thickness and, for this reason, the effect of surface tension is modelled as a volume force.
The surface normal is computed as the gradient of the volume fraction scalar and the interface curvature κ is obtianed as follows:

$$\kappa=\nabla\cdot\frac{\nabla\alpha_L}{|\nabla\alpha_L|} \qquad \textbf{3.5}$$

Finally, the volumetric force due to surface tension is computed as follows:

$$\vec{F}_\sigma = \sigma \frac{\rho}{0.5(\rho_L + \rho_V)} \kappa \nabla \alpha_L \qquad \textbf{3.6}$$

The calculation of surface tension effects on triangular and tetrahedral meshes is not as accurate as on quadrilateral and hexahedral meshes: in FLUENT, the regions, where the surface tension effects are most important, should be meshed with quadrilaterals or hexahedra.
The tracking problem of a sharp and thin interface is very common when the VOF method is used. In fact, the reconstruction of a "clear" interface without diffusion problem can be primarily complex when the mesh is too coarse and unstructured or when the curvature of interface is too small.
For example, a typical diffusion problem can occur when the vapour-liquid interface is reconstructed near the corners of a square minichannel. To avoid this diffusion problem, the mesh of square minichannel has been done with hexahedral cells and it was finer than that of circular one.
All scalar values are shared by the phases throughout the domain, and thus no particular special treatment is needed for the energy or turbulence equations. The following energy equation is solved:

$$\nabla \cdot (\vec{u} \rho h) = \nabla \cdot \left(\lambda_{eff} \nabla T \right) + h_{LV} S \qquad \textbf{3.7}$$

where λ_{eff} is the effective thermal conductivity, h is the specific sensible enthalpy and the last term (i.e. $h_{LV}S$) is the energy source due to phase change. The effective thermal conductivity is computed as follows:

$$\lambda_{eff} = \lambda + \frac{c_p \mu_t}{\mathrm{Pr}_t} \qquad \textbf{3.8}$$

For turbulent condensate film flow, the turbulent conductivity $c_p \mu_t Pr_t^{-1}$ is the dominant term therefore the estimation of the turbulent viscosity μ_t is crucial for the computation of heat transfer. For the numerical simulations presented in this thesis the turbulent Prandtl number is set to $\mathrm{Pr}_t = 0.85$, as reported by Da Riva et al. [27].
The specific sensible enthalpy, as well as the isobaric specific heat, are computed as a weighted average as follows:

$$\varphi = \frac{\alpha_L \rho_L \varphi_L + \alpha_V \rho_V \varphi_V}{\alpha_L \rho_L + \alpha_V \rho_V} \qquad \textbf{3.9}$$

where φ is the specific sensible enthalpy or the isobaric specific heat.
Finally the value of specific sensible enthalpy at temperature T is calculated as follows:

$$h(T) = \int_{T_S}^{T} c_p dT \qquad \textbf{3.10}$$

3.2 Turbulence modeling

The evaluation of turbulence inside the two phases is very important and has been done applying turbulence models based on the Reynolds Averaged Navier Stokes equations (RANS) approach. The two most widely used turbulence models for CFD simulations are the k-ε model and the k-ω model. Both these turbulence models provide the calculation of turbulent viscosity μ_t.
When the flow is turbulent or when the laminar-to-turbulent transition occurs the evaluation of turbulent viscosity μ_t results decisive in the momentum and energy equations, since it affects the viscous stress (i.e. Boussinesq assumption) and the calculation of the effective thermal conductivity (i.e. Eqs. 3.4 - 3.7).
From these considerations, when the turbulence occurs, the second addend (in Eqs. 3.8) of the effective conductivity has a major influence on heat transfer as compared to the molecular conductivity.
It is worth noting that if the turbulent viscosity μ_t is set null, the turbulence inside the flow is suppressed and the momentum and energy equations are developed for a laminar flow.
In this section, three-dimensional and steady state numerical simulations of condensation of different fluids (R134a, R32, R290, R1234ze(E), R717) inside a single minichannel (i.d. D < 3 mm) have been performed and the setting for the turbulence modeling have been fundamental to understand the influence of fluid properties and of mass flux on heat transfer.
The calculation of some all-liquid and all-vapour Reynolds number Re_{LO} and Re_{GO} has been reported to do assumptions about the presence or the absence of turbulence inside the two phases. For example, for R134a at G = 65 kg m^{-2} s^{-1} and D =1 mm Re_{LO} and Re_{GO} are, respectively, equal to 403 and 5253, whereas for the same fluid at G = 200 kg m^{-2} s^{-1} and D = 3.4 mm they are, respectively, equal to 4210 and 54941.
From these considerations, the vapour flow can therefore be considered turbulent, while no a priori assumption can be made for the liquid flow, since, depending on the mass flux, the position along the minichannel and the inner diameter, both turbulent and laminar flows may occur in the condensate film (the local liquid film thickness and velocity vary both in the axial direction and along the channel perimeter).
This is an important observation, since the existing theoretical models for minichannel condensation ([28-30], [31], [21]) rely on the assumption of laminar flow.
Da Riva et al. [27], in order to properly resolve the near-wall region in the condensate film, selected the low-Reynolds number forms of the k-ω turbulence models, where the viscous sublayer and the laminar-turbulent transition are resolved.

It is worth noting that available turbulence models for CFD computations, however, are semi-empirical and have been developed for single-phase flow; therefore their applicability across a vapour-liquid interface has not established.
The same procedure reported by Da Riva et al. [27] has been applied for all numerical simulations: for purposes of evaluation, two different modelling approaches are considered and compared against experimental data. The first approach (referred to as "laminar liquid film") is the most common in microscale condensation and corresponds to the assumption that the flow is laminar in the liquid phase and turbulent in the vapour one. The second approach (referred to as "SST k-ω approach"), instead, a turbulence model has been used throughout the computational domain.

3.2.1 Laminar liquid film approach

The laminar liquid film approach is based on the low-Reynolds number form of the Wilcox's k–ω model [32] and details are provided in Da Riva and Del Col [33]. The formulation of the turbulent viscosity is modified as follows:

$$\mu_t = f_1 \frac{\rho_V k}{\omega} \alpha_V \qquad \textbf{3.11}$$

The coefficient f_1 is equal to 1 in the high-Reynolds-number form of the k-ω model.
In this approach, the coefficient f_1 damps the turbulent viscosity causing a low-Reynolds number correction.
The damping function is calculated as follows:

$$f_1 = \frac{0.024 + \mathrm{Re}_t / 6}{1 + \mathrm{Re}_t / 6} \qquad \textbf{3.12}$$

$$\mathrm{Re}_t = \frac{\rho k}{\mu \omega} \qquad \textbf{3.13}$$

The near wall modeling is very important because solid walls are the main source of vorticity and turbulence. The use of a dumping function allows the use of the same turbulent model also for the cells of the domain close to the wall.
As compared to the usual formulation, the vapour phase volume fraction α_V is added: in the vapour phase the turbulent viscosity μ_t is equal to the value given by the standard low-Re k–ω model, while in the liquid phase the turbulent viscosity μ_t is set equal to zero and laminar flow is imposed. Since in Wilcox's k–ω model [32] the turbulence production is proportional to the turbulent viscosity, the turbulence production is also suppressed in the liquid phase. At the interface, the turbulent viscosity is blended between zero and the value given in the vapour phase.

This turbulence modeling approach is expected to perform better for the simulation test cases at the lowest mass flux, displaying turbulent vapour flow and laminar liquid flow.
The adoption of this approach avoids the uncertainty arising from the use of a turbulence model across the gas–liquid interface, since turbulence is considered only on the vapour side.

3.2.2 SST k-ω approach

In the SST k–ω approach, the low-Reynolds number form of the Shear Stress Transport (SST) k–ω model by Menter [34] is used throughout the computational domain without any modification. As compared to the standard k–ω model of Wilcox [32], this model includes two major modifications:

- The model ensures a gradual change from the standard k–ω model in the inner region of the boundary layer to a high-Reynolds number version of the k–ε model in the outer part of the boundary layer.
- The formulation of the turbulent viscosity is modified to introduce a stress limiter formulation based on the Bradshaw [35] assumption (i.e., the Reynolds shear stress in a boundary layer is proportional to the turbulent kinetic energy).

The second of these modifications is very important for the present work. The turbulent viscosity in the boundary layer is computed using both the standard k–ω model formulation and the formulation based on the Reynolds shear stress form proposed by Bradshaw [35]; then the minimum of the two values is chosen. In this way, in the boundary layers, where the production of turbulent kinetic energy exceeds its dissipation, the magnitude of the Reynolds shear stress is limited as compared to the standard k–ω model. This formulation is fundamental when the strain rate inside the liquid film boundary layer is very high that occurs at high mass flux.
For example, Da Riva [27] have reported a comparison between SST k-ω approach without any stress limiter implemented and the same approach with the Bradshaw [35] assumption. The comparison shows that the heat transfer coefficients computed with the first model are roughly twice as large as the experimental data, while a very good agreement is achieved with the second model (i.e. SST k-ω approach with the stress limiter).
A similar stress-limiter was introduced by Wilcox [32] in a recent revised formulation of the k-ω model. Besides, when using the standard k-ω model together with the VOF method, the adoption of an empirical turbulence damping modification is suggested in order to reduce turbulence when a high velocity gradient exists at the interface between two fluids.
Da Riva et al. [27] have reported an application of these two different computational approaches and a comparison of numerical results against the experimental data obtained by Matkovic et al. [15] during condensation of R134a inside a 1 mm i.d. circular minichannel (Figure 3.1).

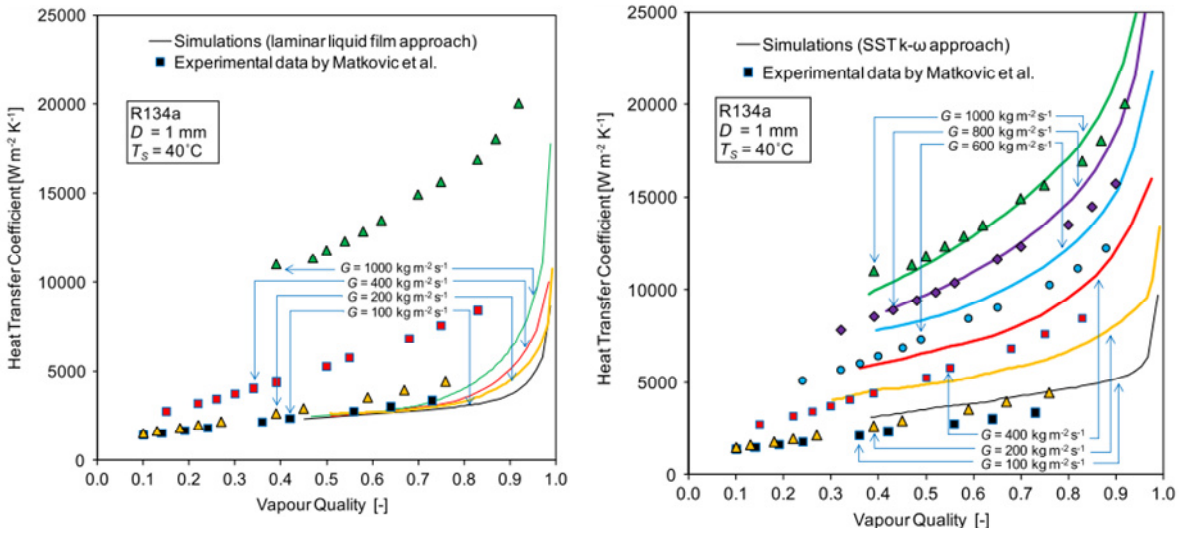

Figure 3.1: Cross-sectional average heat transfer coefficient as a function of vapour quality. Comparison with numerical simulations against experimental data: laminar liquid approach (on left) and SST *k-ω* approach (on right).

As shown by Da Riva et al. [27] the laminar liquid approach displays a weak influence of mass flux on heat transfer coefficient only at high vapour qualities, while for vapour qualities less than approximately x=0.8 the trends overlap. This approach works well at least mass flux, but at increasing of mass flux it strong underpredicts the experimental data. On the contrary, the SST *k-ω* approach simulations dispalys a dependence of the heat transfer coefficient on the mass flux consistent with experimental data. Nevertheless, the transitional low-Reynolds-number turbulence model is used to predict both turbulent and laminar flows without any need of manual tuning, an earlier transition to turbulent flow in the condensate was found in the simulations of test runs in circular minichannel: at 50 kg m^{-2} s^{-1} the same results as the laminar liquid film are obtained; at 100 and 200 kg m^{-2} s^{-1} the experiments are overpredicted by 35% and 54%; and at mass fluxes between 400 and 1000 kg m^{-2} s^{-1}, good agreement with experimental data is achieved. As mentioned above, it is worth highlighting that available turbulence models for CFD computations are semi-empirical and have been developed for single-phase flows; therefore their applicability across a gas-liquid interface has not been established. Furthermore, Da Riva et al. [27] model would deviate from a pure theoretical prediction because of the need to force the laminar solution in the condensate film for a specific range of mass fluxes, based on an *a posteriori* validation against experimental data. For this reason the numerical results obtained in this thesis have been compared against the experimental data of many authors ([15], [12], [13], [24], [11,13], [23]) to understand the validity range of laminar liquid approach and when the influence of mass flux on heat transfer can be considered negligible as compared against the gravity and surface tension effects.

Nevertheless the SST *k-ω* approach simulations at low mass flux displays overpredicted results as compared against the experimental data in some operating conditions, this approach has been however applied to obtain a qualitative analysis of fluid properties influence on condensation heat transfer coefficient inside minichannel at low mass flux.

3.3 Phase change modeling

The numerical technique described by the following equations by Lee [36] are used in the modeling of the phase change process:

$$S = -r\alpha_L\rho_L\frac{T-T_S}{T_S} \qquad T \geq T_S \qquad \textbf{3.14}$$

$$S = -r\alpha_V\rho_V\frac{T-T_S}{T_S} \qquad T < T_S \qquad \textbf{3.15}$$

where S is the source term in the continuity equations and in the energy equation, T is the cell temperature and r is a positive numerical coefficient.
In order to avoid numerical problems of convergence, the amount of mass transferred from one phase to the other at each computational step should never be higher than the total mass of the first phase initially present in the cell. For this reason, the source term S is proportional to the terms $\alpha_V\rho_V$ or $\alpha_L\rho_L$ which describe the amount of vapour and liquid, respectively, present in the cell.
Moving to a higher degree of modeling accuracy, because of molecular kinetics effects during condensation, a temperature drop must exist in the gas phase, and the interface temperature has to be slightly lower than the saturation temperature in order to achieve a finite rate of condensation. This phenomenon occurs very close to the interface over a distance of a few molecular mean free paths in the gas phase. In the literature it is possible to found different equations to evaluate the interfacial heat transfer coefficient (McNaught and Butterworth, [37], [38]). From these equations, the interfacial heat transfer coefficient, at the same operating conditions of numerical simulations (i.e. T_S = 40°C), is calculated at the order of 10^7 W m^{-2} K^{-1}. This implies that the molecular kinetic thermal resistance at the interface is negligible and that, during the condensation of a pure halogenated fluid at common working pressure, the interfacial temperature can be assumed to be equal to the saturation temperature: the Eqs. 3.14 - 3.15 offer a simple numerical technique for implementation of such an assumption as a boundary condition. If at a certain computational step the temperature of a cell in the domain is higher than the saturation temperature, the first of the two equations is used: if this cell belongs to the vapour phase (α_L = 0) no mass transfer is computed; if this cell belongs to the liquid phase (α_L > 0), instead, mass transfer from the liquid to the vapour phase is computed. Besides, the temperature of the cell is decreased by the source term $h_{LV}S$ in energy equation. The computation is analogous for the cells with temperature lower than saturation. In this way, the presence of cells in the vapour phase with temperature lower than the saturation temperature is avoided, as is the presence of cells in the liquid phase with temperature higher than saturation. The source term S is arbitrary fixed; however, mass, momentum and energy are conserved at every computational step. At convergence, the interface

reaches the saturation temperature, while cells in the liquid and vapour phases reach a lower and higher temperature, respectively.

In practice, the interfacial temperature obtained at convergence is not be exactly the saturation temperature. The optimal values for the coefficient *r* strongly depend on the particular problem being solved and suitable values should be found for each case. Excessively small values of *r* lead to a significant deviation between interfacial and saturation temperature. On the other hand, when higher values of the coefficient *r* are used, the interface (i.e., the region of cells with $0 < \alpha_L < 1$) is sharper and thinner, but values of *r* that are too large cause numerical convergence problems.

The main drawback of the approach of Lee [36] is that the numerical coefficient *r* is present in the expressions for the source terms, and the appropriate value must be found through manual tuning for each particular case in order to maintain the interfacial temperature reasonably close to the saturation temperature and, at the same time, avoid divergence issued. Similar approaches are used in the numerical model by Zhang et al. [39] for condensation and Wu et al. [40] and Yang et al. [41] for evaporation. However, in literature more advanced numerical techniques are available. Welch and Wilson [42] modified the enhancement of the VOF method by Youngs [43] in order to directly calculate the discontinuous normal components of the heat flux at the interface and model heat and mass transfer. Another example is Ganapathy et al. [44] that developed original techniques to directly model mass and energy transfer at interface avoiding any need of numerical manual tuning of coefficients. In the present work, coefficients ranging from r =1.0 x 10^5 s^{-1} to r = 6.0 x 10^6 s^{-1} are used and the deviation between area-averaged interfacial temperature of the simulations and the saturation temperature ranges from 1 to 1.3 K.

An example of numerical results obtained at different values of parameter r are shown in Figure 3.2.

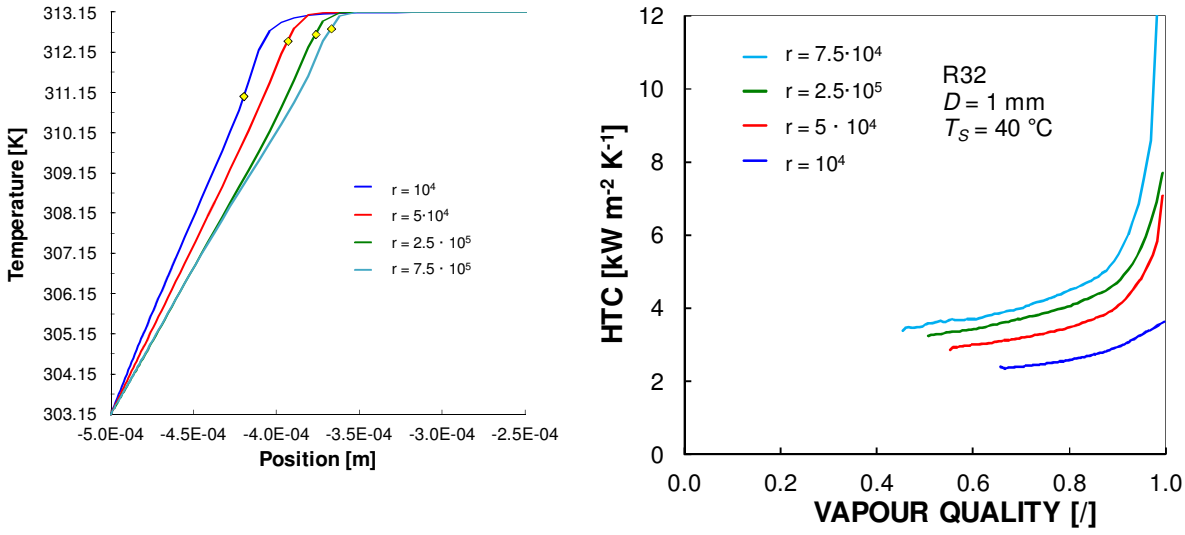

Figure 3.2: Example of temperature profile inside the liquid film (Left) and the local heat transfer coefficient on vapour quality at different values of r (Right).

3.4 VoF simulations of condensation inside a horizontal 1 mm i.d. minichannel

3.4.1 Settings of numerical simulations

In this section three-dimensional and steady-state numerical simulations of condensation process of different refrigerants (R134a,R32,R290,R1234ze(E),R717) inside a single minichannel (i.d. < 3 mm) at low mass flux have been performed using the VOF method, implemented in a commercial package ([45]; Fluent 2015).

Since the steady-state configuration has been set, the wavy flow or intermittent flows such as plug/slug flows cannot be predicted. According to Nema et al. [5], when the hydraulic diameter decreases ($Bo < Bo_{cr}$), the range of the annular flow regime increases and the wavy regime almost disappears at D = 1 mm; while the region of the intermittent regime widens, reflecting a diminishing influence of the gravity force.

From the author's analysis neither a wavy nor an intermittent regime is expected under the conditions of the present work. It is worth highlighting that the criterion applied by Nema et al. [5] was developed using experimental data of R134a condensation at mass flux not lower than 150 kg m^{-2} s^{-1}.

Besides the wavy flow, the entrainment of droplets into the vapour core or the enhancement of the convective heat transfer due to interfacial instabilities cannot be captured in the present numerical simulations. These phenomena can occur when the interfacial shear stress are very high, so at high mass flux, or at low vapour density.

These operating conditions should not verified for these numerical simulations because the investigation of condensation is performed at low mass velocity (G < 200 kg m^{-2} s^{-1}); except for R717 (i.e. ammonia) that at G=150 kg m^{-2} s^{-1} the vapour maximum velocity results almost high (about 14 m s^{-1}).

The validity of the numerical results under the assumption of steady-state regime is, however, verified by means of comparison against experimental data.

Both phases are assumed as incompressible. At the channel inlet the vapour is saturated and the thermodynamic vapour quality is 1. The channel is horizontally oriented, as depicted in Figure 3.3 using the Cartesian axis convention.

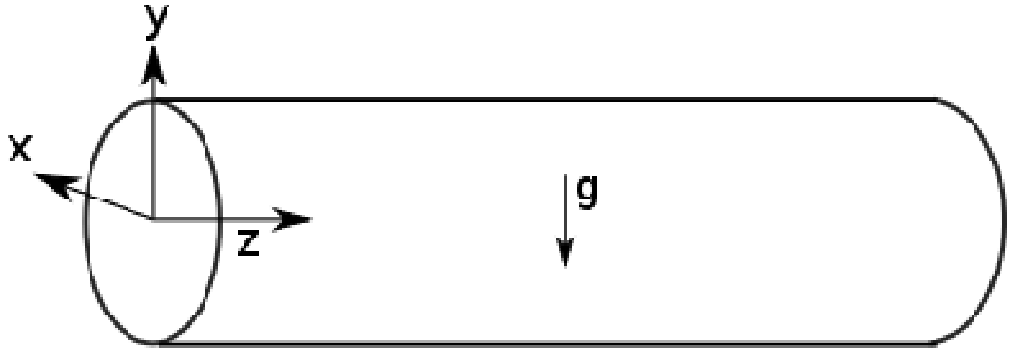

Figure 3.3: Cartesian axis convention for the channel.

The minichannel wall is assumed to be smooth and held isothermal at a uniform temperature of 30°C, while the vapour-liquid interface temperature is set to be uniform and equal to the fluid saturation temperature of 40°C. The saturation temperature drop due to the pressure drop is neglected and the pressure boundary condition is imposed at the outlet. Since the vapour-liquid interface and the wall temperature are constant and uniform the effect of longitudinal conduction is neglected and the saturation-to-wall temperature difference is assumed as constant of 10 K along the minichannel length.
The assumption of a constant wall temperature, instead of constant heat flux, is the closest one to the actual operation of condensers, since the condensing refrigerant must be cooled by means of secondary fluid.
Numerical simulations have been run taking into account or neglecting the influence of gravity and surface tension to understand their influence on the heat transfer and on the liquid thickness. In addition, the numerical results of R134a condensation inside the square minichannel have been compared against those inside the circular one ([20]) to highlight the influence of gravity and surface tension at different diameter shape.
Before the two-phase simulations, single-phase simulations have been performed in order to obtain the fully developed turbulent solution for the vapour flow.
The results of these simulations are then used to set the inlet boundary conditions for the axial velocity, the turbulent kinetic energy and the turbulent specific dissipation rate.
The circular minichannel mesh is formed of around $1.15 \cdot 10^6$ hexahedrons cells and the symmetry conditions for both cross section shapes have been applied. In order to fully resolve the liquid film region, the radial thickness of the cells in the near-wall region is around 0.8 μm, while the mesh is much coarser in the core region due to computation cost reasons; and 450 nodes are used for the axial discretization. In the case of square minichannel, the domain is discretized into $3.88 \cdot 10^6$ hexahedrons cells; the radial thickness of the cells in the near-wall region is around 1 μm, while the mesh is much coarser in the core region; 385 nodes are used for axial discretization. The mesh of square and circular cross section are depicted in Figure 3.4.

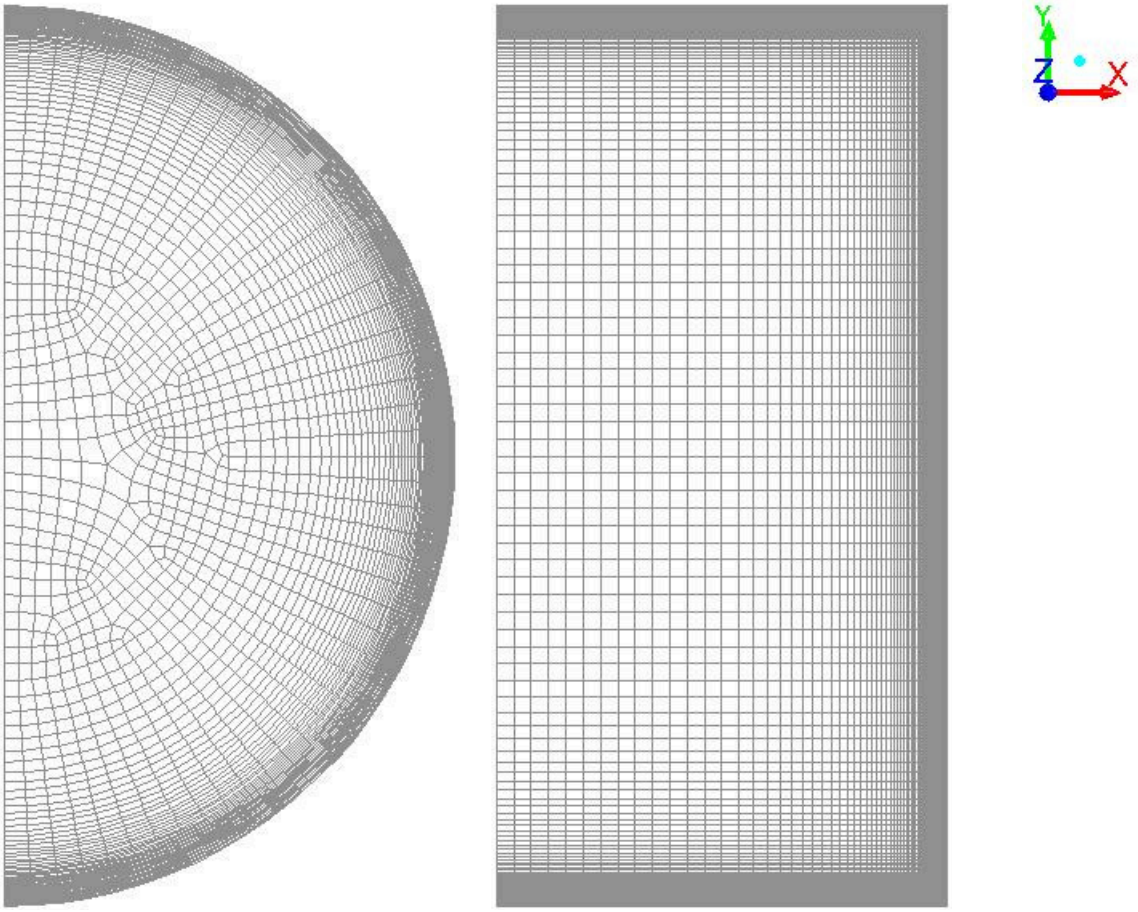

Figure 3.4: Cross-section of the computational mesh for circular (left) and square (right) channel.

The PRESTO! (PREssure STaggering Option) scheme is used for the pressure interpolation, while the pressure-velocity coupling is handled by means of the SIMPLE algorithm. The third order MUSCL scheme is used for the momentum equations, the two turbulence equations and the energy equation. This third-order convection scheme is conceived from the original MUSCL (Monotone Upstream-Center Schemes for Conservation Laws) by blending a central differencing scheme and second-order upwind scheme. Compared to the second order upwind scheme, it has a potential to improve spatial accuracy for all type of meshes by reducing numerical diffusion, most significantly for complex three-dimensional flows.

As declared by Gupta et al. [46], the implementation of surface tension force can induce unphysical velocity near the interface known as 'spurious currents'. This could occurs because the pressure and viscous force terms do not exactly balance the surface tension force. The accurate calculation of gradients can help in minimizing these spurious currents. For these reason, as suggested by the author, the Green-Gauss node-based method have been used for the evaluation of gradients helping to minimize these unphysical pressure oscillation at the vapour-liquid interface.

3.4.2 Effect of the cross section shape

At first, a brief introduction on numerical results at high mass flux is reported and then the topic is focused on the significant role of capillary and gravity on liquid film distribution at low mass flux.

As demonstrated numerically by Bortolin et al.[18] in Figure 3.5, at high mass flux there is almost no effect of the channel cross section shape on the heat transfer coefficient. At such conditions, condensation is controlled by vapor shear stress, and this can be understood considering the dominating role of the mass flux.

The authors have also carried out simulations with and without taking account the surface tension and gravity effects inside 1 mm i.d. square and circular minichannel highlighting the less importance of capillary and gravity forces at high mass flux, Figure 3.6.

Da Riva et al. [27] pointed out that the mass flux dependence, observed in almost all experimental works, can be predicted by numerical simulations only if the laminar film hypothesis is relaxed and some turbulence is accounted for in the liquid film. At these conditions, the shape of the vapor-liquid interface, which is in any case affected by surface tension, does not have a real influence on the heat transfer coefficient because the governing parameter is the effective liquid thermal conductivity induced by turbulence (section 3.2). Since, at high mass velocity, the surface tension and gravity effects are masked by vapor shear stress, the following numerical simulations are presented only at $G \leq 200$ kg m^{-2} s^{-1} and compared against experimental data.

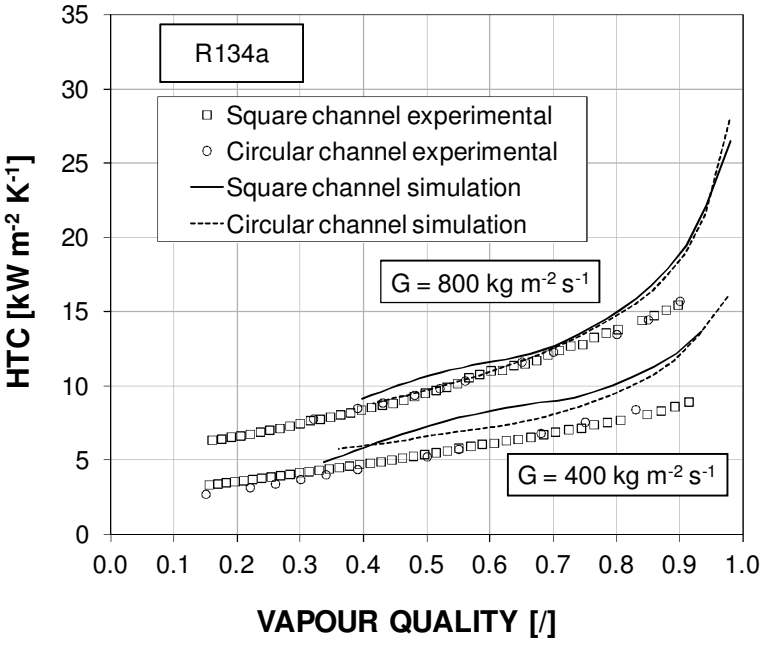

Figure 3.5: Cross-sectional average heat transfer coefficient as a function of vapour quality inside the 1 mm diameter square and circular minichannel at G = 400 kg m^{-2}s^{-1} and 800 kg m^{-2}s^{-1} for R134a (Bortolin et al.[18]).

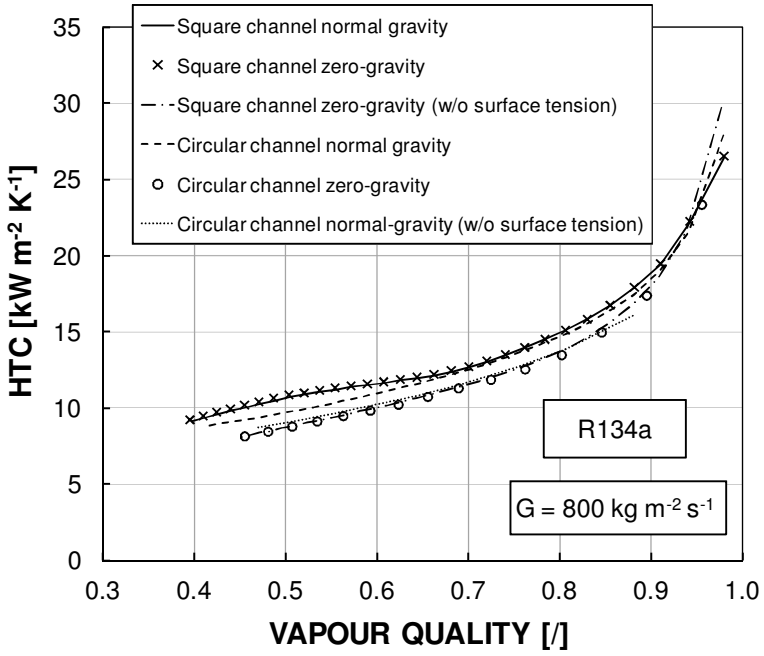

Figure 3.6: Surface tension and gravity effects on heat transfer coefficient as a function of vapour quality inside the 1 mm diameter square and circular minichannel at G = 800 kg m^{-2}s^{-1} for R134a (Bortolin et al. [18]**).**

New numerical simulations of R134a condensation inside a single square minichannel and the results obtained by Da Riva and Del Col [20] inside a single circular minichannel are, here, reported taking into account or not the surface tension and the gravity to highlight the influence of these forces on heat transfer mechanisms. In addition, new numerical results on R32 and R1234ze(E) will be shown for the two different channels.

The details of new simulations and of those done by Da Riva and Del Col [20] are, respectively, summarized in Table 3.1 – Table 3.2.

Since the investigation is focused on the effect of cross section shape of channel at low mass flux, it is worth noting that the all simulations reported in this section 3.4.2 are performed with the laminar liquid film approach.

Table 3.1: Cases of new numerical simulations during condensation process inside circular (C) and square (S) channel at low mass velocity (G < 200 kg m^{-2}s^{-1}).

Fluid	G [kg m^{-2} s^{-1}]	Section shape	Length [mm]	Outlet quality	σ	g
R134a	65	C	35	0.57	Y	Y
R32	100	C	75	0.45	Y	Y
R32	200	C	135	0.45	Y	Y
R1234ze (E)	150	C	120	0.39	Y	Y
R134a	65	S	35	0.53	Y	Y
R134a	100	S	50	0.50	Y	Y
R134a	100	S	50	0.51	Y	N
R134a	100	S	100	0.54	N	N

R134a	200	S	90	0.50	Y	Y
R32	100	S	65	0.46	Y	Y
R32	200	S	120	0.44	Y	Y
R1234ze(E)	150	S	90	0.42	Y	Y

Table 3.2: Cases of numerical simulations of Da Riva and Del Col [20] during R134a condensation process inside circular (C) channel at low mass velocity (G < 200 kg m^{-2}s^{-1}).

G [kg m^{-2} s^{-1}]	Length [mm]	Outlet quality	σ	g
100	75	0.44	Y	Y
100	75	0.45	N	Y
100	125	0.41	Y	N
200	120	0.5	Y	Y

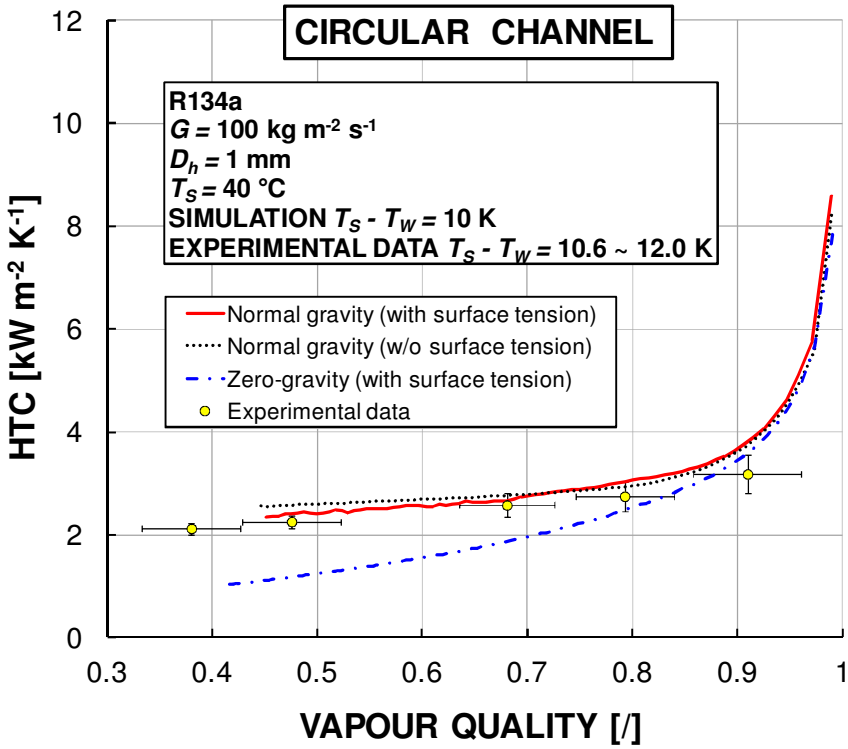

Figure 3.7: Surface tension and gravity effects on heat transfer coefficient as a function of vapour quality inside the 1 mm circular minichannel at G = 100 kg m^{-2}s^{-1}. Numerical results by Da Riva and Del Col [20].

In Figure 3.7 the HTC-x curves of R134a condensation inside circular channel with and without gravity and surface tension effects are reported. From the figure, when the surface tension is not taken into account there is not an appreciable difference between the HTC trends that, in fact, overlaps.

At the same operating conditions, a clear influence of gravity can be seen; for example, when the gravity is not considered, at x = 0.6 the HTC is about 1550 W m^{-2} K^{-1}, i.e. about 40% lower than the value at normal gravity (2560 W m^{-2} K^{-1}).
In Figure 3.8, the HTC-x curves of R134a condensation are reported inside square channel with/without gravity and with/without surface tension effects.
The absence of surface tension leads to a clear decrease of HTC. For example, when the surface tension is not considered, at x = 0.6 the HTC is about 1405 W m^{-2} K^{-1}, i.e. about 57% lower than the value with surface tension activated (3300 W m^{-2} K^{-1}).
At G = 100 kg m^{-2} s^{-1}, the turbulence inside the liquid film becomes negligible and the heat transfer phenomena is primarily function on the distribution of liquid film.
From this observation, it could be interesting to analyze the behavior of condensate film thickness obtained by means of numerical simulations underlining more clearly the different contribution of surface tension and gravity inside circular and square channel.

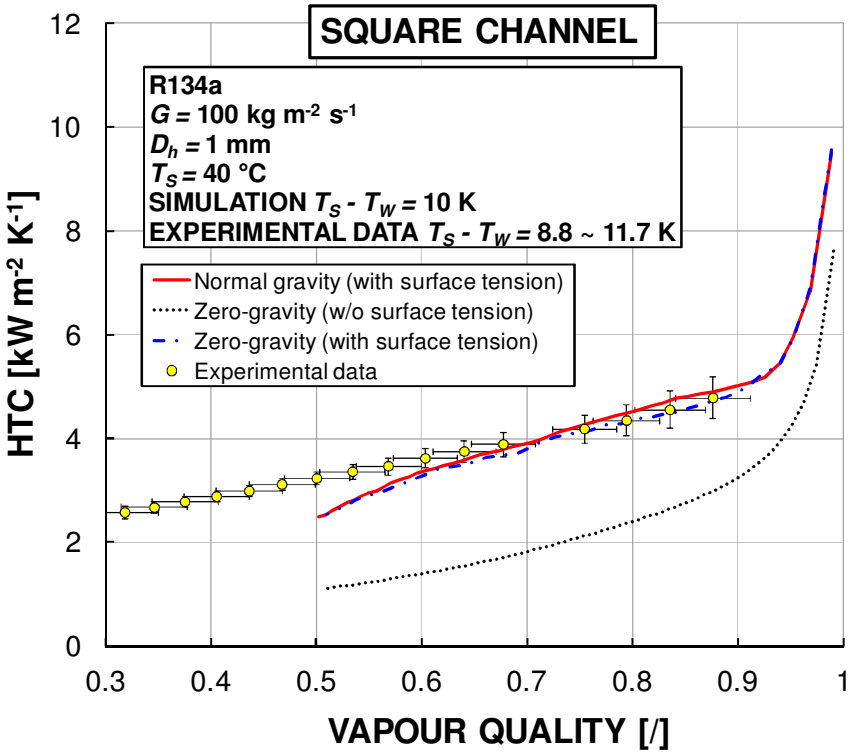

Figure 3.8: Surface tension and gravity effects on heat transfer coefficient as a function of vapour quality inside the 1 mm square minichannel at G = 100 kg m^{-2}s^{-1}. Experimental data by Del Col et al. [19].

In Figure 3.9 and Figure 3.10 the liquid-vapour interface tracked by means of VOF simulations and the condensate liquid thickness are shown with the aim to analyze the distribution of liquid film inside the two channels (from the bottom to the top of channel: from -90° to 90°).
In Figure 3.11 the local heat transfer coefficient is reported in function on the angular coordinate to compare the effect of surface tension and gravity from heat transfer point of view inside the circular and square channel.

In Figure 3.9 and Figure 3.10, inside the square channel the surface tension pulls the liquid towards the corners thinning at the centre of each flat side and the stratification is not still observed at vapour quality of 0.6.
Since at the flat sides the liquid film is very thin (i.e. the minimum value is about 5.5 μm) the local heat transfer coefficients reaches very high values (e.g. at angular coordinate of 0° the HTC is about 10 kW m^{-2} K^{-1}, Figure 3.11) and the major part of heat transfer is transferred at these regions of channel.
Considering from -90° to -65°, -25° to 25° and 65° to 90° the regions where the liquid film is thin (see Figure 3.10), and computing the angular weighted average of local heat transfer coefficient, the 89% of heat transfer rate occurs here.
When the surface tension is not considered, the liquid film thickness results almost constant around the wall of channel (e.g. the value is about 50 μm, Figure 3.9 and Figure 3.10) and at the flat sides the local heat transfer coefficient is reduce to a maximum value of 1.8 kW m^{-2} K^{-1}. In this case, it can be observed that there is no influence of gravity, in fact, as depicted in Figure 3.9 and Figure 3.10 this force does not influence on liquid film thickness.

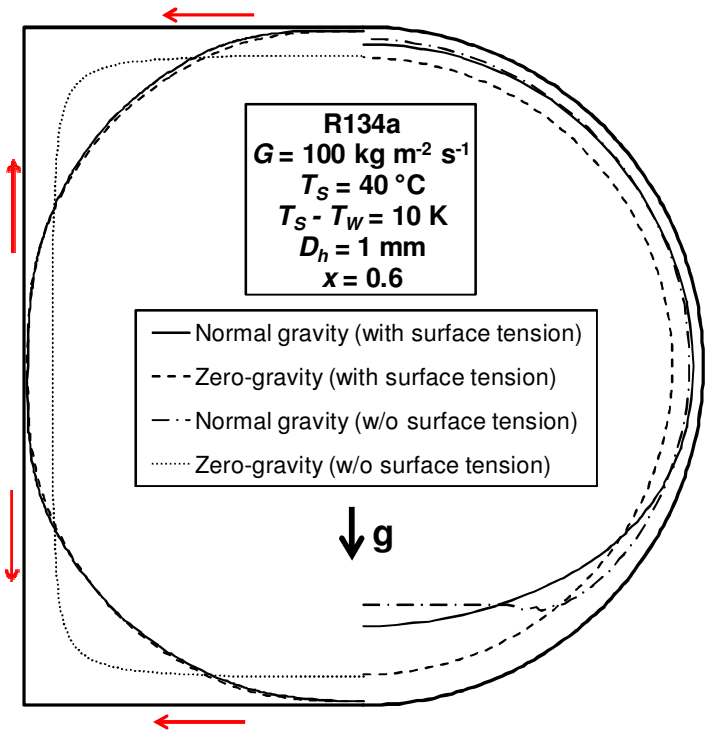

Figure 3.9: Surface tension and gravity effects on the liquid-vapour interface tracked by means of VOF numerical simulations in circular and square minichannel.

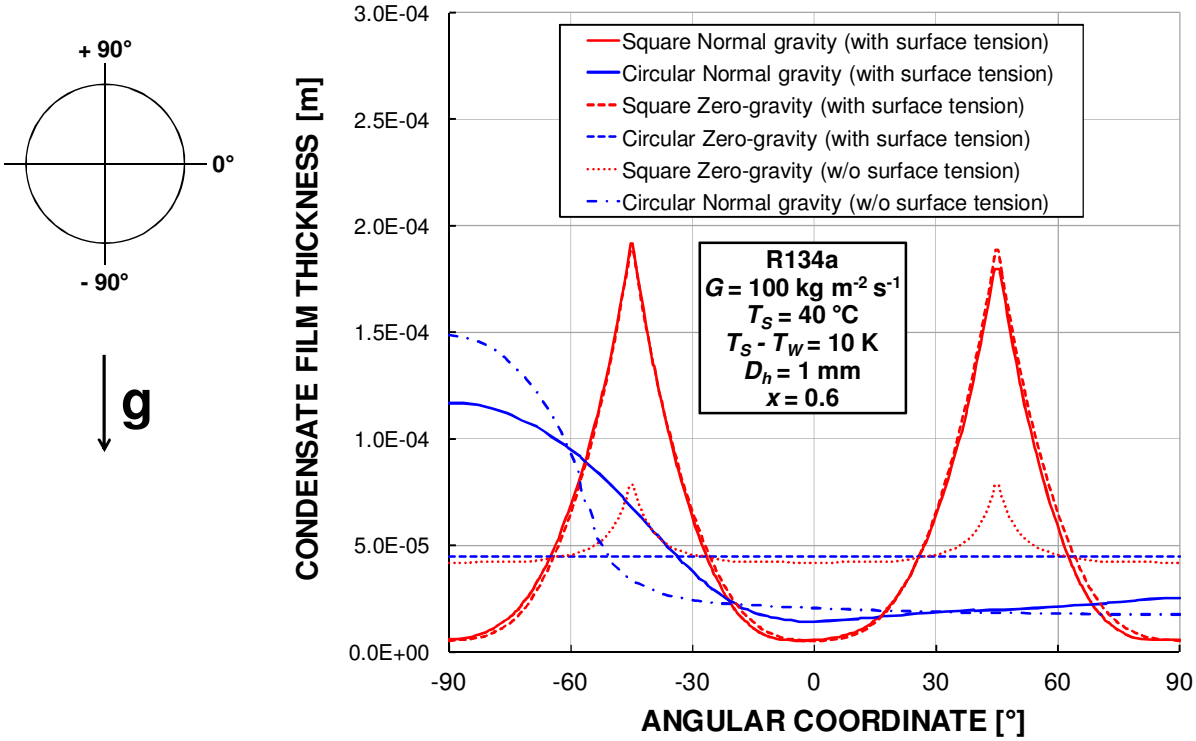

Figure 3.10: Surface tension and gravity effects on the condensate film thickness obtained by numerical simulations in circular and square minichannel.

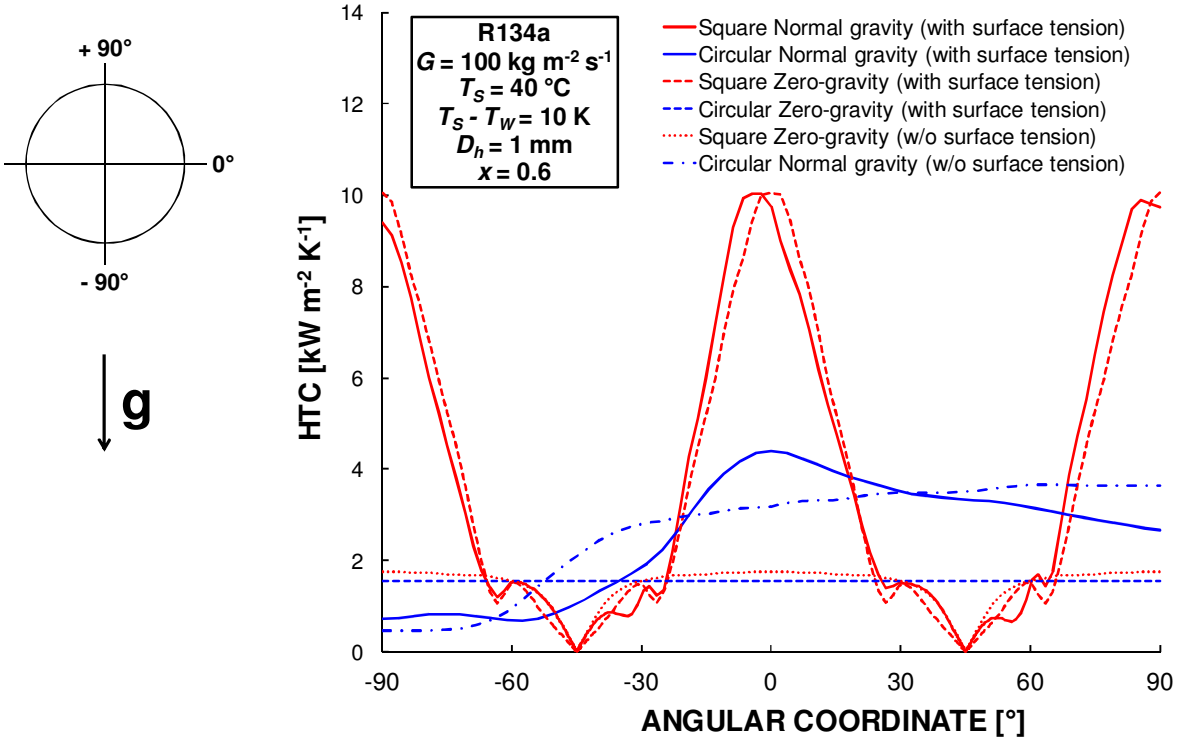

Figure 3.11: Surface tension and gravity effects on the local heat transfer coefficient in circular and square minichannel.

Inside the circular channel, instead, the gravity promotes the stratification having a thin liquid film at the top and a thicker film at the bottom. This phenomenon allows to reach high local heat transfer coefficients from -30° to 90°, having the 87% of heat transfer in this range of angular coordinate.

In Figure 3.10 the influence of surface tension on interface can be also noted. As shown in Figure 3.9, the surface tension pulls the liquid towards the upper side of circular channel thinning the liquid film at 0° (i.e. the minimum value is about 14 μm) and keeping it at the top: the maximum value of local heat transfer coefficient is reached at the middle of channel with a value of 4.4 kW m^{-2} K^{-1}. If the surface tension is not included in the model, a similar value of HTC is achieved at top with a liquid thickness of 17.5 μm. Therefore, there is an influence of surface tension on liquid film distribution but its contribution on the cross sectional average of HTC results negligible.

When the gravity is not considered, instead, a strong reduction of local HTC can be detected with a uniform liquid thickness of 45 μm and a constant HTC value of 1.6 kW m^{-2} K^{-1}, as shown in Figure 3.11.

In conclusion, at these values of vapour qualities and mass velocity, where the annular flow is aspected by Coleman and Garimella [4], the gravity has the major role inside the circular minichannel whereas the capillary forces are important inside the square one. When these forces are not considered an almost uniform liquid film is obtained around the channel perimeter getting worse the condensation heat transfer.

Furthermore, since the liquid film inside the square channel is very thin at flat side the cross sectional average of HTC is higher than that inside the circular channel.

Hereinafter, the influence of cross section shape on HTC is explained along the channel during the condensation process of different fluids and comparisons between the numerical results and the experimental data (reported in section 2.2.3) are here shown.

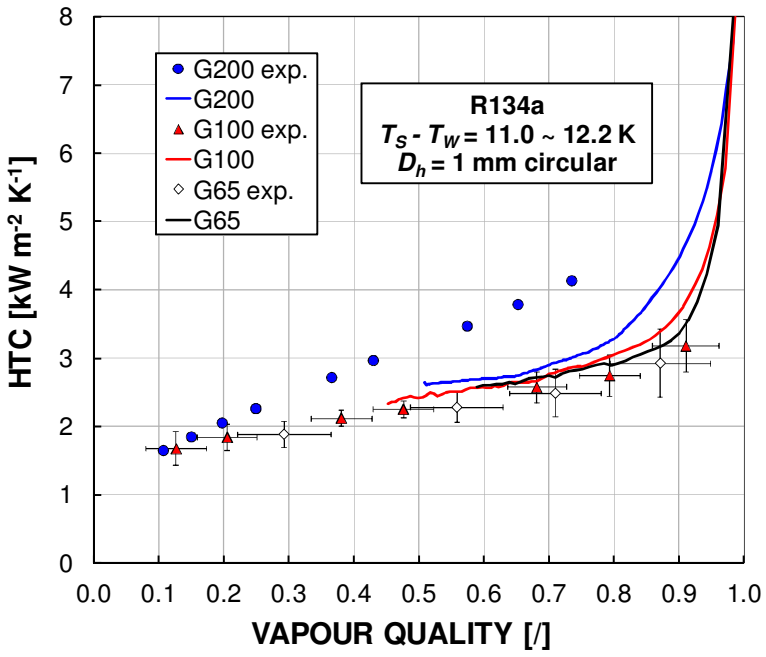

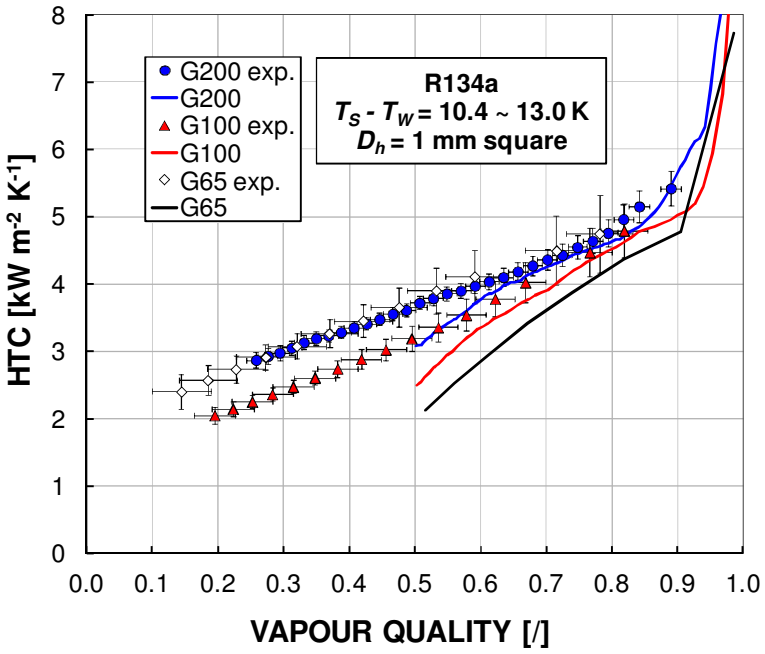

Figure 3.12: Experimental and calculated R134a condensation heat transfer coefficients using VOF simulations. Top: circular. Bottom: square.

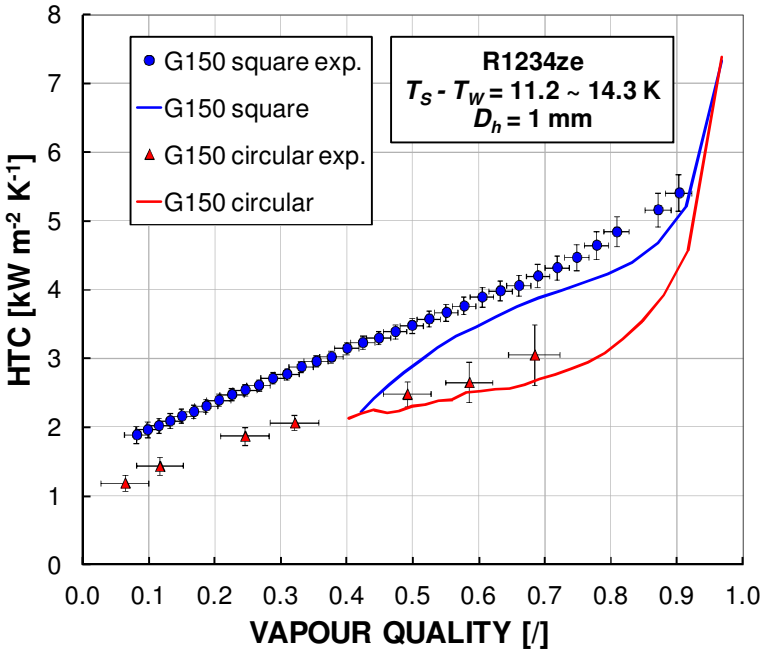

Figure 3.13: Experimental and calculated R1234ze(E) condensation heat transfer coefficients using VOF simulations inside circular and square channel.

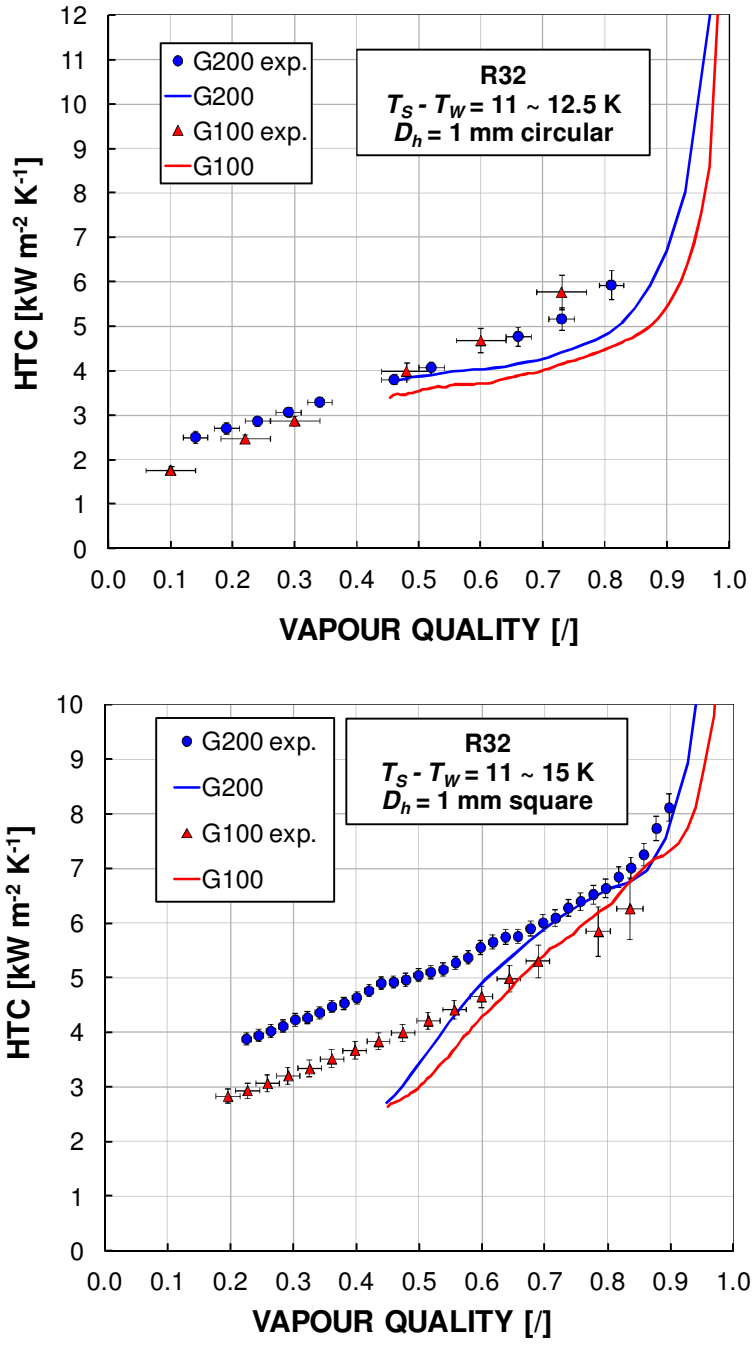

Figure 3.14: Experimental and calculated R32 condensation heat transfer coefficients using VOF simulations. Top: circular. Bottom: square.

In Figure 3.12 -Figure 3.14 experimental and calculated heat transfer coefficients assuming laminar liquid film are shown for R134a, R1234ze and R32. Good agreements between simulations and experimental data are found and reported in Table 3.3. Here the average deviation e_R and the standard deviation σ_N are calculated considering two bounds of vapour quality range: the lowest value of vapour quality reached by each numerical simulation and the highest value of vapour quality measured in the experimental data.

Table 3.3: Comparison between experimental and calculated cross section average heat transfer inside circular (C) and square (S) channel with laminar film approach.

Fluid	G [kg m^{-2} s^{-1}]	Section shape	e_R	σ_N
R134a	65	C	9.8	1.4
R134a	100	C	6.9	3.2
R134a	200	C	-24.8	2.8
R32	100	C	-17.8	5.3
R32	200	C	-10.4	5.2
R1234ze (E)	150	C	-8.4	2.2
R134a	65	S	-25.9	8.9
R134a	100	S	-9.1	5.8
R134a	200	S	-5.5	3.7
R32	100	S	-12.0	13.5
R32	200	S	-15.8	15.0
R1234ze(E)	150	S	-12.8	5.63

The average deviations show also an earlier laminar to turbulent transition much more evident for the circular channel as compared to the square one. For example, this phenomenon clearly occurs for R134a, when the mass flux effect on HTC become visible at G = 200 kg m^{-2} s^{-1} for circular minichannel but not for square one, where the laminar liquid film approach works well again.

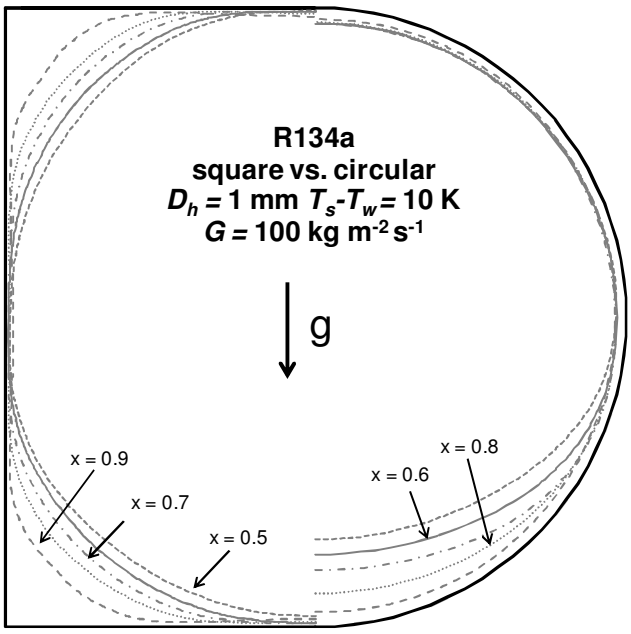

Figure 3.15: The evolution of vapour-liquid interface during R134a condensation inside circular and square minichannel.

In Figure 3.15 the vapour-liquid interfaces tracked by VOF simulation during R134a condensation in square and circular minichannels are shown. When the vapour quality decreases two different phenomena can be noted:

- Inside the circular channel the liquid is drained by the gravity and the "pool" is thicker at the bottom of the channel during condensation. At the same time the film thickness is hold almost constant at the upper side, where almost all the heat flow rate is rejected.
- Inside the square channel, instead, the liquid film grows at the corner and the flat sides where the liquid film is thin are reduced more and more, decreasing uniformly the HTC along angular coordinate.

The comparison between the numerical results of R32 condensation at G = 200 kg m^{-2} s^{-1} and at x = 0.7 and x = 0.45 are shown in Figure 3.16 to highlight the last consideration.

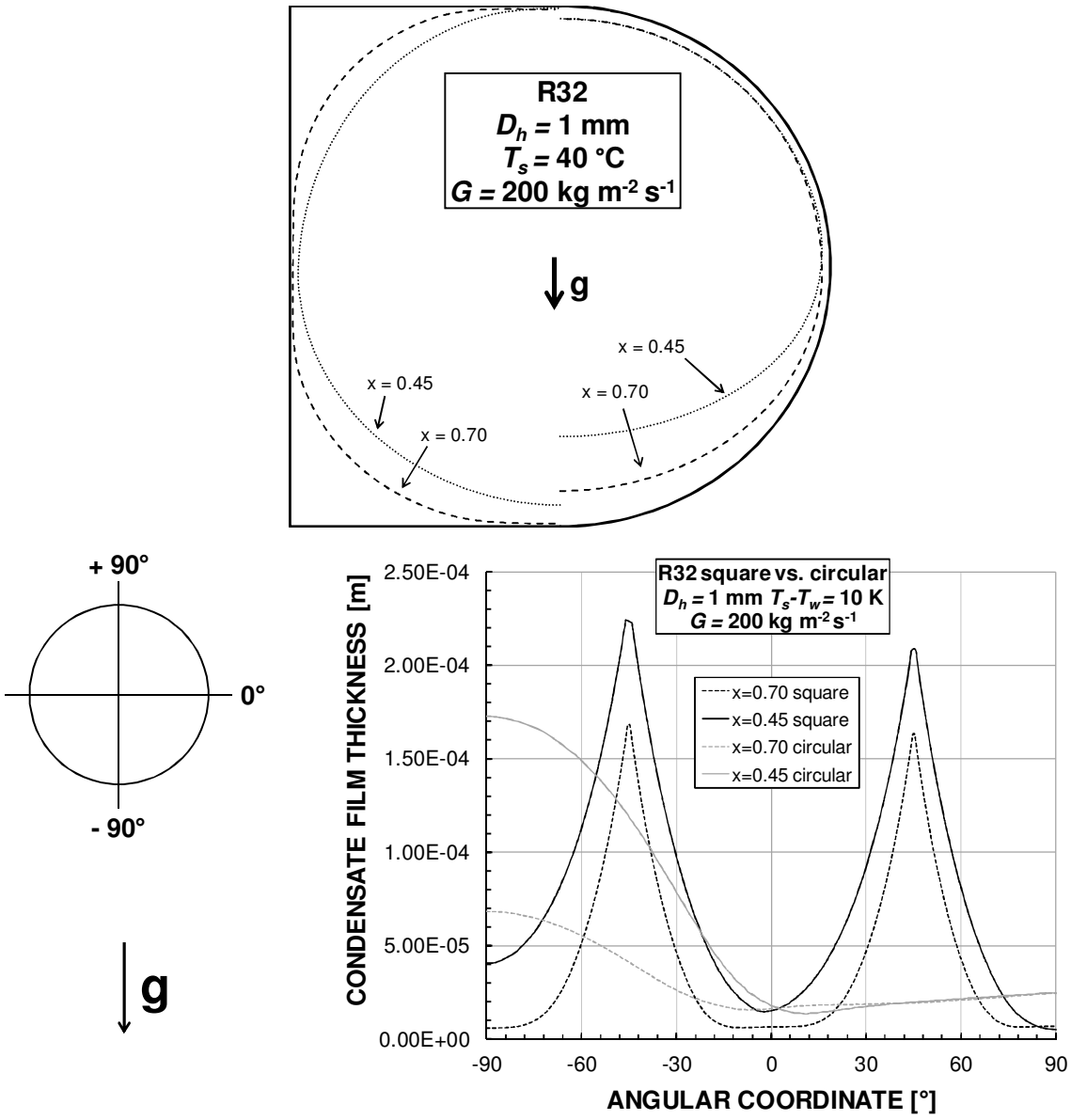

Figure 3.16: Liquid-vapour interface (Top) and condensate film thickness (Bottom) as a function of the angular coordinate during R32 condensation at two values of vapour quality.

In particular, at x = 0.45, an occurring of stratification can be also seen inside the square channel in case of R32 at G = 200 kg m^{-2} s^{-1}; from -60° to 80°, the liquid film is thicker than that in the circular channel.

From these observations and Figure 3.12 - Figure 3.14, the following conclusions can be done:

- the HTC trends are more flatter for circular channel as compared to square one. For example, for R134a from x = 0.8 to x = 0.6 the HTC decreases from 3060 to 2580 W m^{-2} K^{-1} in circular channel and from 4550 to 3350 W m^{-2} K^{-1} inside the square one;
- for $x \geq 0.6$ the enhancement of the heat transfer coefficient in the square channel with respect to the circular one is reproduced by numerical simulations;
- for vapour quality below 0.5, the heat transfer coefficient inside the circular minichannel becomes higher than that inside the square minichannel.

About the last note, this result is found only in numerical simulations and it is also predicted by the theoretical model of Wang and Rose [29]. On the contrary, all experimental data show in section 2.2.3 higher heat transfer coefficient for the square channel also at low values of vapor quality.

The dimensionless criterion of Nema et al. [5] has been applied for R32, R134a and R1234ze at mass flux lower than 200 kg m^{-2} s^{-1} to investigate the reasons of this different behavior between numerical results and experimental data at low vapour qualities (i.e. x < 0.6). This criterion proposed by authors is useful to evaluate the flow patterns inside 0.96 mm i.d. circular minichannel during the condensation process and, thus, the transition region between annular and plug/slug flow.

This procedure has been applied considering the "small diameter criteria" since for all cases the bond number was lower than the bond critical number. At these conditions the two-phase flow displays different behavior as compared to that at macro scale due to the influence of capillary forces, such as the importance of annular and plug/slug flow respect to the wavy flow.

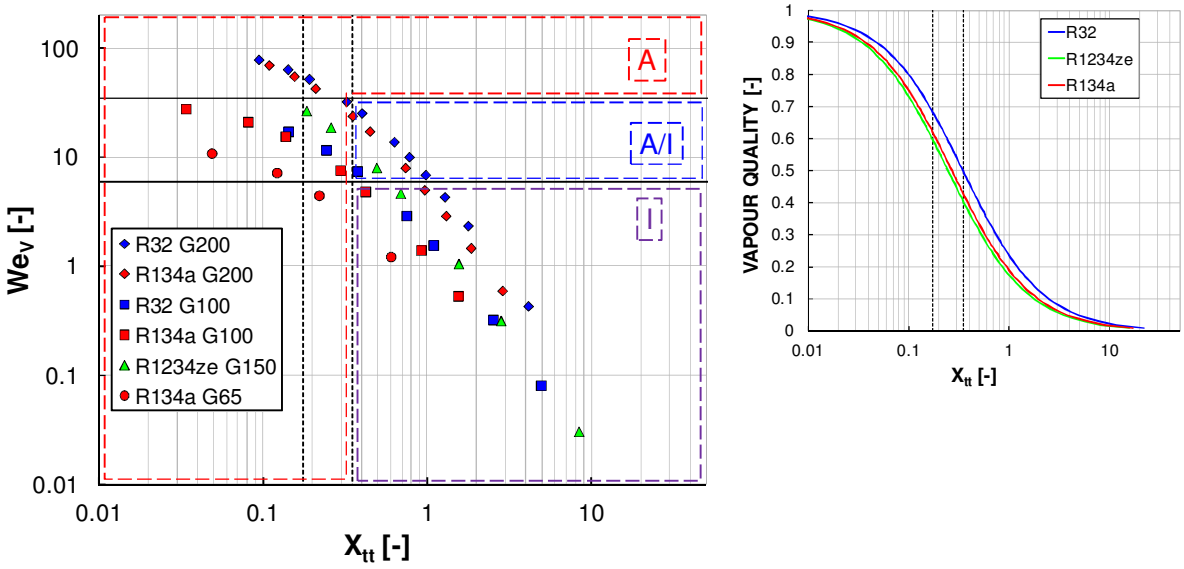

Figure 3.17: The application of Nema et al.[5] model for R32, R134a and R1234ze inside 0.96 mm i.d. circular minichannel.

As shown in the Figure 3.13, at G = 150 kg m^{-2} s^{-1} the vapour quality x_{cross}, at which there is the cross between the HTC trends of circular and square channel for R1234ze(E), is equal to 0.4. The same value can be obtained from Figure 3.17 considering the Martinelli parameter $X_{tt,slug}$ and the vapour quality x_{slug} ,at which the transition annular to plug/slug is aspected by the dimensionless criterion for R1234ze(E).
The same procedure can be applied for R32 and R134a at G = 200 kg m^{-2} s^{-1}, where the vapour quality x_{slug} are, respectively, about 0.5 and 0.45.
From these observations, the transition region between annular and plug/slug flow could explain the discrepancy found between numerical simulations and experiments at low quality. In fact, as mentioned in section 3.4.1, the numerical simulations are steady state and the intermittent cannot be predicted.
It is worth noting that when the mass flux is lower than 150 kg m^{-2} s^{-1} the vapor quality x_{cross} and x_{slug} tend to be different. At $G \leq$ 150 kg m^{-2} s^{-1} the intermittent regime starts earlier [4] and the x_{cross} increases, whereas the x_{slug} evaluated by the model remains constant.
This occurs because the Nema et al. [5] model is not developed for mass flux lower than 150 kg m^{-2} s^{-1}.

3.4.3 Effect of the refrigerant properties

The analysis is focused on the influence of refrigerant properties (i.e. the vapour density ρ_V, the liquid molecular thermal conductivity λ_L and the liquid molecular dynamic viscosity μ_L) on heat transfer during condensation in minichannel at low mass velocity.
For this reason, beside R134a, R32 and R1234ze(E), the numerical results of R290 and R717 condensation inside circular minichannel at $G \leq$ 200 kg m^{-2} s^{-1} are presented in this section. The main information on simulations are shown in detail in Table 3.4.

Table 3.4: Cases of new numerical simulations of R717 and R290 condensation in circular channel at G<200 kg m^{-2}s^{-1} (surface tension and gravity are considered).

Fluid	G [kg m^{-2} s^{-1}]	Approach	Length [mm]	Outlet quality
R717	75	Laminar	110	0.43
R717	75	SST k-ω	70	0.40
R717	150	SST k-ω	120	0.36
R290	100	Laminar	150	0.41
R290	100	Laminar	270	0.43
R290	200	SST k-ω	120	0.37

The experimental data are reported to validate the numerical simulations and highlighting which approach about liquid flow assumption works better.
In Figure 3.18, the comparisons between the numerical results and the experimental data by Fronk and Garimella [23] for R717 (D = 1.4 mm) and data by Del Col et al. [24] for R290 have been reported (D = 1 mm).

From the average deviations e_R listed in Table 3.5 and from the HTC-x trends depicted in Figure 3.18, it is confirmed that for R717 the SST *k-ω* approach work better than laminar one; and for R290 the laminar liquid film approach holds the experimental trend only at G = 100 kg m^{-2} s^{-1} .

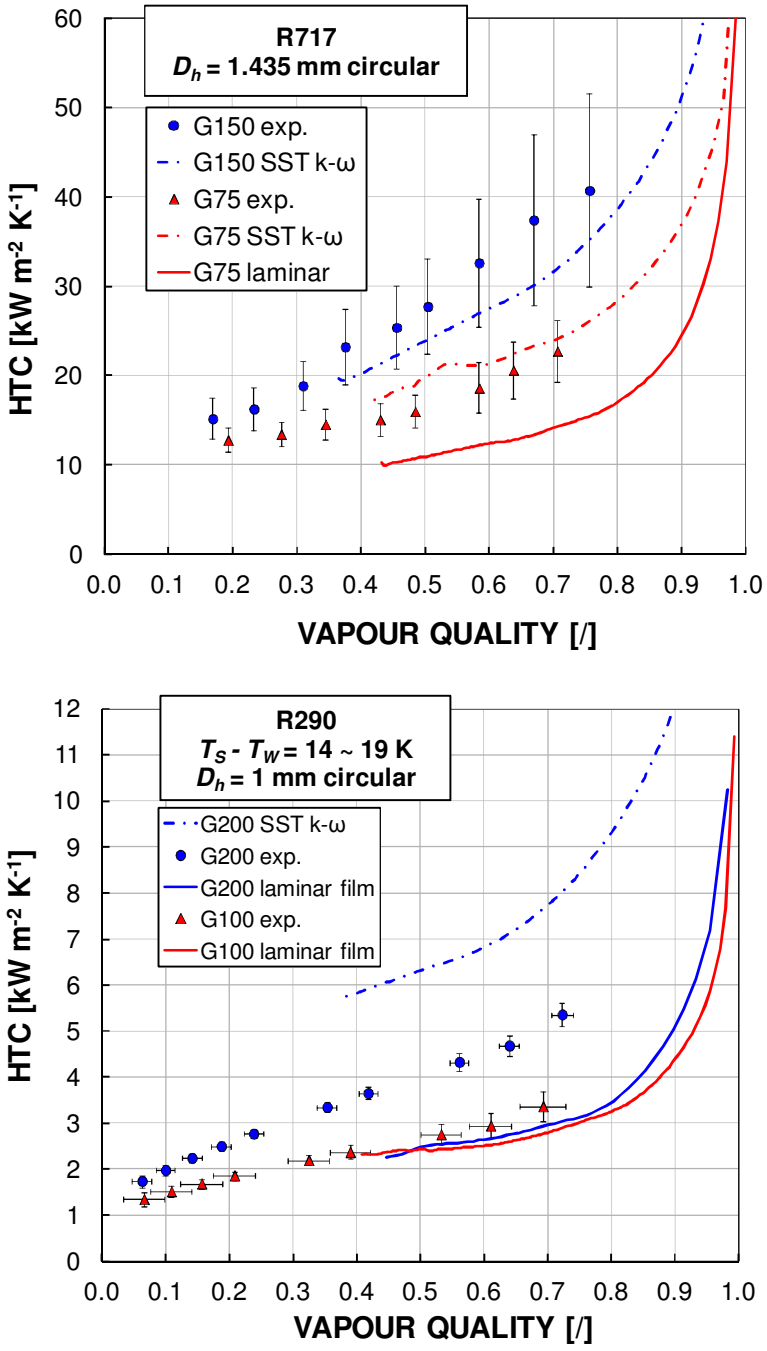

Figure 3.18: Experimental and calculated heat transfer coefficients by means of VOF simulations. Top: results for R717. Bottom: results for R290.

Table 3.5: Comparison between experimental and calculated cross section average heat transfer inside circular channel for R717 and R290.

Fluid	G [kg m^{-2} s^{-1}]	Approach	e_R	σ_N
R717	75	Laminar	-35.2	1.4
R717	75	SST k-ω	14.6	4.7
R717	150	SST k-ω	-15.3	1.6
R290	100	Laminar	-11.3	3.9
R290	200	Laminar	-40.8	1.2
R290	200	SST k-ω	55.5	4.4

For R290, at G = 200 kg m^{-2} s^{-1} both the methods do not predict well the experimental data having wide values of average deviation: -40.8% and 55.5% for laminar and SST k-ω approach, respectively.

Before discussing on the average deviations for different refrigerants when varying the mass velocity, the influence of refrigerants properties on liquid film distribution and local heat transfer coefficients are analyzed.

This study has been treated evaluating the liquid film thickness and the heat transfer coefficients along the angular coordinate obtained by numerical simulation at similar value of mass velocity ($G \leq$ 150 kg m^{-2} s^{-1}) at the same vapour quality of 0.6.

The comparison between numerical results of different fluid is done assuming the laminar liquid approach, except for the ammonia, where the SST k-ω approach works better.

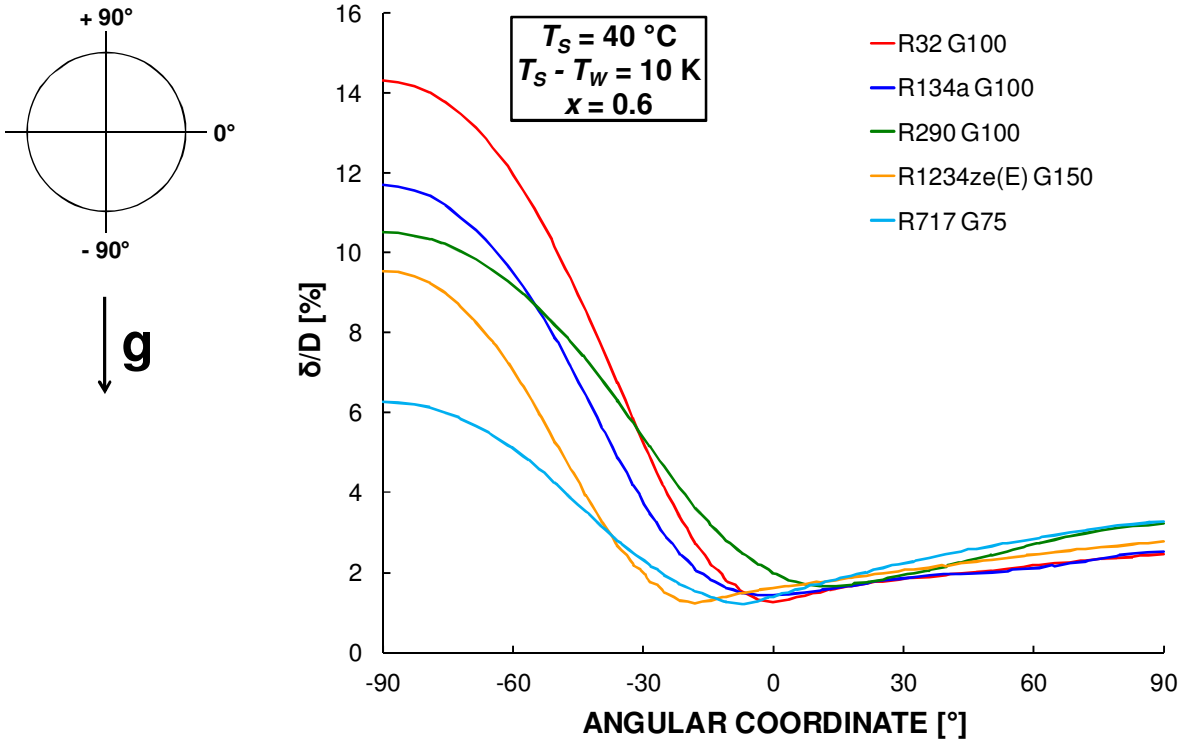

Figure 3.19: Percentage ratio of liquid film thickness on inner diameter (D = 1.4 mm for R717 and D = 1 mm for other refrigerants) along angular coordinate.

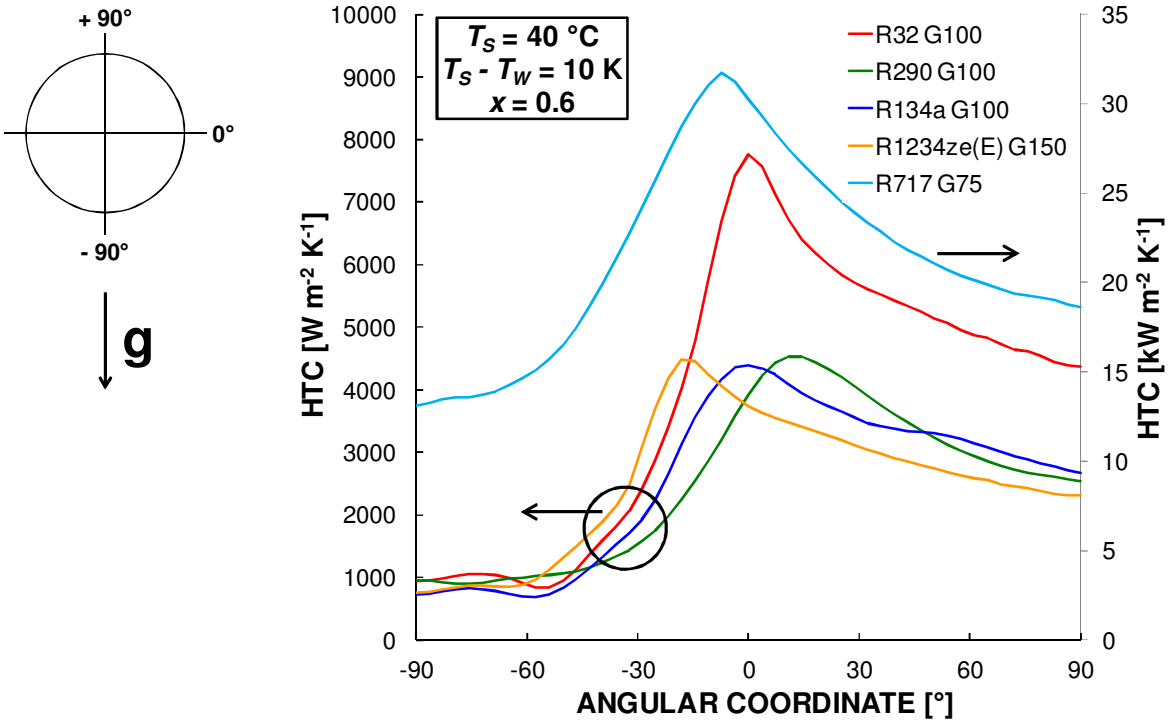

Figure 3.20: The heat transfer coefficient along angular coordinate.

As depicted in Figure 3.19 - Figure 3.20, the liquid film distribution and heat transfer coefficients at a fixed vapour quality can be different depending on the properties of the fluid:

- the liquid film thickness and distribution depends mainly by vapour liquid density. For example, at similar mass velocity R32, having the highest ρ_V, the vapour velocity and the interfacial shear stress on liquid by vapour are very low (at G = 100 kg m^{-2} s^{-1}, vapour velocity is about 1.36 m s^{-1}). In this case the gravity effect is more highlighted and the liquid film distribution is much asymmetric (i.e. at -90° the percentage ratio is 14.3% and at 90° is 2.5%). When the vapour density decreases, the vapour velocity increases and the liquid film results much thin and symmetric (i.e. for R717 at -90° the percentage ratio is 6.3% and at 90° is 3.3%).
  This behavior can be detected for propane and ammonia, where ρ_V is, respectively, equal to 30.2 and 12.0 kg m^{-3} having vapour velocity higher as compared to R32 and R134a (6.25 m s^{-1} for ammonia at G = 75 kg m^{-2} s^{-1} and 3.33 m s^{-1} for propane at G = 100 m s^{-1}).
- as mentioned in section 3.4.2 when the mass flux is low the heat transfer coefficient is more influenced by molecular liquid conductivity. This aspect can be detected by trends of HTC along angular coordinate for different fluids. For example, as depicted in Figure 3.20, R1234ze(E) is the fluid with lowest liquid conductivity (i.e. λ_L = 6.9 mW m^{-1} K^{-1}) having low heat transfer coefficients at the top of channel, where the major part of heat transfer is rejected.

For R32 and R717, instead, the liquid conductivity is very high (i.e. λ_L = 115 mW m^{-1} K^{-1} for R32 and λ_L = 443 mW m^{-1} K^{-1} for R717) as compared to R290, R134a and R1234ze(E) showing the highest trend of HTC. Furthermore, it can be noted that in case of R717, due to much symmetric liquid thickness, the HTC trend is not very different at top and bottom of channel (18 kW m^{-2} K^{-1} versus 15 kW m^{-2} K^{-1}) as compared to the other fluids.

The effect of fluid properties on liquid film and heat transfer coeffcient has been performed considering only the laminar liquid film approach assuming the amount of turbulence inside the liquid film as negligible (except for R717).
In Table 3.6 the values of average deviations for all simulations are reported to highlight how good is the laminar liquid approach to hold the experimental HTC trends for different fluids inside the circular channel and the following observations can be done:

- at mass flux lower than 150 kg m^{-2} s^{-1} the condensation heat transfer coefficient of R290, R134a and R1234ze(E) are predicted by the laminar liquid film approach with deviations below 11%;
- At $G \leq$ 200 kg m^{-2} s^{-1} for R32 the laminar film approach holds the experimental trends (i.e. at G = 200 kg m^{-2} s^{-1} the absolute value of e_R is 10%).
- For R134a at G = 200 kg m^{-2} s^{-1} the laminar liquid film approach underpredicts experimental results with an average deviation e_R = -24.8%, whereas the turbulent film approach (SST k-ω), as reported in Da Riva et al. [27], overpredicts by around 50% the experimental data. A similar behavior has been found for R1234ze(E) since these two refrigerants have similar properties.
- The same considerations can be done for R290 where at G = 200 kg m^{-2} s^{-1} the laminar approach underpredicts experimental data with an average deviation e_R = -40.8%, and the SST k-ω approach overpredicts by around 55.5 %.
- R717 is the only fluid among those investigated here for which the heat transfer coefficient predictions with the SST k-ω approach are better than those obtained with the laminar liquid film approach at both mass fluxes (75-150 kg m^{-2}s^{-1}).
  It was experimentally found that with this fluid the effect of mass velocity on the heat transfer coefficient was still important also at such low values of G (Figure 2.10). On the contrary, for R32, R1234ze(E), and R134a, the experimental heat transfer coefficients at mass flux lower than 150 kg m^{-2}s^{-1} almost overlaps (Figure 2.2 - Figure 2.4).

From the average deviations obtained by the comparison between the numerical results and experimental data, it is clear that this study poses a question mark on the turbulence transition in the liquid film at the present operating conditions.

Table 3.6: Comparison between experimental and calculated cross section average heat transfer inside circular channel for all fluid tested.

Fluid	*G* [kg m^{-2} s^{-1}]	Approach shape	e_R	σ_N
R134a	65	Laminar	9.8	1.4
R134a	100	Laminar	6.9	3.2
R134a	200	Laminar	-24.8	2.8
R32	100	Laminar	-17.8	5.3
R32	200	Laminar	-10.4	5.2
R1234ze (E)	150	Laminar	-8.4	2.2
R717	75	Laminar	-35.2	1.4
R717	75	SST k-ω	14.6	4.7
R717	150	SST k-ω	-15.3	1.6
R290	100	Laminar	-11.3	3.9
R290	200	Laminar	-40.8	1.2
R290	200	SST k-ω	55.5	4.4

Since the present issue regards the possible occurrence of some turbulence in the liquid film, it might be interesting to look at available criteria to determine whether the laminar film assumption should be relaxed.

Cioncolini and Thome [47] reported an algebraic turbulence modeling in adiabatic and evaporating annular two-phase flow, focusing in particular on momentum and heat transfer through the annular liquid film.

With assumption of shear-driven annular liquid films as fluid-bounded flows, this turbulence model provides both velocity and temperature profiles through the liquid films and relates both turbulent eddy diffusivities ν_t^+ and α_t^+ with the length scale characteristic, which should capture the size of the turbulent eddies in shear-driven annular films.

In this algebraic model the length scale that is assumed to characterize shear-driven annular films is the dimensionless average liquid film thickness δ^+.

For low values of δ^+ both turbulent eddy diffusivities are predicted to be null. This means that the turbulence is not presence in the liquid film, so it is laminar.

In this section, the algebraic model has been applied and the average film thickness δ^+ and the wall shear stress τ_W have been calculated as cross-sectional averages from the numerical simulations and the liquid properties have been evaluated at the wall temperature and saturation pressure.

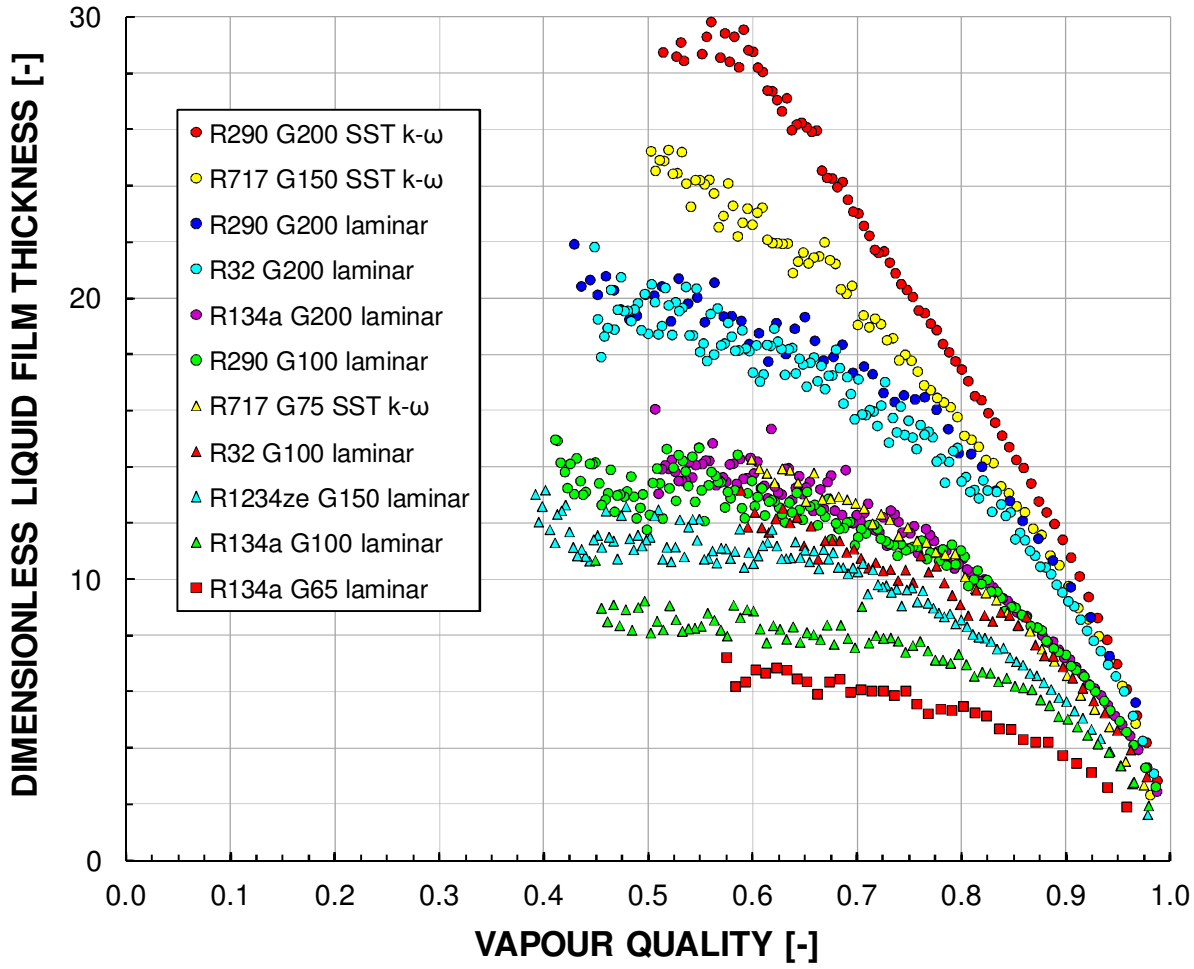

Figure 3.21: Dimensionless liquid film thickness for R134a, R1234ze(E), R32, R290 and R717 at different mass velocities inside a 1 mm diameter circular cross section minichannel.

As shown in Figure 3.21, it is worth noting that, for a given mass velocity and vapor quality, R717 and R290 have the highest dimensionless film thickness, suggesting an earlier transition to turbulent flow at lower mass velocities as compared to the other refrigerants. This aspect is due to low vapour density and low molecular liquid viscosity of R717 and R290, having a high vapour velocity at the same mass flux and promoting the turbulence inside the liquid film. As depicted in Figure 3.22, in fact, at the similar mass flux the vapour velocity of R717 and R290 results higher than that of other refrigerants, such as the interfacial velocity and the local strain rate. These results provide an explanation why R717 and R290 displays a strong effect of mass flux on the heat transfer coefficient between 100 and 200 kg $m^{-2}s^{-1}$.

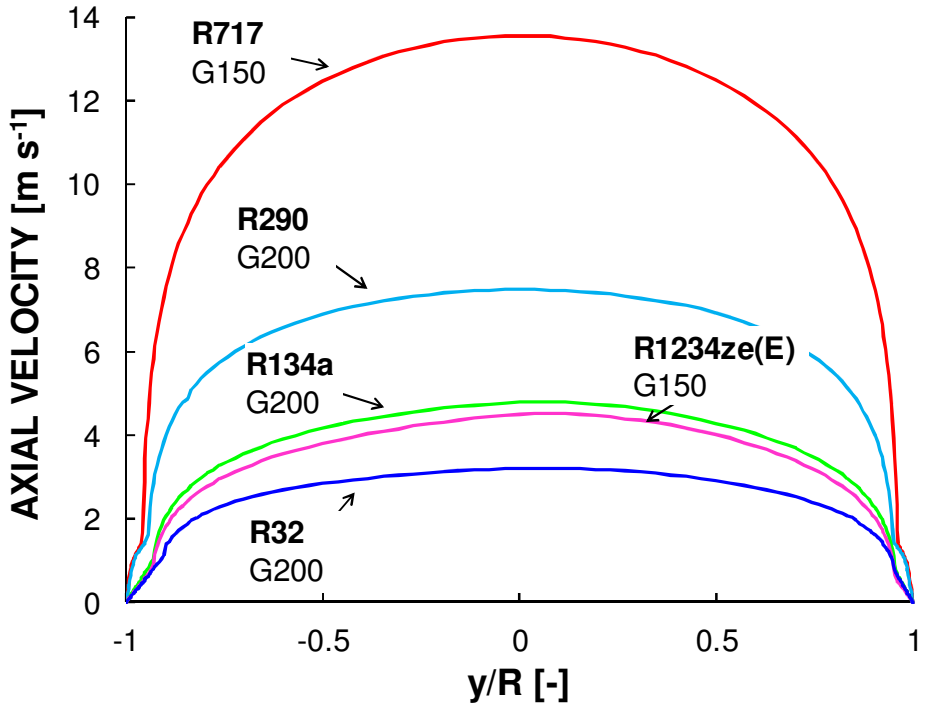

Figure 3.22: Axial velocity profiles for R717, R290, R134a, R1234ze, R32 inside circular minichannel at mass velocity equal to 150 and 200 kg m^{-2} s^{-1} and vapour quality of 0.8.

3.5 VoF simulations of condensation inside a horizontal 3.4 mm i.d. circular minichannel

3.5.1 Introduction

Before showing the VOF simulations of condensation process inside a minichannel with an inner diameter larger than that presented in previous section, some considerations are discussed in this paragraph to highlight the importance of channel size from a point of view of heat transfer and flow pattern.

The understanding of occurring of flow regimes and the transition between them is fundamental to accurately model the heat transfer during condensation.

The particular flow regime is obtained by the balance between gravity, inertia and surface tension forces; the magnitude of these forces are in function of fluid properties, tube size and vapour quality.

Early studies were focused to capture the two-phase flow pattern inside the large tubes.

For example, Baker [48] defined the first flow pattern map for air-water mixtures using the superficial velocities of phases as coordinates with pipe diameters ranging from 102 to 258 mm. Mandhane et al. [49] developed new flow map combining experimental data (12.7 mm ≤ D_h ≤ 165.1 mm) with the available maps using the superficial velocities and physical corrections taking into account the effect of fluid properties; in this case the effect of diameter on flow pattern and transitions not was explicitly considered.

A well-known flow map is that developed by Taitel and Dukler [50] with a theoretical approach using five dimensionless groups based on physical concepts to consider the transition between flow regimes. The approach was to visualize a stratified liquid and then to determine the mechanism by which a change from stratified flow can be expected to take place. By authors this is possible since the existence of a specific flow pattern at specified gas and liquid rates is independent of the path used to arrive at that state.

The analysis was performed considering five basic flow regimes: smooth stratified, wavy stratified, intermittent (no distinctions between slug and plug), annular with dispersed liquid and dispersed bubble. With the application of these five parameter for flow regime transitions the operating conditions in terms of phases mass flow rates, pipe diameter and pipe inclination are taken into account.

These experimental and theoretical works are referred to pipe diameter larger than 10 mm and when this geometric parameter decreases differences are expected in the relative magnitude of gravitational, shear and surface tension forces on the flow regime transitions.

For example, Coleman and Garimella [3] investigated the effect of tube diameter and shape on flow regime transitions for co-current two-phase flow of air-water mixtures ranging the hydraulic diameters from 5.5 to 1.3 mm. The authors compared their data with the available flow maps used for large tubes (Taitel and Dukler [50], Weisman [51]) concluding that maps developed for large tubes (D_h ≥ 10 mm) could not be extended to channel at small scale. Similar considerations were observed by Fukano et al. [52] comparing their small diameter flow maps (1 mm ≤ D_h ≤ 4.9 mm) with the Mandhane et al. [49] one. In this

analysis the authors identified the flow pattern for each data point highlighting disagreements between their data with that of Mandhane [49]: the disappearing of wavy and separated flows in horizontal capillary tubes, the occurring of an axisymmetric horizontal flow and the major role of surface tension on flow pattern as compared to the large tubes.

In the literature the studies on two-phase flow inside minichannels are fewer and, in general, the shift of transition lines due to the diameter size and fluid properties is yet unclear.

Basing on an extensive R134a condensation database (1 mm ≤ D_h ≤ 4.91 mm, 150 < G < 750 kg m^{-2} s^{-1}), Nema et al. [5] developed a flow regime transition criteria with dimensionless numbers, such as the Martinelli parameter, Froude number, Bond number and vapor-phase Weber number.

From these parameters the authors defined four major flow regimes (annular, wavy, intermittent and dispersed flow) and indentified the transition from small channel to large one focusing on the transition to intermittent flow.

For large channel diameter Taitel and Duckler [50] suggested that this transition occurs from stratified wavy flow when the liquid level in the pipe is above the pipe center line: when there is a wave on vapour-liquid interface, the gas accelerates, the pressure in the gas phase decreases allowing the growth of wave and, at the same time, forming a depression near the wave. Now, if the level is above the middle of channel (Martinelli parameter equal to 1.6), the peak of wave reaches the top before the depression reaches the bottom having a blockage of the gas passage and the occurring of slug. Otherwise the phenomenon of slugging results impossible.

When the diameter size decreases, Coleman and Garimella [4] have verified that the minimum liquid fraction required to reach the intermittent flow becomes lower than that in conventional channel until a value of Martinelli parameter equal to 0.3521.

To capture this behavior at varying diameter, Nema et al. [5] defined the critical bond number that represents the relative importance of surface tension and gravitational forces at the point at which stratified or annular flow changes to intermittent flow when the minimum liquid volume to form a slug is satisfied:

$$Bo_{cr} = \frac{1}{\left(\frac{\rho_L}{\rho_L - \rho_V} - \frac{\pi}{4}\right)} \qquad \textbf{3.16}$$

The authors suggested this value as indicator of contribution of gravity and capillary forces on flow pattern. When the influence of capillary forces on flow pattern is higher ($Bo < Bo_{cr}$, for small diameter) the slugs are formed since the surface tension pulls the liquid film blocking the gas flow.

At large diameter, the vapor inertia forces increases affecting the occurrence of transition to intermittent flow due to a destabilization and disruption of liquid bridges. For this reason, the minimum liquid fraction required must be higher.

From this criteria the authors taked into account the effect of diameter on transition lines of flow map and the importance of surface tension at small scale. Hereinafter, the authors have developed two different transition criteria between the different major regimes for small tubes ($Bo \leq Bo_{cr}$) and large ones ($Bo \geq Bo_{cr}$) using dimensionless numbers. In particular, for large tubes annular, wavy, intermittent and dispersed flow are considered and for small tubes, instead, the wavy flow is not expected, as shown in Figure 3.23.

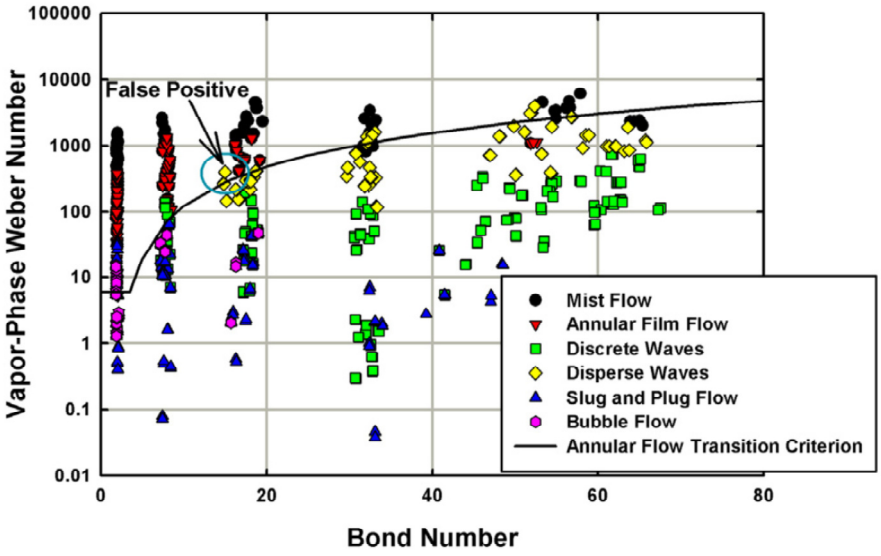

Figure 3.23: Annular flow transition criterion proposed by Nema et al. [5]

From these considerations, in the following table the values of Bond and critical Bond number for the fluids tested during condensation inside a single 1 mm i.d. channel are reported:

Table 3.7: Comparison between Bond and Bond critical number for all fluid tested.

Fluid	Bo	Bo_{cr}
R134a	1.76	3.84
R1234ze(E)	1.51	3.96
R32	1.80	3.29
R290	0.83	3.51
R717	0.56	4.24

As shown in Table 2.1, according to Nema et al. [5], since in all cases the Bond number is lower than the critical value, the small tube criteria can be applied and the direct transition between annular and intermittent flow is expected.

In this section, VOF simulations of R134a condensation in a single horizontal circular channel of diameter equal to 3.4 mm are presented.
As mentioned above, when the inner diameter increases the two-phase flow map can change and the importance of surface tension becomes lower having a transition to

intermittent flow from the wavy (stratified) flow. In this case the Bond number results equal to 20.29, thus the large tube criteria should be applied and the wavy flow is expected between the annular and intermittent flow, as shown from experimental visualizations of [7][8] reported in Figure 3.24.

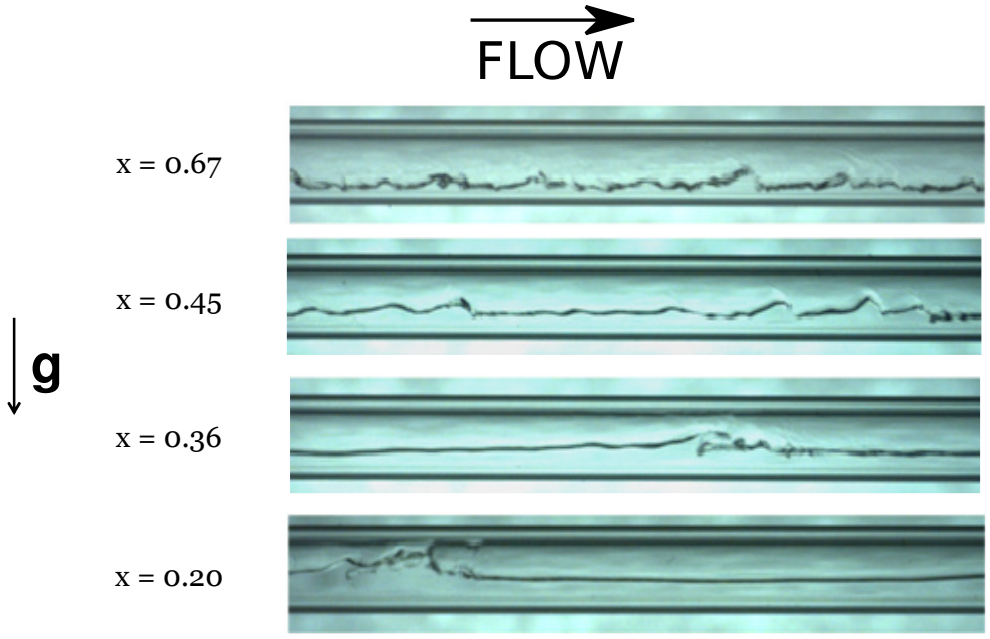

Figure 3.24: Flow pattern during condensation of R134a at 40°C saturation temperature, mass velocity equal to 100 kg m^{-2} s^{-1} at different vapour qualities (data by Azzolin [7,8]).

The importance of surface tension at varying the inner diameter from 1 to 3.4 mm can be also investigated by three-dimensional and steady-state simulations taking into account gravity and surface tension force.

3.5.2 The influence of surface tension

In Figure 3.26 the vapour-liquid interfaces tracked by VOF simulations, that have been run with and w/o the surface tension for the 1 mm and 3.4 mm channel with laminar liquid film assumption, are depicted. It must be noted that in Figure 3.26 a different scale factor is used for the two channels and the ratio between scale factors is 3.4. At these operating conditions, in both channels, the effect of gravity is visible: this force promotes the liquid stratification, thinning the liquid film in the upper side of the tube. The liquid stratification is more evident in the case of the larger channel. The contribution of the surface tension on the liquid film distribution along the channel perimeter is different when the inner diameter increases. This aspect can be observed by the shape that interface takes comparing the case with and without the surface tension inside the channel of 1 mm and 3.4 mm. In Figure 3.26, in case of D = 1 mm (left), when the surface tension is taken into account, the liquid film is thinned at the middle of the tube and becomes thicker at the

bottom. When the surface tension is equal to zero, the liquid-vapour interface changes in significant way in case of D = 1 mm as compared to that obtained in D = 3.4 mm.

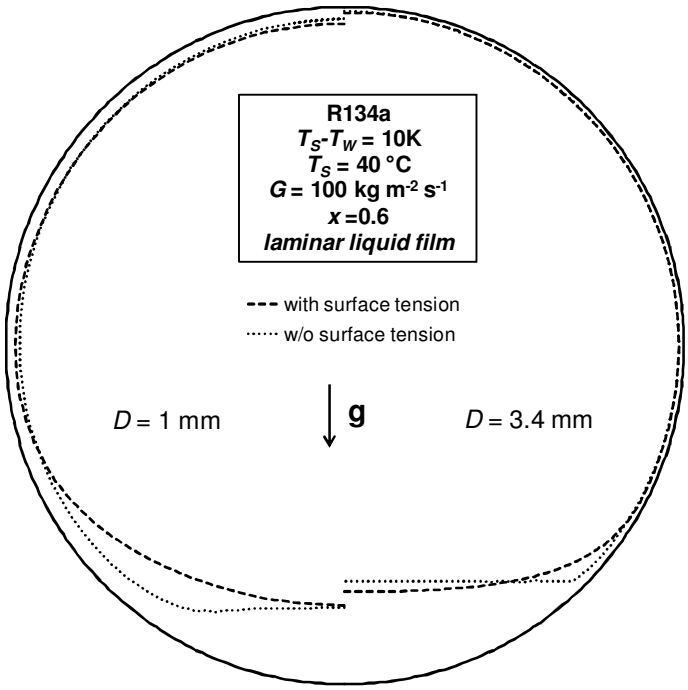

Figure 3.25: Vapor-liquid interface at x = 0.6 and G = 100 kg m^{-2} s^{-1} in 1 mm and 3.4 mm channel with and w/o surface tension.

In Figure 3.26 the local value of δ_L/D (liquid film thickness to diameter ratio) is plotted against the angular coordinate for both the channels.

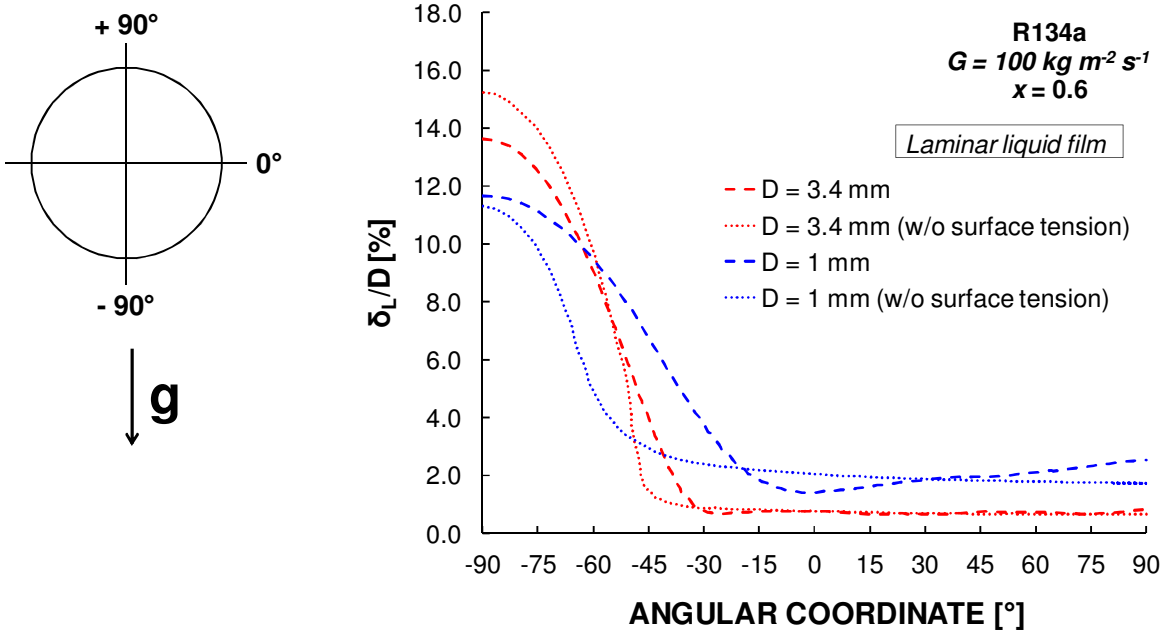

Figure 3.26: Vapor-liquid interface at x = 0.6 and G = 100 kg m^{-2} s^{-1} in 1 mm and 3.4 mm channel with and w/o surface tension (Top); the percentage ratio of liquid film thickness on inner diameter (Bottom) along angular coordinate.

In the 1 mm diameter channel, capillary forces affect the distribution of liquid film: when considering surface tension, the minimum thickness (14 μm) is obtained at the middle of channel (θ = 0°) instead of at the top of channel (θ = +90° and δ_L = 25 μm); whereas, when the surface tension is null, the minimum thickness (17 μm) is achieved at the top of channel (θ = +90°). When considering the 3.4 mm diameter channel with or without surface tension, the shape of the δ_L/D curves is similar: the minimum thickness is reached at the top of channel (θ = +90° and δ_L = 30 μm). Therefore it can be concluded that, when the inner diameter increases, the contribution of surface tension on the liquid film distribution becomes negligible. Furthermore, when the surface tension is considered, it is worth noting that the mean liquid film thickness calculated in the 1 mm channel (about 40 μm) is lower than that calculated in the 3.4 mm channel (about 120 μm). This aspect explains the higher heat transfer coefficient measured inside the 1 mm diameter channel as compared to the one measured inside the 3.4 mm channel, as it will be further shown in Figure 3.29.
The effect of surface tension detected in the present numerical study is consistent with the analysis developed by Nema et al. [5] on the transition criteria from small to large channel.
In fact, at saturation temperature of 40 °C, the critical Bond number Bo_{cr} for R134a is 3.84; in the case of 1 mm the Bond number (Bo = 1.76) is lower than critical one, instead in the 3.4 mm diameter channel, the Bond number is equal to 20.3. When the value of Bond number is lower than critical one, the authors predict an important role of surface tension on the flow patterns, otherwise its influence is negligible.

3.5.3 Validation against experimental data

The three-dimensional and steady state simulations of R134a condensation in a single horizontal 3.4 mm i.d. circular minichannel are here reported. The numerical modeling and the settings of simulations (boundary conditions, mesh, ..) are the same of that in section 3.4.1. In this case, the mesh has been scaled in the radial direction: the radial thickness of the cells in the near-wall region is, however, enough to fully resolve the viscous sublayer in the liquid film region since the dimensionless distance from the wall of the first cell is lower than one as well as in the previous simulations.
When the diameter size increases, at the same mass flux, the vapour and liquid inertia forces are higher and the assumption of liquid flow as laminar would have to be relaxed since the laminar approach could not correctly predict the experimental trends. For this reason the numerical simulations have been performed with the two different approaches of liquid film: laminar and SST k-ω approach.
The details of new simulations are listed in Table 3.8 and the all-liquid Reynolds number are also reported to highlight the question mark on the liquid flow assumption.

Table 3.8: Cases of new numerical simulations of R134a condensation in 3.4 mm i.d. circular channel at G < 200 kg m^{-2}s^{-1} (surface tension and gravity are considered).

G [kg m^{-2} s^{-1}]	Re_{LO}	Approach	Length [mm]	Outlet quality
50	1053	Laminar	175	0.55
100	2106	Laminar	420	0.40
200	4212	Laminar	630	0.51
50	1053	SST k-ω	220	0.30
100	2106	SST k-ω	340	0.51
200	4212	SST k-ω	350	0.44

The comparison between the numerical results and the experimental data reported by Azzolin [7,8] at the same operating conditions is shown in Figure 3.27 -Figure 3.28.

It is worth underlining that the experimental data points have been selected for saturation-to-wall temperature difference ranging from 7 K to 15 K, while in the simulations this difference is 10 K in the whole computational domain.

At G = 100 kg m^{-2} s^{-1} the influence of ΔT_{SW} on experimental local heat transfer coefficient is almost weak, while this dependence results clear at G = 50 kg m^{-2} s^{-1}.

In Table 3.9 the relative errors e_R and standard deviations σ_N between numerical results and experimental test are reported.

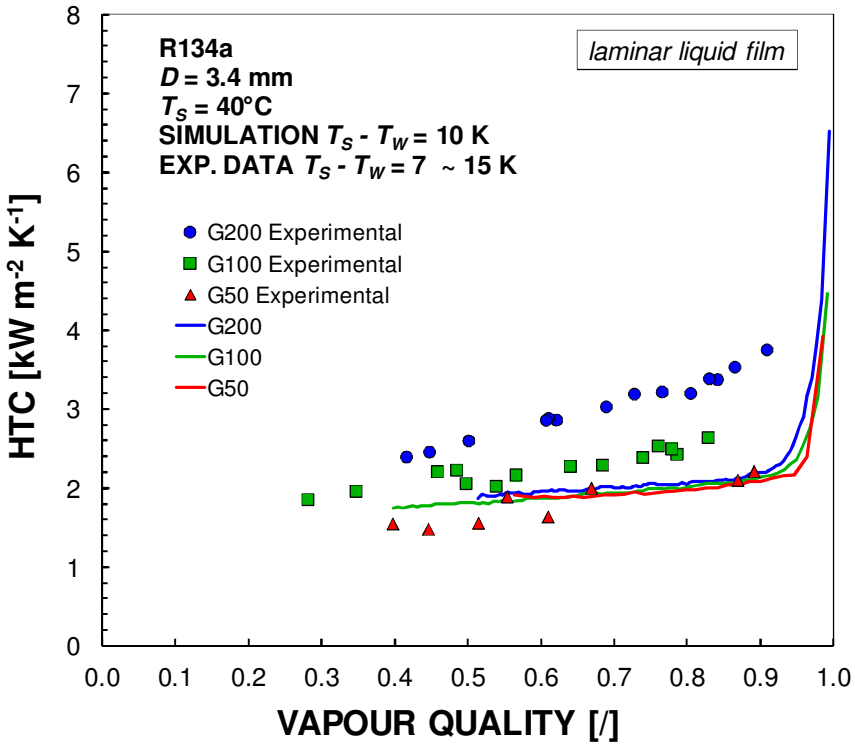

Figure 3.27: Cross-sectional average heat transfer coefficient as a function of vapour quality inside the 3.4 mm i.d. circular channel. Simulation with laminar liquid film approach and experimental data from [7,8].

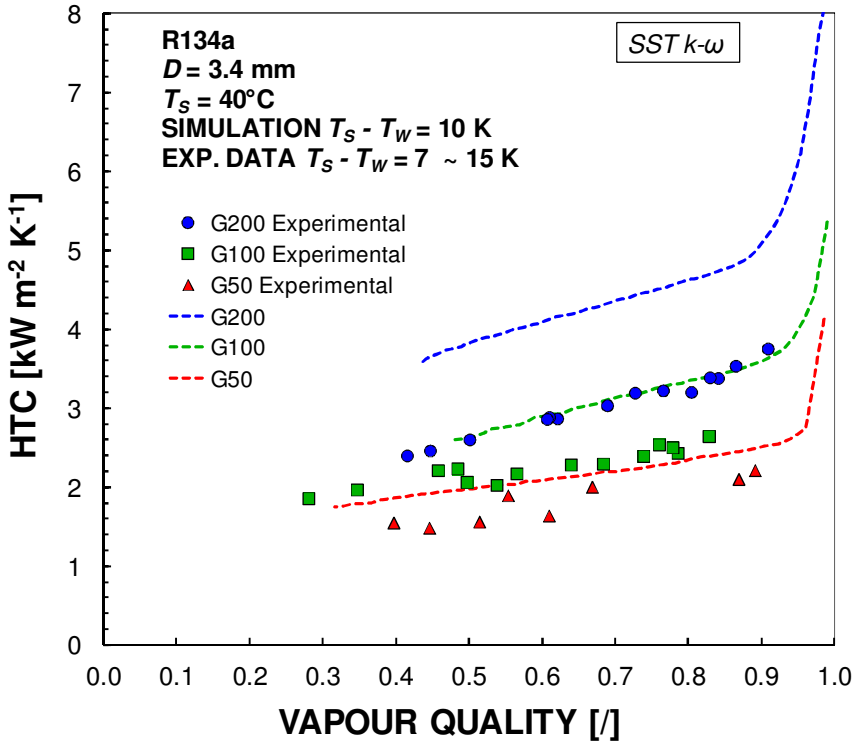

Figure 3.28: Cross-sectional average heat transfer coefficient as a function of vapour quality inside the 3.4 mm i.d. circular channel. Simulation with SST *k-ω* approach and experimental data from [7,8].

Table 3.9: Comparison between experimental and calculated cross section average heat transfer inside 3.4 mm i.d. circular channel at $G < 200$ kg m^{-2}s^{-1}.

G [kg m^{-2} s^{-1}]	Re_{LO}	Approach	e_R [%]	σ_N [%]
50	1053	Laminar	1.2	5.5
100	2106	Laminar	-18.1	1.3
200	4212	Laminar	-34.6	3.6
50	1053	SST *k-ω*	16.4	3.0
100	2106	SST *k-ω*	28.4	3.5
200	4212	SST *k-ω*	38.4	3.0

As depicted in Figure 3.27, the laminar liquid approach displays a very weak influence of mass flux at high vapour qualities, while for vapour qualities lower than 0.9 the three series overlap. As reported in Table 3.9, at a mass velocity G = 50 kg m^{-2} s^{-1} a very good agreement is found between numerical results and experimental data, with a relative error below 2%. Considering that, as reported in Azzolin et al. [7,8] and after illustrated in Section 3.5.4, at such conditions, the vapor-liquid interface is flat without the presence of waves, the good agreement between simulations and experiments is an important validation of the present numerical technique. In fact, since only steady-state numerical simulations are considered in this Section, a reliable comparison between numerical results and experimental data can be done only when the flow pattern is annular or annular-stratified. A satisfactory

prediction is also found for mass velocity G = 100 kg m^{-2} s^{-1} even if in this case the deviation is about -18.1% (Azzolin et al. [7,8] observed a stratified-wave flow at 100 kg m^{-2} s^{-1}). When moving to the highest mass velocity (G = 200 kg m^{-2} s^{-1}) the experimental data are underpredicted by the present simulation by 35%: this is related to the presence of turbulence in the liquid film and waves at the liquid/vapor interface. A deep discussion is reported in the next sections.

In Figure 3.28 the numerical results have been compared against the experimental data considering also the SST k-ω approach. It is worth noting that, as explained in section 3.2, in this approach the low-Reynolds number form is included to consider the transition from laminar to turbulent regime inside the liquid film. As reported in Table 3.9 the SST k-ω approach performs worse than laminar liquid approach at G = 50 kg m^{-2} s^{-1} and G = 100 kg m^{-2} s^{-1}; whereas at G = 200 kg m^{-2} s^{-1}, the both approaches show comparable deviations which values are above 30 %. The bad work of SST k-ω approach to predict the heat transfer coefficient for $G \leq$ 200 kg m^{-2} s^{-1} could be due to an earlier prediction of laminar-to-turbulence transition by this method. Similar difficulties of this approach to catch carefully the transition to turbulence were seen also for HTC trends inside the channel of 1 mm at the same mass velocities (Da Riva et al. [27]).

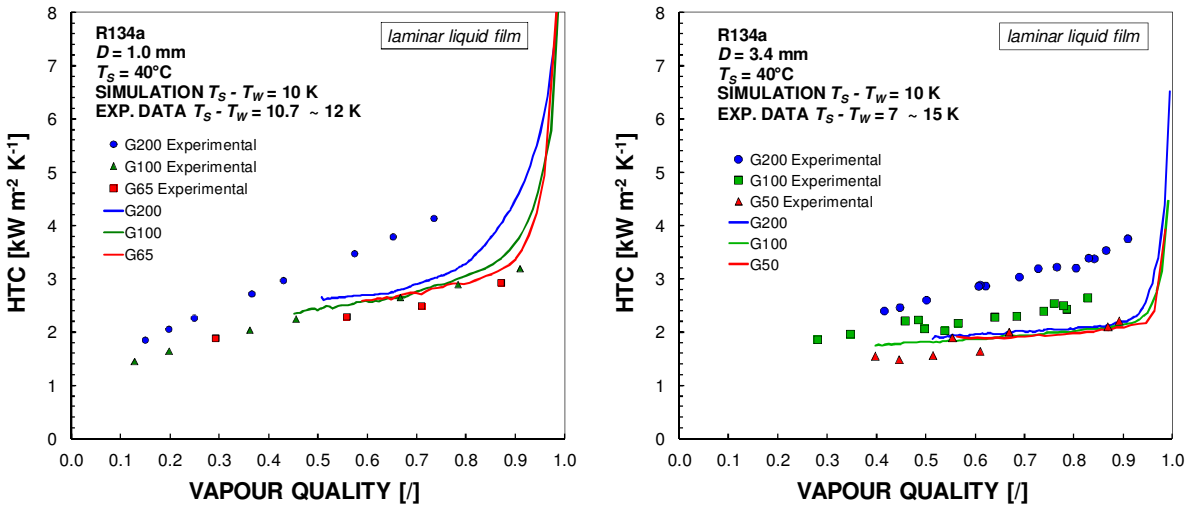

Figure 3.29: Effect of channel size between 1 mm (Left) and 3.4 mm (Right) horizontal channel.

In Figure 3.29, the experimental data and the numerical results (with laminar liquid film approach) obtained in both channel are reported to highlight the effect of channel size. As shown in this figure, the experimental data in D = 3.4 mm display an higher influence of mass velocity ranging from 200 kg m^{-2} s^{-1} to 50 kg m^{-2} s^{-1} as compared to those obtained inside the channel of 1 mm: at increasing of inner diameter and at the same mass flux, the vapour and liquid inertia forces are higher promoting the turbulence inside the liquid film and the interfacial instabilities. For this reason, when the laminar liquid film approach is adopted, an higher underprediction of experimental HTC trend at G = 200 kg m^{-2} s^{-1} can be observed for 3.4 mm as compared to the case of 1 mm. As previously demonstrated in Section 3.4.3 and by Da Riva et al. [27], in the 1 mm channel, for mass velocity $G \leq$ 100 kg

m^{-2} s^{-1} a good agreement between numerical simulations and experimental data is found: the relative error e_R is always below 10% with a standard deviation σ_N less than 3%. Furthermore, according to the experimental visualizations by Coleman and Garimella [4] of R134a condensation inside horizontal circular channels, the stratified-wavy regime is not present at D = 1 mm and the intermittent flow is expected only for x < 0.45, ensuring the steady-state assumption to successfully predict the condensation heat transfer coefficient for x > 0.5.

From the aforementioned considerations about the two-phase flow and the turbulence issue of liquid film in 1 mm and 3.4 mm channel at $G \leq 200$ kg m^{-2} s^{-1}, the reason about the underestimation of experimental data at G = 100 kg m^{-2} s^{-1} by laminar liquid approach in D = 3.4 mm can be due to two phenomena occurring for $G \geq 100$ kg m^{-2} s^{-1}:

- the presence of waves at the vapor-liquid interface in the case of the bigger channel;
- the transition to turbulent flow that is achieved earlier in the channel with D = 3.4 mm.

3.5.4 Analysis of heat transfer inside the channel

The analysis is focused on condensation inside a horizontal channel of 3.4 mm where, in according to Nema et al. [5], the large channel criteria has to be applied to predict correctly the flow pattern because the Bond number is higher than critical one.

In Figure 3.30 the flow pattern during R134a condensation inside the 3.4 mm i.d. circular channel is depicted [7,8] at two values of mass velocities (i.e. G = 50 kg m^{-2} s^{-1} and 100 kg m^{-2} s^{-1}) and at a vapour quality of 0.7.

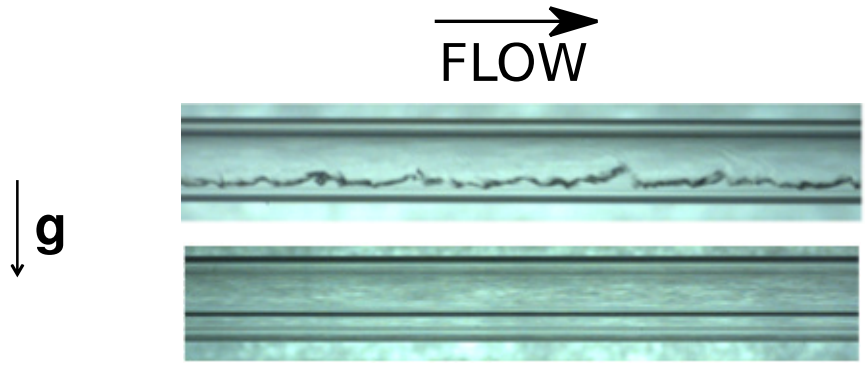

Figure 3.30: Flow pattern during condensation of R134a at 40°C saturation temperature, mass velocity equal to 100 kg m^{-2} s^{-1} (Top) and at 50 kg m^{-2} s^{-1} (Bottom) at x =0.7 [7,8]**.**

Smooth stratified flow was recorded at G = 50 kg m^{-2} s^{-1} without instabilities at the vapour-liquid interface and thus steady-state numerical simulations can be adopted. Instead, at G = 100 kg $m^{-2}s^{-1}$, the presence of waves can be detected at the bottom of the channel and the flow can be classified as wavy-stratified flow. This type of two-phase flow regime could in principle be studied with three-dimensional and transient numerical simulations; unfortunately such simulations are very time-expensive with a significant increase of the

execution time with respect to steady state simulations. However, in the present Section, some considerations about the importance of interfacial waves are presented analyzing the local heat transfer coefficients obtained with steady-state simulations.
The presence of waves at interface can improve the heat transfer coefficients from many point of view as studied by El Hajal et al. [6] and Thome et al. [53].

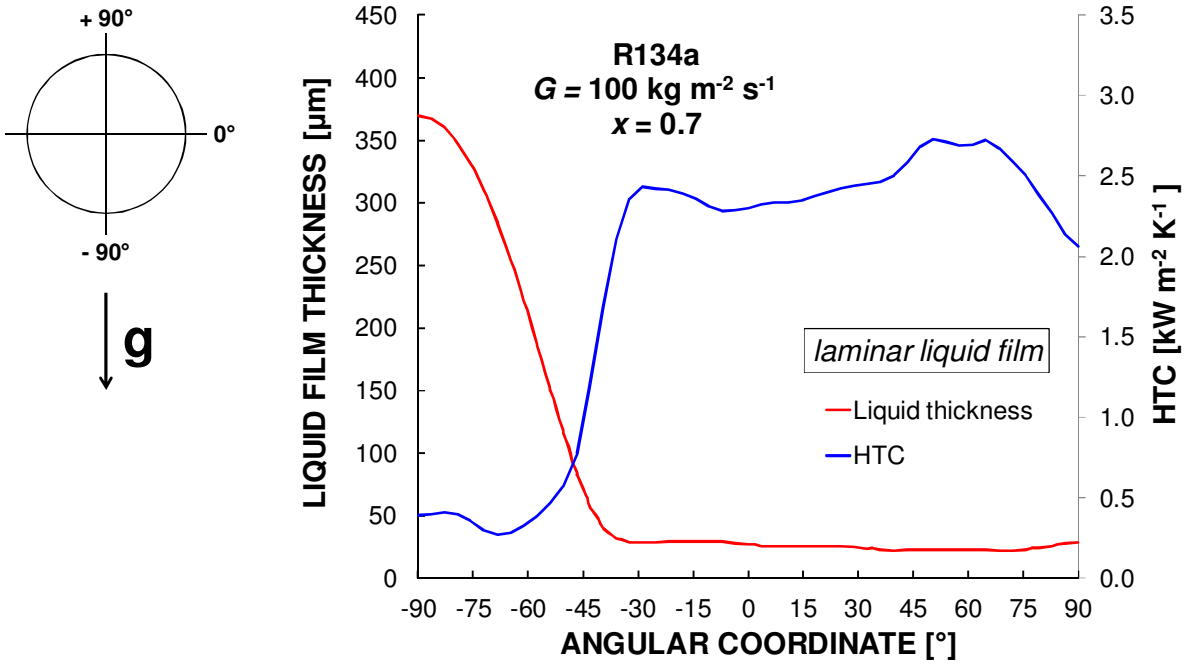

Figure 3.31: The liquid film thickness and the local heat transfer coefficient along angular coordinate obtained by laminar liquid film approach at G = 100 kg m^{-2} s^{-1} and x = 0.7 in 3.4 mm i.d. channel.

In Figure 3.31 the liquid film thickness and the local heat transfer coefficient are plotted vs the angular coordinate at G = 100 kg m^{-2} s^{-1} and x = 0.7 inside the 3.4 mm horizontal channel. Moving from the top (θ = +90°) to the bottom (θ = -90°) of channel, the thickness of liquid film is almost constant with a value of about 25.5 µm and then it increases until 370 µm when moving from -30° to -90°.
In Eq. 3.17 $q^*(\theta_1,\theta_2)$ is the ratio between the heat flow rate transferred between the angular positions θ_1 - θ_2 and the total heat flow rate in half channel. To evaluate the distribution of heat transfer in the upper part of channel where the film is thin and on the bottom where the liquid stratifies, the ratio $q^*(\theta_1,\theta_2)$ has been calculated for the following two cases: θ_1 = +90° and θ_2 = -30°; θ_1 = -30° and θ_2 = -90°.

$$q^*\Big|_{\vartheta_1}^{\vartheta_2} = \frac{\int_{\vartheta_1}^{\vartheta_2} q'(\vartheta)d\vartheta}{\int_{-90^\circ}^{90^\circ} q'(\vartheta)d\vartheta} \qquad \textbf{3.17}$$

Thus the ratio $q^*(\theta_1,\theta_2)$ results 85% for the upper side and 15% for lower side of the channel as illustrated in Figure 3.32. The weighted average heat transfer coefficient along the channel perimeter is equal to 1889 W m^{-2} K^{-1}.
With the aim to consider a possible heat transfer enhancement at the bottom of the channel due to the presence of waves at the vapor-liquid interface (stratified-wavy flow, Figure 3.30), the value of heat transfer coefficient obtained from steady-state simulations (Figure 3.31) has been enhanced by 25% and 100% for angles ranging between -90° and -30°.

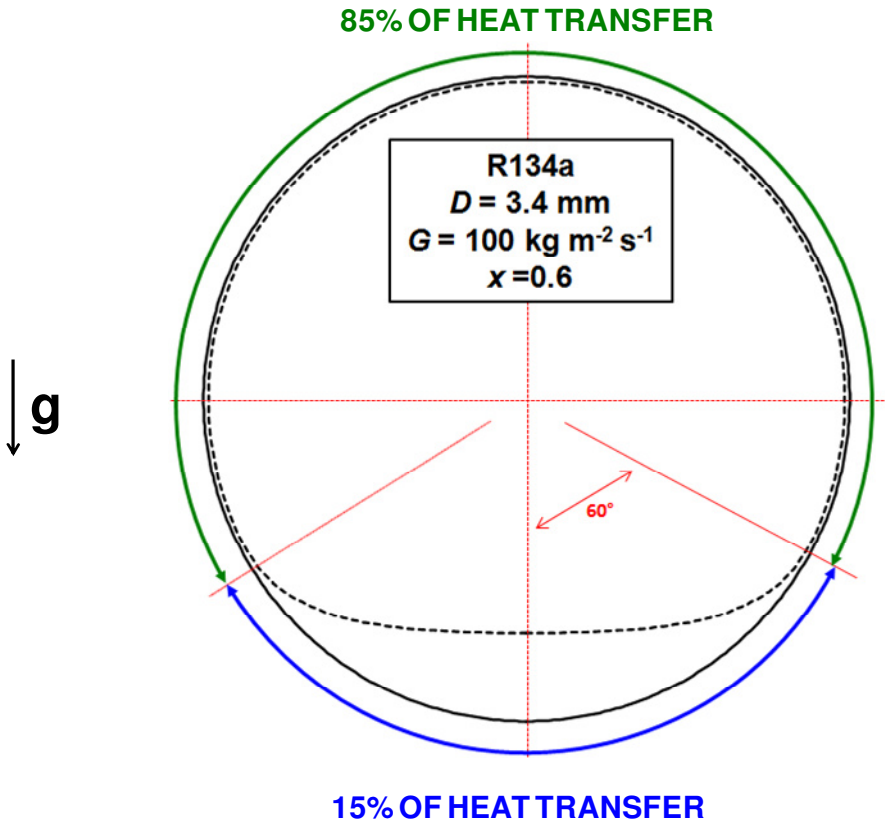

Figure 3.32: Distribution of heat transfer inside a horizontal channel of 3.4 mm during condensation at G = 100 kg m^{-2} s^{-1}.

For the first case (25 % enhancement for angles between -30° and -90°), the ratio $q^*(\theta_1,\theta_2)$ is 81.8% for the upper part (+90° to -30°) and 18.2% for lower part of the channel (-30° to -90°): the weighted average heat transfer coefficient results 1940 W m^{-2} K^{-1}. For the second case (100% enhancement for angles between -30° and -90°), the ratio $q^*(\theta_1,\theta_2)$ is 79.3% for the upper part (+90° to -30°) and 20.7% for the bottom of the channel (-30° to -90°): the weighted average of heat transfer coefficient is equal to 2037 W m^{-2} K^{-1}. The relative errors e_R, evaluated between the heat transfer coefficients calculated with the procedure above reported and the experimental data by Azzolin et al. [7,8] (2350 W m^{-2} K^{-1} at x = 0.7 and G = 100 kg m^{-2} s^{-1}) are -17.4% for the first case and -13% for the second case. From these considerations it can be concluded that, when the interfacial waves are relegated only at the bottom of channel where the liquid film is thick, their contribution on the enhancement of

the average heat transfer coefficient is limited and steady-state numerical simulations can still give satisfactory results as reported in Table 3.9

3.5.5 Analysis of turbulence inside the liquid film

From Figure 3.29 it is evident that for G = 200 kg m^{-2} s^{-1} steady-state numerical simulations with the assumption of laminar liquid film underestimate experimental data for both the channel diameters. From the visualizations by Coleman and Garimella [4] wavy flow is not expected in the 1 mm channel at this conditions. In the case of the 3.4 mm diameter channel, stratified-wavy flow is present, however, from the consideration previously reported in previous section, if the waves takes place at the bottom of the channel, their presence is not enough to explain the difference between experimental data and numerical simulations. The second motivation of the underestimation of the heat transfer coefficient at G = 200 kg m^{-2} s^{-1} is the transition from laminar to turbulent flow in the liquid film. For R134a, at G = 200 kg m^{-2} s^{-1} the all-liquid Reynolds number Re_{LO} is 1240 and 4220, respectively, for D = 1 mm and D = 3.4 mm. From the numerical analysis by Da Riva et al. [27], in 1 mm diameter channel, the transition to turbulent flow was detected at a mass flux of about 200 kg m^{-2} s^{-1}, where Re_{LO} is equal to 1240. In this section, the criterion by Cioncolini et al. [54] has been applied with the aim to predict the laminar-to-turbulent transition in the liquid flow.

Cioncolini et al. [54] presented an indirect method to approximately identify the emergence of turbulence in shear-driven annular liquid films, showing that the turbulence intensity in annular liquid films appears to be weaker than in single-phase boundary layers. The authors asserted that the turbulence structure in the annular liquid film is determined by the dimensionless average liquid film thickness δ+ and they proposed the following δ^+ ranges:

- $\delta^+ \leq 9$, laminar flow;
- $\delta^+ \geq 40$, turbulent flow;
- $9 \leq \delta^+ \leq 40$, transition to turbulent flow.

In Figure 3.33 the dimensionless liquid film thickness is plotted against vapor quality for R134a at 40°C saturation temperature, mass flux ranging from 50 to 200 kg m^{-2} s^{-1}, 1 mm (top) and 3.4 mm (bottom) diameter channel. The criterion by Cioncolini et al. [54] has been developed considering vertical upflow conditions and thus axisymmetrical flow with uniform liquid film thickness. As shown in Section 3.5.2, in the present case, the channels are in horizontal configuration and liquid stratification occurs leading to a non-uniform liquid film thickness along the perimeter of the channel. Since for D = 3.4 mm this effect is more pronounced as compared to that in D = 1 mm, in Figure 3.33, for the first case the film thickness δ^+ and the wall shear stress τ_W have been calculated only with reference to the upper part of the channel where the liquid film thickness is almost constant (e.g. θ_1 = +90° and θ_2 = -30° for the conditions in Figure 3.32). In fact, it is just in this part of the channel where most of the heat is transferred and thus a correct prediction of the laminar-to-turbulent transition is fundamental to obtained reliable numerical results.

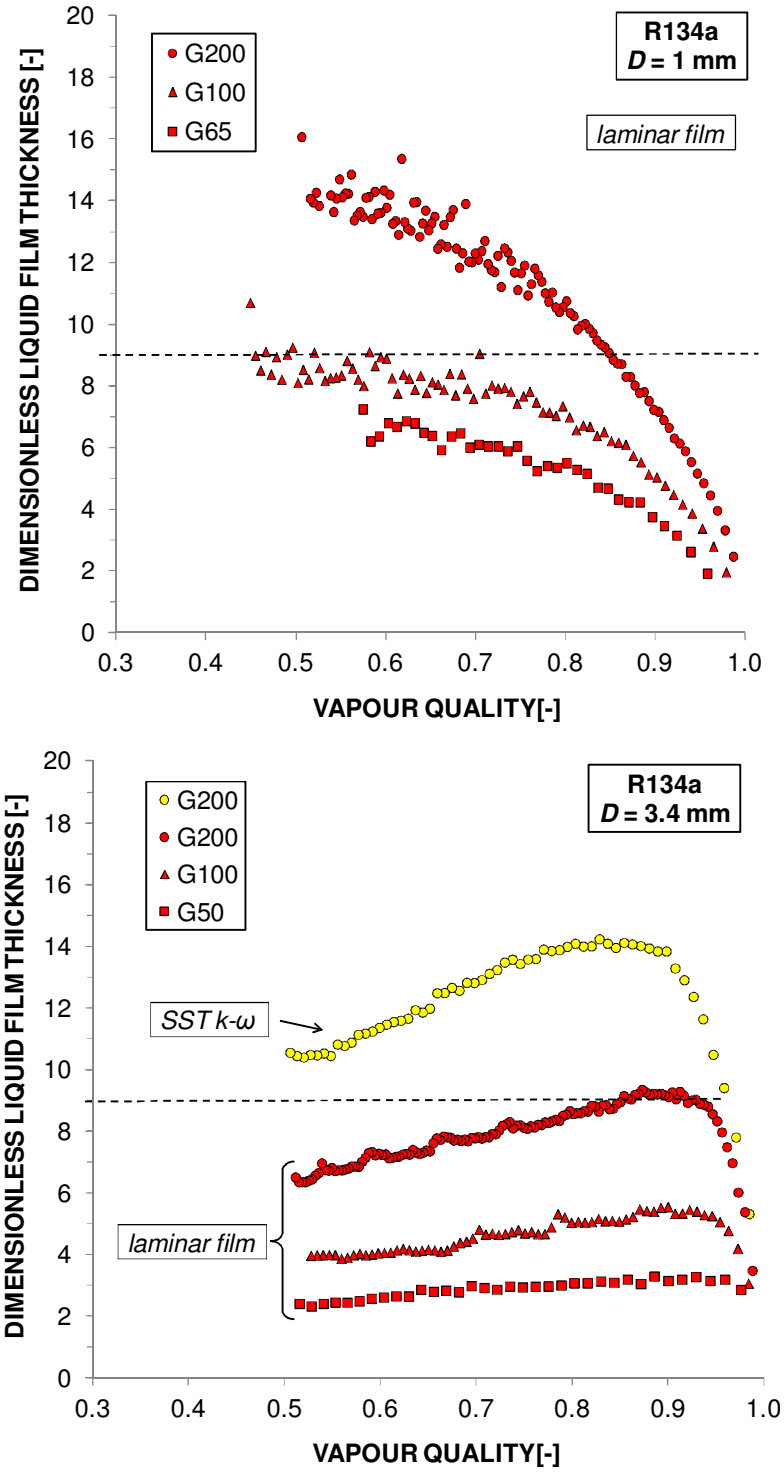

Figure 3.33: Dimensionless liquid film thickness for R134a at different mass velocities inside a 1 mm (top) and a 3.4 mm (bottom) horizontal channel with the criterion reported in Cioncolini et al. [54].

As shown in Figure 3.33, the dimensionless liquid film thickness δ^+ evaluated inside both the channels falls in the laminar zone for $G \leq 100$ kg m^{-2} s^{-1}, whereas, for $G = 200$ kg m^{-2} s^{-1}, the criterion by Cioncolini et al. [54] predicts a transition between laminar and turbulent flow. At $G = 200$ kg m^{-2} s^{-1} in the 1 mm diameter channel and in the 3.4 mm diameter

channel, the assumption of laminar liquid film must be relaxed and some turbulence should be considered inside the liquid film to predict the experimental data.

3.6 VoF simulations of downflow condensation inside a vertical 3.4 mm i.d. minichannel

The numerical results of R134a condensation inside 3.4 mm in vertical downflow are here presented. The settings of simulations are the same of those reported in previous sections.
During the experimental tests the angle of inclination of the channel can be affected by an experimental uncertainty carrying on a not-completely perfect axisymmetric two-phase flow that can be, instead, achieved by numerical simulations. However, this aspect has resulted irrelevant during the experimental test and the data reduction of heat transfer coefficient, so it has been neglected when the numerical simulations and the experimental data have been compared.
In the literature few works deal with the numerical analysis of two-phase flow in vertical channels. For example, the adiabatic churn flow inside a conventional and vertical channel has been studied by Da Riva and Del Col [55] considering an axisymmetric domain. The bubbly flow has been modeling and compared against experimental visualizations by Kebriaee et al. [56] and also here the axisymmetric condition has been assumed. An example of two-phase numerical simulations during upflow condensation in conventional vertical pipe through a three-dimensional domain is that reported by Qiu et al. [57].
A three-dimensional domain is chosen when the numerical analysis is focused on a non-vertical or non-axisymmetric two-phase flow, such as dispersed or churn flow. In the churn flow analysis reported by Da Riva and Del Col [55], instead, since the two-phase flow was obtained by the injection of liquid through a porous wall placed around the wall of pipe the assumption of axisymmetric flow was justified.
From these considerations, the domain of numerical simulations is bi-dimensional taking advantage of axisymmetrical condition during the vertical-downflow condensation.
The assumption of an axisymmetrical flow permits to have an high reduction of computational cost, primarily for the unsteady simulations where the time computation increases significantly.
The domain of the simulations is composed by about $3 \cdot 10^5$ quadrilateral cells. The numerical models (i.e. assumption on liquid flow, phase change models and so on) and the boundary conditions are the same of those reported in section 3.4.1. Also here the gravity force has been taken into account and in this case its direction is parallel to the two-phase flow.
The details of simulations of vertical downflow condensation inside 3.4 mm channel are listed in Table 3.10.

Table 3.10: Cases of numerical simulations of R134a condensation in 3.4 mm i.d. vertical circular channel at G < 200 kg m^{-2}s^{-1}.

G [kg m^{-2} s^{-1}]	Approach	Length [mm]	Outlet quality
50	Laminar	500	0.32
100	Laminar	900	0.40
100	SST k-ω	300	0.44
200	SST k-ω	410	0.45

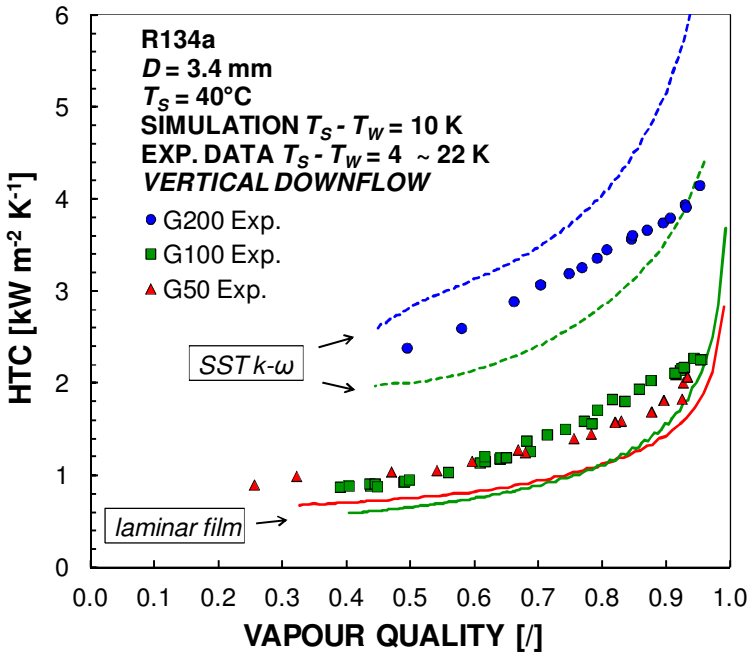

Figure 3.34: Cross-sectional average heat transfer coefficient as a function of vapour quality inside 3.4 mm i.d. circular channel during vertical downflow condensation. Simulations with SST k-ω and laminar liquid film are shown.

Table 3.11: Comparison between experimental and calculated cross section average heat transfer inside 3.4 mm i.d. vertical circular channel at G ≤ 200 kg m^{-2}s^{-1}.

G [kg m^{-2} s^{-1}]	Approach	e_R [%]	σ_N [%]
50	Laminar	-28.4	1.9
100	Laminar	-33.0	1.9
100	SST k-ω	86.8	16.9
200	SST k-ω	16.7	2.2

In Figure 3.34 the experimental and numerical local heat transfer coefficient are reported on vapour quality at G ≤ 200 kg m^{-2} s^{-1} during downflow condensation inside a single 3.4 mm vertical and circular channel.

From this figure the following considerations can be done:

- the HTCs at G = 100 kg m^{-2} s^{-1} and 50 kg m^{-2} s^{-1} overlap and an visible effect of mass flux can be detected at $G \geq$ 100 kg m^{-2} s^{-1};
- notwithstanding at G = 100 kg m^{-2} s^{-1} and 50 kg m^{-2} s^{-1} the effect of mass flux is negligible, the laminar film approach tends to underpredict the experimental data;
- at G = 200 kg m^{-2} s^{-1} the SST k-ω approach holds the experimental trend with reasonable accuracy;
- the experimental test have been performed with a saturation-to-wall temperature difference ranging from 4 K to 22 K and there is not an influence of this parameter on HTC trends during condensation.

To discuss these aspects the comparison between the numerical and experimental HTC at $G \leq$ 200 kg m^{-2} s^{-1} inside vertical and horizontal channel is also reported in Figure 3.35.

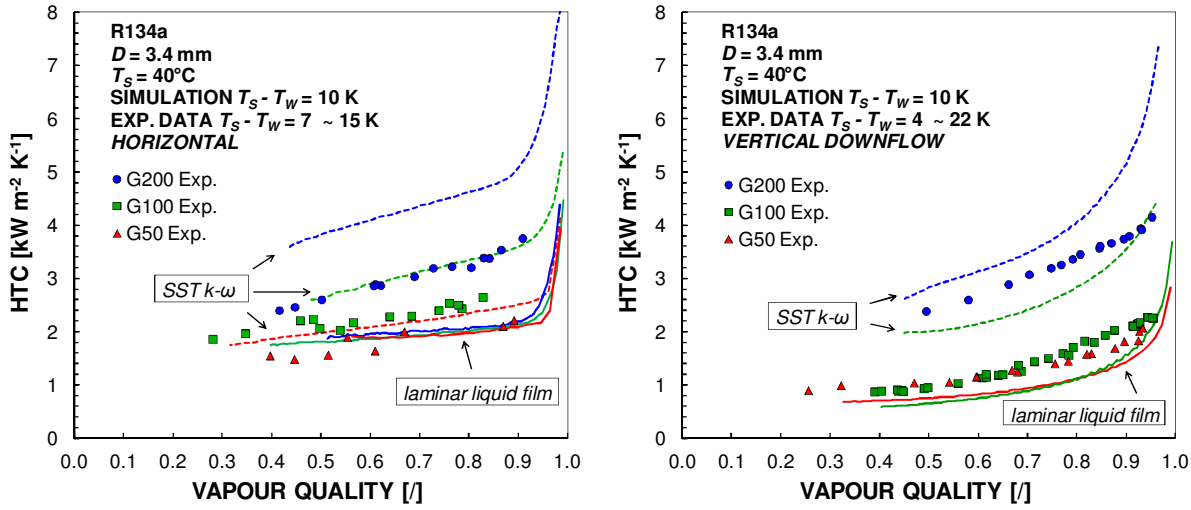

Figure 3.35: Effect of inclination inside 3.4 mm channel. Left: horizontal; right: vertical downflow.

From Figure 3.35 the following considerations can be done:

- A decrease of local HTCs inside the vertical channel can be observed as compared to those inside the horizontal channel both in experimental tests and numerical simulations. This behavior is clear at G = 100 kg m^{-2} s^{-1} and G = 50 kg m^{-2} s^{-1}.
  In fact, at x=0.5 and at G = 100 kg m^{-2} s^{-1} the ratio between the two HTCs is about 2.7 and 2.2, respectively, by numerical and experimental results; and at x = 0.5 and at G = 50 kg m^{-2} s^{-1} the ratio between the two HTCs is about 2.4 and 1.6, respectively, by numerical and experimental results. At G = 200 kg m^{-2} s^{-1}, instead, the deviation of the HTCs becomes lower and, thus, from this value of mass flux the magnitude of vapour shear stress starts to be higher as compared to that of gravity force. As already explained in section 3.4.2, this decrease of HTC at two different orientations of channel is due to the liquid distribution film.
- At low mass flux, the saturation-to-wall temperature difference displays an influence on local HTC coefficient for horizontal case; for this reason, only the

experimental tests with a saturation-to-wall temperature difference near 10 K have been chosen for the comparison against numerical simulations. This procedure has not been applied for experimental tests obtained inside the vertical channel.

- At G = 100 kg m^{-2} s^{-1} and G = 50 kg m^{-2} s^{-1} the HTC are almost overlapped inside the vertical channel, but it does not occur inside the horizontal channel both in numerical results and experimental data.
- At G ≤ 100 kg m^{-2} s^{-1} the experimental HTC trends obtained inside the vertical channel are strongly underpredicted by laminar liquid approach (over -25%) as compared to those inside the horizontal channel.
- At G = 200 kg m^{-2} s^{-1} the SST k-ω approach holds the experimental trend for vertical down-flow configuration with a lower deviation as compared to that obtained for horizontal configuration.

The last point can be explained applying the model presented by Cioncolini et al. [54] to approximately identify the occurring of turbulence in shear-driven annular liquid films as reported in Figure 3.33. In this figure the Cioncolini et al. [54] model has been applied at varying mass flux from 50 kg m^{-2} s^{-1} to 200 kg m^{-2} s^{-1} during the vertical downflow condensation. As shown, the dimensionless liquid film thickness δ^+ evaluated falls in the turbulent zone for G = 200 kg m^{-2} s^{-1}, whereas, for G < 200 kg m^{-2} s^{-1}, the criterion by Cioncolini et al. [54] predicts a transition between laminar and turbulent flow. For this reason, in this case the HTC trend at G = 200 kg m^{-2} s^{-1} is well predicted with the SST k-ω approach, whereas at G ≤ 100 kg m^{-2} s^{-1} the laminar liquid flow must be relaxed and some turbulence should be considered inside the liquid film to hold the experimental data as compared to the horizontal configuration.

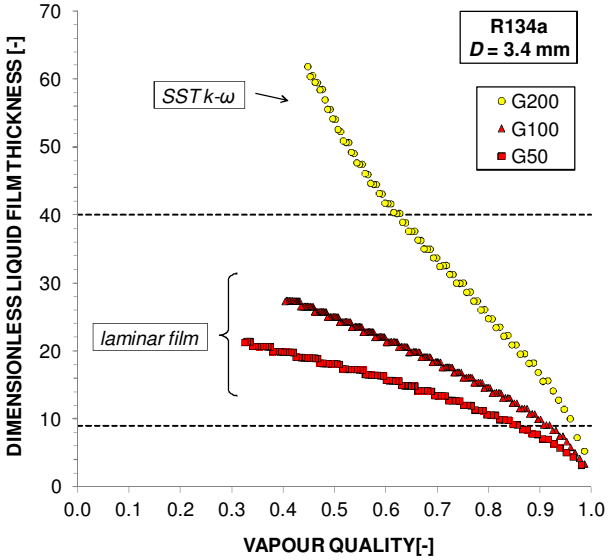

Figure 3.36: Dimensionless liquid film thickness for R134a at different mass velocities inside a 3.4 mm vertical channel (downflow condensation) with the criterion reported in Cioncolini et al. [54].

To explain this phenomenon, the distribution of turbulent viscosity, obtained by the numerical simulations with SST k-ω approach, inside the liquid film in horizontal channel at G = 200 kg m^{-2} s^{-1} and at x = 0.6 is depicted in Figure 3.37. Here, the amount of

turbulence is focused on the bottom of the channel and at the top, instead, the liquid film is thinner and the amount of turbulence is lower. Therefore, when the channel is horizontal, the major part of heat flow rate is exchanged at the top of channel (85%, as discussed in Section 3.5.4) where the occurring of turbulence is mitigated.

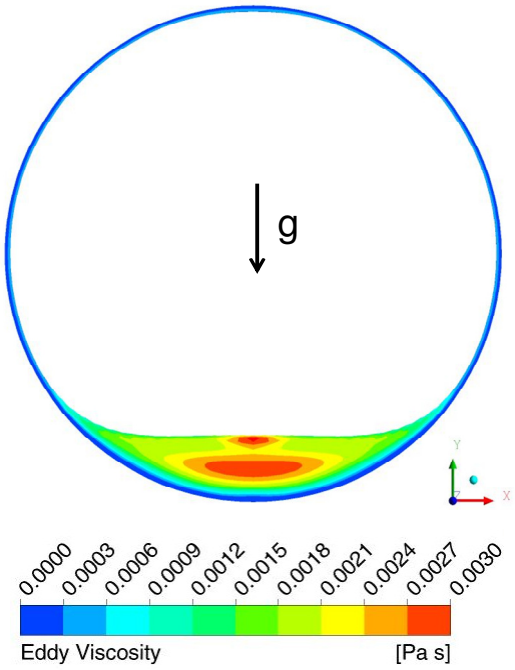

Figure 3.37: Distribution of Turbulent or Eddy viscosity μ_T inside the liquid film for horizontal channel at G = 200 kg m^{-2} s^{-1} and x = 0.6.

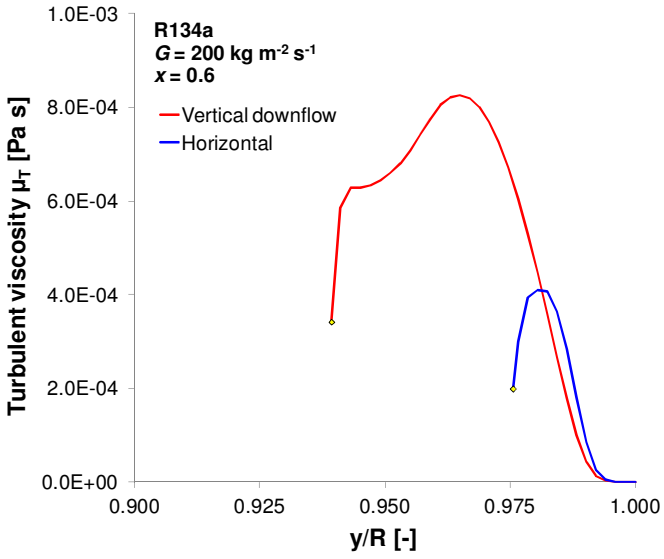

Figure 3.38: Distribution of Turbulent or Eddy viscosity μ_T inside the liquid film for vertical channel and on the top of channel for horizontal configuration at G = 200 kg m^{-2} s^{-1} and x = 0.6.

In Figure 3.38 the distribution of turbulent viscosity inside the liquid film is plotted versus dimensionless height of channel for both orientations at the same value of mass flux and vapour quality; for the horizontal configuration the μ_T distribution on the top of channel is depicted. Inside the vertical channel the heat flow rate is uniformly exchanged along the

wall perimeter and the amount of turbulence in the liquid film is higher than that evaluated in horizontal channel. These considerations explain:

- the different locations of δ^+ trends in Figure 3.33 and Figure 3.36 for horizontal and vertical channel ranging mass flux from 50 to 200 kg m^{-2};
- the better prediction of HTC trend by SST k-ω approach in vertical channel as compared to that in horizontal channel at G = 200 kg m^{-2};
- the numerical issues to evaluate some turbulence by SST k-ω approach inside the liquid film in the upper side of horizontal channel to hold the experimental trends.

In Figure 3.39 the experimental visualizations in the same channel, at horizontal and vertical downflow configuration, have been depicted at G = 50 kg m^{-2} s^{-1} and G = 100 kg m^{-2} s^{-1}.

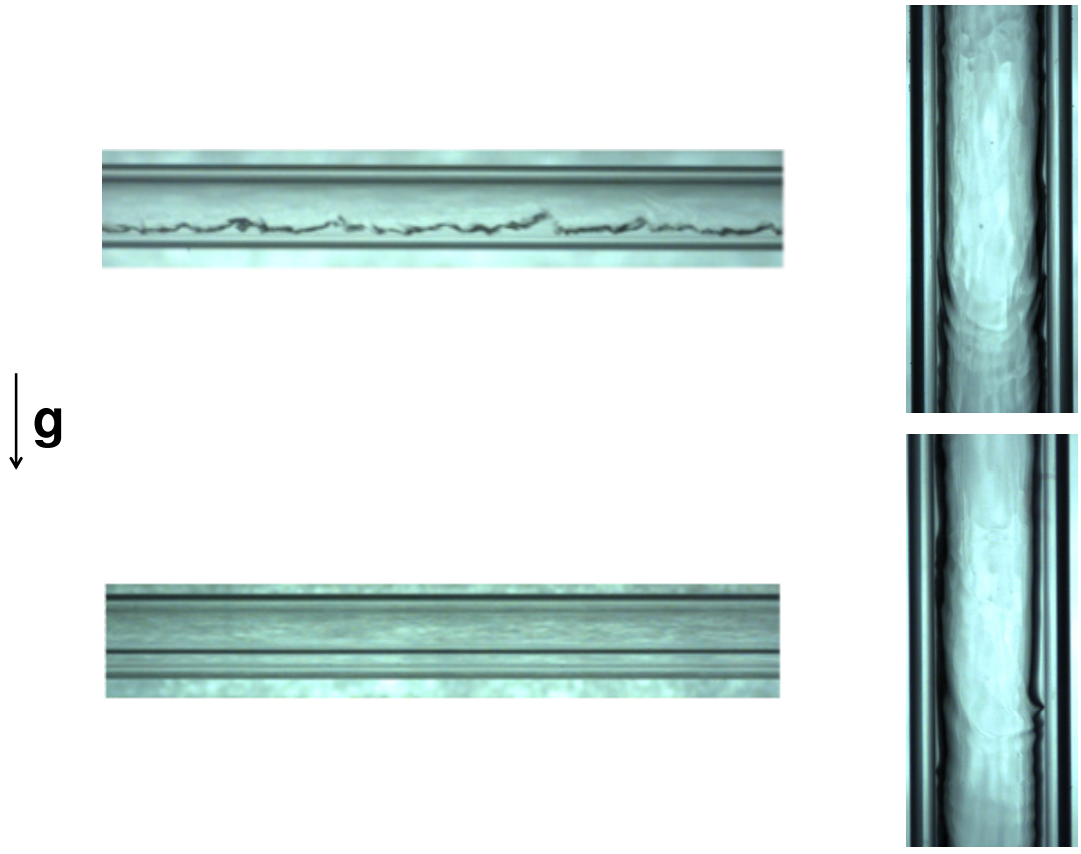

Figure 3.39: Flow pattern during condensation of R134a at 40°C saturation temperature, mass velocity equal to 100 kg m^{-2} s^{-1} (Top) and at 50 kg m^{-2} s^{-1} (Bottom) at the same vapor quality of 0.7 in horizontal (data of[7]) and vertical channel.

From G = 50 kg m^{-2} s^{-1} to G = 100 kg m^{-2} s^{-1} the occurring of waves at vapour-liquid interface can be detected inside the horizontal channel.
In section 3.5.4 it has been verified that, since the presence of waves is detected at the bottom of channel (where the liquid film is more thicker and the rate of heat transfer is less than 20%), their influence on local heat transfer coefficient results limited.

When the channel is vertically oriented, instead, the waves occurs along the whole perimeter of channel affecting in significant way the liquid flow features (liquid thickness, velocity, turbulent viscosity..) and the heat transfer. In addition, at decreasing of mass flux, in vertical channel the occurring of wave again persists as compared to two-phase flow detected in horizontal channel. Therefore, in this case the steady-state condition must be relaxed to able to predict the interfacial waves along the whole perimeter of channel and to understand their influence from a heat transfer and momentum point of view.
For this reason in the next section 4 the unsteady-state numerical simulations have been performed to capture the occurring of instabilities at interface and to analyze the annular-wavy flow during condensation inside a single 3.4 mm vertical channel.

3.6.1 Influence of gravity at larger channel

Here, a brief analysis of gravity force effect on liquid film distribution and heat transfer has been reported to highlight the importance of gravity at larger inner diameter.

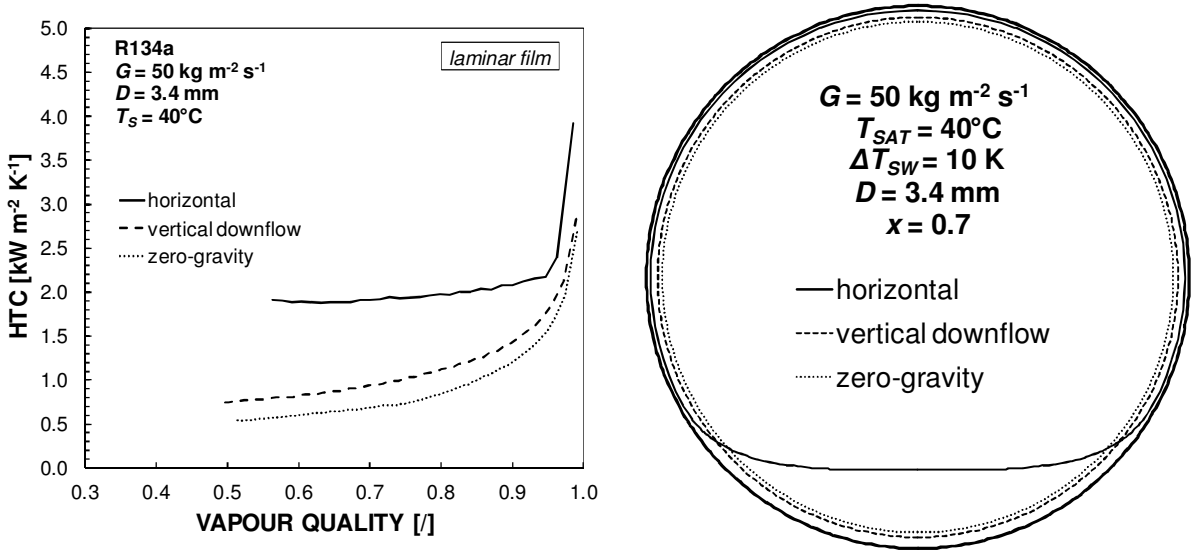

Figure 3.40: The gravity effect inside a single circular channel of 3.4 mm (horizontal, vertical downflow and zero-gravity).

In Figure 3.40 the HTC trends and the vapour-liquid interfaces have been obtained by the VOF numerical simulations at G = 50 kg m^{-2} s^{-1} considering the horizontal, vertical-downflow and zero-gravity configuration.
When the channel is vertical or the gravity is not taken into account a constant film thickness is obtained around the whole perimeter of channel and a significant decrease of local heat transfer coefficient can be detected. For example, at x = 0.7 when the channel is vertical in downflow configuration and when the gravity is zero there is, respectively, a heat transfer coefficient decrease of 51% (liquid thickness of 75 μm) and 64% (liquid thickness of 100 μm) as compared to the horizontal channel. In fact, as shown in figure, in horizontal channel, the gravity promotes the stratification thinning the liquid film (liquid thickness of

30 μm) along the major part of channel at the upper side increasing the cross-sectional average heat transfer coefficient.

It is worth noting that these results have been obtained at worst conditions since the simulations are done in steady-state condition and the enhancement of heat transfer due to the presence of waves is not considered [53]. However, similar results are experimentally obtained by Adelaja et al. [58] inside a circular channel of 8.38 mm during R134a horizontal and vertical downflow condensation. For example, at G = 100 kg m^{-2} s^{-1} and at x = 0.75 the authors declared a local heat transfer coefficient equal to 2600 W m^{-2} K^{-1} in horizontal condition and equal to 1300 W m^{-2} K^{-1} in vertical downflow condition, having a decrease of about 50%.

When the diameter is lower (e.g. $D \leq 1$ mm), as analyzed by Da Riva et al. [20], the effect of gravity becomes negligible and the numerical results are very similar in vertical and zero-gravity configuration.

When the diameter is larger this is not true and the contribution of gravity at these operating conditions is present. In fact, in vertical channel the gravity thins the liquid film along the channel having a visible increase of heat transfer coefficient: for example, at G = 50 kg m^{-2} s^{-1} and at x=0.7 there is an decrease of 28% in terms of heat transfer coefficient during zero-gravity condensation.

4 TRANSIENT VOF SIMULATIONS OF DOWNFLOW CONDENSATION INSIDE A VERTICAL MINICHANNEL

4.1 Introduction: the significance of unsteady state simulations

The evaluation of heat transfer coefficient during the two-phase flow is very complex due to the presence of vapour-liquid interface, the different flow regimes and the spatial distribution of phases. Besides the development and the validation of empirical correlations to predict the heat transfer coefficient, a more complete understanding and theoretical model of two-phase flow and heat transfer mechanisms inside channel at small scale are necessary for the design and optimization of heat exchangers.

In the previous sections, the numerical simulations were focused on condensation of different fluids inside minichannels at low values of mass velocity (i.e. $G \leq 200$ kg m^{-2} s^{-1}) and at 40°C of saturation temperature. These simulations have been performed in steady-state and the vapour-liquid interface tracked by VOF method is smooth and the interfacial instabilities during condensation phenomena are not predicted. For this reason, the flow pattern simulated is limited to be annular or smooth stratified. The numerical results obtained by this settings have been validated against experimental data and a good agreement has been achieved.

This goal has been reached because the major of tested operating conditions occurred when:

- the flow pattern was mosty annular and the wavy flow was not expected due to importance of surface tension force at small scale ($Bo<Bo_{cr}$). In this case the annular flow occupied the major part of channel during condensation and the transition to the intermittent flow was directly achieved;
- at larger scale ($Bo>Bo_{cr}$) inside a horizontal channel where the interfacial waves were detected at the bottom of channel and their influence on global heat transfer was limited.

Actually when the annular-wavy flow is present or the transition from annular to intermittent flow is occurring, the steady-state condition must be relaxed to be able to predict the vapour-liquid interface area in minichannel during condensation. Experimentally, the flow instabilities in minichannel still represents a challenge even for the latest experimental techniques for measurement due to the small length and time scale involved, so that data reduction has for long been limited to a time-average value of heat transfer coefficient and pressure drop.

The recent advances on infrared thermometry combined with high speed flow visualizations give access to local heat transfer coefficient trends and flow pattern ([3],[4]). Nevertheless, many aspects of two-phase flow such as local fluid dynamics and the influence of interfacial instabilities on heat transfer, remain inaccessible to experiments.

For these reasons, in this section, numerical simulations of R134a condensation inside a vertical channel have been performed in unsteady-state conditions.

The aim of this part of thesis is to assess the capability of VOF method to capture the interfacial instabilities and the distribution of phases inside the minichannel during the vertical downflow condensation.
In the literature, the unsteady-state simulations are usually targeted to the analysis of single phenomenon or specific flow regime. In fact, in many works, numerical simulations are performed to associate the fluid dynamics and heat transfer with the growth of a single bubble in flow boiling conditions. Other CFD studies can be found in the literature that analyze the flow boiling of two/multiple bubbles, the nucleation phenomena, the operating conditions that promote the coalescence of bubbles inside minichannel, and the condensation of single bubble in a subcooled flow boiling.
The brief review above reported highlights that the majority of the works is focused on boiling and evaporation heat transfer and only few studies are focused on transient condensation. For example, Ganapathy et al. [44] applied the VOF method in unsteady-state conditions to investigate the condensation mechanisms for different flow pattern detected inside a single microchannel of diameter equal to 100 μm. In this work, the authors avoids the assumption to utilize a fixed interfacial profile between the liquid and vapour phase developing an alternative method for the phase change phenomena that simultaneously considers the momentum, heat transfer and mass transfer equations. The authors compared the pressure drops, the Nusselt numbers obtained by numerical simulations against the correlation data found in the literature at these operating conditions, obtaining a reasonably good agreement for both parameters with a mean absolute error of about 20%. In addition, the authors simulated the condensation flow patterns and compared them against the available experimental visualization data in the literature. In their work the refrigerant was R134a, the mass flux at the inlet was ranged from 245 to 615 kg m^{-2} s^{-1} and the channel wall was maintained at a constant heat flux varying from 200 to 800 kW m^{-2}.
Another example is the work of Qiu et al. [57]. The transient VOF model was adopted to simulate the heat transfer characteristics of forced convective condensation of steam upward flow in vertical pipe. The range of mass flux and vapour quality of these numerical simulations was, respectively, from 130 to 6400 kg m^{-2} s^{-1} and from 0 to 0.4, at a saturation pressure of 5MPa and at a fixed wall temperature of 535.09 K inside a conventional channel of 12 mm. From the numerical simulations various flow patterns could be detected, such as bubbly flow, slug flow, churn flow and annular flow; then the results of flow pattern were compared against the regime map of Hewitt and Roberts [59]. Furthermore, the author analyzed the velocity field characteristic of each flow pattern and its influence from heat transfer point of view.
In the present thesis unsteady simulations using the VOF method have been performed to capture the interfacial instabilities during R134a condensation in a single 3.4 mm i.d. circular minichannel in vertical downflow configuration. For this analysis the mass flux and vapor quality range, respectively, from 50 to 200 kg m^{-2} s^{-1} and from 0.7 to 0.4 at 40°C of saturation temperature have been investigated. The numerical results on flow patterns are

also compared against the experimental visualizations obtained at Two-Phase Heat Transfer Laboratory at the University of Padova.

4.2 Settings of unsteady numerical simulations

In this section different studies found in the literature have been considered, in particular, for the spatial mesh and the settings of numerical simulations (e.g. the Courant number).
About the governing equations for the continuity, momentum, energy conservation and for turbulence variables the transient term is here taken into account as compared to the numerical simulations presented in previous sections to introduce the rate of increase/decrease of variables in time.
The main differences between settings of unsteady-state simulations and those of steady-state ones are:

- the optimization of numerical domain for the analysis of unsteady-state phenomena
- the numerical solvers

4.2.1 Spatial mesh

A two-dimensional domain has been considered taking advantage of the axisymmetric configuration when the channel is vertically oriented. The optimization of the mesh type and size is a fundamental step to obtain a reduction of computational cost and reliable results. In fact, when performing unsteady-state simulations, a decrease of the element size leads to a reduction of the time step increasing dramatically the computational effort. Considering the works available in the literature, a typical issue encountered in two-phase flow simulations is due to the very thin liquid film near the channel wall, in particular when:

- the flow is annular at high vapour quality;
- waves occur at vapour-liquid interface with zones between the waves characterized by thin film;
- the Taylor or slug flow occurs. A thin liquid film separates these bubbles from the wall and also connects the two successive liquid slugs.

Some researchers have done numerical simulations of slug/Taylor flow in microchannels showing the presence of dry walls since a not-sufficiently refined grid was used to capture the thin liquid film between the bubble and the wall. Gupta et al. [46] developed a methodology to simulate Taylor flow in horizontal microchannels using the VOF method predicting the liquid film thickness, void fraction, bubble velocity and pressure drops. The authors discuss the importance of element size to capture the liquid thickness in the numerical simulations of Taylor flow inside a 0.5 mm i.d. circular channel. They reported three types of mesh, having element size equal to 12.5 μm (D/10), 5 μm (D/100) and 2.4 μm. The authors declared that the 5 μm grid is able to capture the liquid film initially but the film is disrupted as the bubble moves forward and that the grid needs further refinement to capture the complex flow field around the bubble. They proposed also finer mesh, but declared that the ultra-refined grids are not only computationally expensive but

they also cause increased non-physical pressure jumps across the interface, arising from the use of high order discretization. Finally, Gupta et al. [46] presented a criterion based on Capillary number: a minimum of five elements are needed across the liquid film and they can be evaluated by the following equations:

$$\frac{\delta}{D} = 0.67 Ca^{2/3} \quad \textbf{4.1}$$

$$\frac{\delta}{D} = \frac{0.67 Ca^{2/3}}{1 + 2.5\left(1.34 Ca^{2/3}\right)} \quad \textbf{4.2}$$

where the Capillary number Ca is evaluated by:

$$Ca = \frac{\mu_L (U_{LS} + U_{GS})}{\sigma} \quad \textbf{4.3}$$

where U is the superficial velocity of the phase, σ is the surface tension and μ the molecular dynamic viscosity.

Gupta et al. [46] obtained a δ equal to 12 μm for a inner diameter of 0.5 mm, thus the mesh size should be about 2.4 μm to have a sufficient accuracy to capture the liquid film.

Furthermore, to address the three conflicting requirements of having a uniform square grid in the region where the gas-liquid interface is present, sufficient near wall fine mesh to capture the liquid film and reasonable computational cost, the authors decided to adopt a grid having uniform square elements of size 5 μm in the core and rectangular elements (2.4 μm x 5 μm) in the 12 μm thick film region.

Also Ganapathy et al. [44] used the equation 4.1 and other ones based on Capillary number to carefully chose the element size. The authors performed numerical simulation of different two-phase flow during condensation inside a circular channel of 100 μm and from an independent mesh analysis ensured that an uniform grid of 5 μm (i.e. $D/20$) is sufficient to have a good resolution of liquid film. Another example is the work of saturated flow boiling inside a microchannel during the slug flow regime reported by Magnini and Thome [60], where a uniform grid of 1.67 μm (i.e. $D/300$) is used to have the minimum resolution of the liquid film capable of adequately solving the flow and heat transfer in the film. Applying the equations above, the minimum element size have been evaluated for a inner diameter of 3.4 mm varying the mass velocity from 200 kg m^{-2} s^{-1} to 50 kg m^{-2} s^{-1} and vapour quality from 0.9 to 0.3 obtaining a minimum value of about 17 μm (i.e. $D/200$). Therefore, form the consideration above presented, a uniform square grid having an element size of 20 μm ($D/170$) has been adopted in the present unsteady-state numerical simulations.

4.2.2 Settings of transient solver

For the transient solver the variable time-stepping strategy through the Courant number C has been applied. The Courant number C is a non-dimensional quantity defined as the ratio of the time step size used by the transient solver to the characteristic time required for a fluid element to flow through a control volume. The latter is calculated based on the cell volume and the sum of outing fluxes, obtaining the time it would take for the fluid to empty out of cell. The smallest such time is used to determine the appropriate size of time step to be chosen in order to remain within the specified value of Courant number.
A very low value of Courant number corresponds to a very small time-step size and is associated with a high computational cost and high predictive accuracy. An high Courant number may result in poor accuracy of transient flow features and possibility divergence of the solution.
In Ansys/Fluent the default value of Courant number for solving the volume fraction is 0.25; this value is also typically used by various works in the literature. Whereas the Courant number used for solving the remain equations (i.e. momentum, turbulence and energy equations) can assume various values in the literature. In general, for the remain transport equation a common value lower than 1, it is sufficient to avoid numerical problems. For the numerical simulations reported here the Courant number was varied from 0.6 to 0.85.

4.2.3 Domain and boundary conditions

About the set-up of numerical domain the works of Magnini and Thome [60] and Adelaja et al. [57] has been considered. The authors decided to split the domain in two or three parts. The same procedure has been applied for the present simulation, as depicted in Figure 4.2, to predict the unsteady-state phenomena in two-phase flow during condensation or evaporation:

- the first section is long 10 D and is adiabatic. This section is fundamental to obtained a development of velocity and volume fraction field for an unsteady flow (Figure 4.1).

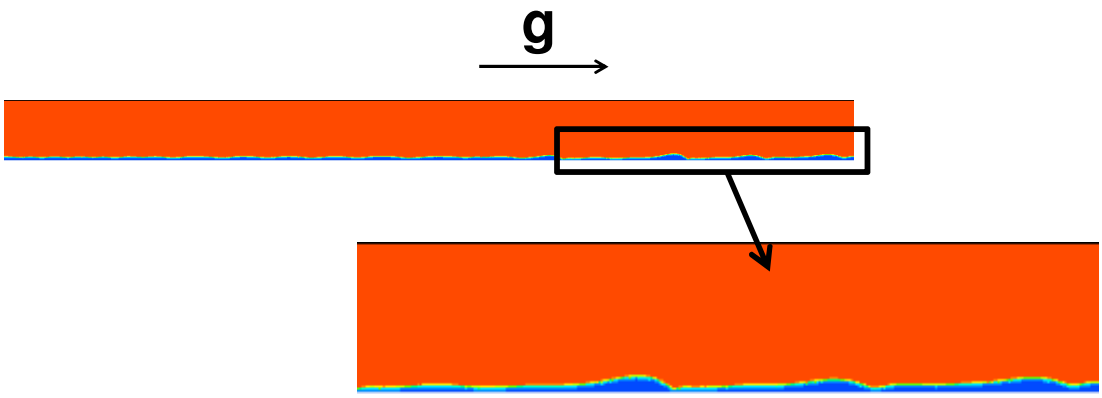

Figure 4.1: Development of interfacial instabilities at the inlet of the channel. The vapor phase is colored in red and the liquid phase in blue.

- the cooled section is long 40 *D* and a fixed wall temperature of 30°C has been taken as boundary condition. Here the annular-wavy downflow condensation inside a single and circular 3.4 mm i.d. minichannel takes place and the influence of interfacial instabilities, such as the presence of waves at vapour-liquid interface and the entrainment, on the heat transfer and momentum point of view can be numerically investigated.
- The third sector is a 5 *D* long adiabatic zone.

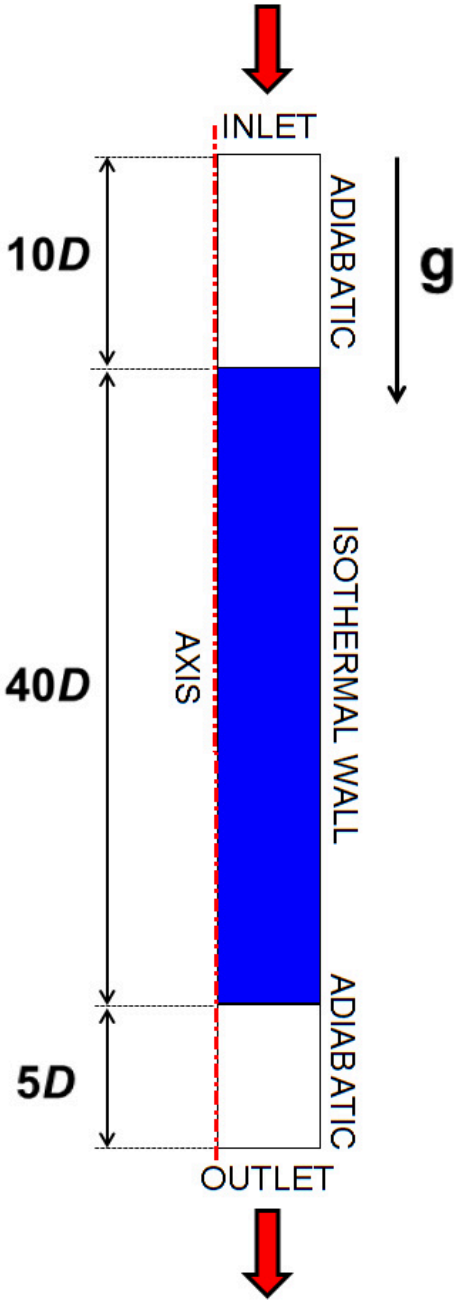

Figure 4.2: The simulation domain.

The element size of the grid is equal to 20 μm and the whole domain is discretized into $7.95 \cdot 10^5$ quadrilateral elements. The grid is uniform in order to well catch the liquid-vapour interface even if it moves far from the channel wall, due to the presence of waves.
The vapour enters into the minichannel at saturated condition with a saturation temperature of 40°C and at desired value of vapour quality. From previous two-phase steady-state simulations the profile of the velocity, the turbulent kinetic energy, the turbulent specific dissipation rate and volume fraction have been imposed at the inlet of channel for the unsteady-state simulations; the profiles are referred to a vapour quality of about 0.7 and 0.6 at mass velocity of 100 kg m^{-2} s^{-1} and 200 kg m^{-2} s^{-1}, respectively.
No-slip condition has been imposed at the wall, while pressure is fixed as condition at the outlet. The same phase change and surface tension models previously described in Sections 3.1-3.2-3.3 have been adopted. The SST k-ω turbulence model has been applied to investigate the influence of waves on turbulent viscosity inside the liquid film.
The volume fraction equation is integrated in time with a first order explicit scheme and the PLIC (Piecewise Linear Interface Calculation) scheme has been used for the advection of vapour-liquid interface. An implicit first order time scheme is used to solve the momentum, turbulence and energy equations and third order schemes are used for their spatial discretization. The PISO (Pressure Implicit Splitting of Operators) algorithm has been applied for the pressure-velocity coupling and the PRESTO! (Pressure Staggering Option) scheme is used for the pressure interpolation. The Green-Gauss node-based scheme has been considered for evaluate the gradient of scalars. The convergence criterion has been set to a value of 10^{-5} of the normalized absolute residuals for all the flow equations.

4.3 Validation against flow visualizations

Before showing the numerical results on local heat transfer coefficients and the predicted two-phase flow during annular-wavy condensation obtained inside a single 3.4 mm i.d. circular minichannel vertically oriented, a qualitative validation between numerical simulations against experimental flow visualizations have been performed.
The analysis is focused on annular-wavy condensation and, since the inner nature of vertical-downflow condensation is believed to be the presence of a uniform liquid film thickness around the channel wall, the numerical simulations have been performed taking advantage of bi-dimensional and axisymmetric geometry.
By considering the problem as axisymmetrical, the presence of quasi spherical droplets in the vapour core along the axis of channel cannot be rightly handled. Furthermore, the computational cell size could be not small enough to get a good resolution of the interface of small droplets inside the vapour core or of small vapour bubbles inside the liquid film. This could occur if the size of these phenomena is smaller than the element size of the grid (i.e. 20 μm).
Here, the comparison between two-phase flow regimes obtained by numerical simulations and the experimental visualizations is presented at two mass velocities G = 100 kg m^{-2} s^{-1} and G = 200 kg m^{-2} s^{-1}; for simulations in the cooled section the fluid changes its vapour quality from 0.7 to 0.45 at G = 100 kg m^{-2} s^{-1} (Figure 4.3 - Figure 4.4) and from 0.6 to 0.45

at G = 200 kg m^{-2} s^{-1} (Figure 4.5 - Figure 4.7). Figure 4.3 and Figure 4.4 show the simulated two-phase flow regimes at G = 100 kg m^{-2} s^{-1} at two different values of average vapour quality x = 0.69 and x = 0.5. The vapour phase is colored in red, whereas the liquid phase is depicted in blue. It can be observed that the numerical simulations are able to predict the existence of interfacial waves as observed in the same conditions of experimental visualizations. In particular, at a fixed mass velocity, when the vapour quality decreases, the waves become sharper and their frequency decreases.

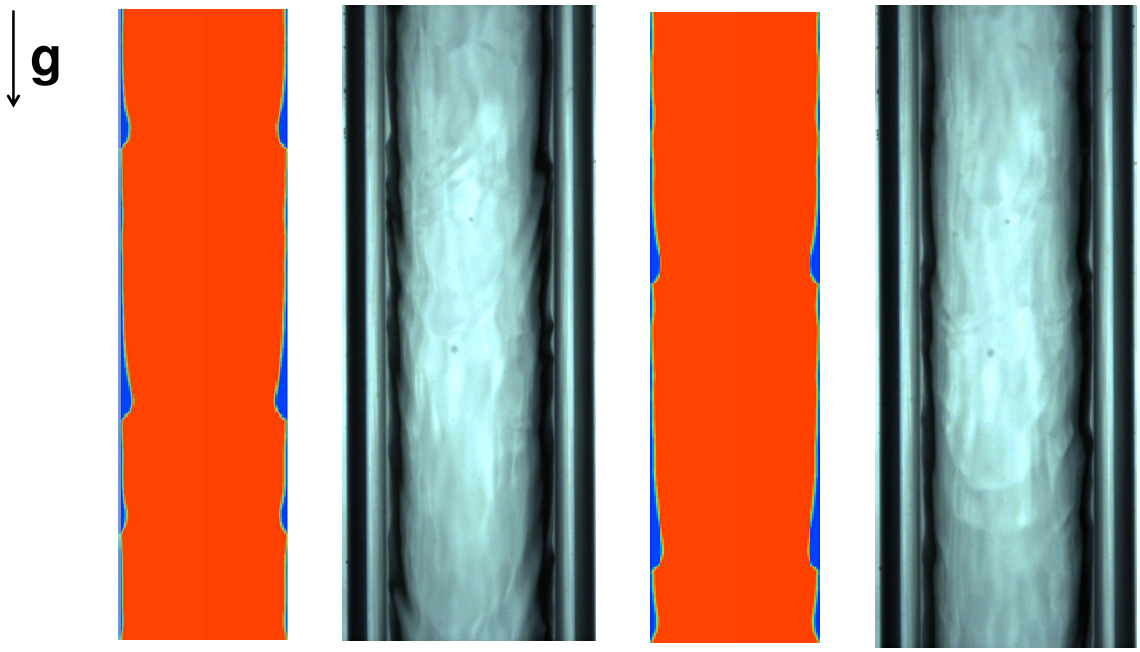

Figure 4.3: Comparison between predicted and experimental two-phase flow at G = 100 kg m^{-2} s^{-1} and at x=0.69.

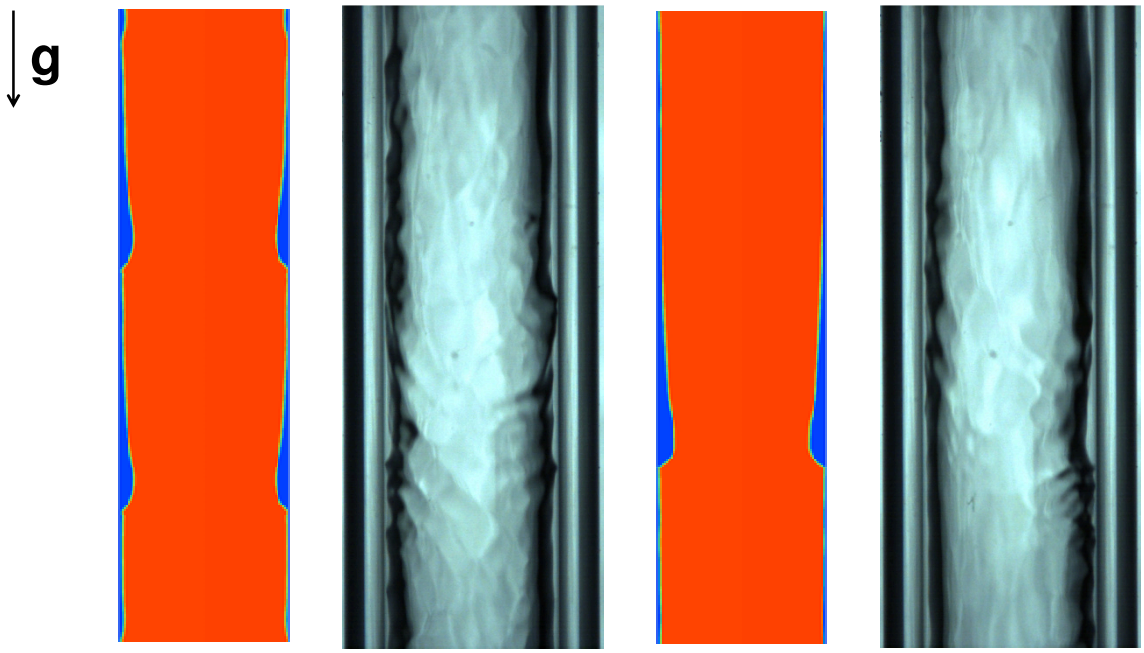

Figure 4.4: Comparison between predicted and experimental two-phase flow at G = 100 kg m^{-2} s^{-1} and at x=0.50.

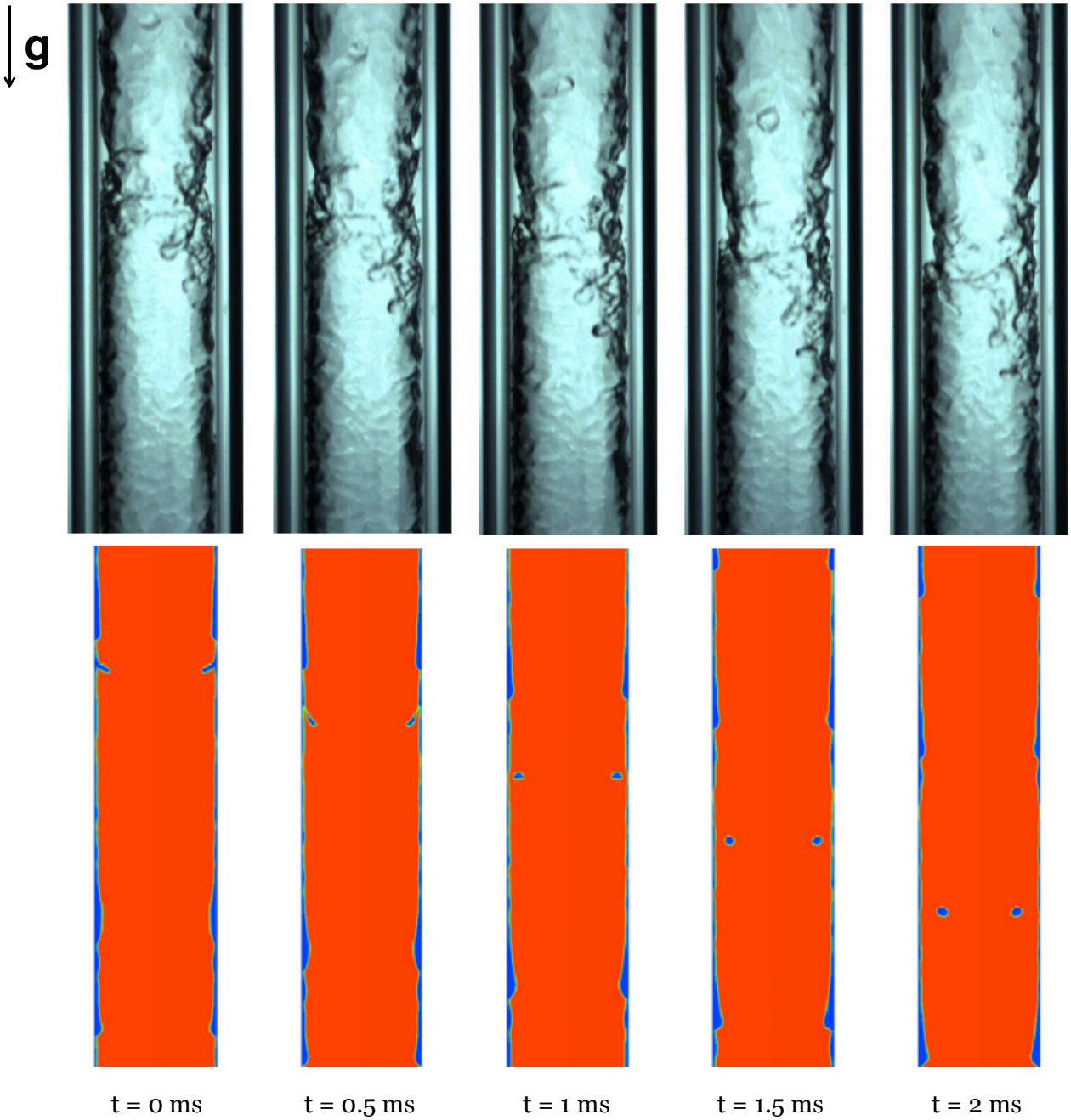

Figure 4.5: Comparison between predicted and experimental two-phase flow at G = 200 kg m^{-2} s^{-1} and at x = 0.57.

In Figure 4.5, numerical results are reported together flow visualizations at G = 200 kg m^{-2} s^{-1} and x = 0.57. Comparing the flow patterns of Figure 4.5 with the ones illustrated in Figure 4.3 and Figure 4.4, it can be observed that, when the mass flux is increased, the vapor-liquid interface becomes more disturbed due to the higher vapour shear stress stress

on the liquid film. In Figure 4.6, the computed shape of the liquid film inside the cooled sector of the tube is reported along the axial coordinate for mass velocity G =100 kg m^{-2} s^{-1} and G =200 kg m^{-2} s^{-1}. Considering the same channel length (i.e. 80 mm), at G = 100 kg m^{-2} s^{-1} the vapour quality varies from 0.6 to 0.43 and the liquid waves grow up moving downstream as the condensation proceeds. When moving to G = 200 kg m^{-2} s^{-1}, the outlet vapour quality changes from 0.6 to 0.53 and the frequency of the waves is found to increase.

Beside the occurring of interfacial waves, when the mass velocity increases other phenomena can be detected by means of unsteady-state numerical simulations. The vapour phase can rip some liquid from the annular film, with the formation of liquid entrainment in the vapour phase (Figure 4.5). In Figure 4.7, the evolution of a liquid droplet inside the vapour core is shown along the channel axis. The comparison is made at four time steps of 1 ms and a good agreement is found between the numerical simulations and the experimental visualizations.

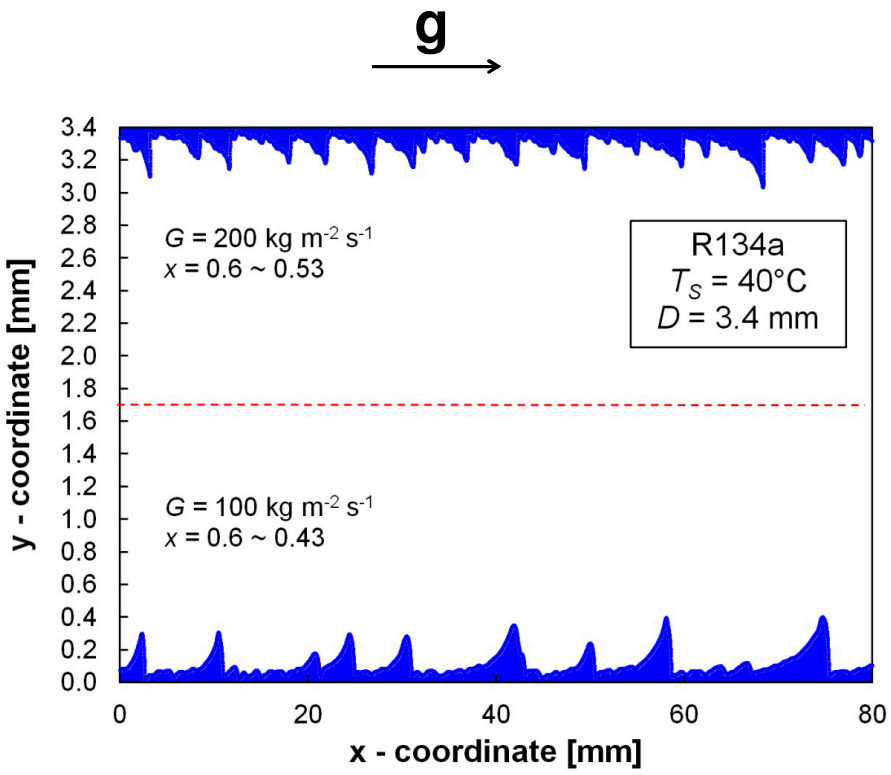

Figure 4.6: Influence of mass velocity on the interfacial waves at two different mass velocities.

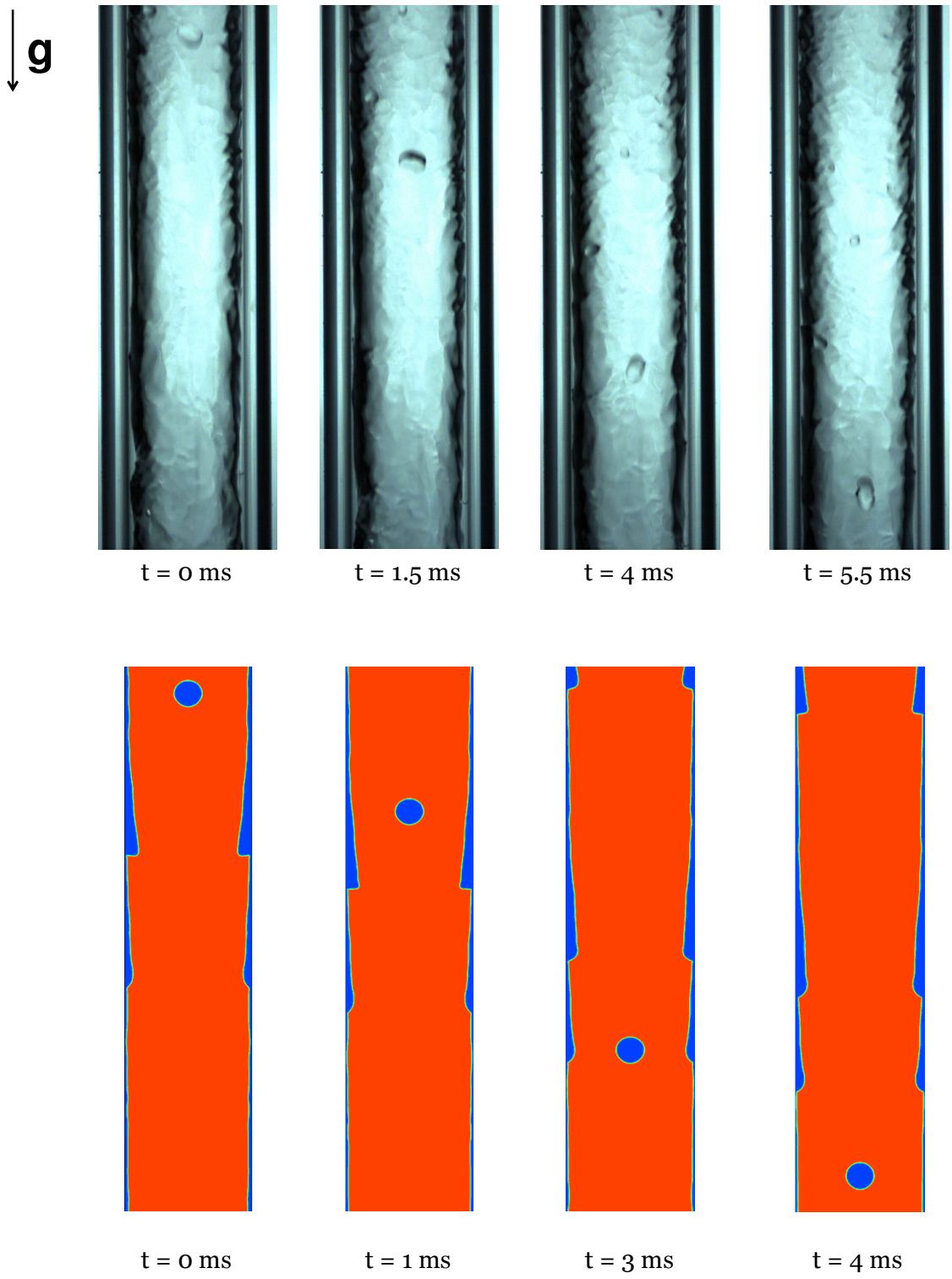

Figure 4.7: Comparison between predicted and experimental two-phase flow at G = 200 kg m^{-2} s^{-1} and at x=0.47.

4.4 The annular-wavy flow field

In Figure 4.8 - Figure 4.9 the velocity and pressure field inside vapour core obtained from the numerical simulations during R134a downflow condensation inside a 3.4 mm channel are reported. Mass velocity is equal to 100 kg m^{-2} s^{-1} and vapour quality is 0.5.
The presence of waves at vapour-liquid interface can locally affect the velocity and pressure field in function of the shape, the frequency and the height of wave.
At the same value of mass velocity, at channel inlet the shear of vapour is transmitted to the liquid film across the interface increasing the number of waves.
At these operating conditions there are numerous and small waves and the velocity and pressure fields are influenced primarily near the interface, whereas along the axis the influence of waves is almost negligible.

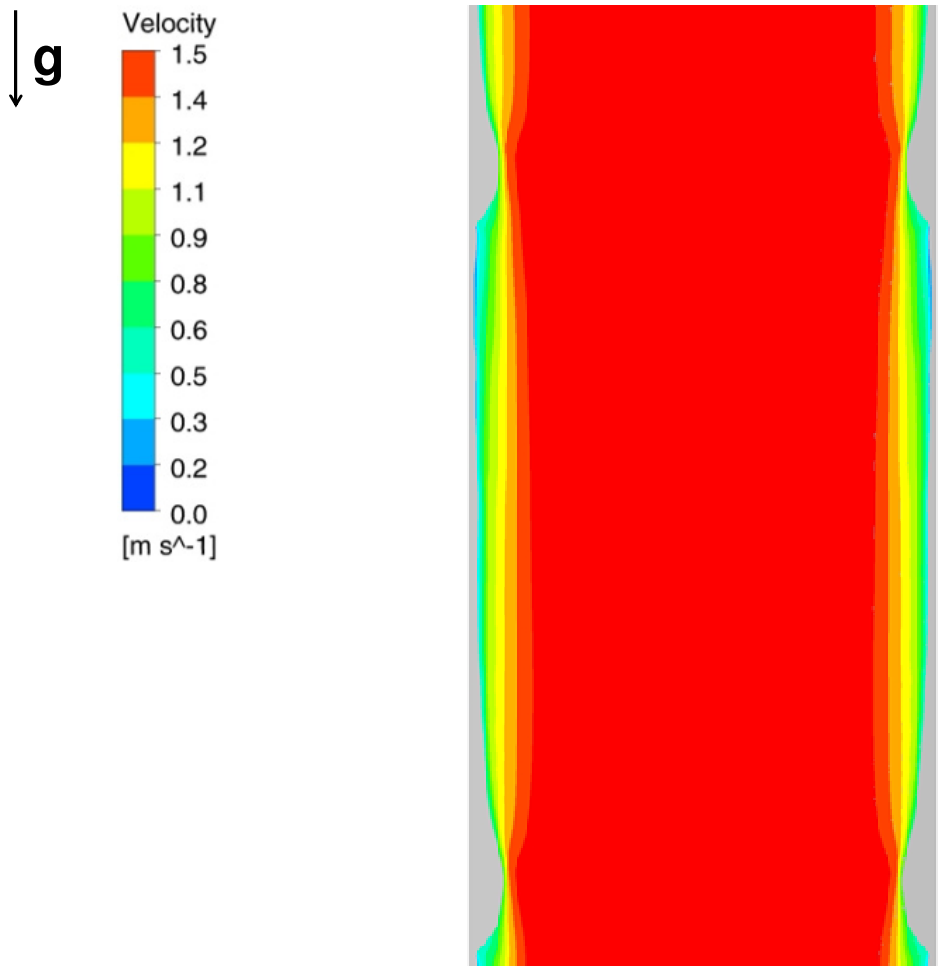

Figure 4.8: Velocity field in vapour core in annular wavy flow at G = 100 kg m^{-2} s^{-1} at x = 0.69.

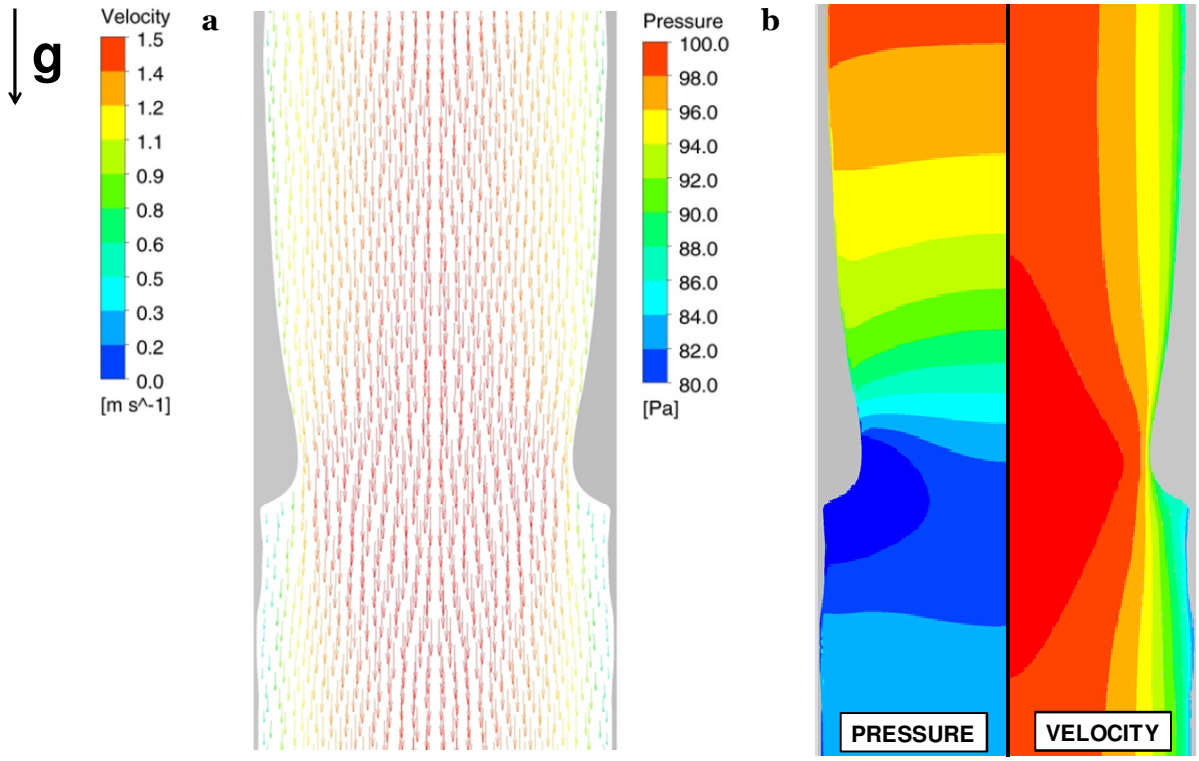

Figure 4.9: Results of the numerical simulations during downflow condensation inside a 3.4 mm channel (G = 100 kg m^{-2} s^{-1} and x = 0.5). a) Vectors of vapour velocity b) Pressure field (left) and Velocity magnitude field (right) inside the vapour core.

Moving downstream, the vapour velocity decreases and the liquid thickness increases: the vapour stress is lower having a lower number of waves and, at the same time, higher wave crest.

In this case the height of waves is enough to disturb the velocity and pressure field also at the channel axis. In fact, at increasing of wave height the flow is similar to that obtained when a fluid is forced to flow through an orifice. Near this obstacle the vapour velocity increases reaching the maximum velocity at the crest of wave, at the same time the local pressure decreases and a depression region occurs near the crest of wave. The depression region pulls the wave towards the axis of channel. At this point, as discussed in section 3.5.1, if the crest of wave reaches the axis of channel before the trough reaches the wall then the blockage of vapour could occur through a liquid bridge and the transition wavy-to-intermittent could take place.

Considering the present simulations and the analysis reported by Thome et al. [53] the presence of waves is expected to affect in significant way the condensation heat transfer and due to the following phenomena:

- the waves have a non-sinusoidal shape and lead to a reduction of the mean thickness of film;
- the entrainment of liquid droplet inside the vapour core can occur reducing further the liquid thickness;
- the turbulence intensity increases the liquid waves (Figure 4.10), thus promoting the heat transfer.

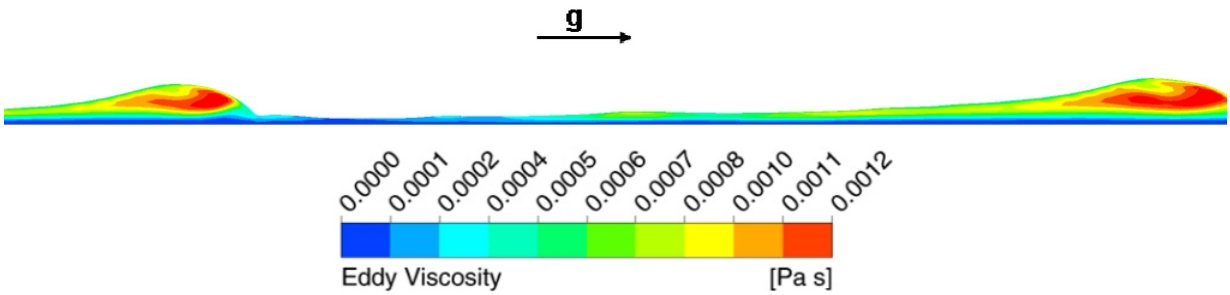

Figure 4.10: Liquid turbulent viscosity inside a wave.

4.5 Predicted two-phase flow in annular-wavy downflow condensation

The development in time of the two-phase obtained by numerical simulation has been here reported for all tested cases.

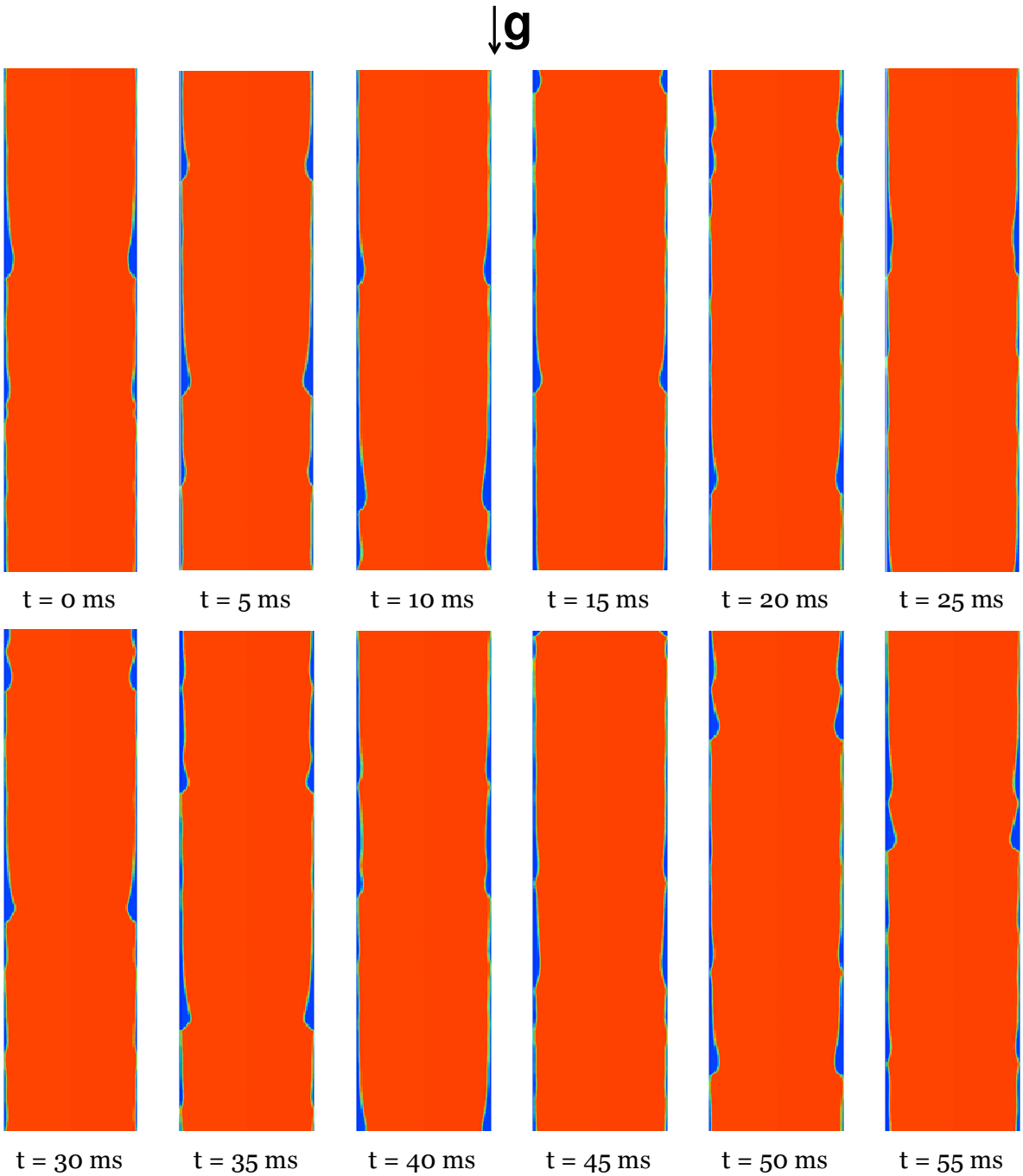

Figure 4.11: Predicted two-phase flow during condensation at G = 100 kg m^{-2} s^{-1} and at x = 0.69.

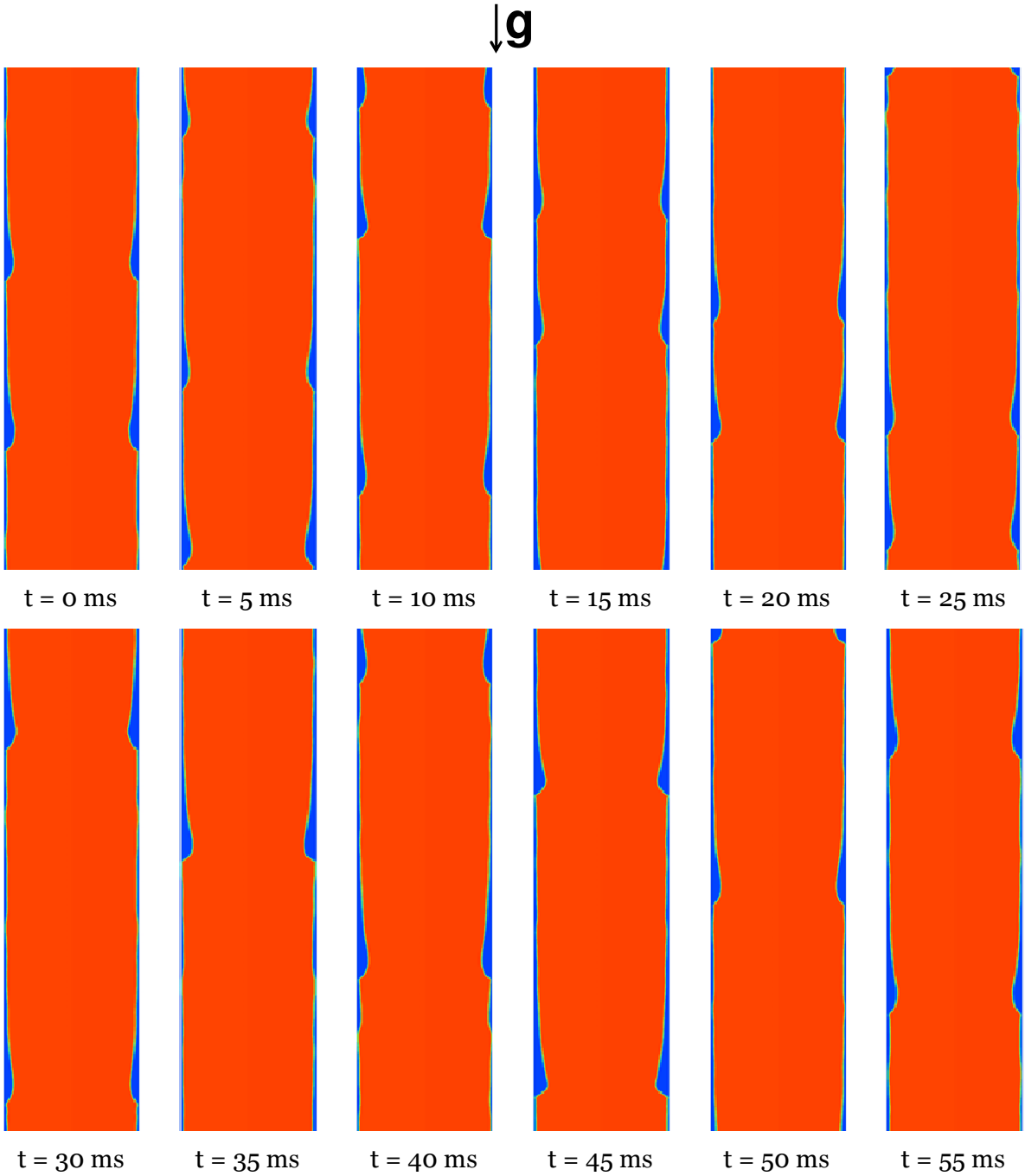

Figure 4.12: Predicted two-phase flow during condensation at G = 100 kg m^{-2} s^{-1} and at x = 0.60.

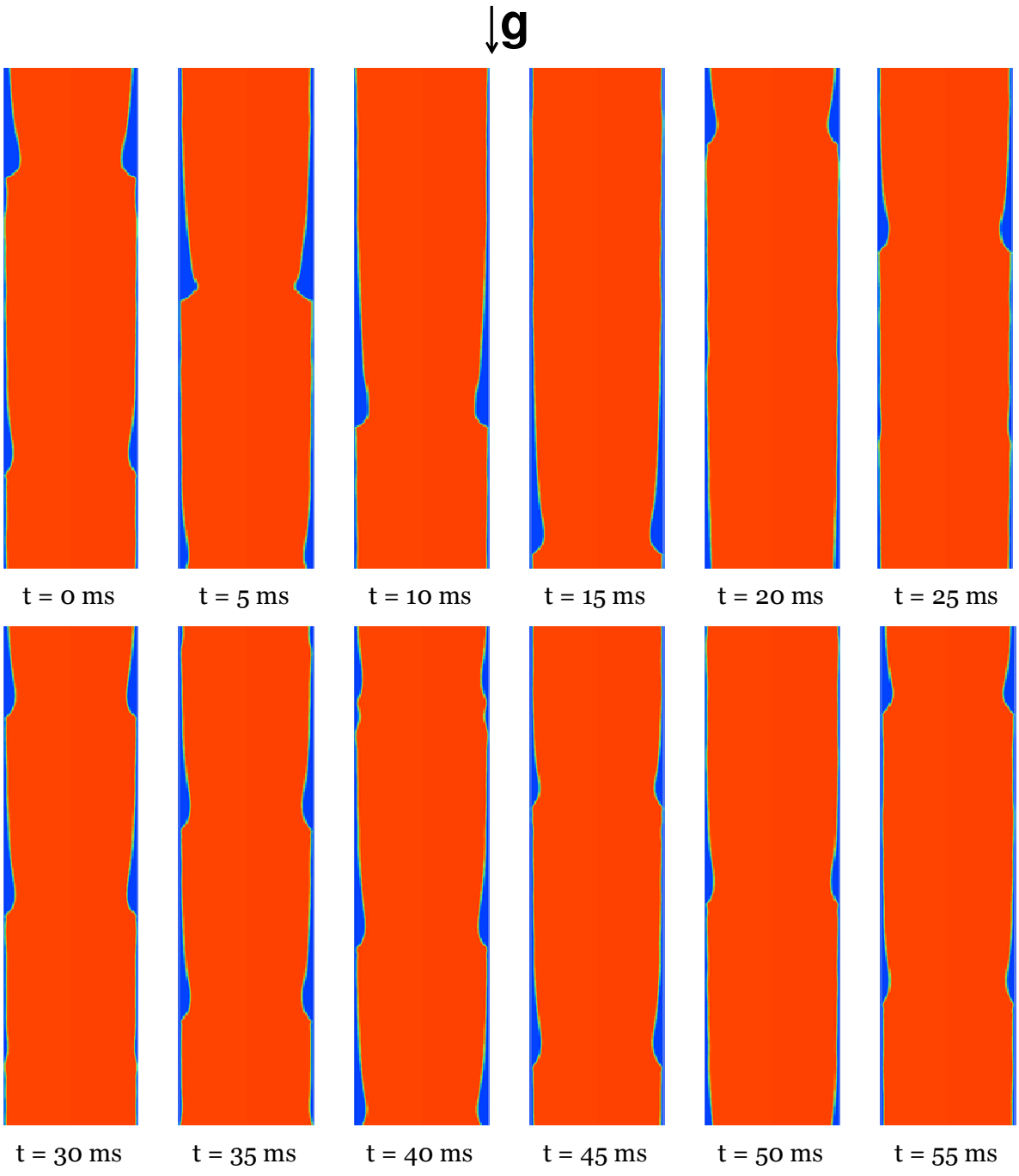

Figure 4.13: Predicted two-phase flow during condensation at G = 100 kg m^{-2} s^{-1} and at x = 0.50.

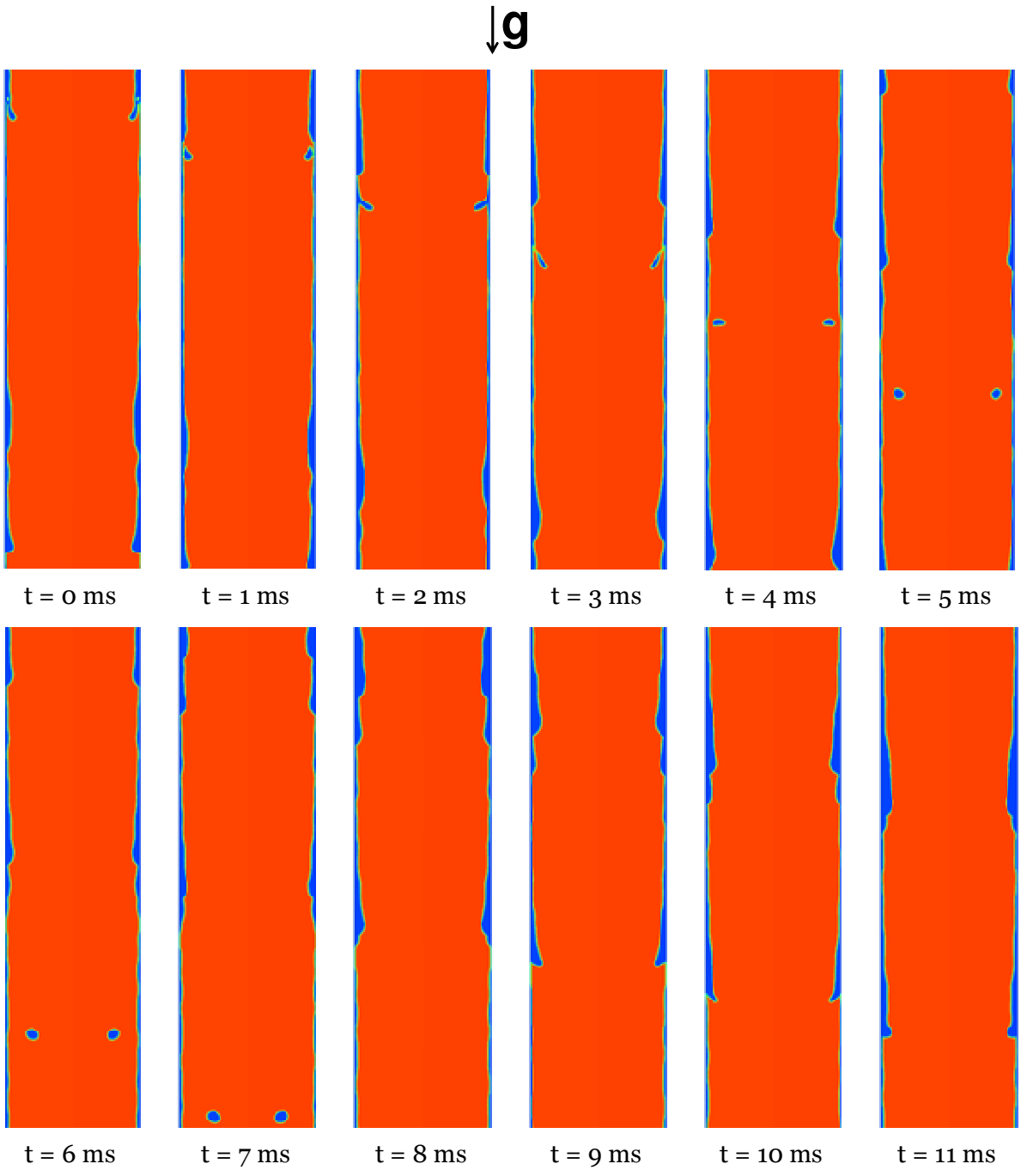

Figure 4.14: Predicted two-phase flow during condensation at G = 200 kg m^{-2} s^{-1} and at x = 0.57.

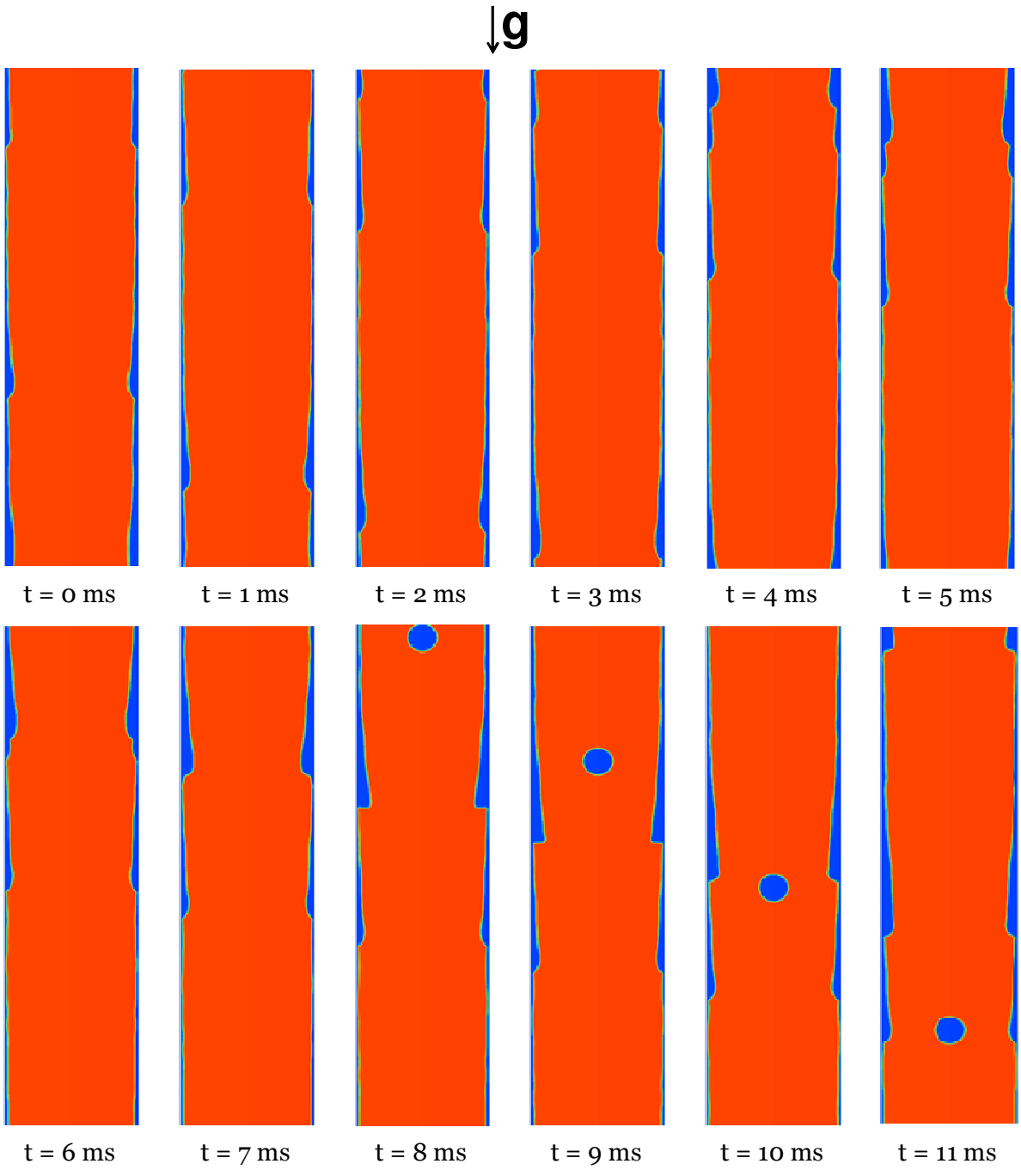

Figure 4.15: Predicted two-phase flow during condensation at G = 200 kg m^{-2} s^{-1} and at x=0.47.

4.5.1 Entrainment

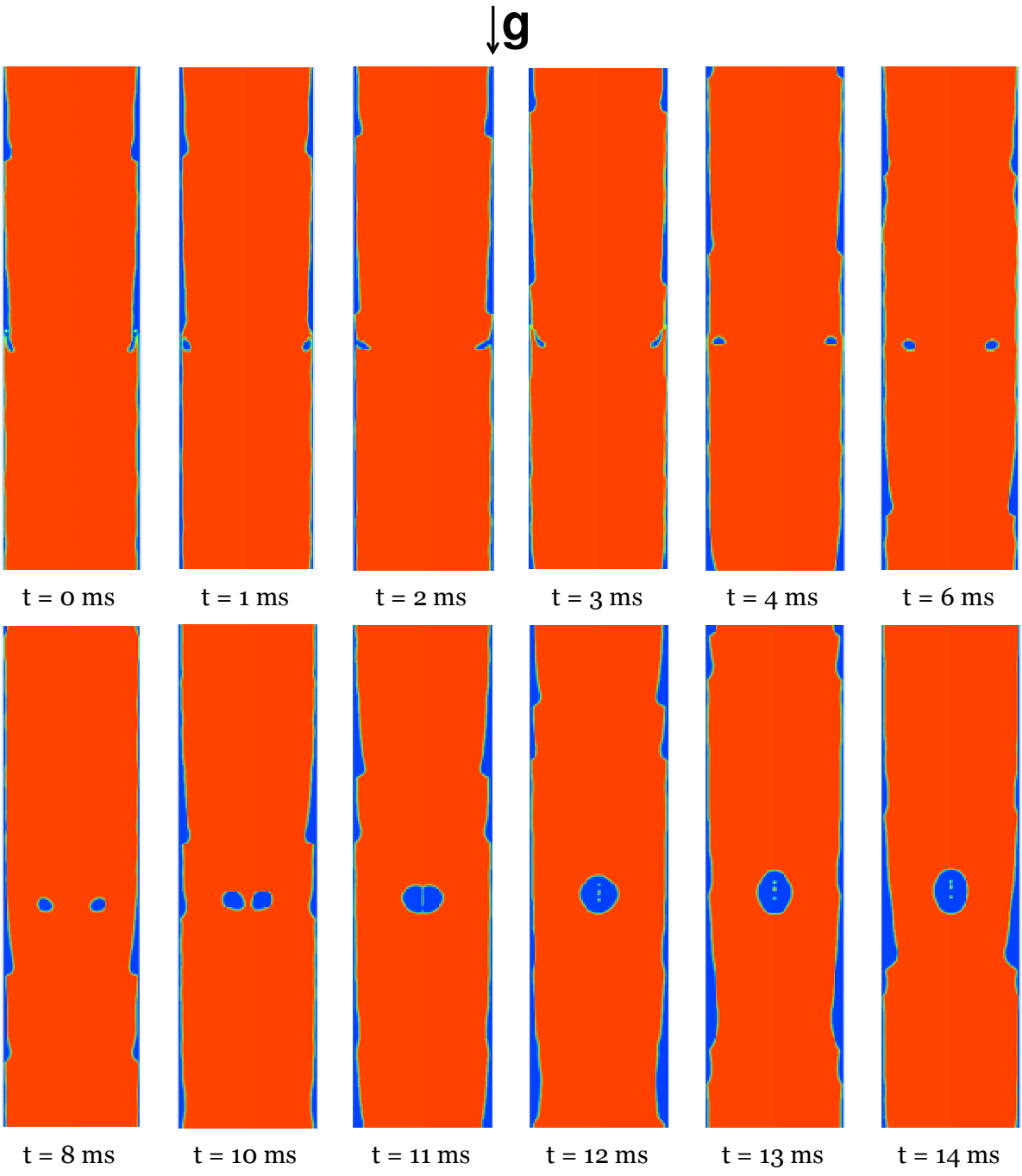

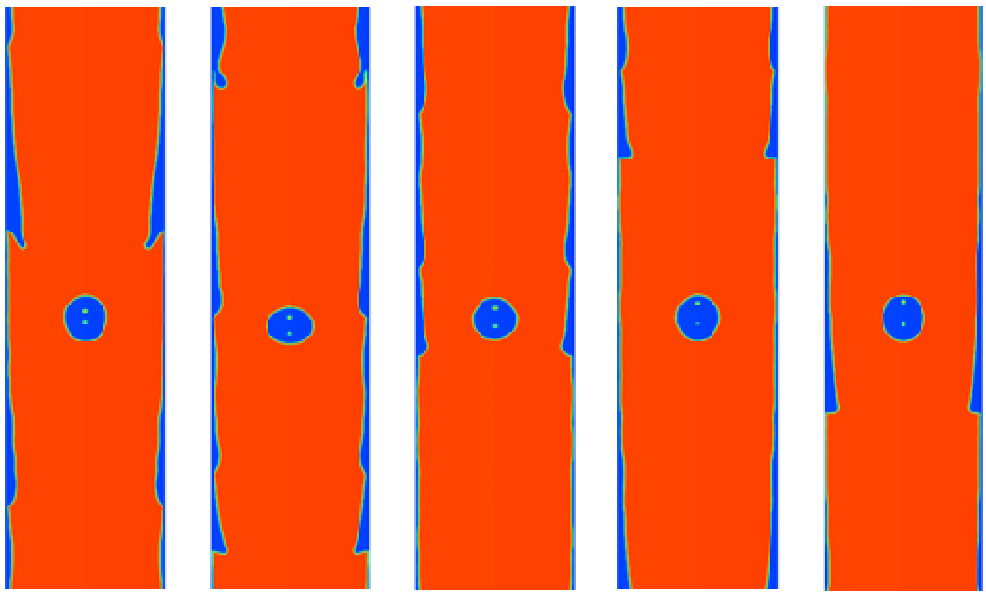

Figure 4.16: Entrainment at G = 200 kg m^{-2} s^{-1} along the cooled section.

As shown in Figure 4.16, the evolution of entrainment has been followed using a moving window as compared to the previous figures. At higher mass velocity the interfacial shear can rip some part of liquid film. As shown in Figure 4.16, this phenomena occurs in these phases:

- the vapour shear stress carry on the interfacial roughness and the wave formation at interface (t = 0-2 ms);
- if the vapour forces are enough high, the vapour transfers the shear to the liquid film at the wave crest promoting the stretch of wave towards the vapour core (t = 2-3 ms);
- the wave is stretched until some liquid is ripped (t = 3-4 ms) and the presence of liquid droplet inside vapour core can be detected;
- the vapour accelerates the liquid droplets towards the channel axis. This occurs through the stretching and the constriction of liquid droplet by action of vapour (t = 12-24 ms)

By experimental visualizations in Figure 4.7, it can be observed that the liquid droplet is about at the axis of channel and is stretched and constricted as predicted in numerical simulations. However, in experimental visualizations, the liquid droplet does not move perfectly along the axis having a slight non-axisymmetric moving, but this behaviour cannot be catched by numerical simulations due to the axisymmetric flow assumption.

4.5.2 Vapour bubbles inside the liquid film

In experimental visualizations the presence of bubbles has been detected. The phenomenon is more difficult to predict by numerical results because the size of bubble is similar to the

element size of the mesh. For this reason a finer mesh would be necessary to capture the vapour bubbles inside the liquid film.
An example of vapour bubble captured by numerical simulations (using a moving window as in Figure 4.16) and by experimental visualizations is shown in the figure Figure 4.17).
This phenomena occurs in similar way to the entrainment. The wave is stretched by vapour shear, but then the liquid at the crest is not ripped and, when the wave fall down, some vapour bubbles are trapped by the liquid film.

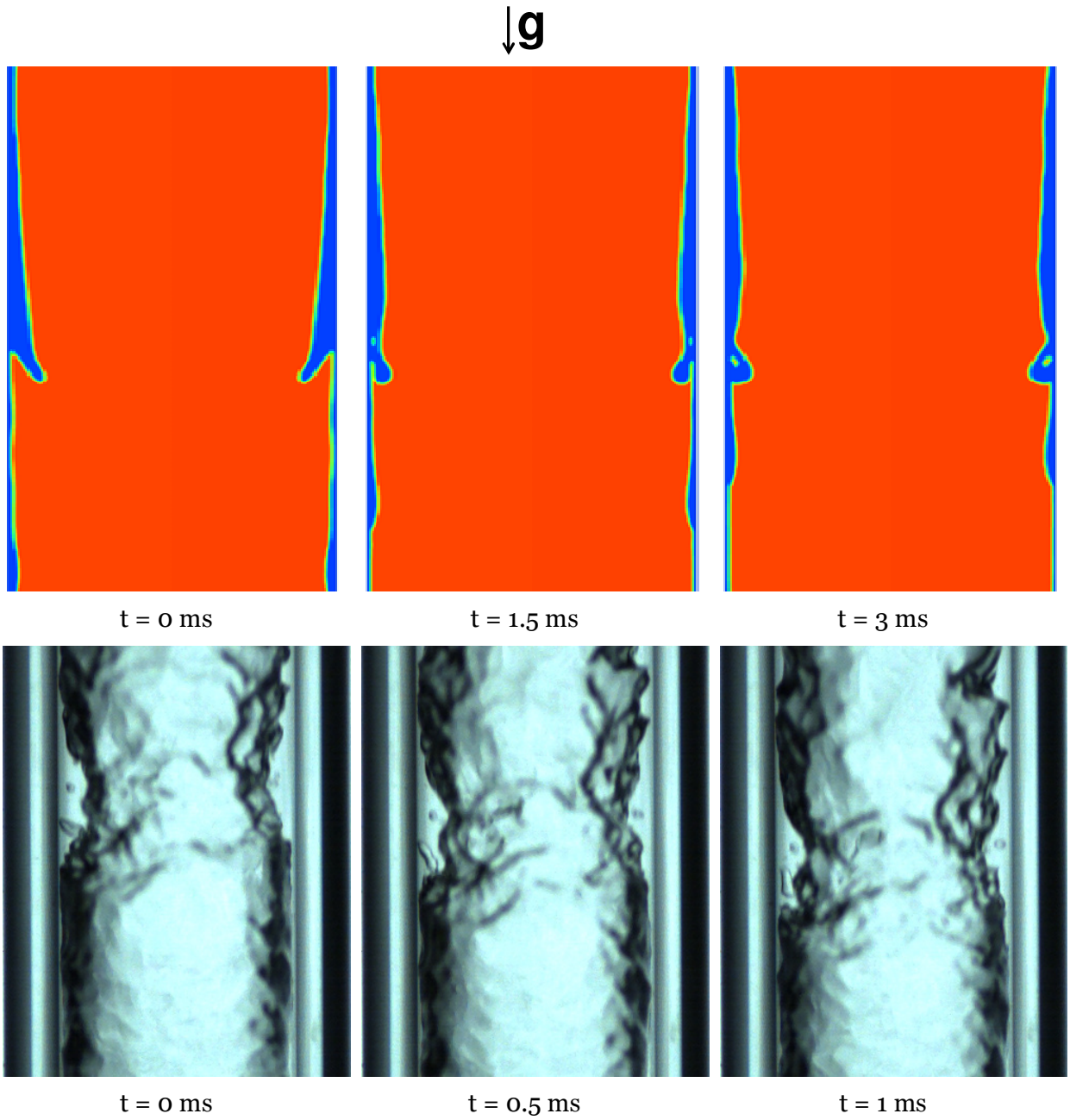

Figure 4.17: Evolution of vapour bubbles trapped inside the liquid film at G = 200 kg m^{-2} s^{-1}.

4.6 Influence of interfacial waves: steady-state vs unsteady-state simulations

From the previous sections the following aspects have been verified:

- the numerical simulations can catch the waves at vapour liquid interface detected in the experimental simulations;
- the features of waves is a function of vapour stress that is directly related to the mass velocity and the vapour qualities;
- when the mass velocity is increased, the entrainment and the presence of vapour bubbles in the liquid film are detected by experimental visualizations and numerical simulations;
- when the wave height increases the flow is similar as that when the fluid is forced to flow through an orifice;
- the interfacial roughness and the entrainment carry on a reduction of liquid film thickness and the vapour shear promotes the eddies formation inside the liquid film;

The same conclusions reported above could be obtained simply by unsteady-state simulations without heat transfer and phase change.

In fact the influence of vapour quality on two-phase flow could be performed varying the inlet boundary conditions using the velocity, turbulence and volume fraction profiles previously obtained by steady-state simulations. Besides these results on two-phase flow, the main goal of work is to verify the influence of unsteady-state phenomena on heat transfer. For this reason, the comparison between the unsteady-state and steady-state simulations is here proposed at G = 100 and G = 200 kg m^{-2} s^{-1}. It is worth noting that for all unsteady-state numerical simulations the SST k-ω approach has been applied. For comparison, a simulation has also been reported at G = 100 kg m^{-2} s^{-1} with the laminar liquid film approach.

The details of unsteady-state simulations of vertical downflow condensation inside 3.4 mm channel are listed in Table 4.1.

Table 4.1: Cases of unsteady-state numerical simulations of R134a condensation in 3.4 mm i.d. vertical circular channel at G < 200 kg m^{-2}s^{-1}

G [kg m^{-2} s^{-1}]	Approach	Length [mm]	Quality range
100	SST k-ω	136	0.7-0.44
200	SST k-ω	136	0.6-0.46

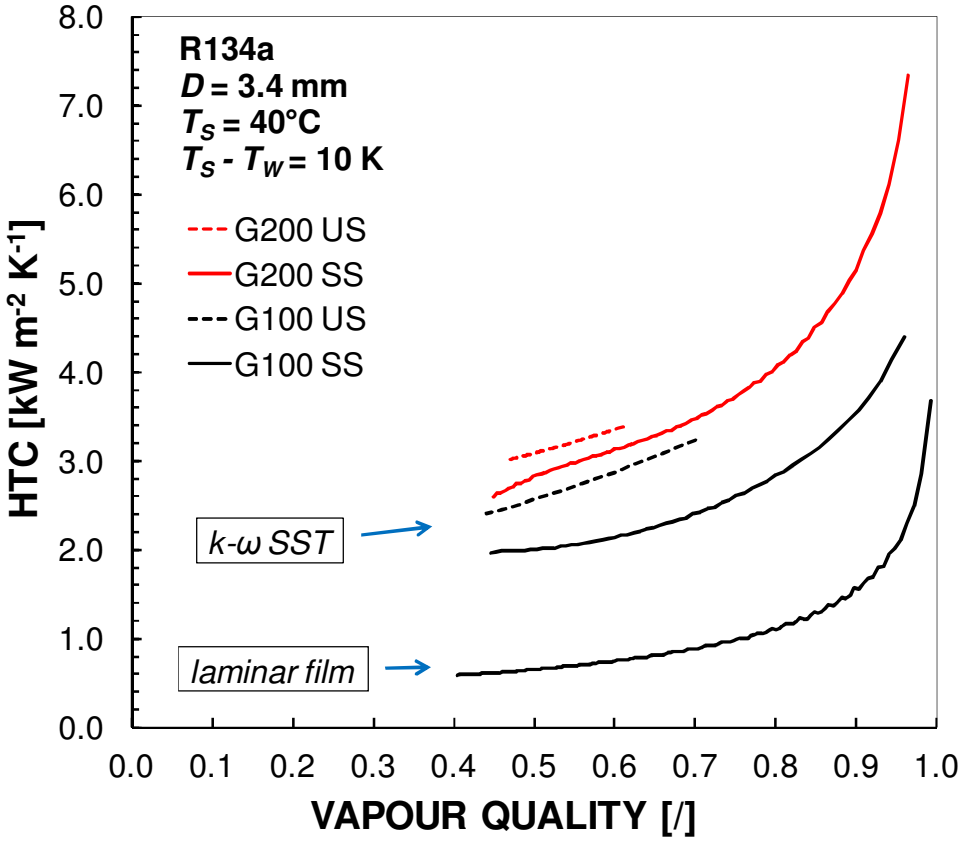

Figure 4.18: Heat transfer coefficient plotted vs vapor quality during vertical downflow condensation inside a 3.4 mm channel: comparison between unsteady-state (US) and steady-state (SS) numerical simulations at two mass velocities *G* [kg m^{-2} s^{-1}].

In the case of unsteady-state simulations, the results plotted in Figure 4.18 have been obtained evaluating, at a given position along the channel axis, the time averaged values of heat transfer coefficient and vapour quality. As shown in Figure 4.18, for all the mass velocities, a heat transfer coefficient enhancement is found when considering the transient simulations. In particular, such enhancement is more visible at G = 100 kg m^{-2} s^{-1} (+25%) whereas at G = 200 kg m^{-2} s^{-1} the heat transfer coefficient considering waves formation is about 8% higher with respect to the case of flat liquid film. Therefore, at increasing mass flux the turbulence inside the liquid film masks the effect of interfacial instabilities on condensation heat transfer.

As discussed in Section 4.4, the heat transfer coefficient augmentation is due to two distinct contributions: a lower average liquid film thickness and an intensification of the turbulence inside the liquid film. For example, in the case at G = 100 kg m^{-2} s^{-1}, the heat transfer coefficient considering only the liquid molecular thermal conductivity (and thus neglecting the contribution of the turbulent thermal conductivity to the heat transfer) is increased by about 40% with respect to the laminar steady-state case (without waves). Therefore the remaining part of the heat transfer coefficient enhancement (+245%) is due to a higher turbulence in the liquid film caused by waves.

NOMENCLATURE

Bo	[-]	$[(\rho_L - \rho_V)gD_h^2]/\sigma$
Bo_{cr}	[-]	$[\rho_L/(\rho_L - \rho_V)-\pi/4]^{-1}$
C	[-]	Courant number
Ca	[-]	Capillary number
D	[m]	Internal diameter
e_p	[%]	Percentage deviation, $e_p=100*(HTC_{CALC}- HTC_{EXP})/ HTC_{EXP}$
e_R	[%]	Average deviation, $e_R=(1/N_p)\sum e_p$
g	[m s^{-2}]	Acceleration due to gravity
G	[kg m^{-2}s^{-1}]	Mass flux
HTC	[W m^{-2}K^{-1}]	Cross-sectional average heat transfer coefficient
J_V	[-]	$xG/[gD_h\rho_V(\rho_L-\rho_V)]^{0.5}$
L	[m]	Channel length
N_p	[-]	Number of data points
p	[bar]	Pressure
q'	[W m^{-2}]	Heat flux
R	[m]	Channel radius
S	[kg m^{-3} s^{-1}]	Mass source due to phase change
T	[K]	Temperature
t	[s]	Time
u_τ	[m s^{-1}]	Friction velocity $(\tau_W/\rho_L)^{1/2}$
U_{VS}	[m s^{-1}]	xG/ρ_V
U_{LS}	[m s^{-1}]	$(1-x)G/\rho_L$
x	[-]	Vapour quality
X_{tt}	[-]	$(\mu_L/\mu_V)^{0.1}(\rho_V/\rho_L)^{0.5}[(1-x)/x]^{0.9}$
y	[m]	Y - coordinate

Greek characters

α	[-]	Volume fraction
α_t^+	[-]	Dimensionless turbulent eddy diffusivity for heat
δ	[m]	Condensate liquid thickness
δ^+	[-]	Dimensionless average liquid film thickness, $\delta u_\tau \rho_L/\mu_L$
θ	[°]	Angular coordinate
λ	[W m^{-1}K^{-1}]	Molecular thermal conductivity
μ	[Pa s]	Molecular dynamic viscosity
ν_t^+	[-]	Dimensionless turbulent eddy diffusivity for momentum

ρ	[kg m^{-3}]	Density
σ	[N m^{-1}]	Surface tension
σ_N	[%]	Standard deviation, $\sigma_N=\{[\sum(e_p-e_R)^2]/(N_p-1)\}^{0.5}$
τ_W	[Pa]	Wall shear stress

Subscripts

CALC	Calculated
EXP	Experimental
L	Liquid
S	Saturation
V	Vapour
W	Wall

PART II: THE APPLICATION OF MINICHANNEL TECHNOLOGY IN HEAT PUMPS

5 PHYSICAL MODEL OF WATER-TO-WATER AND AIR-TO-WATER HEAT PUMP

5.1 Introduction

Heat pumps are reverse cycle machines that move thermal energy opposite to the direction of spontaneous heat flow by transferring heat from a cold space (source) and releasing it to a warmer one (sink) using mechanical work at the compressor. In such systems, the refrigerant, referred as “primary fluid”, performs a thermodynamic cycle characterized by two pressure levels.

At the high pressure level, there is the condensation of refrigerant and the heat flow rate is rejected to a secondary fluid (usually air or water), with an increasing of the temperature of the secondary fluid. Instead, at the low pressure level, there is the evaporation of refrigerant and the heat flow rate is transferred from a secondary fluid to the refrigerant. The primary fluid passes from low to high pressure through the compressor and from high pressure to low pressure trough an expansion valve.

This description is the common operation of a heat pump that can be assume different configurations depending on the available sink/source, the amount and the trend of heating or cooling power demanded by user, the refrigerant used and what tasks must be satisfied by the same system.

The reversible dual source heat pump is a very innovative device to satisfy the heating and cooling demand. This system gives the possibility to exchange heat with air or water, performing as a air-to-water or water-to-water reversible heat pump, respectively. Furthermore, when the water is used as sink/source, the heat flow rate can be rejected or removed through borehole heat exchangers (BHEs) installed in the ground.

In the literature few works can be found and other research is needed to understand the operating features of this system in terms of seasonal performance, logical control and design.

Urchueguía et al. [61] presented an experimental comparison between a Ground Coupled Heat Pump (GCHP) and a conventional Air-to-Water Heat Pump (AWHP) during a full seasonal cycle (i.e. about 17-19 kW and 16 kW of nominal heating and cooling capacities). These reversible systems were linked, in parallel, to the same building with the same load and climatic conditions to have a good comparison between the two systems in terms of energy performance. In this investigation, on air side the conventional air heat exchanger are used and, on ground side, 6 borehole heat exchangers of 50 m depth were distributed in a rectangular configuration. The heat pump was optimized to use propane (R290) as refrigerant improving the efficiency in terms of capacity and Coefficient Of Performance (COP). The authors observed that the GCHP achieved an averaged efficiency improvement

of 73% and 60% as compared to AWHP in heating and cooling mode, respectively. Nevertheless, in this work the authors did not consider the possibility to use alternatively GCHP and AWHP to obtain higher performance as dual-source system.
Another example is reported by Pardo et al. [62] that analyze several reversible HVAC configurations to study the improvement of the efficiency combining a GCHP and an AWHP. Furthermore, solutions with the adoption of a thermal storage has been evaluated by authors to allow the decoupling energy generation from energy distribution, the size reduction of the heat pump and the mitigation of thermal load peaks effects on the system performance. The authors studied the performance of each configuration considering the thermal load of an office building in Mediterranean areas (i.e. nominal thermal load of about 45 kW). In this numerical study, when the hybrid solution was adopted, the GCHP supplied the thermal energy to the thermal load and, if this element had not enough capacity to supply the demanded thermal energy, the AWHP was switched on. Here, the authors considered the hybrid solution as the operation in series of the two heat pumps, switching on first the GCHP due to an higher COP than AWHP. About the AWHP, a conventional air heat exchanger was applied and about GCHP the vertical borehole heat exchangers of 100 m depth were used and connected in parallel. During the analysis the authors considered the total electrical energy consumption of each layout subdividing it in three components: the electrical energy of the heat pumps, the water pumps and the air fan. From the numerical results (i.e. during cooling season with a inlet water temperature of 7°C on user side) the authors observed an higher efficiency of 'GCHP+AWHP' (COP ≈ 3.2) configuration as compared to GCHP (COP ≈ 3.1) and AWHP (COP ≈ 2); furthermore, when the thermal storage was adopted, a reduction of the heat pump capacities and an higher performance were observed, making the hybrid heat pump with the thermal storage ('HC' configuration) the HVAC layout with the highest efficiency (COP ≈ 3.85). Finally, the authors did also an interesting investigation on cost assessment of each layout showing the AWHP as the cheapest one when only the installation costs were considered; but when the evolution of the cost was plotted, the best energy efficiency improves the cost performance along a longer period of time. For this reason the 'GCHP+AWHP' and 'HC' layout showed the best pay-back period (i.e. 20 and 16 years, respectively, if compared against the AWHP) and long term cost efficiency.
This second part of the present work has been devoted to the development of a physical model of a reversible dual source (water/air) heat pump, as shown in Figure 5.1.
A reversible GCHP and AWHP are coupled and linked in parallel to define the operation of a dual-source heat pump. In this way the advantages of these two different systems can be combined. As reported by brief review above, the GCHP performs better than AWHP during the seasonal cycle. The temperature of ground is almost constant during the operation and allows lower pressure ratio in the heat pump as compared to the AWHP which performance is affected by the strong variation of outdoor conditions. In fact, in the European Mediterranean region the outdoor air temperature can achieve values below 0°C during the winter and values above 35°C during the summer. At these operating conditions the pressure ratio of the thermodynamic cycle of refrigerant becomes higher and more

input electrical power is needed; furthermore, during the winter season, the external surface of air heat exchanger can be under 0°C carrying on the occurring of frost, the increase of local thermal resistance and some operating problems, such as the obstruction of cross section on air side. Accordingly this needs for defrost cycle causing the decrease of AWHP performance. On the other hand, the presence of AWHP in a dual-source heat pump allows the reduction of number of borehole heat exchangers decreasing the installation costs of a GCHP. If there is an imbalance between heating and cooling demand during the full seasonal cycle, the overcooling/overheating of ground (called as 'ground fouling', [63]) will occur decreasing the performance of a GCHP over time. So, the possibility of exchange heat with air would limit this phenomenon and also would allow higher efficiency of whole system than a GCHP during the intermediate season (for example, spring or autumn) according to conditions of air temperature. From these observations the dual source would achieved better pay back period due to higher performance as compared to an AWHP and a GCHP.

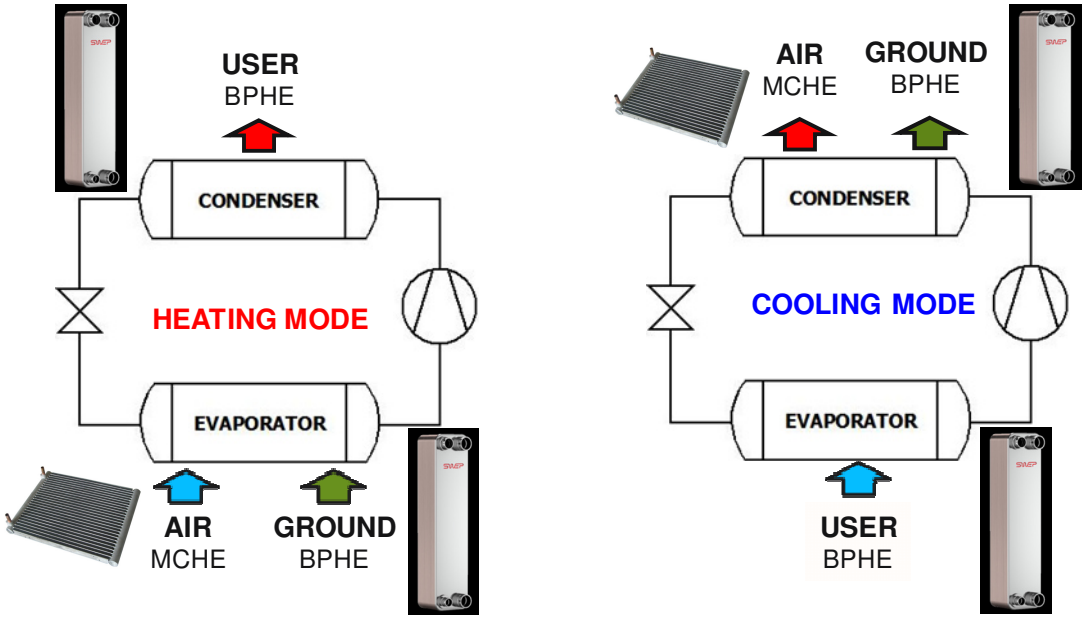

Figure 5.1: Design of a reversible dual source heat pump operating in heating (left) and cooling (right) mode.

Besides the innovative layout of this system, the technology of minichannel heat exchanger has been considered to obtain a significant reduction of refrigerant charge (Del Col et al., [64]) and of the device size. The reduction of refrigerant charge is very important for safety reasons when using natural refrigerants and for limitation of greenhouse gases emissions when using halogenated refrigerants. In addition, since the whole system can be used in the reversible way to satisfy the heating and cooling demand, a small amount of fluid means a more reactive system when varying the operating conditions.

For this reason, as depicted in Figure 5.1, on the air side, a MiniChannel Heat Exchanger (MCHE) has been considered as a possible solution to replace the fin-and-coil heat exchanger commonly used in this type of applications ([61], [62]). On the water side,

instead, brazed plate heat exchangers ($D_h \leq 3$ mm) are used as condenser/evaporator. Furthermore, the application of a compressor coupled with a variable speed electrical motor has been taken into account to adapt the heat flow rate given by the machine to the user demands and to achieved higher efficiency at partial heating/cooling load.
The physical model of the reversible dual-source heat pump presented in this part of thesis has been realized in Matlab/Simulink® environment and it is able also to simulate both stationary and transient conditions.
The model of the heat pump is called physical because the condenser and the evaporator of the system are discretized into several elements where correlations have been applied to evaluate the local heat transfer and the pressure drops. These correlations are available in the literature and can be applied with different types of refrigerant and geometry. In fact, the aim of the present work is to evaluate the heat pump performance, considering the effect of refrigerant properties (e.g. R134a, R290, R32), different configuration (single source or dual source) and sizing of components of the machine in relation to the heating demanded by the user.
Before showing the computational procedures of dual-source heat pump, the operation of overall system is described to define the choice of model inputs.
On the user side the refrigerant transfer heat with the water through a BPHE, whereas on the opposite side the refrigerant can transfer heat with air or water using, respectively, a MCHE or a BPHE. In particular, when the water is selected as source (heating mode) or as sink (cooling mode), this secondary fluid flows through vertical borehole heat exchangers allowing the heat transfer with the ground. During the heating mode, at low pressure level, the refrigerant evaporates removing heat from air or from ground and then condenses rejected it on the user side at high pressure level. The pressure gap is strictly related to the level temperature of sink and source and the global heat transfer coefficient between the refrigerant and the secondary fluids. Then the refrigerant closes the cycle through an expansion valve simulated as an isenthalpic process. During the cooling mode, instead, the heat is removed from the user side and it is rejected to air or ground. During the seasonal cycle, the heating or cooling demand varies and the frequency of inverter coupled with the compressor can be adjusted to satisfy the partial load.
On the user side, the mass flow rate and the inlet water temperature can be chosen at varying of desired level and glide temperature. On air side, the face velocity can be selected and the inlet thermodynamic values of air will be function of outdoor climatic conditions. When the heat transfer with ground is taken into account, the mass flow rate of the secondary fluid (water or brine water) can be chosen and its temperature is calculated by the model evaluating the balance of the heat flow rate at the evaporator/condenser and that at the ground. If the numerical analysis is limited to the heat transfer with water, neglecting the presence of ground, then the inlet water temperature becomes a new input of model (as compared to the undisturbed temperature of the ground). Besides the input reported above, the geometries and the materials of each heat exchanger (BPHE, MCHE, BHE), the type of refrigerant (R134a, R290, R32..), the subcooling at condenser, the superheating at evaporator and the thermodynamic properties of ground can be defined. It is worth noting

that the type and the performance of compressor is taken into account using the compressor maps declared by manufacturer selection software (e.g. Bitzer, Dorin, Danfoss, Copeland..), so if different refrigerant is used then a different compressor must be selected. In particular, the size of compressor set the nominal heating and cooling capacities of the dual-source heat pump and after the other components of the system must be properly sized. From this brief description of dual-source heat pump, in the following table the input and output of the physical model are summarized.

Table 5.1: Input and output of dual-source heat pump model.

	INPUT	OUTPUT
USER WATER	Mass flow rate Inlet temperature	Heat transfer coefficient Pressure drops Outlet conditions
REFRIGERANT	Subcooling Superheating	Heat transfer coefficient Pressure drops Cooling/Heating capacity Saturation temperatures
AIR	Face velocity Inlet temperature Inlet specific humidity	Heat transfer coefficient Pressure drops Outlet conditions
GROUND WATER	Pure water or brine concentration Mass flow rate	Heat transfer coefficient Pressure drops Local temperatures
GROUND	Thermal properties Undisturbed ground temperature	Local temperatures
COMPRESSOR	Frequency Compressor maps Swept Volume	Isentropic Efficiency Volumetric Efficiency Power consumption Refrigerant mass flow rate
BPHE, MCHE, BHE	Geometry	

The dual source model can be divided in three macro-parts due to the two available configurations, i.e. Air-Water Heat Pump (AWHP) and Water-to-Water Heat Pump (WWHP), taking into account the possibility of transferring heat with the ground (i.e. Ground Coupled Heat Pump, GCHP).

In this chapter 5 the two first macro-parts of the system are modeled. In particular, the computational procedure used to describe the behaviour of each component (BPHE evaporator/condenser, MCHE and compressor) of the reversible heat pump is presented in detail (geometric parameters, flow chart, input/output and predicting correlations used to

evaluate HTC and pressure drops). Then, the physical models of each component are put together to simulate the performance of water-to-water and air-to-water heat pump.
In the last chapter 6, instead, the numerical analysis of transferring heat with the ground is discussed and the physical model of vertical borehole heat exchangers and of GCHP are reported. Finally, from the GCHP and AWHP models it has been possible to define the best control of the dual-source heat pump, deciding the best source to use at different operating conditions.

5.2 Introduction to the model of heat exchangers and compressor for AWHP and WWHP

5.2.1 Brazed plate heat exchanger geometry (BPHE)

The BPHEs are widely used in several applications, such as heating/cooling system, food processing and chemical industry. This type of heat exchanger is composed by thin, rectangular and corrugated steel plates that are stacked together. The distance between the plates creates the passages where the hot and cold fluid streams, as depicted in Figure 5.2.

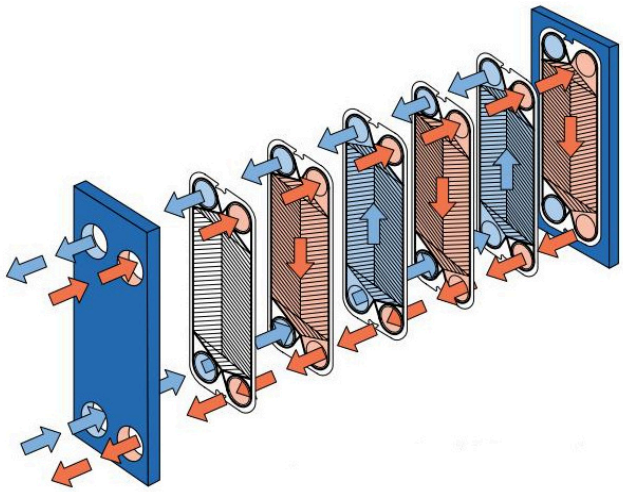

Figure 5.2: The hot and cold fluid streams in a BPHE.

The distance between two parallel plates can vary depending on the mass flow rate of fluids and the maximum pressure drops allowed. The plates are corrugated providing a larger heat transfer area-per-unit-volume and a higher heat transfer coefficient strictly linked to smaller flow cross section, flow disruption and the generation of secondary flows (e.g. swirl, vortex and helical flow). For these features the BPHEs are compact allowing a reduction of refrigerant charge and are flexible to modify the total heat transfer area by adding/removing the plates.
As shown in the literature, the two-phase flow inside a BPHE is affected by complex features encouraged by the corrugation and the inter-plate passages that make a real challenge the evaluation of the local heat transfer coefficients and of the frictional pressure drop at varying of operating parameters (e.g. mass flux, vapour quality, heat flux, flow regime and plate surface structure) during condensation and evaporation process. For this

reason, in most of the experimental works found in the literature, the empirical correlations for heat transfer coefficients and frictional pressure drops are strictly limited to specified operating range, fluids or plate geometry. Before presenting the computational procedure of BPHE as condenser and evaporator, the main geometrical parameters, that are the input of the physical model and that can influence the thermo-hydraulic performance of BPHE, are here reported.

The angle between the corrugation and the vertical axis is called in the literature chevron angle β, as depicted in Figure 5.3. Instead, in many works, the inclination angle (that is complementary to the chevron angle) is used. The plates of the heat exchanger can be stamped with low or high chevron angle and, during their stacking, plates with different chevron angles can be arranged together in either a symmetric or mixed way. A plate with a higher chevron angle promotes higher thermal performance and higher pressure drops as compared to that with lower corrugation angle.

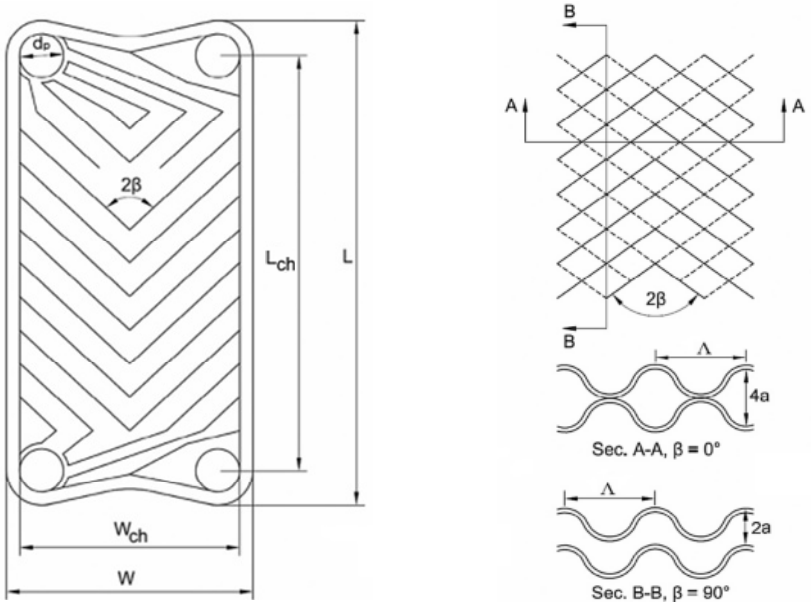

Figure 5.3: Corrugation features of chevron plates.

The severity of sinusoidal surface waviness can be essentially described by two dimensionless parameters: the plate corrugation aspect ratio γ and the enlargement factor, φ:

$$\gamma = \frac{4a}{\Lambda} \qquad \textbf{5.1}$$

$$\varphi \approx \frac{1}{6}\left(1+\sqrt{1+A^2}+4\sqrt{1+\frac{A^2}{2}}\right) \qquad \textbf{5.2}$$

where a and Λ are the respective amplitude (depth of corrugation) and wavelength (pitch) of a sinusoidal surface corrugation. The enlargement factor can be approximated for a

sinusoidal corrugation from a three-point integration formula, using the dimensionless corrugation parameter A:

$$A = \frac{2\pi a}{\Lambda} \qquad \textbf{5.3}$$

Considering the effective length L_{ch} and width W_{ch} of a plate and the enlargement factor φ, the definition of effective hydraulic diameter can be applied:

$$D_h = \frac{4 \cdot W_{ch} \cdot L_{ch} \cdot b}{\left(2 \cdot W_{ch} \cdot L_{ch} \cdot \varphi\right)} = \frac{2 \cdot b}{\varphi} \qquad \textbf{5.4}$$

In a BPHE, the total number of plates N_p is the sum of the total effective plates N_{eff} and two plates (at the ends of HE) that close the circuitry of BPHE and do not take part to the heat transfer between the two streams:

$$N_{eff} = N_p - 2 \qquad \textbf{5.5}$$

From the total effective plates and the enlargement factor φ (ratio between the effective heat transfer area and the plate projected area), it is possible to obtain the total heat transfer area A_{tot}:

$$A_{tot} = N_{eff} W_{ch} L_{ch} \varphi = N_{eff} A_{eff,1p} \qquad \textbf{5.6}$$

Given the total number of plates and considering the flowing of water through the channels at the ends of BPHE, the number of channels on water and refrigerant side can be obtained. In addition, the occurring of mal-distribution on the BPHE performance has not been investigated.

5.2.2 Computational procedure for BPHE evaporator

In this section and in the following one (5.2.3) the predicting correlation to evaluate the frictional pressure gradient and the local heat transfer along the evaporation and condensation are presented. Besides the correlations applied in the physical model of BPHE, different correlations have been however reported to show the discrepancies in predicting the heat transfer and pressure drop. As reported by Amalfi et al. [65,66], most research work until now has only resulted in prediction methods of limited application, instead of refined general correlations for predicting the local heat transfer coefficients and pressure drops. The reason for this is probably due to the fact that the heat transfer process is very complex and geometry dependent, and because typically only in-house data are used rather than larger data sets independently measured data. Heat transfer mechanisms in

BPHEs are in fact a complex function of the flow regime, geometry of the system, properties of the fluids, heat flux and many other parameters. Finally in this and the following section the computational procedure adopted for the BPHE as evaporator/condenser is discussed in detail, showing also inputs, outputs and the flow chart of the heat exchanger model.
Before showing the model of the BPHE, the evaporation heat transfer coefficients (Kim et al.[67], Huang et al.[68], Hsieh and Lin [69,70], Danilova et al. [71], Donowski and Kandlikar, Han et al. [72], Longo et al.[73,74], Amalfi et al. [65,66]) and the frictional pressure drop (Hsieh and Lin [69,70], Amalfi et al. [65,66], Huang et al.[68], Han et al. [72], Ayub [75]) obtained from different correlations available in the literature are presented. The correlations have been applied at the operating condition reported in the Figure 5.4-Figure 5.5.

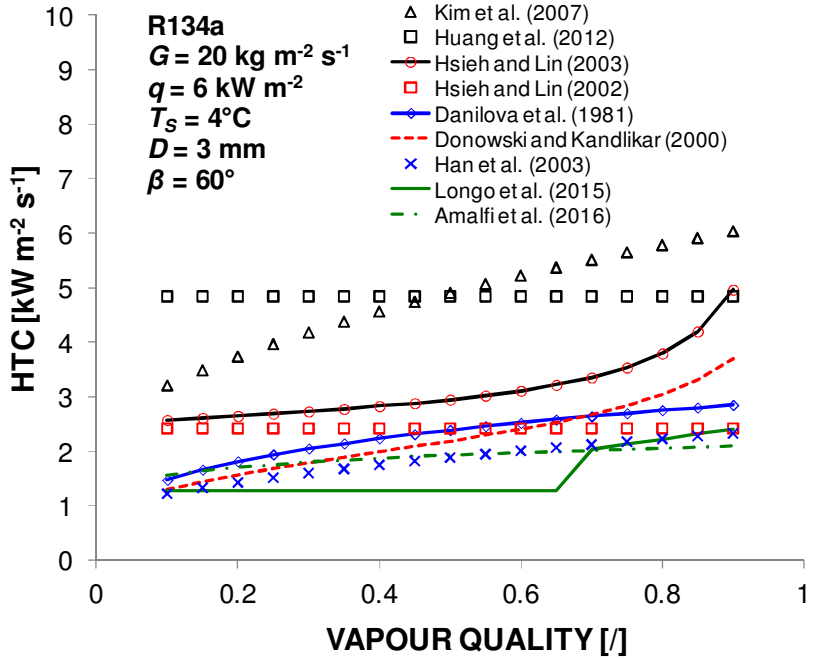

Figure 5.4: Predicted evaporation heat transfer coefficient for R134a versus vapour quality inside a BPHE.

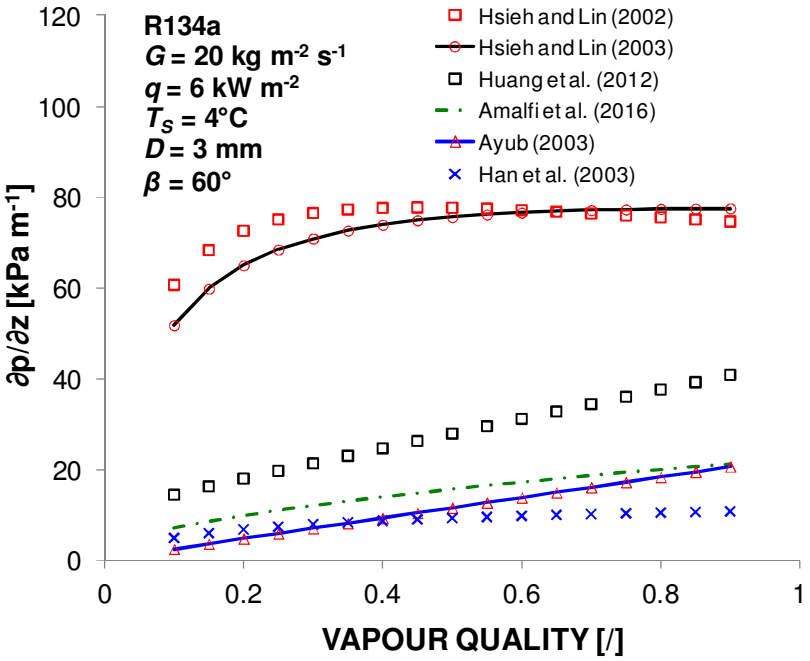

Figure 5.5: Predicted evaporation frictional pressure gradient for R134a versus vapour quality.

Similar discrepancies in the predicting the local heat transfer coefficient and frictional pressure gradient are shown by Amalfi et al. [65,66] and Eldeeb et al. [76] according to the correlation used. In particular for evaporation, as reported by Amalfi [65,66], this can be meanly due to different aspects as:

- Most prediction methods are based only their own specific experimental data, without inclusion of independent data, and most are simple reformulations of in-tube prediction methods.
- The large discrepancy of the data sets due to different data reduction procedures and larger experimental uncertainty for some operating conditions, such as at low mass flux region where the dependency of different parameters is more pronounced;
- There are not transition criteria available to establish the type of evaporation process (i.e. nucleate or flow boiling) and the presence of different flow pattern is not taken into account;
- In most experimental works the influence of different parameters (fluid, mass flux, vapour quality, heat flux...) on evaporation process is not separately investigated to understand and highlight the contribution of single parameter at different operating conditions.

From these considerations, the Amalfi et al. [65,66] model has been considered in the evaporator model to predict the local heat transfer coefficient and the frictional pressure gradient. The authors performed a detail comparison of several prediction methods to a broad database and finally proposed a new prediction method for flow boiling within plate heat exchanger basing on the dimensional analysis and the multiple regression technique. Furthermore, Amalfi et al. [65,66] model considers the effect of chevron angle and

hydraulic diameter size developing a criteria transition based on the Bond number to separate the macro- and micro-scale feature[77]s.
With regard to the evaluation of local heat transfer and frictional pressure drop for the single-phase flow, the well-known equations of Martin [77][78] have been applied.
Besides the frictional pressure drop, the total pressure drop Δp_{tot} in two-phase flow consists of several components:

$$\Delta p_{tot} = \Delta p_g + \Delta p_{acc} + \Delta p_{fr} + \Delta p_p \qquad \textbf{5.7}$$

The elevation (Δp_g)and acceleration (Δp_{acc}) pressure losses may be evaluated theoretically by the homogeneous model:

$$\Delta p_g = \rho_m \cdot g \cdot L_{ch} \qquad \textbf{5.8}$$

$$\Delta p_{acc} = G^2 \cdot \Delta x \cdot \left(\frac{1}{\rho_v} - \frac{1}{\rho_l} \right) \qquad \textbf{5.9}$$

The pressure drops across the evaporator inlet and outlet ports and manifolds are usually evaluated with the Shah and Focke [78] correlation:

$$\Delta p_p = 0.75 \cdot N_{pass} \cdot \left[\left(\frac{G^2}{2 \cdot \rho} \right)_{in} + \left(\frac{G^2}{2 \cdot \rho} \right)_{out} \right] \qquad \textbf{5.10}$$

with ρ_{in} and ρ_{out} that are referred to the state of the refrigerant at the inlet and outlet ports and with the number of passages N_{pass} in the BPHE circuitry. It is worth noting that in the physical model of the BPHE evaporator/condenser a single passage has been considered and that this component of the total pressure drop has been verified to be very low, so it has been neglected. The frictional pressure drop are evaluated with the following equation:

$$\Delta p_{fr} = 2 \cdot f \cdot \frac{L_{ch} \cdot G^2}{D_h \cdot \rho_m} \qquad \textbf{5.11}$$

where f is the Fanning friction factor and is obtained by the aforementioned empirical correlations found in the literature for the two-phase flow. In the equation reported above the two-phase mean density ρ_m is calculated by the homogeneous model:

$$\rho_m = \left[x_m / \rho_v + (1 - x_m) / \rho_l \right]^{-1} \qquad \textbf{5.12}$$

It is worth noting that the same components of total pressure drops can be calculated also for the single phase flow only if the Fanning friction factor is evaluated with a correlation for single phase flow and the density is that of vapour or liquid.
In the Table 5.2, the input and output of the BPHE evaporator model are listed.

Table 5.2: Input and output of BPHE evaporator model.

	INPUT	OUTPUT
WATER	Mass flow rate Inlet temperature	Heat transfer coefficient Pressure drops Outlet conditions
REFRIGERANT	Mass flow rate Condensation temperature Subcooling Superheating Isentropic efficiency	Heat transfer coefficient Pressure drops Evaporation temperature Cooling capacity
BPHE	Geometry	Evaporation length Dryout length Superheating length

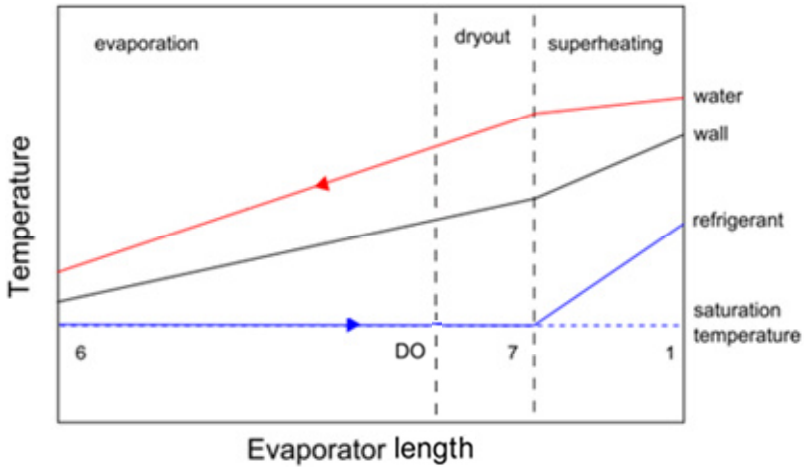

Figure 5.6: Refrigerant, wall and water temperature profile plotted along the evaporator length.

As depicted in Figure 5.6, the heat exchanger is divided into three sections: evaporation region (6-DO), dryout zone (DO-7) and superheating zone (7-1). In each of these parts, calculations are performed to evaluate the heat flow rate, pressure drop, logarithmic mean temperature difference, local temperatures and pressures on refrigerant and water/brine side.
As shown in the flow chart reported in Figure 5.7, the program starts with the reading of the input data and it assumes a guess value of the outlet saturation temperature. The guess value is properly selected to avoid a possible cross between the temperature profiles of refrigerant and water. From the input data (condensation saturation temperature and subcooling), the enthalpy can be calculated at the inlet of the evaporator (point 6, Figure

5.6). The pressure at point 6 can be evaluated from the guessed saturation temperature. At this point, the main iterative cycle can start and the check of the calculated length against the available is performed at each iteration. At first, the total flow rate at the evaporator and all the variables on the water side are calculated (i.e. outlet water temperature, heat transfer coefficient and pressure drops).
On the refrigerant side, instead, the following procedure is performed for the evaporation and the dryout region:

- each region is divided in elements to improve the accuracy of the calculated temperature profile. This aspect is very important because the local heat transfer coefficient varies along the evaporator primarily when the dryout process occurs;
- guess value of length and heat flow rate for each region and element is defined;
- the vapour quality at the inlet of each region is calculated (evaporation zone) or fixed (dryout and superheating zone). In this way the vapour quality at the ends of evaporation and dryout region are defined. The variation of vapour quality along these regions is divided by the number of elements of each region and, thus, the inlet/outlet vapour quality of each element is determined via incremental.
- The thermodynamic properties, the outlet temperature, the local heat transfer and pressure drop on refrigerant side are calculated in the element;
- Knowing the inlet and outlet condition of refrigerant, the heat flow rate is updated and the outlet water temperature is obtained;
- From these information it is possible to calculate the global heat transfer coefficient, the logarithmic mean temperature difference and so the updated value of element length can be found. This value is then set at the beginning of cycle until the deviation between the updated and the old value is enough low; then, the outlet conditions of each element are set equal to those at the inlet of the following element. Finally, when the length of all elements are obtained then the length of the region is updated and set at the beginning of cycle and the same check reported above is performed for the region length.

Regarding the superheating region a similar procedure is cited above, but in this case it is applied for only one element.
When the iterative cycle of each region is closed, the sum of length of all regions is compared with the effective length of the evaporator L_{ch} and the following equation is applied:

$$L_{mod} = \frac{L_{evap} + L_{dryout} + L_{sup}}{L_{ch}} \qquad \textbf{5.13}$$

From L_{mod} the saturation temperature at the outlet of evaporator is updated as follows:

$$T_{EVAP\_new} = T_{m,w} + \left(T_{EVAP\_old} - T_{m,w}\right) \cdot L_{mod} \qquad \textbf{5.14}$$

where $T_{m,w}$ is the mean water temperature and T_{EVAP_old} and T_{EVAP_new} are, respectively, the previous and updated evaporation saturation temperature. In Eq. 5.13, if the L_{mod} is lower than one, it means that the evaluated heat flow rate is higher than the effective one and, so, the saturation temperature must be increased. Otherwise the saturation temperature must be decreased. To avoid convergence issues and the possible cross of the water and refrigerant temperature profiles, the updating of saturation temperature is performed through a damping factor $gain_E$. After the updating of outlet saturation temperature, the pressure at the inlet of evaporator is updated (point 6), considering the outlet saturation pressure and the total pressure drop previously calculated. Then, the main iterative cycle restarts and goes on until the check between the calculated and effective evaporator length is verified.

It should be mentioned that the dryout vapor quality is fixed at 0.95. In fact, as reported by Amalfi et al. [65], even if the dryout is reached before reaching complete evaporation, typically this aspect can be ignored. In particular, in the dryout zone a linear interpolation has been applied from the heat transfer coefficient obtained in saturated condition at x = 0.95 and the one that pertains to single phase condition (i.e. superheating):

$$h_x = h_{x=x_{DO}} \cdot \frac{x_m - x_7}{x_{DO} - x_7} + h_{x=1} \cdot \frac{x_m - x_{DO}}{x_7 - x_{DO}} \qquad \textbf{5.15}$$

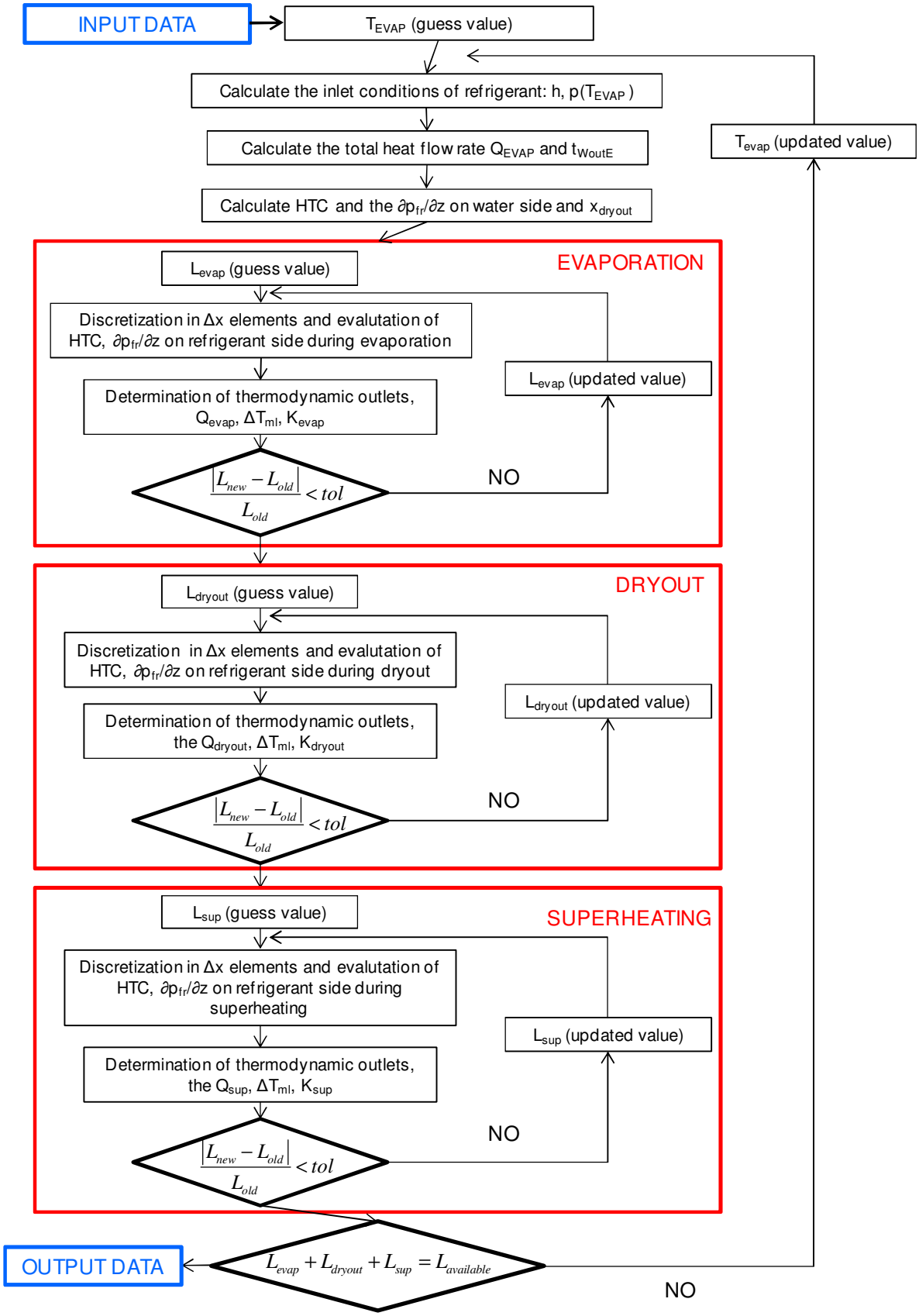

Figure 5.7: Flow chart of the BPHE evaporator model.

5.2.3 Computational procedure for BPHE condenser

Before showing the BPHE condenser model, the most-know correlations, found in the literature, have been considered in Figure 5.8 - Figure 5.9 to evaluate the condensation heat transfer coefficient (Yan et al. [79], Mancin et al. [80,81], Longo et al. [73,74], Kuo et al. [82], Han et al.[72] and Shah [83]) and the frictional pressure gradient (Kuo et al. [82] and Amalfi et al. [65,66]) at the operating conditions specified on the figures. It is worth noting that there is not a correlation obtained by dimensional and multiple regression analysis using a wide range of data points as compared to the evaporator case. In addition, in the literature there are fewer correlations developed for heat transfer and pressure drops for condensation than for evaporation in PHEs, as reported by Eldeeb et al. [76]. The local heat transfer and frictional pressure drop during the condensation process can be affect by various parameters, such as vapour quality, mass flux, heat flux, superheating, fluid and geometrical BPHE features. From these observations:

- the correlations found in the literature are applicable to limited operating conditions and to particular BPHE geometries;
- more research of condensation process inside BPHE is necessary and a good-prediction of condensation heat transfer can be more difficult as compared to the evaporation process.

However, Longo et al. [73,74] performed several experimental tests on condensation of various refrigerants (R134a, R410A, isobutane, propane, propene, R236fa, R1234yf, R22, R32, R744) inside a small BPHE with herringbone plates and a corrugation angle of 65° at varying mass flux and heat flux. The authors used this large set of data points from their own work to develop two correlations representing gravity-controlled condensation for equivalent Reynolds numbers below 1600 and forced convection condensation for equivalent Reynolds number higher than 1600. Nevertheless their heat transfer correlation did not consider the possible effect of BPHE geometrical features on condensation(enlargement factor, chevron angle, height and pitch of corrugation…), the authors compared their model to 516 experimental data points obtained by different research groups reporting a mean absolute percentage deviation lower than 16%.

Mancin et al. [80,81] investigated the partial condensation of R32, R410A and R407C inside different BPHE geometries varying the mass flux, the vapour quality, the saturation-to-wall temperature difference and the inlet vapour superheating. The authors also developed a model to evaluate the condensation heat transfer considering the influence of mass velocity, vapour quality, saturation-to-wall temperature difference and fluid properties. Here, the condensation heat transfer coefficient is calculated considering the gravity and shear dominated condensation. When the condensation was driven by gravity then the heat transfer was calculated by the Nusselt theory [84]; when the condensation was controlled by vapour shear stress, instead, the heat transfer was calculated as suggest by Cavallini et al. [1]. To combine the two contributions the transitions for condensation were based on the dimensionless gas velocity as suggested by Shah [10] and Cavallini et al. [1][10]. Mancin et al. [80,81] compared their model against their experimental

condensation data of R32, R410A, R407 and other data on R744 with an absolute deviations lower than 7%.

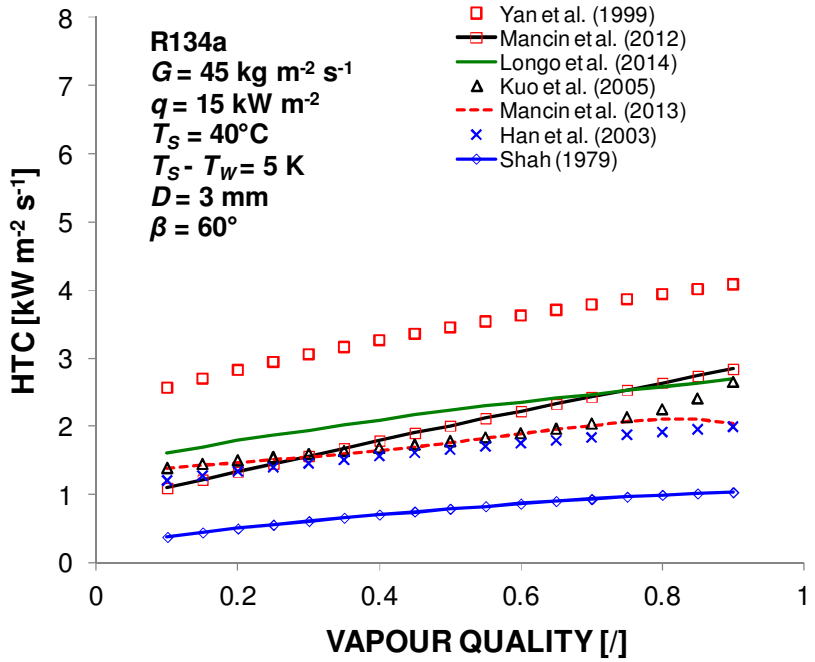

Figure 5.8: Predicted condensation heat transfer coefficient for R134a versus vapour quality inside a BPHE.

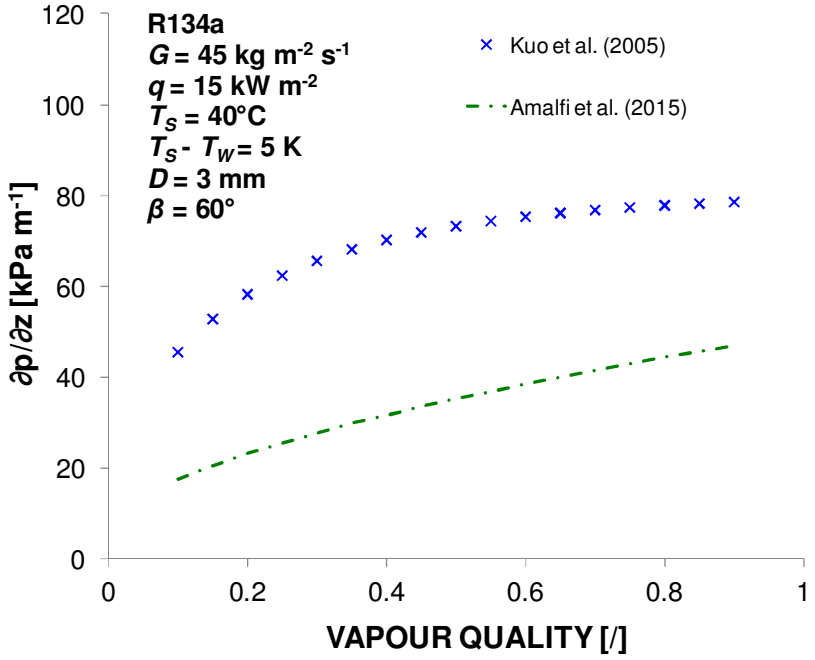

Figure 5.9: Predicted condensation frictional pressure gradient for R134a versus vapour quality.

Since Mancin et al. [80,81] and Longo et al. [73,74] developed their correlations using a relatively large set of data points, these correlations have been selected to evaluate the local heat transfer coefficient during the condensation of saturated vapour.
Regarding the frictional pressure drop, instead, the works found in the scientific literature rarely distinguish the total pressure drops into the different components, such as frictional, gravity and acceleration pressure drops. In general, there are very few experimental works performed in adiabatic conditions to develop a model for the frictional pressure drop evaluation. Since the Amalfi et al. [65,66] proposed a new prediction method for the frictional pressure drop not only during flow boiling, but also during two-phase flow in adiabatic condition, their method has been applied in the condenser model.
In the Table 5.3, the input and output of the BPHE evaporator model are listed.

Table 5.3: Input and output of BPHE condenser model.

	INPUT	OUTPUT
WATER	Mass flow rate Inlet temperature	Heat transfer coefficient Pressure drops Outlet conditions
REFRIGERANT	Mass flow rate Evaporation temperature Subcooling Superheating Isentropic efficiency	Heat transfer coefficient Pressure drops Condensation temperature Heating capacity
BPHE	Geometry	Desuperheating length Sup. vap.condensation length Sat. vap.condensation length Subcooling length

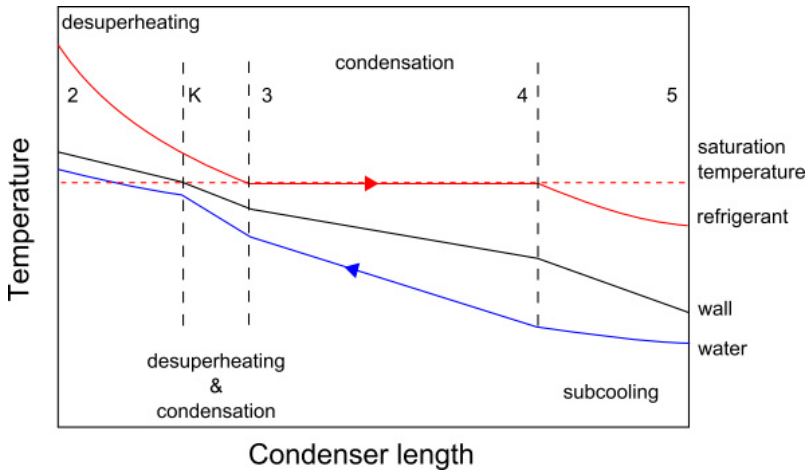

Figure 5.10: Refrigerant, wall and water temperature profile along the condenser length.

As depicted in Figure 5.10, the heat exchanger is divided into four sections: desuperheating (2-K), condensation of superheated vapour (K-3), condensation of saturated vapour (3-4)

and subcooling (4-5). In each of these parts, calculations are performed to evaluate the heat flow rate, pressure drop, logarithmic mean temperature difference, local temperatures and pressures on refrigerant and water/brine side.
As shown in the flow chart reported in Figure 5.11, the program starts with the reading of the input data and it assumes a guess value of the inlet saturation temperature. From the input data (evaporation saturation temperature, superheating and isentropic efficiency), the enthalpy can be calculated at the inlet of the condenser (point 2, Figure 5.10). The pressure at point 2 can be evaluated from the guessed saturation temperature.
The algorithm of program is similar the one adopted for the evaporator model. At the beginning of the main iterative cycle the comparison between the wall and the saturation temperature has been considered to understand if the condensation occurs at the inlet or if there is a desuperheating without condensation and only sensible heat transfer is exchanged between the refrigerant and the wall. This phenomenon usually occurs if the discharge gas temperature at the outlet of compressor is high (e.g. for R32 the vapour temperatures at the inlet of condenser can achieved values until 100°C as compared that for R134a).
The length of desuperheating has been calculated with an iterative method to match the wall temperature with the saturation temperature at the end of this heat transfer region.
About the condensation of superheated vapour, the correlation of Webb [85] has been applied to combine, at the same time, the sensible heat flow rate due to the superheated vapour core and the latent heat flow rate due to the condensation at the wall:

$$q'_{sup} = q'_{sens} + q'_{lat} \qquad \textbf{5.16}$$

$$h_{sup} \cdot (T_{SAT} - T_{wall}) = h_{fc} \cdot (T_{bulk} - T_{SAT}) + h_{SAT} \cdot (T_{SAT} - T_{wall}) \qquad \textbf{5.17}$$

with the temperature of vapour core T_{bulk}, the saturation temperature T_{SAT}, the wall temperature T_{wall}, the sensible (h_{fc}) heat transfer coefficient and the latent one (h_{SAT}). The h_{fc} has been calculated with Martin [77] and the saturated condensation heat transfer coefficient h_{SAT} could be calculated with Longo [73,74] or Mancin [80,81].
From Eq.5.17 it is possible to define the effective heat transfer coefficient referred to saturation-to-wall temperature difference:

$$h_{sup} = h_{fc}F + h_{SAT} \qquad \textbf{5.18}$$

$$F = \frac{T_{bulk} - T_{SAT}}{T_{SAT} - T_{wall}} = \frac{\Delta T_{surr}}{T_{SAT} - T_{wall}} \qquad \textbf{5.19}$$

with F physically defined as the degrees of superheat ΔT_{surr} divided by the condensing temperature difference for saturated vapour (T_{SAT} - T_{wall}). The F-factor asymptotically approaches zero as the superheat is depleted (i.e. condensation of saturated vapour).

The Eq. 5.17 does not consider the mass transfer effect at vapour-liquid interface. In fact the movement of the condensing vapour to the condensing surface will also result in bulk convection of superheated vapour, which will aid in cooling of the superheated vapour. This component is function of the mass flux condensation and the latent heat of the condensing vapour:

$$h_{fc}^{*} = h_{fc} + c_{p,v} \cdot \frac{q'_{lat}}{\gamma} \qquad \textbf{5.20}$$

The Eq.5.18 becomes:

$$h_{sup} = F\left(h_{fc} + c_{p,v} \cdot \frac{q'_{lat}}{\gamma} \right) + h_{SAT} \qquad \textbf{5.21}$$

Finally, the heat transfer and the frictional pressure drop along the desuperheating and subcooling section are evaluated by the [77].
As depicted by the condenser flow chart in Figure 5.11, when the iterative cycle of all sections is closed, the sum of length of all regions is compared with the effective length of the condenser L_{ch} and the following equation is applied:

$$L_{mod} = \frac{L_{des} + L_{svc} + L_{cond} + L_{sub}}{L_{ch}} \qquad \textbf{5.22}$$

Then, the condensation saturation temperature is updated as follows:

$$T_{COND\_new} = T_{m,w} + \left(T_{COND\_old} - T_{m,w} \right) \cdot L_{mod} \qquad \textbf{5.23}$$

where $T_{m,w}$ is the mean water temperature and T_{COND_old} and T_{COND_new} are, respectively, the previous and updated condensation saturation temperature.
To avoid convergence issues and the possible cross of the water and refrigerant temperature profiles, the updating of saturation temperature is performed through a damping factor $gain_C$. After the updating of saturation temperature, the pressure at the inlet of condenser is updated (point 2), considering the saturation pressure equal to that at the inlet of condenser. Then, the main iterative cycle restarts and goes on until the check between the calculated and effective evaporator length is verified.

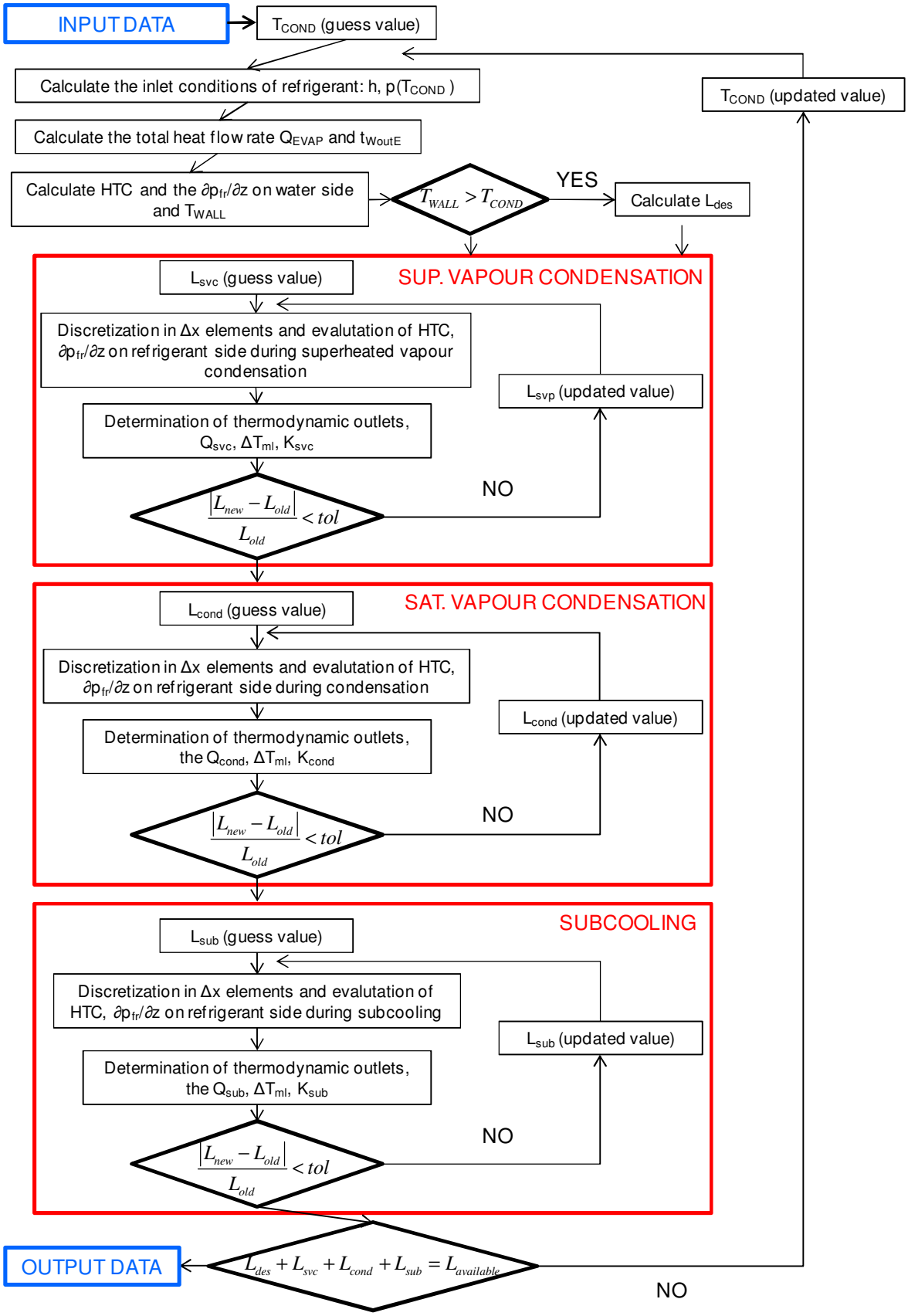

Figure 5.11: Flow chart of the BPHE condenser model.

5.2.4 Minichannel Heat Exchanger (MCHE)

The minichannel air heat exchangers are built with flattened tubes that, at the ends, are placed in two circular or D-shaped headers (Figure 5.12). The minichannels are extruded from the tubes and can have different geometrical shape (circular, rectangular) with or without internal fins. These heat exchangers are usually labeled with a HH-PP-NP(M or P) abbreviation, where HH and PP are respectively the height and the depth of tube, NP is the number of channels; M or P if the channels are or not internally micro-finned.
The multi-ports are in parallel and between them there are fins alternatively placed. Each fin is bent more times on itself and is connected with tubes by brazing. In this way, this manufacturing procedure defines the channels on the air side.
The heat exchanger can also have one or more passages and ranks. In this section a MCHE with one passage and one rank is considered mitigating the performance penalization due to the refrigerant mal-distribution that primarily occurs inside an evaporator along the inlet header.

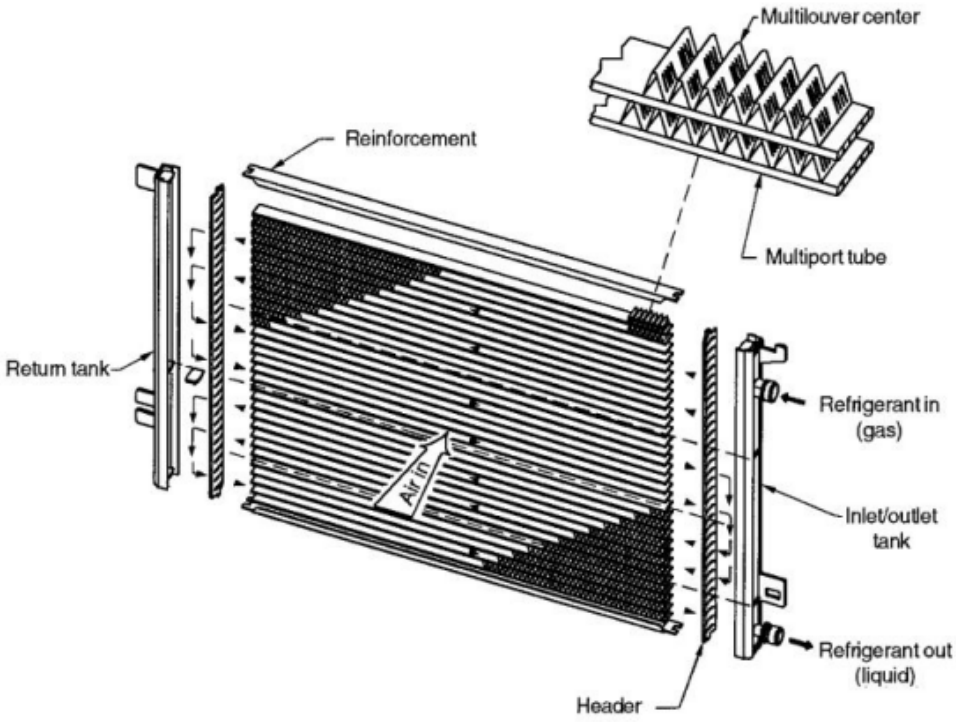

Figure 5.12: Sketch of a minichannel air heat exchanger with vertical headers.

In addition, in the physical model of MCHE the multi-ports are rectangular and plain; and ,on air side, the triangular channels with corrugated louver are considered (Figure 5.13).
From these information, the geometrical features of air heat exchanger on air and refrigerant side can be defined for the physical model (i.e. number and the geometry of channels, the length and the pitch of tubes, the dimensions of fins and louvers).

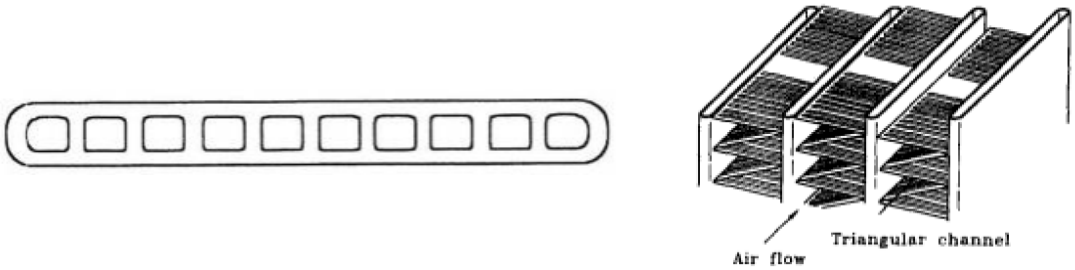

Figure 5.13: The layout of multi-port (left) and fins (right).

5.2.5 Computational procedure for the minichannel heat exchanger

This section presents the numerical model developed to simulate a minichannel air-to-refrigerant heat exchanger working as condenser or evaporator.

Some assumptions have been considered in the model: first of all, all the multiport channels are fed in parallel with the same mass flow rate and vapour quality. As mentioned above, one rank and a single passage have been considered with the aim to avoid possible maldistribution problems in the heat exchanger when working as evaporator. Thank to this assumption, it is possible to discretize the finned heat exchanger in a series of elementary sections composed by a portions of tube and the corresponding fins. The hypotheses underlying this approach are the followings:

1) Each element can be analyzed as an independent heat exchanger, neglecting the heat exchanged through the fins of two adjacent elements and along the multi-port channels.

2) The total finned area is equally divided between the elements.

4) The air properties and the dew temperature is evaluated at the air inlet conditions ([86-88]).

5) The fins are completely wet or completely dry. In particular the check of fin wet conditions are performed comparing the dew temperature against a weighted mean value between the multi-port external temperature and the temperature at the middle of the fin.

6) In summer condition, when the air dehumidification occurs, the liquid film thickness is considered to be constant with a value of 0.127 m and a thermal conductivity of 0.6 W m^{-1} K^{-1} [89];the heat removed from the condensate moisture is neglected. The arbitrary number of subdivisions of the tubes allows to change the number of elements in which the heat exchanger is divided.

7) When the dehumidification occurs, the total heat flow rate is evaluated from a single thermodynamic property (i.e. enthalpy) and the single potential method of Threlkeld [90] is adopted, where the ratio between the sensible component and the latent one is defined by Lewis number [91].

8) On refrigerant side, the same regions reported in 5.2.2 - 5.2.3 during evaporation and condensation has been considered.

9) The headers are considered as completely adiabatic and are divided in elements which length is equal to tube pitch. Here, the total pressure drop is also calculated in the headers taking into account the distribution of mass flow rate in the multi-port channels;

The input and the output of the model are reported in detail in Table 5.4 for the MCHE evaporator - Table 5.4 for the MCHE condenser.

Table 5.4: Input and output of evaporator MCHE model.

	INPUT	OUTPUT
AIR	Face velocity Inlet air temperature Specific Humidity	Heat transfer coefficient Pressure drops Sensible heat flow rate Latent heat flow rate Output conditions
REFRIGERANT	Mass flow rate Subcooling Superheating Condensation temperature Isentropic efficiency	Heat transfer coefficient Pressure drops Evaporation temperature Cooling capacity
MCHE	Geometry	Evaporation length Dryout length Superheating length External wall temperature

Table 5.5: Input and output of evaporator MCHE model.

	INPUT	OUTPUT
AIR	Face velocity Inlet air temperature Specific Humidity	Heat transfer coefficient Pressure drops Sensible heat flow rate Output conditions
REFRIGERANT	Mass flow rate Subcooling Superheating Evaporation temperature Isentropic efficiency	Heat transfer coefficient Pressure drops Condensation temperature Heating capacity
MCHE	Geometry	Desuperheating length Sup. vap.condensation length Sat. vap.condensation length Subcooling length

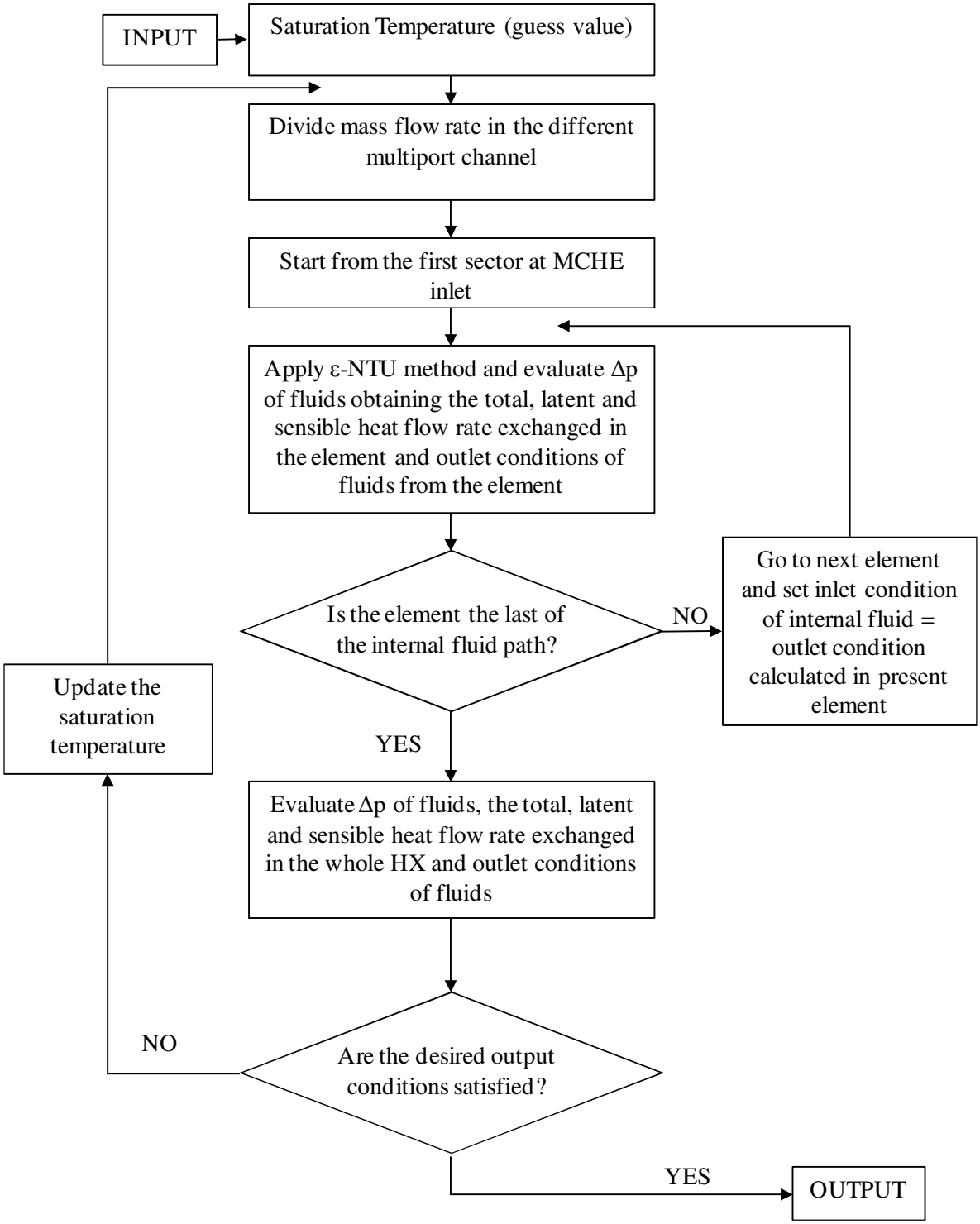

Figure 5.14: Flow chart adopted for the minichannel heat exchanger numerical model.

From the flow chart (Figure 5.14), it is possible to see that the model starts reading the input and evaluates a first guess for the saturation. The inlet conditions on the air side of each element are the same and they have given to the program as input . On the refrigerant side, the total mass flow rate is supposed to equally distribute in the different minichannels. All the elements are considered as heat exchangers and the conditions of fluids at the outlet of each of them are evaluated through the $\varepsilon - NTU$ method, using the correlations that are

later reported. The resolution of the elements starts from the inlet of the internal fluid and follows its path through the multiport channel, setting the inlet conditions of the following element as the outlet conditions evaluated in the previous one, as reported in Figure 5.15.

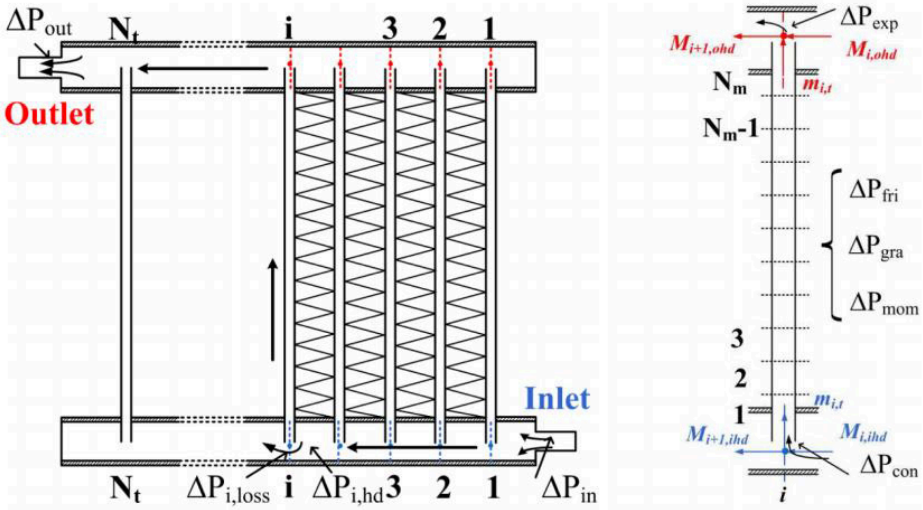

Figure 5.15: Discretization of the MCHE in the model and the evaluation of local pressure drops along multi-port channels and headers.

Once the all the elements are considered, the outlet conditions of last element are compared to the outlet desired conditions that are specified in the input of the model (i.e. superheating in case of evaporator or subcooling in case of condenser). If the difference of these parameters is lower than a specified value, the model gets out the numerical results.

As mentioned above, the model is implemented by subdividing each multiport channel into a fixed number of elements of equal length and each tube is studied as an independent cross-flow heat exchanger. A sketch of single element is depicted in Figure 5.16.

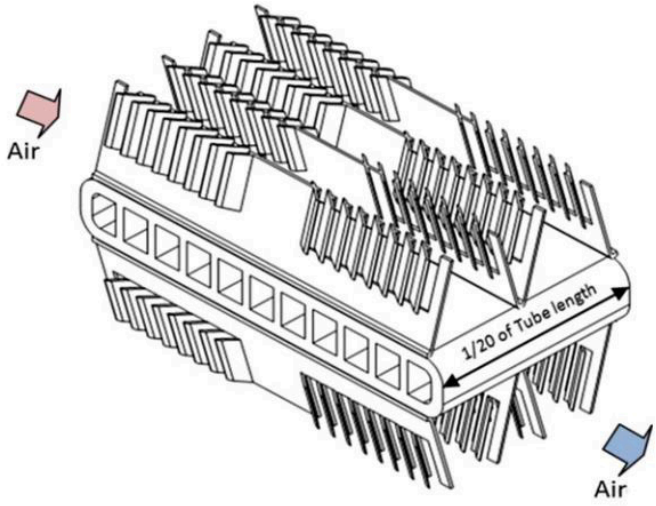

Figure 5.16: Schematic of one control element.

In each elements the $\varepsilon - NTU$ method is applied to evaluate the efficiency and then the heat flow rate:

$$Q = \varepsilon \cdot Q_{max} \qquad \textbf{5.24}$$

with the maximum heat flow rate Q_{max} that is defined as that heat flow rate exchanged between the two fluids at the same inlet temperature inside an heat exchanger with infinite heat transfer area in perfect countercurrent configuration. The value of Q_{max} is function of different conditions as: the thermal capacity of two fluids, the occurring of dehumidification and if the flow of refrigerant is single- or two-phase.
The efficiency ε, instead, is function of the Number of Transfer Units (NTU), the ratio between the thermal capacities of two fluids and the configuration of heat transfer process.
The NTU is in turn evaluated from the global heat transfer coefficient UA which is obtained with different equations in case of dry and wet conditions.
Considering dry conditions, the global heat transfer coefficient UA is evaluated using:

$$UA = \frac{1}{R_{ref} + R_{cond,wall} + R_{air}} = \frac{1}{\frac{1}{h_{ref} \cdot A_i} + R_{cond,wall} + \frac{1}{h_{air} \cdot A_e \cdot \eta_{sup\_fin,dry}}} \qquad \textbf{5.25}$$

The heat transfer coefficient on refrigerant side (h_{ref}) and on air (h_{air}) that can be calculated with the correlations reported later. The A_i and A_e are respectively the internal and external heat transfer area of each element and the fin efficiency $\eta_{sup\_fin,dry}$ at dry conditions is evaluated as:

$$\eta_{sup\_fin,dry} = 1 - \left(1 - \eta_{fin,dry}\right) \cdot \frac{A_{fin,e}}{A_{fin,e} + A_{tube,e}} \qquad \textbf{5.26}$$

$$\eta_{fin,dry} = \frac{tanh\left(m_{dry} \cdot F_l / 2\right)}{m_{dry} \cdot F_l / 2} \qquad \textbf{5.27}$$

$$m_{dry} = \sqrt{\frac{2h_{air}}{\lambda_{fin}\delta_{fin}}\left(1 + \frac{\delta_{fin}}{F_d}\right)} \qquad \textbf{5.28}$$

with the fin ($A_{fin,e}$) and tube surface ($A_{tube,e}$), the fin length F_l, the fin thickness δ_{fin} and the fin depth δ_{fin}.

When dehumidification is present, the global heat transfer coefficient UA^* is referred to an enthalpy difference UA^*, as reported by Threlkeld.

$$UA^* = \frac{1}{R_{ref}{}^* + R_{cond,wall}{}^* + R_{air}{}^*}$$

$$= \frac{1}{\frac{\bar{b}_{ref,wall}}{h_{ref} \cdot A_i} + R_{cond,wall} \cdot \bar{b}_{wall} + \frac{\bar{b}'_{film}}{h_{air,wet} \cdot A_e \cdot \eta_{sup\_fin,wet}}} \quad \textbf{5.29}$$

Here the fin efficiency $\eta_{sup\_fin,wet}$ at wet conditions is evaluated with McQuiston [92] equations:

$$\eta_{sup\_fin,wet} = 1 - \left(1 - \eta_{fin,wet}\right) \cdot \frac{A_{fin,e}}{A_{fin,e} + A_{tube,e}} \quad \textbf{5.30}$$

$$\eta_{fin,wet} = \frac{tanh\left(m_{wet} \cdot F_l / 2\right)}{m_{wet} \cdot F_l / 2} \quad \textbf{5.31}$$

$$m = \sqrt{\frac{2h_{air}}{\lambda_{fin}\delta_{fin}}\left(1 + \frac{C \cdot c_{l,w}}{c_{p,air}}\right)\left(1 + \frac{\delta_{fin}}{F_d}\right)} \quad \textbf{5.32}$$

with the specific heat capacity of water liquid ($c_{l,w}$) and air ($c_{p,air}$), and the ratio between the temperature and specific humidity difference at air and external wall.
The coefficients b [90] in Eq. 5.29 have been calculated at the inlet conditions of each element as:

$$\bar{b}_{ref,wall} = \frac{H^*_{wall,i,in} - H^*_{ref,in}}{T_{wall,i,in} - T_{ref,in}} \quad \textbf{5.33}$$

$$\bar{b}_{wall} = \frac{H^*_{wall,e,in} - H^*_{wall,i,in}}{T_{wall,e,in} - T_{wall,i,in}} \quad \textbf{5.34}$$

$$\bar{b}'_{film} = \left.\frac{dH^*}{dT}\right|_{T=T_{wall,e,in}} \quad \textbf{5.35}$$

where H^* is the enthalpy fictitious value that is obtained when the air flow rate is referred to the saturation conditions at the generic temperature T.
Finally, the air side heat transfer coefficient and pressure drops have been evaluated using different implemented correlations:

- Correlation of Davenport [93].
- Correlation of Chang e Wang (CW,[94]).
- Correlation of Kim e Bullard for dry conditions (KBD,[95,96]).
- Correlation of Kim e Bullard for wet conditions (KBW,[97]).

On the refrigerant side, when the minichannel heat exchanger is working as evaporator and depending on the vapour quality of the refrigerant, different correlations have been used:

- If the refrigerant is in single phase conditions, the HTC is evaluated with Dittus-Boelter [98], Petukhov-Popov [99] and Gnielinski [100] correlations;
- If the vapour quality is between zero and the dryout value, the HTC on the refrigerant side is calculated with Liu-Winterton (LW, [101]), Lazarek-Black (LB, [102]), Kew-Cornwell (KC, [103]), Sun-Mishima (SM, [104]);
- If vapour quality is between the critical value and 1, the heat transfer coefficient is considered to be a the linear interpolation between the value at the dryout and at saturated vapour conditions, as described in Section 5.2.2 in the computational procedure of BPHE evaporator and the vapour quality at dryout is evaluated with correlation developed by Del Col et al. [105].

When the minichannel heat exchangers work as a condenser, instead, the Cavallini et al. [1] correlation is used for the two phase flow and the aforementioned equations of Dittus-Boelter [98], Petukhov-Popov [99] and Gnielinski [100] are used for single-phase.
For evaporation and condensation case the two-phase frictional pressure drop are evaluated with the Cavallini et al. [106] correlation.

5.2.6 Numerical Validation of MCHE model

The validation of model has been performed comparing numerical results against the experimental data obtained by Yun [107]. In this evaluation, the minichannel performs as evaporator, the air is cooled and the dehumidification takes place. In this way a good prediction of both sensible and latent can be achieved by the present model.
In Table 5.6 the geometry and the thermodynamic inputs for air/refrigerant reported by Yun [107] have been considered.

Table 5.6. Operating conditions of evaporator minichannel finned coil, Yun (2007).

Themodynamic condition	**Values**
Air	
Temperature, [°C]	20,00
Relative humidity, [%]	50,9
Pressure, [kPa]	101,325
Face Velocity, [$m \cdot s^{-1}$]	
Data 1	0,417
Data 2	0,586
Data 3	0,770

Refrigerant	
Refrigerant	R134a
Inlet saturation temperature, [°C]	6,5
Vapour quality,	0,05
Mass flow rate, [kg·s^{-1}]	0,167

In the Table 5.7 the numerical and the experimental heat flow rate at the evaporator have been reported:

Table 5.7. Numerical and experimental heat flow rate at the evaporator.

Face velocity [m·s^{-1}]	**Heat flow rate [W]**					
	Total		***Sensible***		***Latent***	
	Exp.	***Num.***	***Exp.***	***Num.***	***Exp.***	***Num.***
0,42	314,1	293,0	236,9	231,3	77,2	61,8
0,59	392,8	367,6	293,2	290,1	99,6	77,5
0,77	470,8	448,6	356,7	354,0	114,1	94,7

As reported in the Table 5.7, the numerical results are in good agreement with the experimental data. For the sensible part of the heat flow rate the deviations are about -3%, and for the latent part they are about -25%.

The accuracy of the numerical model is function of the correlation used to evaluate the heat transfer during the evaporation process. For this reason, the application of the all correlation exposed before has been done to understand what combination of correlation on the air and on the refrigerant side permits low deviations between numerical results and experimental data. In total there are 12 combinations (i.e. 3 correlations at air side and 4 at refrigerant side). For each simulation three index has been considered:

$$\Delta\% = 100 \cdot \frac{q_{calc} - q_{exp}}{q_{exp}} \quad \textbf{5.36}$$

$$MDA = \frac{\sum_{i=0}^{n} |\Delta\%|}{n} \quad \textbf{5.37}$$

$$MD = \frac{\sum_{i=0}^{n} \Delta\%}{n} \quad \textbf{5.38}$$

$$SD = \sqrt{\frac{\sum_{i=0}^{n} (\Delta\% - MD)^2}{n-1}} \quad \textbf{5.39}$$

The two equations to evaluate the heat transfer at air and refrigerant side that minimize the index are the correlation of Liu and Winterton [101] for refrigerant and Chang and Wang [94]for air. The MAD, MD and SD index are, respectively, equal to 1.32 %, 1.23 % and 1.65 %. From Figure 5.17, it can be observed that the model of MCHE tends to overestimate the heat transfer. For this reason, it is preferred to select another combination defined by Sun and Mishima [104] for refrigerant and Kim and Bullard (dry condition, [95,96]) for air. In this case, the MAD, MD and SD index are, respectively, equal to 5.95 %, -5.95 % and 1.08 %.

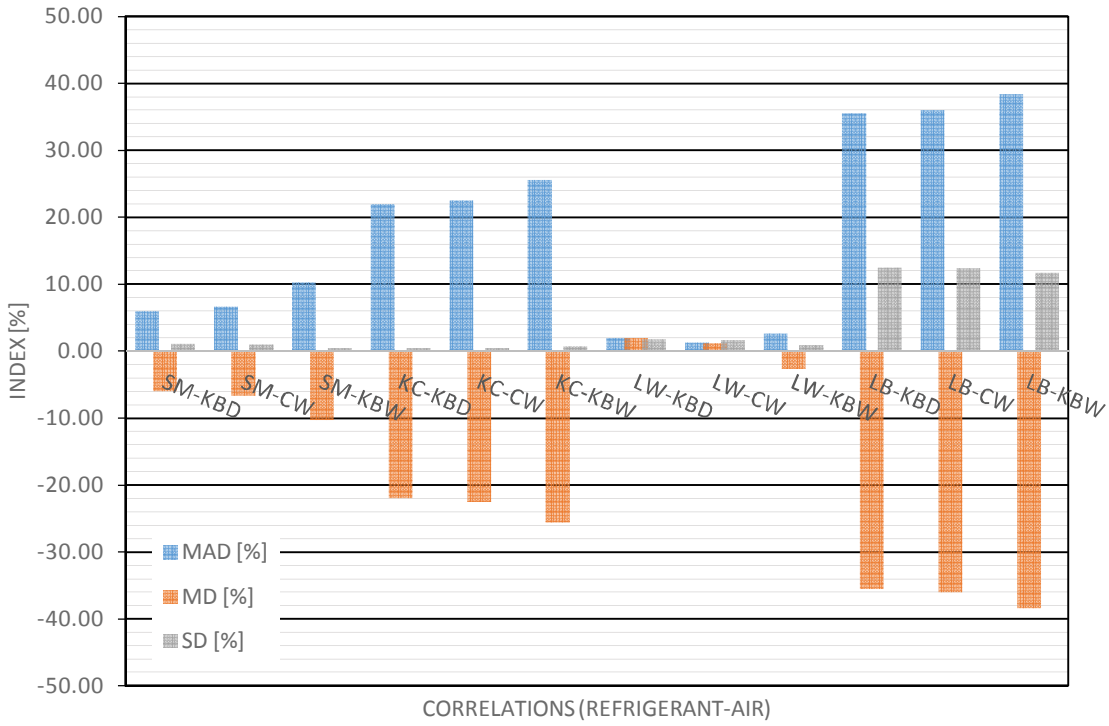

Figure 5.17: The MAD, MD and SD index for all the considered combinations of correlation at refrigerant and air side.

5.2.7 Computational procedure for compressor

In this section the model of compressor is described in detail. In the following Table 5.8 the input and the output of a variable-speed compressor model are reported.

Table 5.8: Input and output for the model of the variable-speed compressor.

	INPUT	OUTPUT
REFRIGERANT	Evaporation temperature Condensation temperature Superheating	Pressure ratio
COMPRESSOR	Geometry Frequency Compressor Maps	Isentropic efficiency Volumetric efficiency Power consumption

The compressor geometry is defined by the swept volume V [cm^3 revolution^{-1}] and the number of pole-pair p. The first parameter can be directly reported by manufacturer data or, in case of a piston compressor, it can be obtained from the number of cylinders, the dimensions of the stroke and the cylinder diameter. From the number of pole-pair p, the compressor speed N is evaluated as:

$$N = 60\frac{fz}{p} \qquad \textbf{5.40}$$

with the frequency fz of the electric motor coupled with the compressor. If an inverter is installed then the speed of electric motor can be modified in according to the desired refrigerant mass flow rate at condenser or evaporator when varying the heating/cooling capacity. When there is not the inverter then the frequency is fixed (i.e. 50/60 Hz) by the electric grid that supplies the electric power to the compressor. Finally the swept volume flow $\dot{V}$ [m^3 s^{-1}] is obtained as follows:

$$\dot{V} = \left(V \cdot \frac{N}{60} \right) \cdot 10^{-6} \qquad \textbf{5.41}$$

The thermodynamic properties of refrigerant (i.e. evaporation and condensation temperature and the superheating) are needed to obtain the output (Table 5.8) having the geometry and the performance maps of compressor. From the evaporation temperature and the superheating, the thermodynamic properties of refrigerant at the suction of compressor are found.

In Eq. 5.41 the swept volume flow is calculated, but in reality the inlet gas volume to compressor is lower and an volumetric efficiency is introduced to describe this process:

$$\eta_{vol} = \frac{\dot{m}_{ref}}{\rho_{in}\dot{V}} \quad \textbf{5.42}$$

with the refrigerant mass flow rate m_{ref} [kg s^{-1}] and the gas density ρ_{in} at the suction.
From the saturation temperatures the pressure ratio is obtained and, considering an isentropic compression, the ideal conditions at the discharge of compressor are defined.
In practice, the work of compressor is larger than the ideal due to a number of different losses compared to an isentropic case and an isentropic efficiency must be introduced:

$$\eta_{is} = \frac{H_{out\_is} - H_{in}}{H_{out} - H_{in}} \quad \textbf{5.43}$$

with the enthalpy at the suction (H_{in}), the enthalpies at the discharge considering an isentropic (H_{out_is}) and an real compression (H_{out}) of refrigerant. The isentropic efficiency includes the mechanical losses due to flow leakage and the undesired heat transfer to the fluid during the compression process. If the compressor is coupled to an electric motor and an inverter, then the electric losses might be considered with an electric efficiency η_{el}. Furthermore, during the compressor process some additional losses due to mechanical friction and heat losses from the compressor to the ambient can occur. Finally, all losses from the electrical power P_{el} to the isentropic compression are taken into account with a global efficiency η_{gl}:

$$\eta_{gl} = \frac{\dot{m}_{ref}(H_{out\_is} - H_{in})}{P_{el}} \quad \textbf{5.44}$$

To obtain the isentropic efficiency from the global efficiency, all the losses that do not contribute to the refrigerant heating must be excluded, such as the external electrical losses (i.e. electrical losses of inverter $\eta_{inverter}$) and the heat losses ε from the compressor to the ambient. From these considerations the following equation that relates the two efficiency has been used:

$$\eta_{gl} = \eta_{is}\eta_{inverter}(1-\varepsilon) \quad \textbf{5.45}$$

Given the labels or the polynomial equations declared by manufacturers, the electrical power consumption P_{el} and the mass flow rate m_{ref} have been obtained from the evaporation and condensation temperature, the superheating and, in case of variable-speed compressor, the inverter frequency. From these results, the isentropic and volumetric efficiency of compressor in Eqs. 5.42 - 5.45 has been, finally, calculated. It is worth noting that the electrical losses of inverter and the additional losses ε has been considered only when they were declared by the manufacturers. If these parameters were not declared, they were neglected and the global efficiency was considered equal to the isentropic one.

However, in the last case, a check has been done between the discharge temperature of the compressor model and that declared by the manufacturer software, and a maximum deviation between them of about 1°C has been observed.
Since the compressor maps are referred to the particular refrigerant, it is possible that the compressor maps for refrigerant, such as R32, and low-GWP fluids (i.e. R1234ze(E), R1234yf and hydrocarbons), are not given by manufacturer software or are not found in the literature. However, in this case, Navarro-Peris et al. [108] reported a dimensionless method that can be employed for a first approach estimation of the compressor performance in non-tested conditions, such as different compressor displacements or speed, or even for a different refrigerant. The authors declared that the non-dimensional mass flow rate, obtained by the same compressor, for two different refrigerants *ref1* and *ref2* can be evaluated as:

$$\dot{m}'_{ref1} = k_1 \cdot \left(1 - F\left(\frac{SH}{T_{EVAP}}\right)\right) \cdot e^{k_2 \cdot rp_{ref1}} \quad \textbf{5.46}$$

$$\dot{m}'_{ref2} = k_1 \cdot \left(1 - F\left(\frac{SH}{T_{EVAP}}\right)\right) \cdot e^{k_2 \cdot rp_{ref2}} \quad \textbf{5.47}$$

with the superheating SH, the evaporation temperature T_{EVAP} [K] and the pressure ratio rp. The F parameter is considered equal to 0.75 [108]. The non-dimensional parameter k_1 and k_2, instead, are referred to the type of compressor (screw, scroll or semi-hermetic compressor). Given the compressor maps for *ref1* and applying the Eq. 5.42 for *ref1*, then the volumetric efficiency and the mass flow rate for *ref2* are evaluated as:

$$\eta_{vol,ref2} = \eta_{vol,ref1} \cdot \left(\frac{\dot{m}'_{ref2}}{\dot{m}'_{ref1}}\right) \quad \textbf{5.48}$$

$$\dot{m}_{ref2} = \eta_{vol,ref2} \cdot \rho_{in,ref2} \cdot \dot{V} \quad \textbf{5.49}$$

In addition, Navarro-Peris et al. [108] declared that the non-dimensional power consumption, obtained by the same compressor, for two different refrigerants *ref1* and *ref2* can be evaluated as:

$$\dot{E}'_{ref1} = \left(\frac{1}{k'_1}\right) + k'_2 \cdot e^{k'_3 \cdot rp_{ref1}} \quad \textbf{5.50}$$

$$\dot{E}'_{ref2} = \left(\frac{1}{k'_1}\right) + k'_2 \cdot e^{k'_3 \cdot rp_{ref2}} \quad \textbf{5.51}$$

Given the compressor maps for *ref1* the following equations reported by the authors have been applied:

$$\tau_{Pel,ref1} = \frac{P_{el,ref1}}{p_{in,ref1} \cdot \dot{V}} \quad \textbf{5.52}$$

$$\tau_{Pel,ref2} = \tau_{Pel,ref1} \cdot \left(\frac{\dot{E}'_{ref2}}{\dot{E}'_{ref1}} \right) \quad \textbf{5.53}$$

Then, the electrical power consumption for *ref2* and the isentropic efficiency have been, respectively, obtained from Eq. 5.52 and Eq. 5.45. This method has been applied for a scroll compressor, where the compressor maps for R410A were reported in the GEOTeCH Horizon 2020 Project and the compressor maps for R32 had to be evaluated. In addition, the evaluated values of mass flow rate and electrical power consumption have been compared against some experimental point for R32 reported in the same project, obtaining a reasonably agreement between them. For this case the electrical inverter losses $\eta_{inverter}$ and the additional losses ε were declared by the manufacturers and were, respectively, equal to 0.96 and 0.05. In the following table, the parameters reported by Navarro-Peris et al. [108] for scroll and semi-hermetic compressor are listed (Table 5.9):

Table 5.9: Parameters for the non-dimensional mass flow rate and power consumption correlation.

Compressor	k_1	k_2	k'_1	k'_2	k'_3
Scroll	1.01	-0.032	0.257	2.12	-1.76
Semi-hermetic	0.95	-0.056	0.474	3.19	-1.198

5.3 Physical model of the reversible Water-to-Water Heat Pump (WWHP)

Here, the three models, previously presented in detail in Sections 5.2.2-5.2.3-5.2.7, are combined together to built the physical model of a water-to-water reversible heat pump. The performance of the WWHP using different refrigerant and compressor (fixed/variable speed, semi-hermetic/screw/scroll) can be evaluated. The brazed plate heat exchanger (BPHE) are used as condenser and as evaporator and different their geometries can be tested. The input and output of model are reported in Section 5.1, where the layout of whole dual-source system has been discussed. As mentioned in Section 5.1, since the heat transfer with ground here has not been considered then the inlet water temperature on the ambient side becomes an input of the model.

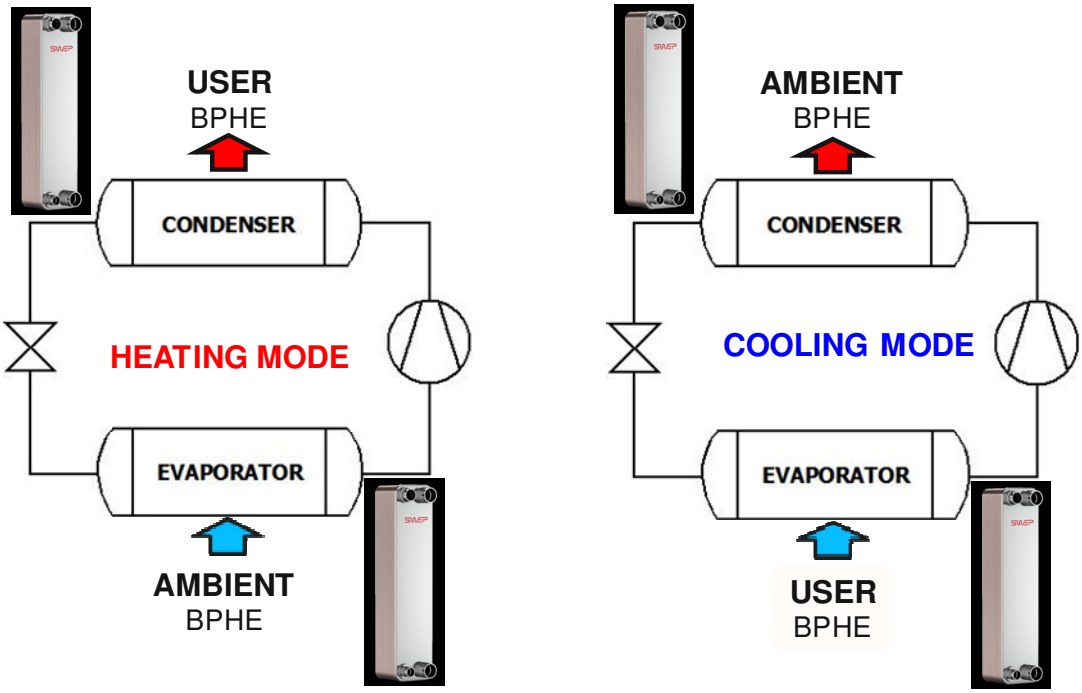

Figure 5.18: Design of a reversible water-to-water heat pump operating in heating (left) and cooling (right) mode.

In Figure 5.18 a sketch of a reversible water-to-water heat pump operating in heating and cooling model is depicted. Considering the input, output and the computational procedure of the BPHE and compressor model, the program starts with a guess value of the saturation temperature at the inlet of condenser and at the outlet of evaporator obtained by the input data (i.e. mass flow rates and inlet temperatures of water, subcooling and superheating). Starting from these guess values, compressor maps, frequency and superheating, the following quantities can be obtained: the isentropic and the volumetric efficiency, the refrigerant mass flow rate, the Coefficient Of Performance (COP), and the pressure ratio. At this point, the subsystem of the evaporator and the condenser have the all input data to perform and update the saturation temperature. The updated value of the saturation temperatures become the new input in the compressor model: the cycle restarts and go on until the saturation temperatures become constant. When the cycle ended then all the output are obtained. In the following paragraphs, the influence of thermodynamic and transport properties of refrigerant on the optimization of the BPHE geometry are studied at similar operating conditions. Then the validation of the WWHP model against experimental data, reported in GEOTeCH Horizon 2020 Project, is presented.

5.3.1 Optimization of the number of plates

In this paragraph, the model has been run with three different fluids (R134a, R290 and R32), with three different compressors and at the same heating capacity (about 16 kW). In particular a variable-speed semi-hermetic compressor for R134a (2DES-3.F1Y, Bitzer), a fixed-speed semi-hermetic compressor for propane (HEX350CC, Dorin) and a variable-speed scroll compressor for R32 (Copeland) have been considered.

The technical data of compressors are reported in the following table:

Table 5.10: Technical data of compressors.

Fluid	Compressor	Inverter	No. Cilinder	Diameter [mm]	Stroke [mm]	Swept volume flow [$m^3\ h^{-1}$]
R134a	Semi-hermetic	Y	2	50	39.3	13.42(@50Hz)
R290	Semi-hermetic	N	2	54	40	15.94(@50Hz)
R32	Scroll	Y	-	-	-	4.5(@50Hz)

In each case the same type of BPHE has been considered (Table 5.11) and the number of plates have been selected to give the same condensation and evaporation temperatures.

Table 5.11: Technical data of BPHE.

Parameter	
Fluid flow plate length, L_{ch} [mm]	466
Fluid flow plate width, W_{ch} [mm]	107
Effective Are, $A_{eff,1p}$ [m^2]	0.058
Corrugation depth, b [mm]	1.82
Chevron Angle, β [°]	60
Plate thickness [mm]	0.5

When comparing the three refrigerants, this model predicts a reduction of the number of plates at the condenser and at the evaporator for R32 as compared to R134a and R290 due to the higher thermal conductivity, as shown in Table 5.12 and Table 5.13. In addition, the frictional pressure drop are lower for R290 as compared to R134a and R32 due to a lower molecular dynamic viscosity.

Table 5.12: Example of application of the model: sizing of condenser for three refrigerants in a water-to-water heat pump (Hot water inlet temperature: 30°C; glide of water temperature: 5K; subcooling: 1K; saturation temperature: 40°C).

			R134a	**R290**	**R32**
	Heating Capacity	[kW]	16.00	15.72	15.7
WATER SIDE	HTC	[$W\ m^{-2}\ K^{-1}$]	11870	12540	16470
	PDs	[kPa]	23.08	26.03	49.09
FLUID SIDE	Mass flux	[$kg\ m^{-2}\ s^{-1}$]	42.4	25.39	44.47
	Inlet cond. temp.	[°C]	39.9	39.97	40.17
	Inlet temp.	[°C]	66.74	69.64	82.91
	Frictional PDs	[kPa]	**13.97**	**10.33**	**15.56**
	Sat. temp. drop	[K]	0.54	0.34	0.27

	HTC	[W m^{-2} K^{-1}]	**2598**	**2750**	**4148**
	ΔT_{ml}	[K]	9.95	9.44	12
	Inlet wall temp.	[°C]	36.76	36.59	37.14
	L_{des}	[m]	-	-	-
	Total plates		**22**	**20**	**14**

Table 5.13: Example of application of the model: sizing of evaporator for three refrigerants in a water-to-water heat pump (Cold water inlet temperature: 12°C; glide of water temperature: 5K; superheating: 5K; saturation temperature: 4°C).

			R134a	**R290**	**R32**
	Cooling Capacity	[kW]	12.45	12.64	12.91
WATER SIDE	HTC	[W m^{-2} K^{-1}]	5519	6207	8557
	PDs	[kPa]	9.55	11.39	20.66
FLUID SIDE	Mass flux	[kg m^{-2} s^{-1}]	23.56	15.23	29.65
	Outlet evap. temp.	[°C]	3.99	4.00	4.00
	Inlet temp.	[°C]	4.69	4.41	4.39
	Inlet quality	[-]	0.25	0.25	0.21
	Frictional PDs	[kPa]	**8.16**	**6.43**	**10.85**
	Sat. temp. drop	[K]	0.70	0.41	0.39
	HTC	[W m^{-2} K^{-1}]	**1850**	**2219**	**4368**
	ΔT_{ml}	[K]	5.03	5.15	5.18
	Total plates		**38**	**32**	**20**

In particular, the reduction of plates is clear at the evaporator, where the number of plates is, respectively, 20, 32 and 38 for R32, R290 and R134a, having a heat transfer area reduction of about 90% from R134a to R32. At the condenser, instead, the number of plates is, respectively, 14, 20 and 22 for R32, R290 and R134a, having a heat transfer area reduction of about 35% from R134a to R32. In this preliminary test, for the evaluation of local heat transfer coefficient during the condensation process of saturated vapour, the correlation of Longo et al. [73,74] has been considered due to the similar chevron angle and the wide range of data of different fluids tested by the authors.
Finally, since this refrigerant shows higher performance as compared to R134a and R290, it has been considered for the whole dual-source system.

5.3.2 Validation of WWHP model

The validation of the physical model of the water-to-water heat pump has been done comparing the numerical results against the experimental data reported in GEOTeCH Horizon 2020 Project.
In this project, the goal is to design an innovative dual source heat pump that can use both ground and air as heat sources.

The refrigerant used is R32 and the aforementioned scroll variable speed compressor is installed. For the validation of the present model, the operation of this device in ground water-to-water configuration has been considered, not taking into account the heat transfer process with the ground through the borehole heat exchangers. For this reason, the secondary fluids used are water, on user side, and propylene glycol, on ground side.
The comparison between the numerical results and some preliminary experimental data has been performed using the BPHE geometry and the compressor map used in the GEOTeCH project.

	TEST 1 (condenser water temperature 40/45 °C, evaporator water temperature 0/-3 °C)											
	Fluid	m_r [kg/s]	Frequency [Hz]	P. el. Comp. [W]	QEVAP [W]	QCOND [W]	SC [K]	SH [K]	Tsat in COND [°C]	Tsat out EVAP [°C]	rp	COP
MODEL	R32	0.01421	35	1274	3344	4531	1.44	6.44	44.21	-5.47	4.03	3.56
EXP.	R32	-	35	1350	3234	4429	1.44	6.44	44.1	-4.95	3.95	3.28
Δ				-5.63%	3.40%	2.30%			0.11	-0.52		8.4%

	TEST 2 (condenser water temperature 40/45 °C, evaporator water temperature 0/-3 °C)											
	Fluid	m_r [kg/s]	Frequency [Hz]	P. el. Comp. [W]	QEVAP [W]	QCOND [W]	SC [K]	SH [K]	Tsat in COND [°C]	Tsat out EVAP [°C]	rp	COP
MODEL	R32	0.01996	50	1763	4701	6296	1.25	5.51	44.61	-6.37	4.20	3.57
EXP.	R32	-	50	1860	4522.6	6303.9	1.25	5.51	44.58	-5.86	4.12	3.39
Δ				-5.22%	3.94%	-0.13%			0.03	-0.51		5.37%

	TEST 3 (condenser water temperature 40/45 °C, evaporator water temperature 0/-3 °C)											
	Fluid	m_r [kg/s]	Frequency [Hz]	P. el. Comp. [W]	QEVAP [W]	QCOND [W]	SC [K]	SH [K]	Tsat in COND [°C]	Tsat out EVAP [°C]	rp	COP
MODEL	R32	0.03077	80	2915	7209	9803	1.15	5.23	45.5	-7.71	4.48	3.36
EXP.	R32		80	3080	6800	9755	1.15	5.23	45.68	-7.6	4.49	3.17
Δ				-5.36%	6.01%	0.49%			-0.18	-0.12		6.18%

Figure 5.19: Comparison between the numerical results of present model against some experimental data obtained in the GEOTeCH Project at different operating conditions.

As reported by Figure 5.19, the numerical results are in good agreement with the experimental data at different operating conditions. The validation of numerical results against experimental data has been performed considering the heat flow rate and saturation temperature at condenser and at evaporator, the electrical power consumption and the COP (defined as the ratio between the heating capacity and the electrical power consumption). From the comparison, a maximum absolute deviation ($|\Delta\%|$ in Eq.5.36)of 2.30%, 6%, 5.6% have been obtained between numerical and experimental results in terms of heating/cooling capacity and electrical power, respectively. About the saturation temperatures, instead a maximum deviation of 0.5 °C has been observed. Any correction factor has been applied to evaluate the local heat transfer during the evaporation process. This highlights the good-work of Amalfi et al. [65,66] correlation to predict the evaporation heat transfer coefficient inside the BPHE. As mentioned in Section 5.2.2, the Amalfi [65,66]

correlation has been obtained from a wide range of data points available literature considering different operating conditions, BPHE geometries and refrigerants. About the heat transfer during saturated condensation process, instead, the lowest correction factor were achieved with the Mancin [81] correlation with a value of 1.5. It is worth noting that more investigations on heat transfer during the condensation process in BPHE are needed, focusing on the effect of different geometrical and operating parameters. In addition, Mancin et al. [81] developed their correlation from experimental data performed in a BPHE with a chevron angle of 65° and tested it on a limited range of data points. About the heat transfer evaluation a correction factor of 1.2 and 1.5 has been applied in the Martin [77] equation on water side and on the refrigerant desuperheating, respectively. The first factor has been used because the Martin [77] equation tends to underestimate the water heat transfer coefficient of about 20%; the second one, instead, has been used to avoid an overestimation of the desuperheating length.

5.4 Physical model of reversible Air-to-Water Heat Pump (AWHP)

Here, the physical model of a reversible air-to-water heat pump is presented and has been built considering the three models reported in Sections 5.2.2-5.2.3-5.2.5-5.2.7. On air side a minichannel heat exchanger is considered and on user side the brazed plate heat exchanger (BPHE) is used as condenser (heating mode) or as evaporator (cooling mode). The input and output of model are reported in Section 5.1, where the layout of whole dual-source system has been discussed. As compared to the WWHP, the inlet temperature and specific humidity of air and the face velocity are the input on the ambient side.

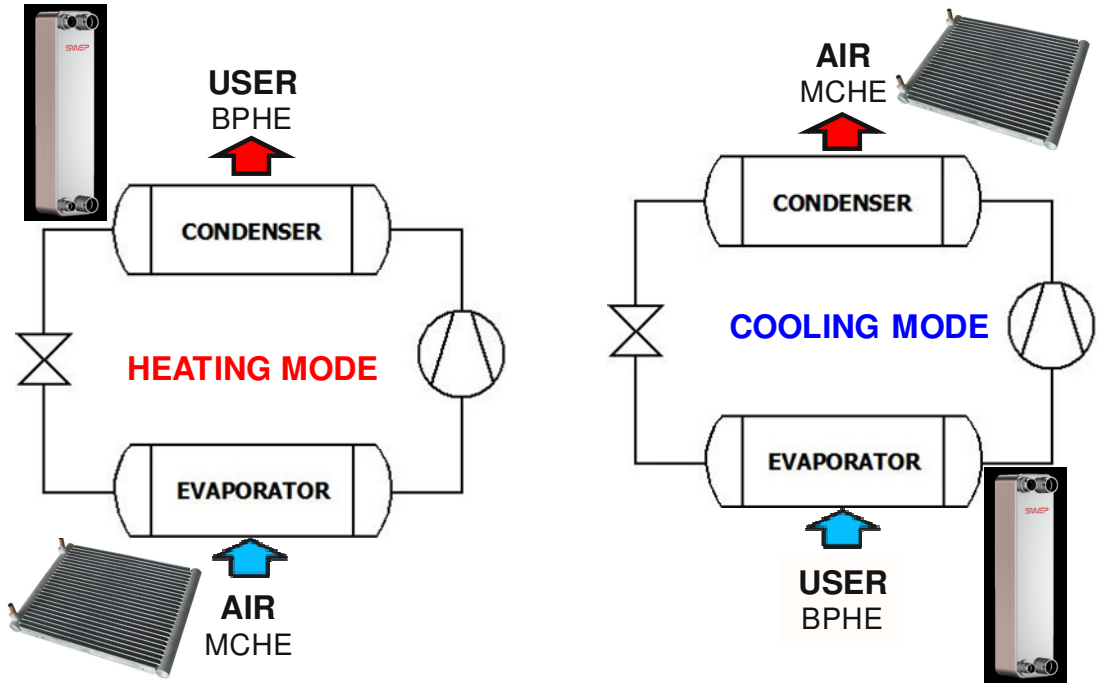

Figure 5.20: Design of a reversible air-to-water heat pump operating in heating (left) and cooling (right) mode.

In Figure 5.20 the sketch of a reversible air-to-water heat pump operating in heating and cooling model is depicted. The logic procedure of the physical model is the same to that adopted in the water-to-water heat pump model.
In this Section, the effect of external air temperature on the AWHP performance has been investigated during heating and cooling mode.
About the minichannel heat exchanger, it has been design for a cooling capacity of 7.45 kW, superheating of 5 K, air inlet temperature of 7°C and a outlet saturation temperature of 0.64°C. The hydraulic diameter of the minichannel is equal to 1 mm and the MCHE geometry is reported in detail in Table 5.14.

Table 5.14: Technical data of MCHE.

MCHE	
Tube length [mm]	1120
Header length [mm]	830
No. of tubes	74
Header diameter [mm]	20
Multi-port tubes	
Tube depth [mm]	16.00
Tube pitch [mm]	11.1
Tube thickness [mm]	0.6
Hydraulic diameter of channels[mm]	1
Channel shape	Rectangular
No. of channels [mm]	7
Fins	
Louver pitch [mm]	1.4
No. of louvers	8
Louver length [mm]	6.4
Fin depth [mm]	16.00
Fin pitch [mm]	1.05
Fin density [m^{-1}]	952
Fin thickness [mm]	0.1

On user side, instead, the geometry of symmetric BPHE is that adopted in GEOTeCH project.
The refrigerant used is R32 and the compressor maps are those referred to variable-speed scroll compressor reported in 5.2.7-5.3.1.

5.4.1 Heating mode

During the heating mode of AWHP, the numerical tests have been performed at varying the inlet air temperature from 0 to 15°C at evaporator while keeping the heating capacity equal to 7.4 kW at an inlet water temperature of 40°C at the condenser. The face velocity and the mass flow rate has been chosen keeping a constant glide temperature of 5K. The superheating was 5K and the subcooling was 1K. In addition, the inlet specific humidity has been set to 0.85 and the latent heat flow rate due to the humidification at the evaporator on air side has not considered. During the numerical tests, the investigation has been focused on the effect of air temperature on evaporation temperature T_{EVAP}, the external wall temperature $T_{wallExt}$ and the Coefficient Of Performance COP_h, that is defines as:

$$COP_h = \frac{Q_{COND}}{P_{el}} \qquad \textbf{5.54}$$

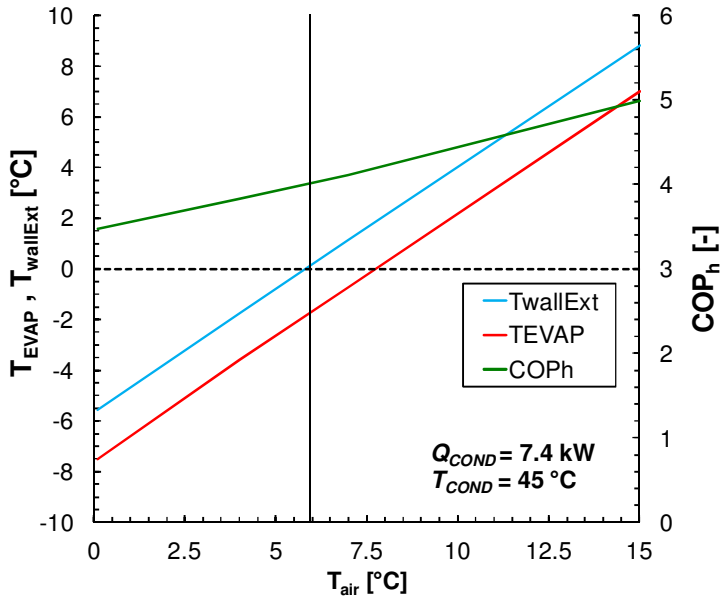

Figure 5.21: Trend of evaporation and external wall temperature and the COP during the heating mode of AWHP at varying the external air temperature.

In Figure 5.21, when the external air temperature decreases from 15 to 0°C the decrease of evaporation temperature from 7 to -7.5°C is observed. While the evaporation temperature decreases, the condensation temperature is almost constant; for this reason the pressure ratio of the thermodynamic cycle increases and the electrical power consumption needed to supplied the same heating capacity at condenser increases, having a reduction of the COP_h from 5 to 3.5. It is worth noting that, as mentioned above, this investigation has been performed neglecting the contribution of latent heat flow rate due to the air dehumidification on COP_h. In addition, when the air temperature is below 6°C (Figure 5.21), the external wall temperature starts to be lower than 0°C. At these operating conditions the water vapour in air condenses on the external wall of MCHE and becomes frost. Over time, the frost thickness grows and the local heat transfer on air side is lower.

The frost occurring carries out some technical and operation problems as the obstruction of fins. This issue can be resolved through defrost mode, where the AWHP is performed in cooling mode for a brief period to mitigate the frost occurring. This operation causes a further decrease of COP_h that in Figure 5.21 has not been considered.

5.4.2 Cooling mode

During the cooling mode of AWHP, the numerical tests have been performed at varying the inlet air temperature from 25 to 35°C at condenser, while keeping the cooling capacity equal to 7.1 kW at a inlet water temperature of 12°C at the evaporator. The face velocity and the mass flow rate has been chosen keeping a constant glide temperature of 5K. The superheating was 5K and the subcooling was 1K. The inlet specific humidity has been set to 0.35 and in this case the air humidification cannot occur because the external wall temperature is always higher than that of air. During the numerical tests, the investigation has been focused on the effect of air temperature on condensation temperature T_{COND} and the Coeffcient Of Performance COP_c, that is defines as:

$$COP_c = \frac{Q_{EVAP}}{P_{el}} \qquad \textbf{5.55}$$

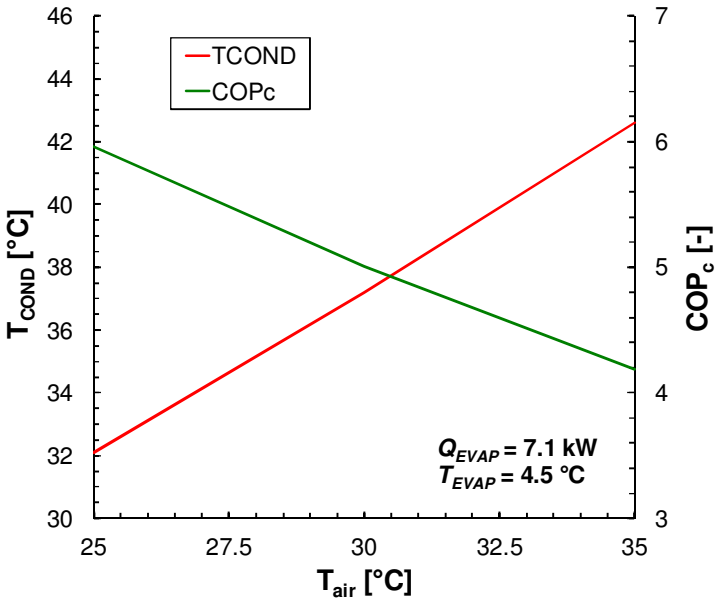

Figure 5.22: Trend of condensation wall temperature and the COP during the cooling mode of AWHP at varying the external air temperature.

In Figure 5.22, when the external air temperature increases from 25 to 35°C the increase of condensation temperature from 32 to 42.6°C is observed. When the condensation temperature increases, the evaporation temperature is almost constant; for this reason the pressure ratio of the thermodynamic cycle increases and the electrical power consumption needed to supplied the same cooling capacity at evaporator increases, having a reduction of the COP_c from 5.96 to 4.20.

In this and previous section, it has been analyzed how much the air temperature significantly affects the AWHP performance during heating and cooling mode. This aspect is fundamental to understand which source/sink must be selected at varying the outdoor conditions to obtain the best performance of a dual-source system; it will be discussed further in the following chapter of thesis.

6 MODEL OF A DUAL-SOURCE HEAT PUMP

6.1 Introduction

In the previous sections, the physical models of a water-to-water and air-to-water reversible heat pump have been presented. In this chapter of thesis, the possibility to exchange heat transfer with the ground on the water side in a water-to-water heat pump is taken into account. This option is available both during the heating mode at the evaporator and during the cooling mode at the condenser. Before showing the physical of Ground-Coupled Heat Pump (GCHP), the analysis of heat transfer inside a borehole heat exchanger is necessary and is presented in detail in this Section. Finally, from the performance comparison between the air-to-water and ground-coupled heat pump, a possible definition of the best control of a dual-source heat pump is discussed, deciding the best source to use at different operating and outdoor conditions.

6.2 Computational procedure for vertical ground-coupled heat exchangers

The model of a single U-tube Borehole Heat Exchanger (BHE) has been here developed.
The fluid (i.e. water or propylene glycol) flows inside a single U-tube and the heat is exchanged between the fluid and the ground through the grout, as depicted in Figure 6.1.

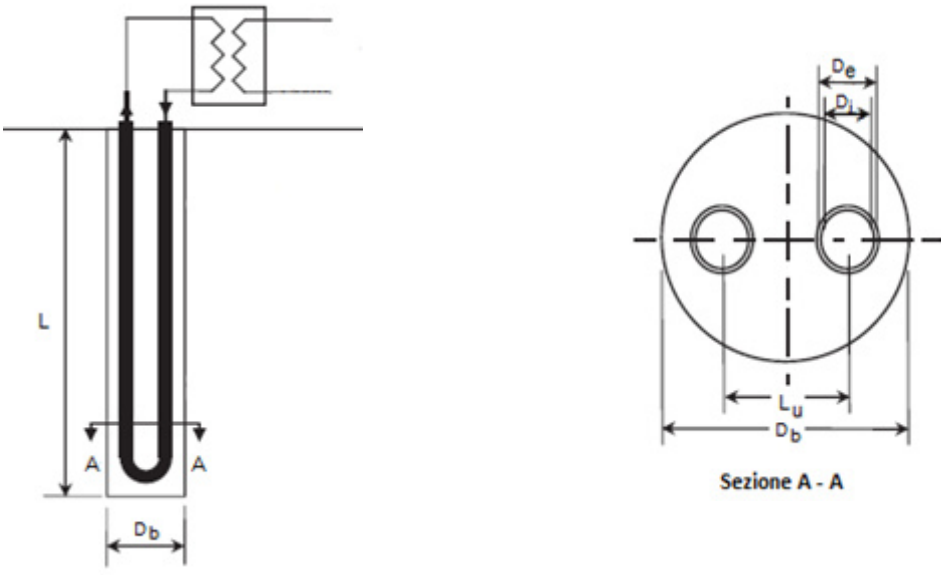

Figure 6.1: Schematic diagram of a vertical U-tube borehole heat exchanger (BHE).

The major models found in the literature are analytic and offer simple, parameter input-based modeling and short computation times, but they usually disregard the transient effects of heat and mass transport in the borehole and hence are not suitable for the prediction of the BHE performance during a long period time. Furthermore, these models

tend to use an equivalent thermal resistance between the fluid and the external surface of grout. This equivalent thermal resistance is usually evaluated through experimental assumptions (Remund, [109]) or by numerical models (Hellstrom [110], Sharqawy et al. [111,112]) applied to a specific BHE geometry. For this reason, the physical model here presented is a Thermal Resistance and Capacity model (TRCM), where all thermal resistances between nodes have been evaluated avoiding the use of an equivalent thermal resistance. In this way, the model can be applied for different geometries and operating condition taking to account the transient thermal behavior of grout and ground in long period time. The all geometry has been discretized in elements along the axial and radial direction, as shown in Figure 6.2.

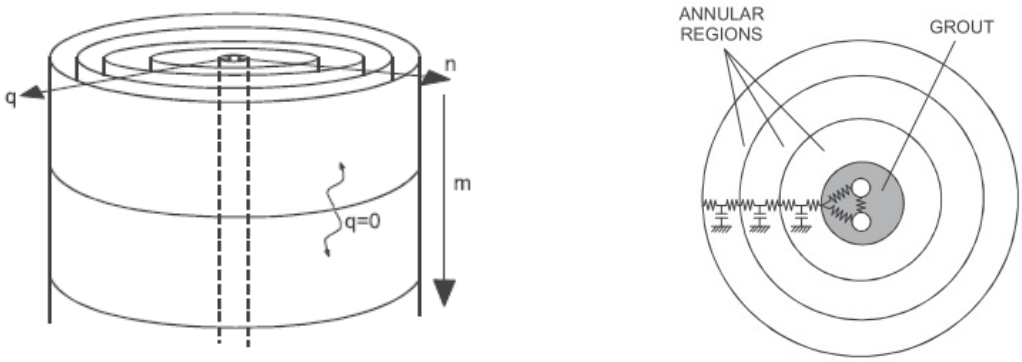

Figure 6.2: The discretization of a vertical Borehole Heat Exchanger (BHE) and the surrounding ground.

A sensivity test has been done to understand how many elements along the radial and the axial direction were necessary. The result of this test suggested 3 elements along the axial direction and 6 elements for the radial discretization of the ground. It is worth noting that the heat transfer by conduction along the axial direction has been neglected since the heat transfer occurs primarily along the radial direction. Hereinafter, the analysis of heat transfer and the thermal resistances inside the borehole heat exchanger is presented adopting the model of Bauer et al. [113]. The calculation of thermal resistances has been done referring to Figure 6.3.

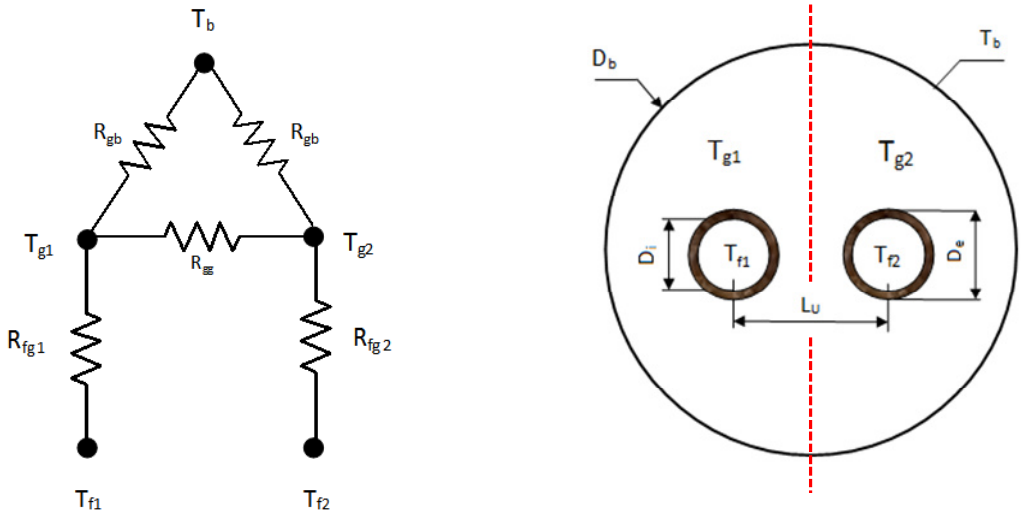

Figure 6.3: Horizontal cross section and the developed TRCM for single U-tube BHE.

As shown in Figure 6.3, the cross section of BHE is defined by five nodes:

- The fluid that flows inside the first leg of BHE (T_{f1});
- The fluid that flows inside the second leg of BHE (T_{f2});
- The grout near the first leg (T_{g1});
- The grout near the second leg (T_{g2});
- The external surface of grout (T_b);

Each node is defined by a thermal capacity C [J K^{-1}]and the heat transfer between two nodes is described by a thermal resistance R [K W^{-1}].

The thermal resistance between the fluid f and the grout g is calculated as sum of three components: the thermal convection on fluid side R_f, the thermal conduction through the pipe $R_{p,1}$ and the grout $R_{p,2}$:

$$R_{fg} = R_f + R_{p,1} + R_{p,2} \quad \textbf{6.1}$$

$$R_f = \frac{1}{Nu \cdot \lambda_f \cdot \pi \cdot \Delta z} \quad \textbf{6.2}$$

$$R_{p,1} = \frac{\ln\left(\frac{D_e}{D_i}\right)}{2 \cdot \pi \cdot \lambda_p \cdot \Delta z} \quad \textbf{6.3}$$

$$R_{p,2} = x \cdot R_g \quad \textbf{6.4}$$

with the node axial length Δz, the Nusselt number Nu and the geometrical parameter x. The convection heat transfer on fluid side is evaluated with Nusselt number Nu, that is calculated with the equations proposed by Gnielinski [100]. The thermal fluid properties has been evaluated with Refprop 9.0 [114] in case of pure water and with correlations [115] found in the[115] literature in case of brine. The geometrical parameter x is defined by Bauer at al. [113] lumping the areas of two pipes of a single U-tube BHE in an equivalent circular area with equivalent diameter in the middle of the borehole (Figure 6.4).

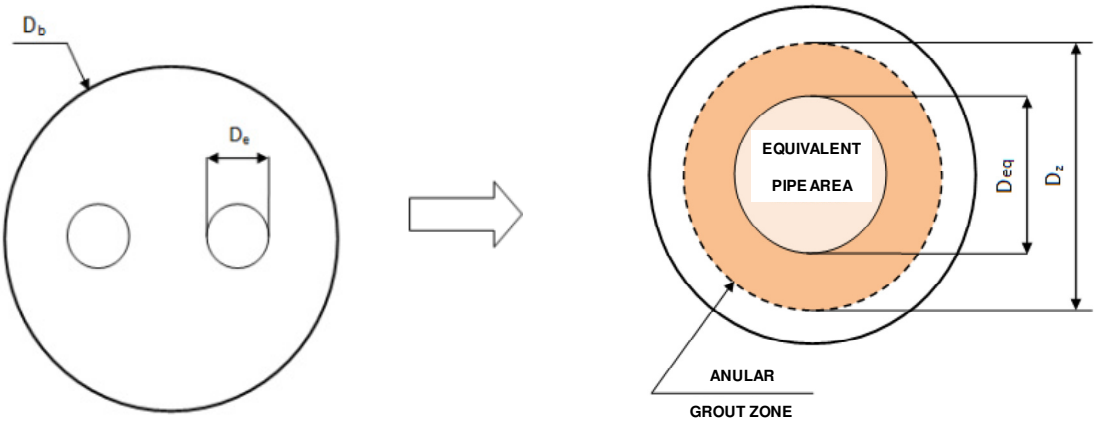

Figure 6.4: The lumping of the areas of pipes in an equivalent circular area.

From the figure above, the geometrical parameter x is obtained by Bauer et al. [113], as follows:

$$x=\frac{\ln\left(\frac{D_z}{D_{eq}}\right)\cdot\frac{1}{2\cdot\pi\cdot\lambda_g}}{\ln\left(\frac{D_b}{D_{eq}}\right)\cdot\frac{1}{2\cdot\pi\cdot\lambda_g}}=\frac{\ln\left(\frac{\sqrt{D_b{}^2+2\cdot D_e{}^2}}{2\cdot D_e}\right)}{\ln\left(\frac{D_b}{2\cdot D_e}\right)};\qquad D_z=\sqrt{\frac{D_b{}^2+D_{eq}{}^2}{2}};\qquad D_{eq}=\sqrt{2}\cdot D_e \tag{6.5}$$

with the borehole diameter D_b. From this definition of x, the thermal resistance between the two parts of grout R_{gg} and between the these two parts and the external surface of borehole R_{gb}:

$$R_{gb}=(1-x)\cdot R_g \tag{6.6}$$

$$R_{gg}=\frac{2\cdot R_{gb}\cdot(R_{ar}-2\cdot x\cdot R_g)}{2\cdot R_{gb}-R_{ar}+2\cdot x\cdot R_g} \tag{6.7}$$

with the thermal resistance of grout R_g and the thermal resistance between the outer walls of the two pipes $R_{ar.}$ These conduction thermal resistances has been evaluated by Bauer et al. [113] as:

$$R_g=\frac{arc\cosh\left(\frac{D_b{}^2+D_e{}^2-L_U{}^2}{2\cdot D_b\cdot D_e}\right)}{2\cdot\pi\cdot\lambda_g\cdot\Delta z}\cdot\left(1.601-0.888\cdot\frac{L_U}{D_b}\right) \tag{6.8}$$

$$R_{ar}=\frac{arc\cosh\left(\frac{2\cdot L_U{}^2-D_e{}^2}{D_e{}^2}\right)}{2\cdot\pi\cdot\lambda_g\cdot\Delta z} \tag{6.9}$$

Since the physical model is also transient then the capacities of each node must be calculated. In the following equations the thermal capacities of fluid (f_1,f_2) and grout (g_1,g_2) nodes:

$$C_f=\rho_f\cdot c_{p,f}\cdot\Delta z\cdot D_i{}^2\cdot\pi/4 \tag{6.10}$$

$$C_g=\rho_g\cdot c_{p,g}\cdot\Delta z\cdot\pi/4\cdot\left(D_b{}^2/2-D_e{}^2\right) \tag{6.11}$$

After the definition of all thermal resistances and capacities, the energy equation referred to each node (shown in Figure 6.3) inside the borehole are reported below.
The contribution of thermal capacity is reported on the left side of equation; whereas, the all heat transfer components are reported on the right side. Since the borehole domain is discretized along the axial direction, the index j is referred to the j-layer along that direction. It is worth noting that the fluid heat flow rate (i.e. $m_f c_{p,f} \Delta T$) must be considered when the equations of fluid nodes are reported.
The equation for the fluid at the first leg of BHE:

$$C_{j,f1} \cdot \frac{dT_{j,f1}}{dt} = -\dot{m}_f \cdot c_{p,f} \cdot \left(T_{j,out\_f1} - T_{j,in\_f1}\right) - \left(\frac{1}{R_{j,fg1}}\right) \cdot \left(T_{j,f1} - T_{j,g1}\right) \quad \textbf{6.12}$$

$$T_{j,out\_f1} = 2 \cdot T_{j,f1} - T_{j,in\_f1} \quad \textbf{6.13}$$

The equation for the fluid at the second leg of BHE:

$$C_{j,f2} \cdot \frac{dT_{j,f2}}{dt} = -\dot{m}_f \cdot c_{p,f} \cdot \left(2 \cdot T_{j,out\_f2} - 2 \cdot T_{j,in\_f2}\right) - \left(\frac{1}{R_{j,fg2}}\right) \cdot \left(T_{j,f2} - T_{j,g2}\right) \quad \textbf{6.14}$$

$$T_{out,f2\_j} = 2 \cdot T_{f2\_j} - T_{in,f2\_j} \quad \textbf{6.15}$$

The equation for the grout part near the first leg of BHE:

$$C_{j,g} \cdot \frac{dT_{j,g1}}{dt} = -\left(\frac{1}{R_{j,gg}}\right) \cdot \left(T_{j,g1} - T_{j,g2}\right) - \left(\frac{1}{R_{j,fg1}}\right) \cdot \left(T_{j,g1} - T_{j,f1}\right) - \left(\frac{1}{R_{j,gb}}\right) \cdot \left(T_{j,g1} - T_{j,b}\right) \quad \textbf{6.16}$$

The equation for the grout part near the second leg of BHE:

$$C_{j,g} \cdot \frac{dT_{j,g2}}{dt} = -\left(\frac{1}{R_{j,gg}}\right) \cdot \left(T_{j,g2} - T_{j,g1}\right) - \left(\frac{1}{R_{j,fg2}}\right) \cdot \left(T_{j,g2} - T_{j,f2}\right) - \left(\frac{1}{R_{j,gb}}\right) \cdot \left(T_{j,g2} - T_{j,b}\right) \quad \textbf{6.17}$$

The equation referred to the external surface of grout is:

$$0 = -\left(\frac{1}{R_{gb}}\right) \cdot \left(T_{j,b} - T_{j,g1}\right) - \left(\frac{1}{R_{j,gb}}\right) \cdot \left(T_{j,b} - T_{j,g2}\right) - \left(\frac{1}{R_{j,s1}}\right) \cdot \left(T_{j,b} - T_{j,s1}\right) \quad \textbf{6.18}$$

For the modeling of the surrounding ground, the De Carli et al. [116] model has been adopted, as shown in Figure 6.5.

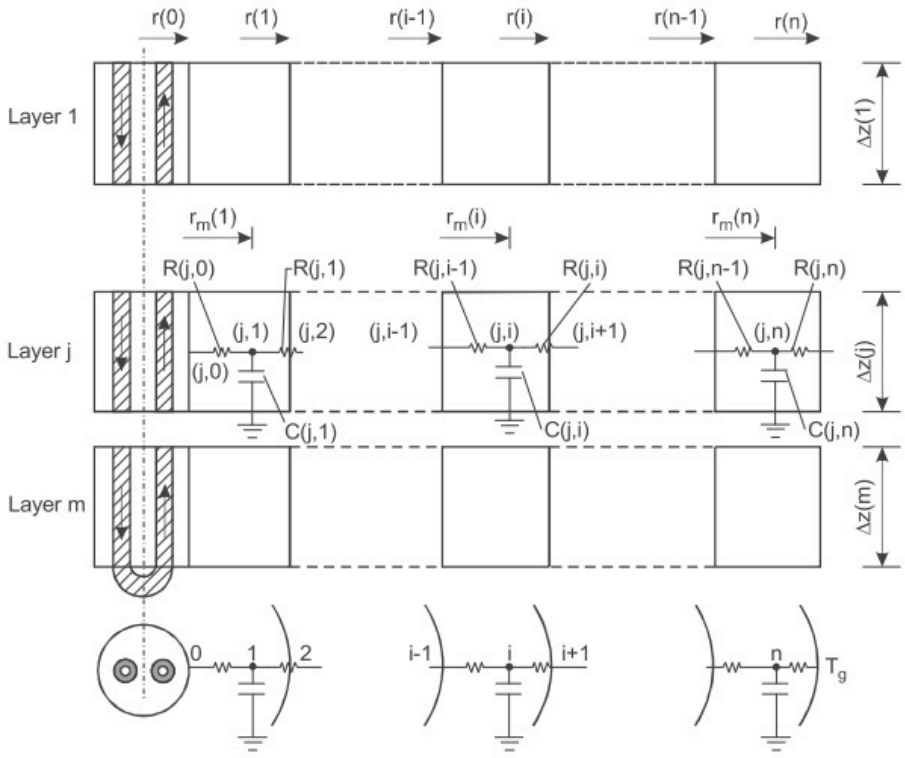

Figure 6.5: Modeling of the surrounding ground.

Here, the energy equation referred to each node of ground annular region (as shown in Figure 6.5) has defined as follows:

$$C_{j,i} \cdot \frac{dT_{j,i}}{dt} = \frac{T_{j,i-1} - T_{j,i}}{R_{j,i-1}} + \frac{T_{j,i+1} - T_{j,i}}{R_{j,i}} \qquad \textbf{6.19}$$

with the conduction thermal resistance R between the adjacent annular region of ground and the thermal capacity C of the annular region of ground.

$$R_{j,i-1} = \frac{\ln\left(r_m(i) / r(i-1)\right)}{2 \cdot \pi \cdot \lambda_s \cdot \Delta z_j}; \qquad R_{j,i} = \frac{\ln\left(r(i) / r_m(i)\right)}{2 \cdot \pi \cdot \lambda_s \cdot \Delta z_j} \qquad \textbf{6.20}$$

$$C_{j,i} = \rho_j \cdot c_j \cdot \pi \cdot \left(r^2{}_i - r_{i-1}{}^2\right) \cdot \Delta z_j \qquad \textbf{6.21}$$

$$r_m(i) = \sqrt{\frac{\left[r^2(i) + r(i-1)^2\right]}{2}} \qquad \textbf{6.22}$$

The equations above reported, describe the thermal balance referred to a node of the ground. The ground is composed of several subregions *j*, each of them characterized by different thermophysical properties, assumed independent of time, mainly determined by mineral composition, porosity content and degree of water saturation.
Usually the part of the ground close to outside air is affected by weather conditions changes. The disturbance due to air temperature penetrates to a depth of some meters and, considering that usually borehole length is close to hundred meters, its influence may be considered negligible. In this model, the heat flux between the fluid inside the first part of the borehole near the ground surface level and the outside air is not considered.
At a distance $r > r_{max}$, from the borehole axis, the temperature is considered equal to the undisturbed ground temperature T_g. The value of this maximum radius r_{max} is related to the ground thermal diffusivity and to the overall time of operation or simulation. In this model the maximum radius, at which the ground temperature can be assumed constant in time, is about 8 m.
In Table 6.1 the input and output of the vertical borehole heat exchanger are reported. It is worth noting that only the single U-tube geometry has been considered. However, Bauer et al. [113] defined the equations to evaluate of all thermal resistances and capacities of each node also in case of double U-tube and coaxial BHE. During the test a uniform ground has been considered. Nevertheless, since in the numerical method a discretization along the axial direction can be applied, a ground composed by different layers can be also simulated.

Table 6.1: Input and output for the ground-coupled heat exchanger model.

	INPUT	OUTPUT
GROUND	Thermal characteristic properties Undisturbed ground temperature	Local temperatures
GROUT	Thermal characteristic properties	Local temperatures
FLUID	Mass flow rate Inlet temperature Type of fluid (pure water or brine)	Heat flow rate Local temperature Outlet temperature
BHE	Geometry	

6.2.1 Numerical results

Here some results obtained from the model have been reported considering different time period, thermodynamic ground properties and operating conditions (e.g. winter/summer). In Table 6.2 the operating conditions of the fluid at the inlet, the geometry of the single borehole heat exchanger and the thermophysical properties of the ground and grout has been listed.

Table 6.2: Operating conditions of the tests.

	Operating conditions	
	Dry ground	*Wet ground*
Bore diameter D_b [m]	0.210	0.210
Inner pipe diameter D_i [m]	0.033	0.033
External pipe diameter D_e [m]	0.042	0.042
Distance of pipes L_U [m]	0.070	0.070
Bore length L [m]	100	
Thermal conductivity of pipe λ_p [W m^{-1} K^{-1}]	0.480	0.480
Thermal conductivity of grout λ_g [W m^{-1} K^{-1}]	2.0	
Grout specific heat c_g [J kg^{-1} K^{-1}]	380	
Grout density ρ_g [kg m^{-3}]	1580	
Thermal conductivity of ground λ_s [W m^{-1} K^{-1}]	1.0	2.1
Ground specific heat c_s [J kg^{-1} K^{-1}]	870	1700
Ground density ρ_s [kg m^{-3}]	2400	1850
Undisturbed ground temperature T_s [°C]	13.30	13.30
Inlet fluid temperature T_{in} [°C]	7/35	
Fluid	Water	
Mass flow rate $\dot{m}$ [kg s^{-1}]	0.200	
Maximum radius r_{max} [m]	8	

Table 6.3: Results during winter conditions at different period time in case of dry and wet ground.

	Winter conditions			
	Wet ground		*Dry ground*	
	Q [W]	$T_{out,f2}$ [°C]	Q [W]	$T_{out,f2}$ [°C]
300 h	1556	8.85	1017	8.21
700 h	1456	8.74	942	8.12

Table 6.4: Results during summers condition at different period time in case of dry and wet ground.

	Summer conditions			
	Wet ground		*Dry ground*	
	Q [W]	$T_{out,f2}$ [°C]	Q [W]	$T_{out,f2}$ [°C]
300 h	5373	28.57	3510	30.8
700 h	5056	28.95	3251	31.11

In Table 6.3 - Table 6.4 the numerical results have been reported considering the winter and summer season and two different type of ground. It can be seen that, both during the

winter and summer condition, the thermodynamic properties of ground influence the performance of BHE.
For the cases of study, the thermal characteristics of the ground influence the heat flow rate of about 50%. Furthermore, the effect of the ground thermal capacity can be observed comparing the results obtained after 300 and 700 hours of operation. The ground is affected by the heat flow rate exchanged with the fluid leading to a decrease of the BHE performance. For example from 300 h to 700 h a decrease of about 6-10% of heat flow rate can be observed.
About the validation of the physical model of borehole heat exchangers, the theoretical model of Yang et al. [117] and the experimental data obtained by Yoon et al. [118] has been considered. During the validation the numerical model has been performed at the same operating and geometrical conditions defined by Yang et al and Yoon et al.. In the first case the borehole heat exchanger worked in summer conditions and an operational time of 720 h has been considered; a deviation of about -15 % (Eq. 5.36) has been obtained in terms of heat flow rate between the physical model and the numerical data declared by the authors [117]. In the second case, the borehole heat exchanger worked in summer conditions and an operational time of 48 h has been considered. Here, a deviation of about -10 % (Eq. 5.36) has been obtained in terms of heat flow rate between the physical model and the experimental data declared by the authors [118].

6.3 Physical model of reversible Ground Coupled Heat Pump (GCHP)

Here, the physical model of a reversible ground coupled heat pump is presented (Figure 6.6) and has been built combining the WWHP and BHE model shown in Sections 5.3 - 6.2. The input and output of model are reported in Section 5.1, where the layout of whole dual-source system has been discussed.

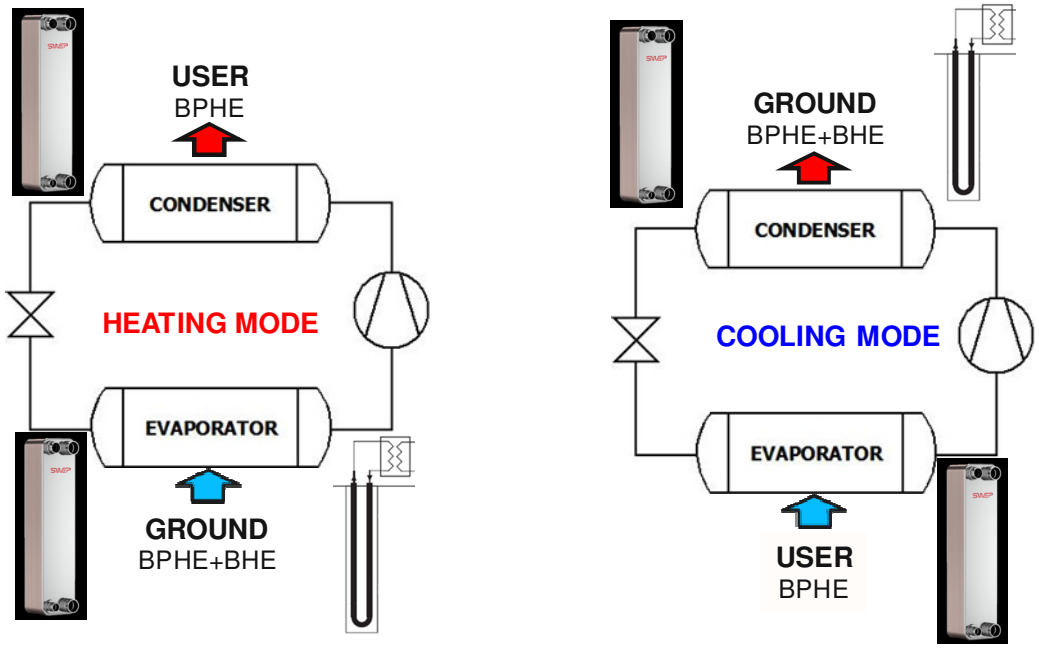

Figure 6.6: Design of a reversible ground source heat pump operating in heating (left) and cooling (right) mode

The coupling of the WWHP and BHE model is achieved through the inlet/outlet fluid temperature at the evaporator (heating mode) or at the condenser (cooling mode).
At the beginning of numerical simulation the inlet fluid temperature on ground side is set equal to the undisturbed ground temperature; after the WWHP model, the fluid temperature at the outlet of evaporator (heating mode) or of condenser (cooling mode) becomes the input of BHE model. Finally, the fluid temperature at the outlet of BHE model is the updated value of the fluid temperature at the inlet of evaporator (heating mode) or of condenser (cooling mode) in the WWHP model.
In this section, numerical simulations have been done to investigate the influence of borehole number and 'ground fouling' on GWHP performance. During these tests, the geometry and refrigerant of WWHP reported in Section 5.3.2, the geometry of BHE and the grout thermodynamic properties reported in Table 6.2 has been adopted.
About the ground the following thermodynamic properties have been considered: λ_s = 1.94 W m^{-1} K^{-1}, c_s = 870 J kg^{-1} K^{-1} and ρ_s = 1400 kg m^{-3}. The fluid on ground side is brine, where the concentration of glycol in the pure water is 0.3.

6.3.1 The influence of the No. BHEs

During the heating mode of GWHP, the numerical tests have been performed at varying the heating capacity from 6 to 12 kW at a inlet water temperature of 40°C at the condenser. The water and brine mass flow rates has been chosen keeping a constant glide temperature of 5K on user side and 3K on ground side. The superheating was 5K and the subcooling was 1K. During the numerical tests, the investigation has been focused on the effect of number of BHEs on evaporation temperature T_{EVAP} and the Coefficient Of Performance COP_h (Eq. 5.54).

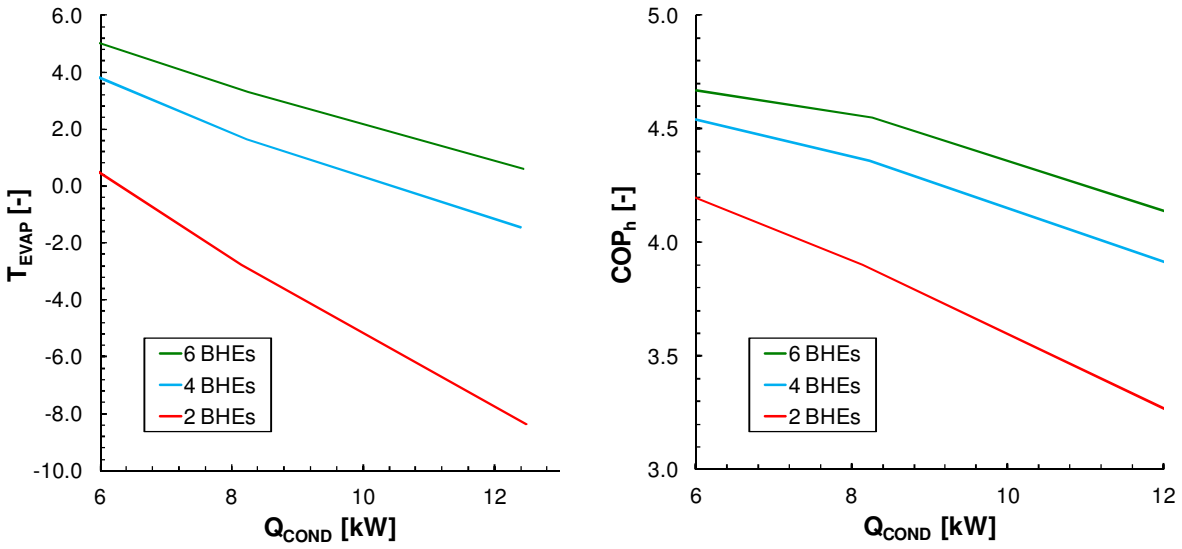

Figure 6.7: Trend of evaporation temperature and *COP* during the heating mode of GWHP at varying the heating power on the user side.

It is worth noting that:

- the influence of the proximity of boreholes on heat transfer in the ground has been neglected;

- the numerical results have been reported considering a GCHP operational time of about 10 hours.

In Figure 6.7, when the heating capacity increases from 6 kW to 12 kW, both the evaporation temperature and the COP_h decrease in all cases. For example, in case of 6 BHEs the evaporation temperature and COP_h decrease, respectively, from 5 to 0.6°C and from 4.67 to 4.10. When the number of BHEs is low, the heat transfer area on ground side is reduced. For this reason, the evaporation temperature has a huge decrease and the electrical power needed to exchange the same heat flow rate is higher, affecting in significant way the GCHP performance. For example, at Q_{COND} = 8 kW, the T_{EVAP} and the COP_h are, respectively, equal to 3.3°C and 4.55 in case of 6 BHEs, and -2.76 °C and 3.9 in case of 2 BHEs. In addition, when the heating capacity is increased, the decrease of GCHP performance is more pronounced at lower number of BHEs. The worst condition is achieved at Q_{COND} = 12 kW in case of 2 BHEs with a COP_h of 3.2.

During the cooling mode of GWHP, the numerical tests have been performed at varying the cooling capacity from 6 to 12 kW at a inlet water temperature of 12°C at the evaporator.
Here, the investigation has been focused on the effect of number of BHEs on condensation temperature T_{COND} and the Coefficient Of Performance COP_c (Eq.5.55).

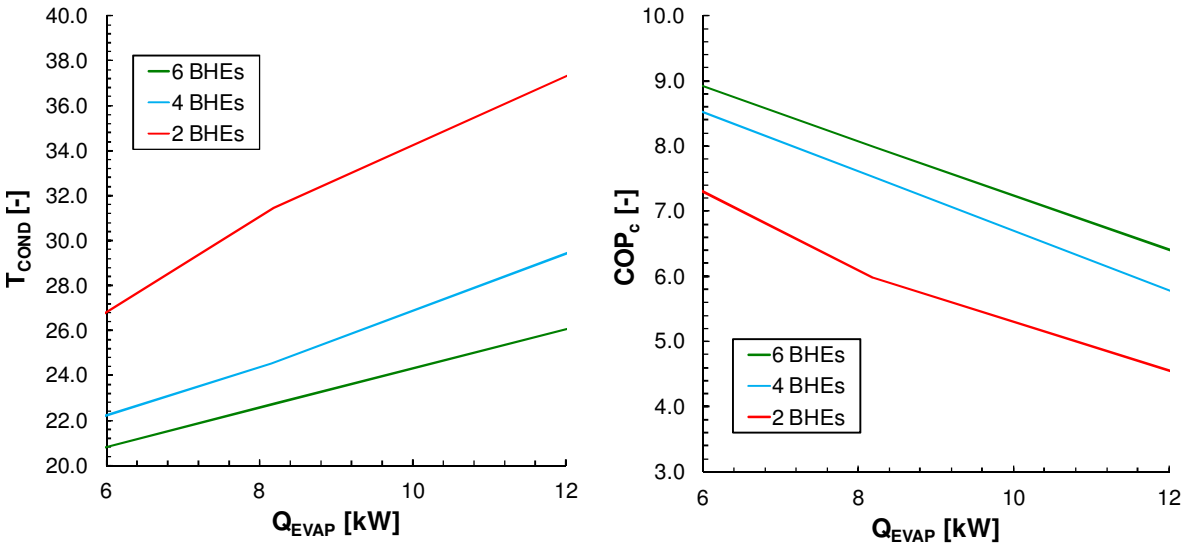

Figure 6.8: Trend of condensation temperature and *COP* during the cooling mode of GWHP at varying the cooling power on the user side.

In Figure 6.8, when the cooling capacity increases from 6 kW to 12 kW, the condensation temperature increases and the COP_c decreases in all cases. For example, in case of 6 BHEs the condensation temperature increases and COP_c decreases, respectively, from 20.7 to 26.5°C and from 9.0 to 6.2. When the number of BHEs is low, the heat transfer area on ground side is reduced. For this reason, the condensation temperature has a huge increase and the electrical power needed to exchange the same heat flow rate is higher, affecting in significant way the GCHP performance. For example, at Q_{EVAP} = 8 kW, the T_{COND} and the COP_c are, respectively, equal to 22.7°C and 8.0 in case of 6 BHEs, and 31.5 °C and 6.0 in case of 2 BHEs. In addition, when the cooling capacity is increased, the decrease of GCHP

performance is more pronounced at lower number of BHEs. The worst condition is achieved at Q_{EVAP} = 12 kW in case of 2 BHEs with a COP_c of 4.5.

6.3.2 Ground fouling

The tests performed in the previous section have been done considering a GCHP operational time of only 10 hours. This value is very small compared to the seasonal operation time and it is not enough large to analyze the effect of 'ground fouling' on GCHP performance.

For this reason, here, the numerical simulations have been performed enlarging the operational time until a value of 1000 h during heating and cooling mode.

In Table 6.5 the COP_h of GCHE has been reported during the heating mode at increasing operating time with a different number of BHEs and at Q_{COND} of about 8 kW. When the time increases the effect of ground cooling on GCHE performance can be noted and its influence has a different behavior at varying the number of boreholes. For example, in case of No. BHEs = 6 the COP_h decreases of 2.2% when the GCHE operates for 1000 h; whereas, in case of No. BHEs = 2, the COP_h decreases of 5.4%.

Table 6.5: Results during winter conditions at different operating time of GCHE varying the number of BHEs.

Winter conditions			
Time [h]	COP_h(@6BHEs)	COP_h(@4BHEs)	COP_h(@2BHEs)
10	4.55	4.36	3.9
500	4.47	4.26	3.73
1000	4.45	4.23	3.69

The same investigation has been performed for the cooling mode of GCHP and at Q_{EVAP} of about 8 kW. Here, when the time increases the ground heating affects the GCHE performance in different way at varying the number of boreholes. For example, in case of No. BHEs = 6 the COP_c decreases of 4.9% when the GCHE operates for 1000 h; whereas, in case of No. BHEs = 2, the COP_c decreases of 15.1%.

Table 6.6: Results during summer conditions at different operating time of GCHE varying the number of BHEs.

Summer conditions			
Time [h]	COP_c(@6BHEs)	COP_c(@4BHEs)	COP_c(@2BHEs)
10	7.99	7.54	5.98
500	7.70	7.09	5.28
1000	7.60	6.95	5.08

In conclusion, from this analysis it has been noted that a lower number of BHEs carries out a lower GCHP performance both in short and long term. This aspect is important because when the GCHP and AWHP will be compared to decide the best source, the logic control of dual source will change according to by the No. of boreholes heat exchangers.

6.4 Logic control of a dual-source heat pump

In this section, the heat transfer with air or with ground are considered on ambient side to identify the best source at varying operating conditions, the No. BHEs and the heating/cooling demanded by the user. As described in Section 5.1 and shown in Figure 5.1, in the dual-source heat pump here presented on the user side, the BPHE heat exchanger is considered, whereas, on the air and ground side, the minichannel heat exchanger and the coupled BPHE-BHE heat exchangers are respectively used.

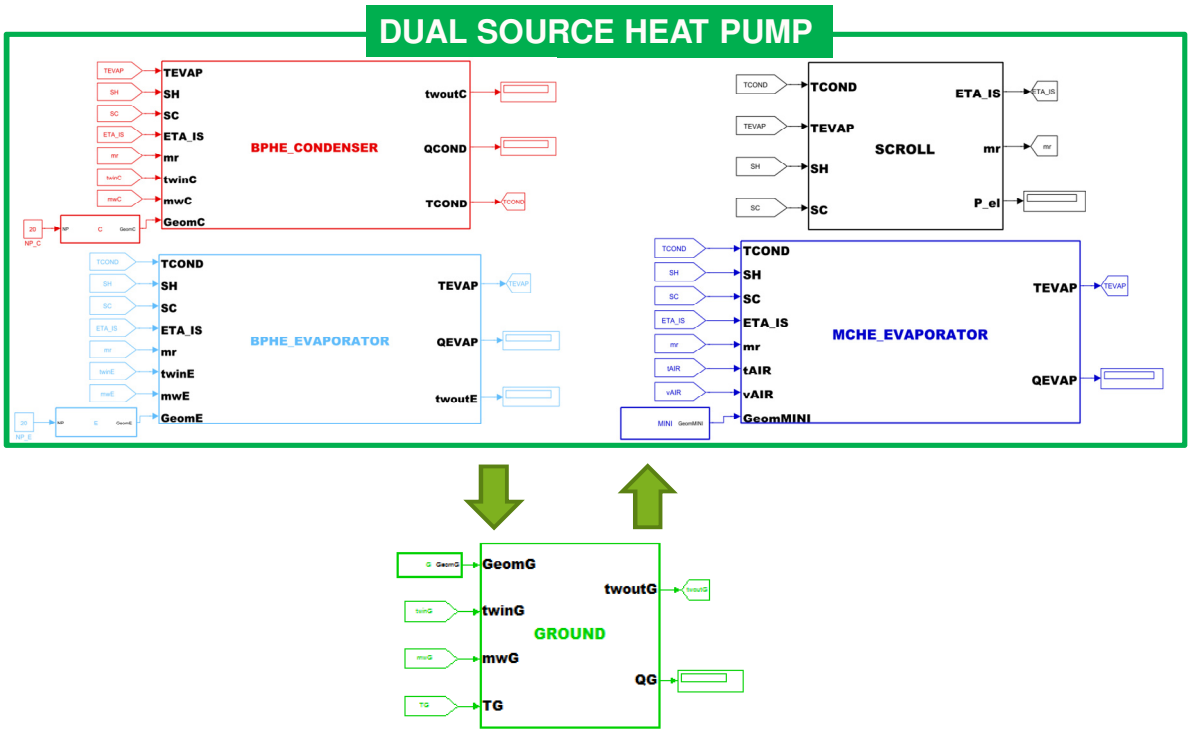

Figure 6.9: Sketch of the transient dual-source heat pump model developed in Matlab-Simulink® environment.

In Figure 6.9 the overall model of the dual-source heat pump, developed in Matlab-Simulink® environment, is here reported during the heating mode. This figure shows the input and the output for all subsystems that are described in detail in Sections 5.2.2-5.2.3-5.2.5-6.2. Each subsystem transfers the necessary information with the other blocks through its input and output. Only when each subsystem has obtained all the input variables from the other blocks, it can run and transfers its output to the near blocks. In this mode, it is possible to study the best strategy control for the machine, deciding through logic controls which source is the best solution to guarantee the highest possible COP. During this investigation, the GCHP and AWHP have been run separately searching at which air temperature the AWHP had the same COP and performed the same heating/cooling capacity demanded by the user.

Before showing the numerical results during the heating and cooling mode, the following considerations are reported:

1) on user side, the BPHE is symmetric and the geometry adopted is that reported in GEOTeCH project and pure water is used as fluid;

2) on ground side, the BPHE is asymmetric and the geometry is that reported in GEOTeCH project;
3) on ground side, the BHE geometry is described in Table 6.2 and brine is used as fluid;
4) on air side, the MCHE geometry is reported in Table 5.14;
5) a scroll compressor is used (i.e. Copeland, Table 5.10) and R32 is adopted as refrigerant;
6) the pure water and brine mass flow rates and the face velocity have been chosen keeping a constant glide temperature of 5 K on user side, 3 K on ground side and 5 K on air side;
7) the superheating and the subcooling are, respectively, equal to 5 K and 1 K;
8) the influence of the proximity of boreholes on heat transfer in the ground has been neglected;
9) the latent heat flow rate due to the occurring of air dehumidification has not taken into account; however a inlet specific humidity of 0.85 and 0.35 have been, respectively, considered during the heating and cooling mode.
10) An operational time of about 10 hours for GCHP has been considered.
11) On the user side, the inlet water temperature is 40°C during the heating mode and 12°C during the cooling mode.

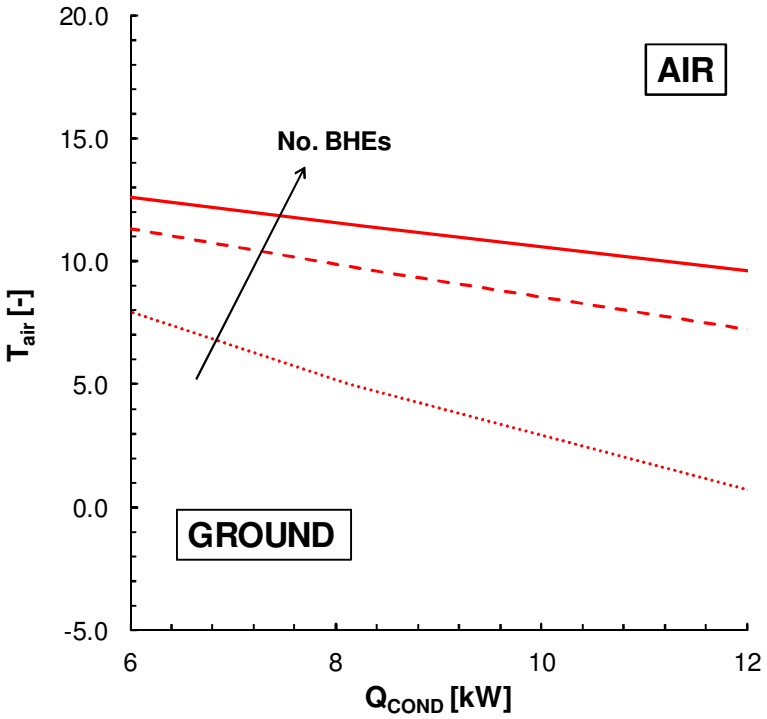

Figure 6.10: Logic control of dual-source heat pump in winter conditions.

In Figure 6.10 the trends of air temperature, at which the AWHP and GCHP have the same COP_h and heating capacity demanded by user, are depicted. These trends have been obtained at varying the number of borehole heat exchangers and ranging the heating

capacity. In case of No. BHEs = 6, the equal performance of two systems is achieved at T_{air} = 12.6 °C and 9.4 °C when the user demands a heating power of 6 kW and 12 kW, respectively. It is worth noting that, when the No. BHEs is lower, the equal performance between the two systems is reached ad lower values of air temperature. For example, in case of No. BHEs = 2, the air temperature varies from 8°C to 0°C when varying the heating capacity from 6 kW to 12 kW. From these numerical results, at decreasing of No. BHEs and increasing of heating capacity, it is more convenient to use the air than the ground as source. In particular, at the worst conditions (i.e. No. BHEs = 2) the dual-source heat pump performs better with air-source if the air temperature during the day is higher than 8 - 0°C when a heating power of 6-12 kW is demanded by the user.

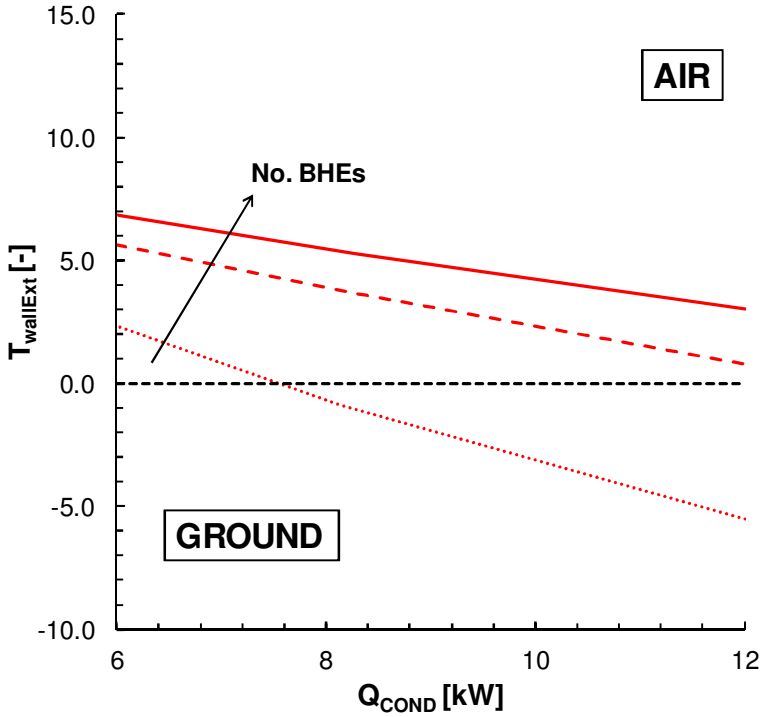

Figure 6.11: Trends of external wall temperature in the MCHE referred to the logic control of dual-source in winter conditions.

The logical control of dual-source heat pump reported in Figure 6.10 does not consider the possible problem of the occurring of frost on air side during the winter conditions. As discussed in Section 5.4.1, this phenomenon can cause technical problems and lower performance of AWHP due to the defrost operations. For this reason, the trends of external wall of MCHE (on air side) have been reported in Figure 6.11 for the same operating conditions of Figure 6.10. In case of the lowest number of BHEs, the outer wall of MCHE becomes below zero at Q_{COND} higher than about 7.6 kW to obtain the equal performance between AWHP and GCHP; whereas for the other cases this aspect has not been noted. In conclusion, nevertheless the map of Figure 6.10 suggests to use the air as source when Q_{COND} varies from 7.6 kW to 12 kW and T_{air} is higher than 5.5°C - 0°C in case of 2 BHEs, it would be better to use however the ground source to avoid the issues of defrost operation

on air side. For this reason, the map of Figure 6.10 would be modified in case of 2 BHEs and the better performance of AWHP will be achieved for higher air temperature.
Considering 0°C as lower limit of the outer wall temperature at which the air is still preferred to use as source in case of 2 BHEs, the map of Figure 6.10 has been modified as shown in Figure 6.12.

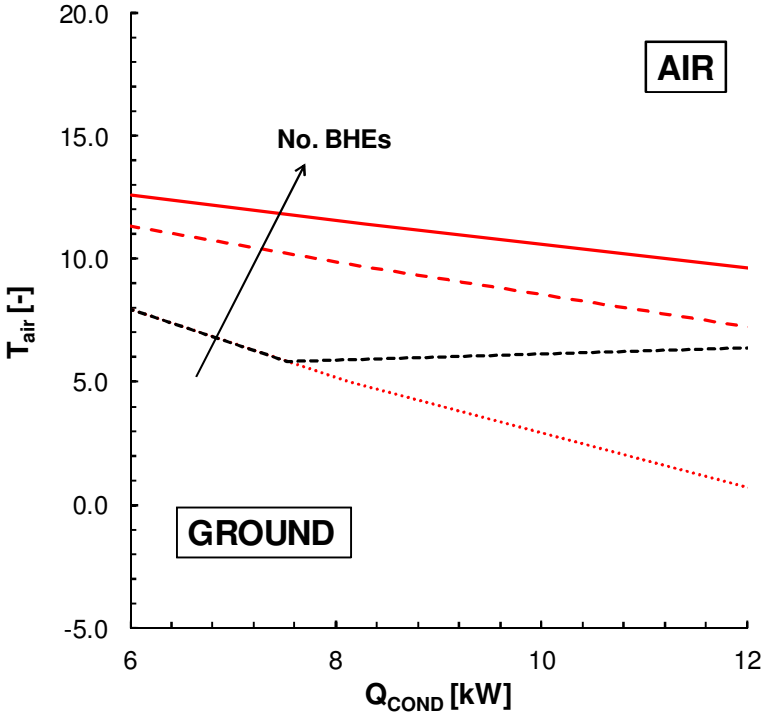

Figure 6.12: The modified map of logic control of dual-source heat pump in winter conditions, considering the defrost issue.

In Figure 6.13 the trends of air temperature, at which the AWHP and GCHP have the same COP_c and cooling capacity demanded by user, are depicted. These trends have been obtained at varying the number of borehole heat exchangers and ranging the cooling capacity. In case of No. BHEs = 6, the equal performance between the two systems is achieved at T_{air} = 14.2 °C and 17.8 °C when the user demands a heating power of 6 kW and 12 kW, respectively. It is worth noting that, when the No. BHEs is lower, the equal performance is reached at higher values of air temperature. For example, in case of No. BHEs = 2, the air temperature varies from 20°C to 28.5°C when varying the cooling capacity from 6 kW to 12 kW. From these numerical results, at decreasing of No. BHEs and increasing of cooling capacity, the operating region, where the air is preferred as source, becomes larger. In particular, at the worst conditions (i.e. No. BHEs = 2) the dual-source heat pump performs better with air-source if the air temperature during the day is lower than 20 – 28.5°C when a cooling power of 6-12 kW is demanded by the user.
From the Figure 6.12 and Figure 6.13 it has been observed that:

- During the heating mode, the ground is the best source when the air temperature are rather frigid (T_{air} < 6°C, in case of No. BHEs = 2);

- During the cooling mode, the ground is the best source when the summer weather is warm (T_{air} > 22°C, in case of No. BHEs = 2);
- If the number of BHEs increases then the operating region, where the ground is preferred as source, becomes larger.

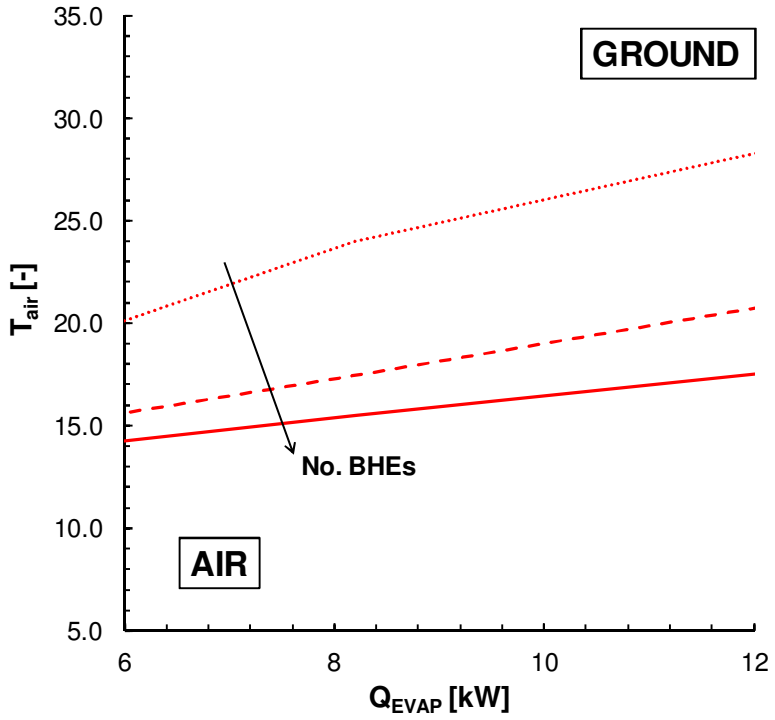

Figure 6.13: Logic control of dual-source heat pump in summer conditions.

From these observations, the dual-source achieves higher *COP* with air source primarily when the outdoor condition are temperate during the heating and cooling season (i.e. typical conditions of mid-season). In addition, it is worth highlighting that:

- the latent heat flow rate on air side has not been into account. When the air dehumidification is considered during cooling season on ambient side, the global heat transfer coefficient on air side is increased and the logic map shown in Figure 6.12 would be in turn modified.
- Since the numerical simulations have been performed taking into account an operating time of 10 h, the effect of ground overcooling during the heating season (or ground overheating during the cooling season) has not been considered. This effect will carry out a worst performance of dual-source system if the ground is intensively as source for a long time, as shown in Table 6.5 and in Table 6.6. For this reason, an optimization of logic control of dual-source is needed to include also the long term effect mitigating the occurring of 'ground fouling'.

In Table 5.1, it has been discussed that the installation cost of an air heat exchanger are lower than that of BHEs. The physical model of AWHP and GCHP have been described in detail in the previous and in this chapter of thesis. These models could be also applied to optimize the design the dual-source system referring to the heating and cooling nominal

power demanded by the user. In this way, it would be possible to decrease the installation cost and improve the pay-back period of the system analyzing the seasonal Coefficient Of Performance at reducing the number of borehole heat exchangers and taking advantage of air heat exchanger during the mid-seasonal periods.

NOMENCLATURE

A	[m²]	Area
b	[m]	Corrugation depth
C	[J K⁻¹]	Thermal capacity
COP	[-]	Coefficient Of Performance
D	[m]	Diameter
f	[-]	Fanning friction factor
fz	[Hz]	Frequency
G	[kg m⁻²s⁻¹]	Mass flux
H	[J kg⁻¹]	Enthalpy
h	[W m⁻² K⁻¹]	Heat transfer coefficient
L	[m]	Length
p	[bar]	Pressure
P_{el}	[W]	Electrical power
Q	[W]	Heat flow rate
R	[K W⁻¹]	Thermal resistance
Re	[-]	Reynolds number
SC	[K]	Subcooling
SH	[K]	Superheating
T	[K]	Temperature
V	[m⁻³]	Volume
W	[m]	Width
x	[-]	Vapour quality

Greek characters

β	[°]	Chevron angle
δ	[m]	Condensate liquid thickness
η	[-]	Efficiency
λ	[W m⁻¹K⁻¹]	Molecular thermal conductivity
μ	[Pa s]	Molecular dynamic viscosity
ρ	[kg m⁻³]	Density
σ	[N m⁻¹]	Surface tension
τ	[s]	Time
φ	[-]	Enlargement factor

Subscripts

c	Cooling
cond	Condensation
des	Desuperheating
dryout	Dryout
evap	Evaporation
f	Fluid
g	Grout
gl	Global
h	Heating
is	Isentropic
lat	Latent
p	Pipe
s	Soil
sat	saturation
sens	Sensible
sub	Subcooling
sup	Superheating
svc	Superheated vapour condensation
vol	Volumetric

7 CONCLUSIONS

The research activity is focused on two-phase heat transfer in minichannels and the application of minichannels in reversible heat pumps.
At small scale new and several physical parameters can influence in significant way the condensation mechanisms. In the present state of art, no numerical model available in the literature has been validated against an experimental data set covering a complete range of operating conditions, channel dimensions and geometries. For this reason, in the first part, a detailed numerical and experimental study of condensation mechanisms inside a single minichannel has been performed, specifically at those operating conditions (low mass flux) that can occur in refrigeration systems and that are the least investigated in the literature due to issues to measure the heat transfer at few watts with low uncertainties. During this analysis the effect of different parameters (e.g. channel geometry, size and orientation, mass flux, fluid properties, gravity, surface tension and unsteady flow) on condensation heat transfer has been studied in detail supporting the numerical investigation with experimental data and visualizations.
In the second part of the thesis the application of minichannel technology has been investigated in a reversible water-to-water and air-to-water heat pump. The use of minichannels in the heat exchangers with air allows to significantly decrease the refrigerant charge as compared to a conventional finned coil heat exchanger. This is particularly useful in a reversible heat pump.
A physical model has been built and validated against experimental data to evaluate the performance of a reversible water-to-water and air-to-water heat pump using minichannels, taking into account the possibility (on the water side) of transferring heat with the ground.
With these models it is possible to predict the performance and to study the best control for a reversible dual source heat pump, deciding which source is the best to be used and at which time during the heating and cooling demand by the user.

1. *Experimental analysis of condensation inside a single minichannel*

Experimental data with R134a and R1234ze(E) condensing inside horizontal 1 mm diameter minichannels with circular and square cross section shapes have been reported enlarging the database of previous works. In addition, at similar channel size (e.g. 1 mm), the experimental data of R134a, R32, R717, R290, R152a and R1234ze(E) have been also considered to analyze the influence of saturation-to-wall temperature difference, channel geometry, mass flux and fluid properties. From this experimental database, at low mass velocity ($G \leq 200$ kg m^{-2} s^{-1}) it has been observed that the influence of mass flux is reduced and the local heat transfer coefficient is significantly affected by the thermal resistance of liquid film.
Considering the heat transfer coefficients during R134a condensation at low mass velocity (from 65 to 150 kg m^{-2} s^{-1}) at varying the water temperature at the inlet of measuring

section, a significant influence of saturation-to-wall temperature difference ΔT_{SW} has been noted primarily at G = 65 kg m^{-2} s^{-1} in the circular channel. In particular at decreasing of ΔT_{SW} the increase of heat transfer coefficient has been observed. The comparison of heat transfer coefficients between the square and the circular channel has been performed for R134a, R1234ze(E), R32 and R152a and for all fluids the enhancement of condensation heat transfer due to the presence of corners has been verified at decreasing of mass flux. The HTC trends of R717 and R32 have shown higher value than those of R134a and R1234ze(E) due to the high liquid thermal conductivity. For the fluids with low vapour density (i.e. high vapour velocity at the same value of mass velocity), a mass flux effect on condensation heat transfer is presented at G around 200 kg m^{-2} s^{-1}. This phenomenon has been noted previously for R290 (ρ_V = 30.2 kg m^{-3}) and R717 (ρ_V = 12.0 kg m^{-3}); whereas it is not present for R32, where the HTC trends at G = 100 kg m^{-2} s^{-1} and G = 200 kg m^{-2} s^{-1} are roughly the same. Finally, an attempt has been done considering the dimensionless gas velocity J_V and the two-phase Weber number We as parameters to determine, respectively, the gravity and surface tension effects.
In this way it has been possible to put limitations on the applicability of macroscale empirical correlations to predict the heat transfer at small scale.

2. *Steady-state VOF simulations of condensation inside a single minichannel*

Numerical simulations using the VOF method have been performed in three-dimensional and steady-state configuration at low mass flux in a single horizontal minichannel during condensation of different fluids, channel geometry, diameter size and operating conditions.
The numerical simulations are an useful tool to obtain an “insight view” for a qualitative analysis, which is almost impossible to achieve experimentally without affecting the phenomenon itself.
In particular the effect of gravity and surface tension forces has been investigated in square channel and the numerical results have been compared against those obtained by Da Riva et al. [20] in the circular channel. When the surface tension and the gravity forces are not considered inside the square and circular channel, a uniform liquid film thickness is obtained along the perimeter decreasing significantly the local heat transfer coefficient. In addition, the numerical simulations are able to catch the enhancement of heat transfer coefficients in square channel as compared to those in circular one as shown in the experimental data for x > 0.5; whereas at lower vapour quality, in accordance with the theoretical model of Wang and Rose [29], the numerical simulations predict higher heat transfer coefficients in circular channel as compared to the experimental data.
With the numerical results and the application of Cioncolini and Thome [47] model, it has been verified that, at same mass velocity, when the vapour density is low (i.e. high vapour velocity) and the molecular liquid viscosity is low (such as R717 and R290) some turbulence can occur inside the liquid film showing some effect of mass velocity also at low mass velocity, explaining in this way the different HTC trends of R717 and R290 as compared to other fluids.

A comparison has been also performed in terms of local heat transfer coefficients along angular coordinate to investigate, at same operating conditions, the local heat transfer coefficient different refrigerants. From this analysis R717 and R32 results the refrigerants with highest heat transfer coefficients as compared to R1234ze(E) and R134a.
Steady-state simulations of R134a condensation inside 3.4 mm horizontal circular channel have been also performed. The numerical results have been validated against experimental data obtained by Azzolin et al. [7]. It has been demonstrated that in larger channels the effect of surface tension become negligible and there is a decrease of heat transfer coefficient due to a higher liquid film thickness along the channel wall (at G = 100 kg m^{-2} s^{-1} and at x = 0.6 the mean liquid film thickness calculated is about 40 μm and 120 μm, for 1 mm and 3.4 mm channel, respectively). Furthermore, from the deviations between the numerical results and experimental data, it has been verified that, in 3.4 mm channel, the mass flux effect on HTC is more pronounced than in 1 mm channel (mass flux from 50 kg m^{-2} s^{-1} to 100 kg m^{-2} s^{-1}). From the analysis of heat transfer in 3.4 mm and the application of Cioncolini et al. [54] model, it has been also demonstrated that this aspect is due to two contributions: the presence of waves at the vapor-liquid interface (as shown by Azzolin et al. [7]) and transition to turbulent flow in liquid film. However, since the interfacial waves occur only at the bottom of the channel where the liquid film is thick, their contribution on the enhancement of the average heat transfer coefficient is limited and steady-state numerical simulations should still give satisfactory results.

3. *Transient VOF simulations of downflow condensation inside a vertical minichannel*

The aim of this part of the thesis is to assess the capability of the VOF method to capture the interfacial instabilities and to investigate their influence on condensation heat transfer. For this reason, the 3.4 mm channel has been oriented in vertical way (where the occurring of waves can be noted along the wall of the channel) and unsteady-state simulations have been performed to predict the two-phase flow during the downflow condensation.
Both in numerical simulations and in experimental visualizations the presence of waves at the vapour-liquid interface and, also, other phenomena (i.e. entrainment), when the mass flux increases, have been shown. Comparing the results of unsteady-state and steady-state simulations, the enhancement of heat transfer coefficient due to the presence of waves has been verified. Finally, it has been demonstrated that the presence of waves carries out a lower average liquid film thickness and an intensification of the turbulence inside the liquid film.

4. *The application of minichannel technology in heat pumps*

In the second part of thesis the application of the minichannel technology has been investigated in a reversible dual source heat pump to satisfy the heating and cooling demand by the user.

This system gives the possibility to exchange heat with air or water, performing as a air-to-water or water-to-water reversible heat pump, respectively; when the water is used as sink/source, the heat flow rate can be rejected or removed through borehole heat exchangers installed in the ground.
The use of minichannels in the heat exchangers with air has been considered allowing to significantly decrease the refrigerant charge as compared to a conventional finned coil heat exchanger. This is particularly useful in a reversible heat pump.
On the water side the brazed plate heat exchanger with a hydraulic diameter lower than 3 mm and on the air side a finned coil using minichannels have been considered as condenser or evaporator; whereas a single U-tube borehole heat exchanger has been considered for the heat transfer with the ground.
The physical model has been described, built and validated against experimental data to evaluate the performance of a reversible water-to-water and air-to-water heat pump using minichannels, taking into account the possibility (on the water side) of transferring heat with the ground.
With these models it is possible to predict the performance and to design a dual source heat pump using minichannels. Finally, it is possible to study the best control for the heat pump, deciding which source is the best to be used and at which time when varying the external air temperature and the number of borehole heat exchangers.

REFERENCES

[1] A. Cavallini, D. Del Col, L. Doretti, M. Matkovic, L. Rossetto, C. Zilio, G. Censi, Condensation in horizontal smooth tubes: A new heat transfer model for heat exchanger design, 27 (2006) 31-38.

[2] K.W. Moser, R.L. Webb, B. Na, A new equivalent Reynolds number model for condensation in smooth tubes, Journal of Heat Transfer. 120 (1998) 410-417.

[3] J.W. Coleman, S. Garimella, Characterization of two-phase flow patterns in small diameter round and rectangular tubes, Int. J. Heat Mass Transf. 42 (1999) 2869-2881.

[4] J.W. Coleman, S. Garimella, Two-phase flow regimes in round, square and rectangular tubes during condensation of refrigerant R 134a, Int. J. Refrig. 26 (2003) 117-128.

[5] G. Nema, S. Garimella, B.M. Fronk, Flow regime transitions during condensation in microchannels, Int. J. Refrig. 40 (2014) 227-240.

[6] J. El Hajal, J.R. Thome, A. Cavallini, Condensation in horizontal tubes, part 1: Two-phase flow pattern map, Int. J. Heat Mass Transfer. 46 (2003) 3349-3363.

[7] M. Azzolin, Experimental study of phase change heat transfer in minichannels for ground and space applications, PhD Thesis (2016).

[8] M. Azzolin, S. Bortolin, D. Del Col, Measurements and visualization during condensation inside a 3 mm diameter channel, 9th International Conference on Multiphase Flow, ICMF-2016. (2016).

[9] M. Zhang, R.L. Webb, Correlation of two-phase friction for refrigerants in small-diameter tubes, Exp. Therm. Fluid Sci. 25 (2001) 131-139.

[10] M.M. Shah, An improved and extended general correlationfor heat transfer during condensationin plain tubes, HVAC and R Research. 15 (2009) 889-913.

[11] A. Cavallini, S. Bortolin, D. Del Col, M. Matkovic, L. Rossetto, Condensation heat transfer and pressure losses of high- and low-pressure refrigerants flowing in a single circular minichannel, 32 (2011) 90-98.

[12] D. Del Col, S. Bortolin, A. Cavallini, M. Matkovic, Effect of cross sectional shape during condensation in a single square minichannel, Int. J. Heat Mass Transfer. 54 (2011) 3909-3920.

[13] D. Del Col, M. Bortolato, M. Azzolin, S. Bortolin, Condensation heat transfer and two-phase frictional pressure drop in a single minichannel with R1234ze(E) and other refrigerants, Int. J. Refrig. 50 (2015) 87-103.

[14] T.M. Bandhauer, A. Agarwal, S. Garimella, Measurement and modeling of condensation heat transfer coefficients in circular microchannels, Journal of Heat Transfer. 128 (2006) 1050-1059.

[15] M. Matkovic, A. Cavallini, D. Del Col, L. Rossetto, Experimental study on condensation heat transfer inside a single circular minichannel, Int. J. Heat Mass Transfer. 52 (2009) 2311-2323.

[16] N. Liu, J.M. Li, J. Sun, H.S. Wang, Heat transfer and pressure drop during condensation of R152a in circular and square microchannels, Exp. Therm. Fluid Sci. 47 (2013) 60-67.

[17] K. Sakamatapan, J. Kaew-On, A.S. Dalkilic, O. Mahian, S. Wongwises, Condensation heat transfer characteristics of R-134a flowing inside the multiport minichannels, Int. J. Heat Mass Transfer. 64 (2013) 976-985.

[18] S. Bortolin, E. Da Riva, D. Del Col, Condensation in a square minichannel: Application of the VOF method, 35 (2014) 193-203.

[19] D. Del Col, M. Bortolato, M. Azzolin, S. Bortolin, Effect of inclination during condensation inside a square cross section minichannel, Int. J. Heat Mass Transfer. 78 (2014) 760-777.

[20] E. Da Riva, D. Del Col, Effect of gravity during condensation of R134a in a circular minichannel: VOF simulation of annular condensation, Microgravity Sci Technol. 23 (2011) S87-S97.

[21] I. Marchuk, Y. Lyulin, O.A. Kabov, Theoretical and experimental study of convective condensation inside a circular tube, Interfacial Phenomena and Heat Transfer. 1 (2013).

[22] S. Nebuloni, J.R. Thome, D. Del Col, Conjugate heat transfer in annular laminar film condensation in microchannels: Comparison of numerical model to experiemental results, 2 (2010) 245-252.

[23] B.M. Fronk, S. Garimella, Heat transfer and pressure drop during condensation of ammonia in microchannels, (2012) 399-409.

[24] D. Del Col, M. Bortolato, S. Bortolin, Comprehensive experimental investigation of two-phase heat transfer and pressure drop with propane in a minichannel, Int. J. Refrig. 47 (2014) 66-84.

[25] T. Boeck, J. Li, E. Lopez-Pages, P. Yecko, S. Zaleski, Ligament formation in sheared liquid-gas layers, Theor. Comput. Fluid Dyn. 21 (2007) 59-76.

[26] J. Brackbill, D.B. Kothe, C. Zemach, A continuum method for modeling surface tension, Journal of computational physics. 100 (1992) 335-354.

[27] E. Da Riva, D. Del Col, S.V. Garimella, A. Cavallini, The importance of turbulence during condensation in a horizontal circular minichannel, Int. J. Heat Mass Transfer. 55 (2012) 3470-3481.

[28] H.S. Wang, J.W. Rose, Film condensation in horizontal circular section microchannels, International Journal of Engineering Systems Modelling and Simulation. 1 (2009) 115-121.

[29] H.S. Wang, J.W. Rose, Theory of heat transfer during condensation in microchannels, Int. J. Heat Mass Transfer. 54 (2011) 2525-2534.

[30] H.S. Wang, J.W. Rose, A theory of film condensation in horizontal noncircular section microchannels, Journal of Heat Transfer. 127 (2005) 1096-1105.

[31] S. Nebuloni, J.R. Thome, Numerical modeling of laminar annular film condensation for different channel shapes, Int. J. Heat Mass Transfer. 53 (2010) 2615-2627.

[32] D.C. Wilcox, Turbulence Modeling for CFD, DCW industries La Canada, CA, 1998.

[33] E. Da Riva, D. Del Col, Numerical simulation of laminar liquid film condensation in a horizontal circular minichannel, Journal of heat transfer. 134 (2012) 051019.

[34] F.R. Menter, Two-equation eddy-viscosity turbulence models for engineering applications, AIAA J. 32 (1994) 1598-1605.

[35] P. Bradshaw, D. Ferriss, N. Atwell, Calculation of boundary-layer development using the turbulent energy equation, J. Fluid Mech. 28 (1967) 593-616.

[36] W.H. Lee, Pressure iteration scheme for two-phase flow modeling, IEEE/Engineering in Medicine and Biology Society Annual Conference. 1 (1980) 407-431.

[37] L.D. Berman, On the effect of molecular-kinetic resistance upon heat transfer with condensation, Int. J. Heat Mass Transfer. 10 (1967) 1463.

[38] H.S. Wang, J.W. Rose, Effect of interphase matter transfer on condensation on low-finned tubes - a theoretical investigation, Int. J. Heat Mass Transfer. 47 (2004) 179-184.

[39] Y. Zhang, A. Faghri, M.B. Shafii, Capillary blocking in forced convective condensation in horizontal miniature channels, Journal of Heat Transfer. 123 (2001) 501-511.

[40] H. Wu, X. Peng, P. Ye, Y.E. Gong, Simulation of refrigerant flow boiling in serpentine tubes, Int. J. Heat Mass Transfer. 50 (2007) 1186-1195.

[41] Z. Yang, X. Peng, P. Ye, Numerical and experimental investigation of two phase flow during boiling in a coiled tube, Int. J. Heat Mass Transfer. 51 (2008) 1003-1016.

[42] S.W. Welch, J. Wilson, A volume of fluid based method for fluid flows with phase change, Journal of computational physics. 160 (2000) 662-682.

[43] D.L. Youngs, Time-dependent multi-material flow with large fluid distortion, Numerical methods for fluid dynamics. 24 (1982) 273-285.

[44] H. Ganapathy, A. Shooshtari, K. Choo, S. Dessiatoun, M. Alshehhi, M. Ohadi, Volume of fluid-based numerical modeling of condensation heat transfer and fluid flow characteristics in microchannels, Int. J. Heat Mass Transfer. 65 (2013) 62-72.

[45] C.W. Hirt, B.D. Nichols, Volume of fluid (VOF) method for the dynamics of free boundaries, Journal of Computational Physics. 39 (1981) 201-225.

[46] R. Gupta, D.F. Fletcher, B.S. Haynes, On the CFD modelling of Taylor flow in microchannels, Chemical Engineering Science. 64 (2009) 2941-2950.

[47] A. Cioncolini, J.R. Thome, Algebraic turbulence modeling in adiabatic and evaporating annular two-phase flow, Int J Heat Fluid Flow. 32 (2011) 805-817.

[48] O. Baker, Simultaneus flow of oil and gas, Oil Gas J. 53 (1954) 185-190.

[49] J.M. Mandhane, G.A. Gregory, K. Aziz, A flow pattern map for gas—liquid flow in horizontal pipes, Int. J. Multiphase Flow. 1 (1974) 537-553.

[50] Y. Taitel, A.E. Dukler, A model for predicting flow regime transitions in horizontal and near horizontal gas-liquid flow, AIChE J. 22 (1976) 47-55.

[51] J. Weisman, D. Duncan, J. Gibson, T. Crawford, Effects of fluid properties and pipe diameter on two-phase flow patterns in horizontal lines, Int. J. Multiph. Flow. 5 (1979) 437-462.

[52] H. Ide, A. Kariyasaki, T. Fukano, Fundamental data on the gas-liquid two-phase flow in minichannels{star, open}{star, open}A preliminary version of this paper was presented at ICMMO5: Third International Conference on Microchannels and Minichannels, held at University of Toronto, June 13-15, 2005, organized by S.G. Kandlikar and M. Kawaji, CD-ROM Proceedings, ISBN: 0-7918-3758-0, ASME, New York, International Journal of Thermal Sciences. 46 (2007) 519-530.

[53] J.R. Thome, J. El Hajal, A. Cavallini, Condensation in horizontal tubes, part 2: New heat transfer model based on flow regimes, Int. J. Heat Mass Transfer. 46 (2003) 3365-3387.

[54] A. Cioncolini, D. Del Col, J.R. Thome, An indirect criterion for the laminar to turbulent flow transition in shear-driven annular liquid films, Int. J. Multiphase Flow. 75 (2015) 26-38.

[55] E. Da Riva, D. Del Col, Numerical simulation of churn flow in a vertical pipe, Chemical Engineering Science. 64 (2009) 3753-3765.

[56] M.H. Kebriaee, H. Karabi, S. Khorsandi, M.H. Saidi, Two phase gas-liquid bubbly flow modeling in vertical mini pipe, 3 (2010) 947-956.

[57] G. Qiu, Z. Wu, Y. Jiang, S. Li, W. Cai, Numerical simulation of condensation of upward flow in a vertical pipe, 1D (2014) Fluids Engineering Division.

[58] A.O. Adelaja, J. Dirker, J.P. Meyer, Convective condensation heat transfer of R134a in tubes at different inclination angles, International Journal of Green Energy. 13 (2016) 812-821.

[59] G.F. Hewitt, D. Roberts, Studies of two-phase flow patterns by simultaneous x-ray and flash photography. (1969).

[60] M. Magnini, J.R. Thome, Computational Study of Saturated Flow Boiling Within a Microchannel in the Slug Flow Regime, Journal of Heat Transfer. 138 (2016).

[61] J.F. Urchueguia, M. Zacares, J.M. Corberan, A. Montero, J. Martos, H. Witte, Comparison between the energy performance of a ground coupled water to water heat pump system and an air to water heat pump system for heating and cooling in typical conditions of the European Mediterranean coast, Energy Conversion and Management. 49 (2008) 2917-2923.

[62] N. Pardo, A. Montero, J. Martos, J.F. Urchueguia, Optimization of hybrid - ground coupled and air source - heat pump systems in combination with thermal storage, Appl. Therm. Eng. 30 (2010) 1073-1077.

[63] N. Kuzmic, Y.L.E. Law, S.B. Dworkin, Numerical heat transfer comparison study of hybrid and non-hybrid ground source heat pump systems, Appl. Energy. 165 (2016) 919-929.

[64] D. Del Col, A. Cavallini, E. Da Riva, S. Mancin, G. Censi, Shell-and-tube minichannel condenser for low refrigerant charge, Heat Transfer Eng. 31 (2010) 509-517.

[65] R.L. Amalfi, F. Vakili-Farahani, J.R. Thome, Flow boiling and frictional pressure gradients in plate heat exchangers. Part 1: Review and experimental database, Int. J. Refrig. 61 (2016) 166-184.

[66] R.L. Amalfi, F. Vakili-Farahani, J.R. Thome, Flow boiling and frictional pressure gradients in plate heat exchangers. Part 2: Comparison of literature methods to database and new prediction methods, Int. J. Refrig. 61 (2016) 185-203.

[67] I. Kim, J. Park, Y. Kwon, Y. Kim, Experimental study on R-410a evaporation heat transfer characteristics in oblong shell and plate heat exchanger, Heat Transfer Eng. 28 (2007) 633-639.

[68] J. Huang, T.J. Sheer, M. Bailey-McEwan, Heat transfer and pressure drop in plate heat exchanger refrigerant evaporators, Int. J. Refrig. 35 (2012) 325-335.

[69] Y.Y. Hsieh, T.F. Lin, Evaporation heat transfer and pressure drop of refrigerant R-410A flow in a vertical plate heat exchanger, Journal of Heat Transfer. 125 (2003) 852-857.

[70] Y.Y. Hsieh, T.F. Lin, Saturated flow boiling heat transfer and pressure drop of refrigerant R-410A in a vertical plate heat exchanger, Int. J. Heat Mass Transfer. 45 (2002) 1033-1044.

[71] G.N. Danilova, V.M. Azarskov, B.B. Zemskov, V. Teploobmen, Plastinchatihispariteljan razichnole geometri – heat transfer in plate evaporators of different geometry, Kholod Tek. 4 (1981) 25-31.

[72] D. Han, K. Lee, Y. Kim, Experiments on the characteristics of evaporation of R410A in brazed plate heat exchangers with different geometric configurations, Appl. Therm. Eng. 23 (2003) 1209-1225.

[73] G.A. Longo, G. Righetti, C. Zilio, A new model for refrigerant condensation inside a brazed plate heat exchanger (BPHE), Proceedings of the 15th International Heat Transfer Conference, IHTC-15. (2014).

[74] G.A. Longo, G. Righetti, C. Zilio, A new computational procedure for refrigerant condensation inside herringbone-type Brazed Plate Heat Exchangers, Int. J. Heat Mass Transfer. 82 (2015) 530-536.

[75] Z.H. Ayub, Plate heat exchanger literature survey and new heat transfer and pressure drop correlations for refrigerant evaporators, Heat Transfer Eng. 24 (2003) 3-16.

[76] R. Eldeeb, V. Aute, R. Radermacher, A survey of correlations for heat transfer and pressure drop for evaporation and condensation in plate heat exchangers, Int. J. Refrig. 65 (2016) 12-26.

[77] H. Martin, A theoretical approach to predict the performance of chevron-type plate heat exchangers, Chem. Eng. Process. 35 (1996) 301-310.

[78] R. Shah, W. Focke, Plate heat exchangers and their design theory, Heat Transfer Equipment Design. 227 (1988) 254.

[79] Y. Yan, H. Lio, T. Lin, Condensation heat transfer and pressure drop of refrigerant R-134a in a plate heat exchanger, Int. J. Heat Mass Transfer. 42 (1999) 993-1006.

[80] S. Mancin, D. Del Col, L. Rossetto, Condensation of superheated vapour of R410A and R407C inside plate heat exchangers: Experimental results and simulation procedure, Int. J. Refrig. 35 (2012) 2003-2013.

[81] S. Mancin, D. Del Col, L. Rossetto, R32 partial condensation inside a brazed plate heat exchanger, 36 (2013) 601-611.

[82] W.S. Kuo, Y.M. Lie, Y.Y. Hsieh, T.F. Lin, Condensation heat transfer and pressure drop of refrigerant R-410A flow in a vertical plate heat exchanger, Int. J. Heat Mass Transfer. 48 (2005) 5205-5220.

[83] M.M. Shah, A general correlation for heat transfer during film condensation inside pipes, International Journal of Heat and Mass Transfer. 22 (1979) 547-556.

[84] W. Nusselt, Die Oberflächenkondensation des Wasserdampfes, Zeit Ver. Deut. Ing (VDI). 60 (1919).

[85] R. Webb, Convective condensation of superheated vapor, Transactions-american society of mechanical engineers journal of heat transfer. 120 (1998) 418-421.

[86] R.W. Hyland, A.W. Wexler, Formulations for the thermodynamic properties of the saturated phases of H2O from 173.15 K to 473.15 K, ASHRAE Trans. 89 (1983) 500-519.

[87] D.G. Kröger, Air-Cooled Heat Exchangers and Cooling Towers, PennWell Books, 2004.

[88] V.W. Peppers, A new psychrometric relation for the dewpoint temperature, Unpubl. Available from ASHRAE. (1988).

[89] R.J. Myers, The effect of dehumidification on the air side heat transfer coefficient for a finned-tube coil, (1967).

[90] J.L. Threlkeld, T.H. Kuehn, J.W. Ramsey, Thermal Environmental Engineering, 3rd ed. Pearson. (1988).

[91] A.H. Hassan, J. Gonzálvez-Maciá, S. Martínez-Ballester, J.R. García-Cascales, Development and Validation of a Minichannel Evaporator Model under Different Dehumidifying Conditions, (2016).

[92] F.C. McQuinston, Fin efficiency with combined heat and mass transfer, ASHRAE Trans. 82 (1975) 87-105.

[93] C. Davenport, Heat transfer and flow friction characteristics of louvred heat exchanger surfaces, (1983).

[94] Yu-Juei Chang, Chi-Chuan Wang, A generalized heat transfer correlation for louver fin geometry, Int. J. Heat Mass Transfer. 40 (1997) 533-544.

[95] M. Kim, C.W. Bullard, Air-side thermal hydraulic performance of multi-louvered fin aluminum heat exchangers, Int. J. Refrig. 25 (2002) 390-400.

[96] M. Kim, C.W. Bullard, Erratum: Air-side thermal hydraulic performance of multi-louvered fin aluminum heat exchangers (International Journal of Refrigeration (2002) 25 (390-400) DOI: 10.1016/S0140-7007(01)00025-1), Int. J. Refrig. 28 (2005) 967-968.

[97] M. Kim, C.W. Bullard, Air-side performance of brazed aluminum heat exchangers under dehumidifying conditions, 25 (2002) 924-934.

[98] W.H. McAdams, Heat transmission, McGraw-Hill. 2nd edn (1942).

[99] B.S. Petukhov, V.N. Popov, Theoretical calculation of heat exchange and frictional resistance in turbulent flow in tubes of an incompressible fluid with variable physical properties, High. Temp. 1 (1963) 69-83.

[100] V. Gnielinski, New equations for heat and mass transfer in turbulent pipe and channel flow, International Chemical Engineer. 16 (1976) 359-368.

[101] Z. Liu, R.H.S. Winterton, General correlation for saturated and subcooled flow boiling in tubes and annuli, based on a nucleate pool boiling equation, Int. J. Heat Mass Transfer. 34 (1991) 2759-2766.

[102] G.M. Lazarek, S.H. Black, Evaporative heat transfer, pressure drop and critical heat flux in a small vertical tube with R-113, Int. J. Heat Mass Transfer. 25 (1982) 945-960.

[103] P.A. Kew, K. Cornwell, Correlations for the prediction of boiling heat transfer in small-diameter channels, Appl. Therm. Eng. 17 (1997) 705-715.

[104] L. Sun, K. Mishima, An evaluation of prediction methods for saturated flow boiling heat transfer in mini-channels, Int. J. Heat Mass Transfer. 52 (2009) 5323-5329.

[105] D. Del Col, A. Cavallini, S. Bortolin, M. Matkovic, L. Rossetto, Dryout during flow boiling in a single circular minichannel: Experimentation and modelling, 2 (2009) 447-456.

[106] A. Cavallini, D. Del Col, M. Matkovic, L. Rossetto, Frictional pressure drop during vapour-liquid flow in minichannels: Modelling and experimental evaluation, Int J Heat Fluid Flow. 30 (2009) 131-139.

[107] R. Yun, Y. Kim, C. Park, Numerical analysis on a microchannel evaporator designed for CO2 air-conditioning systems, Appl. Therm. Eng. 27 (2007) 1320-1326.

[108] E. Navarro-Peris, J.M. Corberan, L. Falco, I. Martinez-Galvan, New non-dimensional performance parameters for the characterization of refrigeration compressors, Int. J. Refrig. 36 (2013) 1951-1964.

[109] C.P. Remund, Borehole thermal resistance: laboratory and field studies, ASHRAE Trans. 105 (1999) 439.

[110] G. Hellström, Ground Heat Storage: Thermal Analyses of Duct Storage Systems, .

[111] M.H. Sharqawy, H.M. Badr, E.M. Mokheimer, Investigation of buoyancy effects on heat transfer between a vertical borehole heat exchanger and the ground, Geothermics. 48 (2013) 52-59.

[112] M.H. Sharqawy, E.M. Mokheimer, H.M. Badr, Effective pipe-to-borehole thermal resistance for vertical ground heat exchangers, Geothermics. 38 (2009) 271-277.

[113] D. Bauer, W. Heidemann, H. Muller-Steinhagen, H.-.G. Diersch, Thermal resistance and capacity models for borehole heat exchangers, Int. J. Energy Res. 35 (2011) 312-320.

[114] E.W. Lemmon, M.L. Huber, M.O. McLinden, NIST Standard Reference Database 23: Reference Fluid Thermodynamic and Transport Properties - REFPROP, Version 9.0, (2010).

[115] A. Melinder, E. Granryd, Secondary refrigerants for heat pumps and low temperature refrigeration - A comparison of thermodynamic properties of aqueous solutions and non-aqueous liquids, Dept. of Applied Thermodynamics and Refrigeration. (1992).

[116] M. De Carli, M. Tonon, A. Zarrella, R. Zecchin, A computational capacity resistance model (CaRM) for vertical ground-coupled heat exchangers, Renewable Energy. 35 (2010) 1537-1550.

[117] W. Yang, X. Liang, M. Shi, Z. Chen, A Numerical Model for the Simulation of a Vertical U-Bend Ground Heat Exchanger Used in a Ground-Coupled Heat Pump, International Journal of Green Energy. 11 (2014) 761-785.

[118] S. Yoon, S. Lee, G. Go, A numerical and experimental approach to the estimation of borehole thermal resistance in ground heat exchangers, Energy. 71 (2014) 547-555.

RINGRAZIAMENTI

L'intero lavoro sviluppato in questa tesi è stato svolto presso il Dipartimento di Ingegneria Industriale nell'Università degli Studi di Padova.
In primis vorrei ringraziare il prof. **Davide Del Col**, il quale è stato mio supervisore durante la tesi di laurea magistrale e incredibile mentore durante il dottorato. Lo ringrazio per la pazienza, per i consigli e per la fiducia che ha riposto nel mio lavoro in questi ultimi anni. Devo al prof. **Davide Del Col** questo importante risultato e gli obiettivi raggiunti in questo lavoro di tesi.
Vorrei ringraziare anche in ordine alfabetico ogni elemento del gruppo di ricerca **S.T.E.T.** che mi ha supportato dal punto di vista scientifico, psicologico e personale. Ringrazio i miei colleghi di ufficio, l'**Amministratore Bortolin Stefano**, che mi ha insegnato il metodo VOF e che ha avuto la pazienza di ascoltare qualsiasi mio dubbio e "pazza" teoria, e **Azzolin Marco**, che mi ha incoraggiato e che mi ha fatto da maestro nel Laboratorio di Scambio Termico Bifase. Ringrazio **Berto Arianna** per avermi sopportato come correlatore di tesi ed a lei do il benvenuto in questo incredibile gruppo di ricerca. Ringrazio **Bisetto Alberto**, per il suo mitico Prosecco DOCG e il suo carattere allegro e festaiolo, **Bortolato Matteo**, per i vari party presso Lignano City e per le sue "motivazioni" giornaliere, e **Diani Andrea** per gli incoraggiamenti sul campo… di calcetto. Vorrei ringraziare il mio burlone collega **Dugaria Simone** che mi ha sopportato durante le missioni in Italia ed all'estero. Ringrazio **Martinez David Estefano** e **Parin Riccardo** per le fughe in mensa Forcellini alle ore 11.45 in punto. Ultimo, ma solo in ordine alfabetico, ringrazio **Rossato Marco** (il "Campione") per il continuo sostegno durante l'impegnativa e difficoltosa stesura della tesi.
Vorrei ringraziare i miei genitori e mio fratello Lorenzo per essermi stati vicino con affetto e per i continui consigli presenti e futuri. Infine ringrazio i miei amici di Verona e Padova per avermi fatto sorridere nei momenti più difficili e delicati di questo periodo importante.